

DEPARTAMENTO DE AUTOMÁTICA, INGENIERÍA ELECTRÓNICA E
INFORMÁTICA INDUSTRIAL

ESCUELA TÉCNICA SUPERIOR DE INGENIEROS INDUSTRIALES
CENTRO DE ELECTRÓNICA INDUSTRIAL

MODELLING AND CONTROL OF
STEPPER MOTORS FOR HIGH
ACCURACY POSITIONING SYSTEMS
USED IN RADIOACTIVE
ENVIRONMENTS

AUTOR:

RICARDO PICATOSTE RUILOPE

Ingeniero en Automática y Electrónica Industrial por la Universidad Politécnica de Madrid

DIRECTORES:

JESÚS ÁNGEL OLIVER RAMÍREZ

Doctor Ingeniero Industrial por la Universidad Politécnica de Madrid

ALESSANDRO MASI

Doctor en Ingeniería de Control e Informática por la Università degli Studi di Napoli Federico II

2014

Tribunal

Tribunal nombrado por el Mgco. y Excmo. Sr. Rector de la Universidad Politécnica de Madrid, el día de 2014.

Presidente: Prof. José Antonio Cobos Márquez, Universidad Politécnica de Madrid

Vocales: Dr. Mark Butcher, CERN

Prof. Marco Storace, Universidad de Génova

Prof. Antonio Lázaro, Universidad Carlos III de Madrid

Secretario: Prof. Pedro Alou Cervera, Universidad Politécnica de Madrid

Suplentes: Pablo Zumel Vaquero, Universidad Carlos III de Madrid

Prof. Jesús Acero Acero, Universidad de Zaragoza

Realizado el acto de lectura y defensa de la Tesis el día de 2014 en la Escuela Técnica Superior de Ingenieros Industriales de la Universidad Politécnica de Madrid.

Calificación:

EL PRESIDENTE

LOS VOCALES

EL SECRETARIO

A la tía Mari
“*A la aceitera ...*”

Acknowledgements (Agradecimientos)

I would like to express my deepest appreciation to my CERN supervisor, Alessandro Masi, who gave me the opportunity which allowed this thesis to become a reality. Thanks for the support and encouragement to never stop, no matter how hard things could be.

Equally important has been my supervision and guidance from my university. For all the support and wise counselling, specially in spite of the difficulties that the distance imposes, I want to thank my thesis director, Jesús Ángel Oliver.

Thanks to my working colleagues, in special to Mark, for the help and support all along this work. Thanks to all the students with whom I was so lucky to work. The collaboration with you has been fundamental. Also an important thanks goes to my international friends, whom has been like a family in this distant land.

Para mis agradecimientos personales comenzaré utilizando una cita de mi escritor favorito, Antoine de Saint-Exupèry: “*No es la distancia la que sirve para medir la lejanía*”. Y empiezo con ella porque las circunstancias me han llevado a estar lejos de la mayoría, es por eso que quiero agradecer el esfuerzo que habéis hecho para que la distancia no nos aleje.

Empiezo dando las gracias a mi familia, la cual ha más que demostrado que siempre estará ahí para mí, apoyándome y dándome cariño. ¡Espero que tengamos la oportunidad de celebrar muchas más Picatostadas! Y no sólo mi familia más cercana. A todos mis tíos y primos, y a la abuela, muchas gracias por seguir siendo una familia tan especial y de la que me siento tan orgulloso de ser parte.

Me gustaría también agradecer todas las personas que han pasado por mi vida durante este tiempo, y que ahora siguen cerca o dispersos por el mundo. Los primeros como siempre son los Pichos. Aunque la distancia ha puesto las cosas difíciles, seguiremos dando guerra. A mi familia en Suiza, englobada en *Ola k ase*. Cada vez está más repartidos por el mundo, ¡pero nunca parando de crecer! Lo hemos pasado muy bien juntos, y que siga siendo así. A mis compañeros de IAEI y la EUITI. Con vosotros cada vez que podemos reunirnos, parece que nos dijimos adiós ayer mismo. A mis amigos del INTA, esas grandes personas que te encuentras en el camino y que a veces tienes la suerte de poder conservar.

Para el final como no, dejo lo más importante. Gracias a Isa por ser mi compañera en este viaje. En esta especie de odisea que es la vida y por haber sobrevivido, el uno apoyado sobre el otro, a todas las tormentas. Por estar conmigo y ser mi familia, pareja y amiga. Gracias por ese futuro que ya compartimos y que empieza hoy.

Abstract

Hybrid Stepper Motors are widely used in open-loop position applications. They are the choice of actuation for the collimators in the Large Hadron Collider, the largest particle accelerator at CERN. In this case the positioning requirements and the highly radioactive operating environment are unique. The latter forces both the use of long cables to connect the motors to the drives which act as transmission lines and also prevents the use of standard position sensors. However, reliable and precise operation of the collimators is critical for the machine, requiring the prevention of step loss in the motors and maintenance to be foreseen in case of mechanical degradation.

In order to make the above possible, an approach is proposed for the application of an Extended Kalman Filter to a sensorless stepper motor drive, when the motor is separated from its drive by long cables. When the long cables and high frequency pulse width modulated control voltage signals are used together, the electrical signals differ greatly between the motor and drive-side of the cable. Since in the considered case only drive-side data is available, it is therefore necessary to estimate the motor-side signals. Modelling the entire cable and motor system in an Extended Kalman Filter is too computationally intensive for standard embedded real-time platforms. It is, in consequence, proposed to divide the problem into an Extended Kalman Filter, based only on the motor model, and separated motor-side signal estimators, the combination of which is less demanding computationally. The effectiveness of this approach is shown in simulation. Then its validity is experimentally demonstrated via implementation in a DSP based drive. A testbench to test its performance when driving an axis of a Large Hadron Collider collimator is presented along with the results achieved. It is shown that the proposed method is capable of achieving position and load torque estimates which allow step loss to be detected and mechanical degradation to be evaluated without the need for physical sensors.

These estimation algorithms often require a precise model of the motor, but the standard electrical model used for hybrid stepper motors is limited when currents, which are high enough to produce saturation of the magnetic circuit, are present. New model extensions are proposed in order to have a more precise model of the motor independently of the current level, whilst maintaining a low computational cost. It is shown that a significant improvement in the model fit is achieved with these extensions, and their computational performance is compared to study the cost of model improvement versus computation cost. The applicability of the proposed model extensions is demonstrated via their use in an Extended Kalman Filter running in real-time for closed-loop current control and mechanical state estimation.

An additional problem arises from the use of stepper motors. The mechanics of the collimators can wear due to the abrupt motion and torque profiles that are applied by them when used in the standard way, i.e. stepping in open-loop. Closed-loop position control, more specifically Field Oriented Control, would allow smoother profiles, more respectful to the mechanics, to be applied but requires position feedback. As mentioned already, the use of sensors in radioactive environments is very limited for reliability reasons. Sensorless control is a known option but when the speed is very low or zero, as is the case most of the time for the motors used in the LHC collimator, the loss of observability prevents its use. In order to allow the use of position sensors without reducing the long term reliability of the whole system, the possibility to switch from closed to open loop is proposed and validated, allowing the use of closed-loop control when the position sensors function correctly and open-loop when there is a sensor failure.

A different approach to deal with the switched drive working with long cables is also presented. Switched mode stepper motor drives tend to have poor performance or even fail completely when the motor is fed through a long cable due to the high oscillations in the drive-side current. The design of a stepper motor output filter which solves this problem is thus proposed. A two stage filter, one devoted to dealing with the differential mode and the other with the common mode, is designed and validated experimentally. With this filter the drive performance is greatly improved, achieving a positioning repeatability even better than with the drive working without a long cable, the radiated emissions are reduced and the overvoltages at the motor terminals are eliminated.

Resumen en Castellano

Los motores paso a paso híbridos son utilizados frecuentemente en aplicaciones en lazo abierto. Este tipo de motor es la elección como actuador en los colimadores del Gran Colisionador de Hadrones, LHC por sus siglas en inglés, el mayor acelerador de partículas en el CERN, donde los requerimientos de posicionamiento y el entorno de alta radiación son únicos. Dicho entorno requiere el uso de cables de gran longitud que actuarán como líneas de transmisión, lo que impedirá el uso de sensores de posicionamiento estándar. Sin embargo, la operación de los colimadores de una forma fiable y precisa es crítica para un funcionamiento seguro del acelerador, siendo necesaria la prevención de pasos perdidos en los motores así como la previsión de mantenimiento en caso de haber una degradación excesiva de los mecanismos.

Para que lo mencionado sea posible se propone una estrategia para el uso del Filtro Extendido de Kalman en un drive sin sensores para motores paso a paso, cuando el motor se encuentra separado del drive por cables de gran longitud. Al utilizar dichos cables en conjunto con fuentes conmutadas, las señales eléctricas en el lado del drive y en el lado del motor presentan grandes diferencias. Ya que en este caso sólo la información en el lado del drive estará disponible, será necesario estimar las señales eléctricas en el lado del motor. Modelar el sistema en su conjunto, incluyendo cable y motor, para su uso en un Filtro Extendido de Kalman tiene un coste computacional excesivo que no puede ser satisfecho con sistemas embebidos estándar.

A raíz de ello, se propone dividir el problema en la aplicación del Filtro Extendido de Kalman al motor y usar estimadores para las señales en el lado del motor independientemente, pero de forma que la carga computacional de ambas partes por separado sea menor. La efectividad de la propuesta es demostrada en simulación y después validada experimentalmente implementando la solución en un drive basado en una DSP. Se presenta asimismo el banco de pruebas para

testear el comportamiento del drive controlando uno de los ejes de un colimador del LHC junto con los resultados obtenidos. Se muestra que el método propuesto es capaz de lograr estimaciones del par externo aplicado al motor y la posición del mismo con suficiente precisión para detectar la pérdida de pasos y evaluar la degradación mecánica del colimador sin necesidad de sensores.

Los algoritmos utilizados requieren un modelo preciso del motor, pero ciertas observaciones demuestran que el modelo estándar utilizado para motores paso a paso híbridos presenta ciertas limitaciones cuando las corrientes aplicadas son suficientemente altas para provocar la saturación del circuito magnético. Se proponen nuevas extensiones del modelo eléctrico del motor para lograr una mayor precisión en el modelado del mismo independientemente del nivel de corriente aplicado, y a la vez manteniendo una baja carga computacional. Dichas extensiones muestran una gran mejora en el ajuste del modelo y la carga de computación implicada es comparada para estudiar el coste de la mejora del modelo contra el coste computacional. La aplicabilidad de las extensiones al modelo propuestas queda demostrada utilizando el nuevo modelo en un Filtro Extendido de Kalman ejecutado en tiempo real, utilizando las estimaciones de corriente para cerrar el lazo de control de corriente y realizando la estimación de las variables mecánicas del sistema.

Un problema adicional del uso de motores paso a paso es el desgaste sufrido por la mecánica movida por los mismos, debido a la brusquedad del movimiento aplicado por este tipo de motores cuando son controlados en su forma estándar, es decir, en lazo abierto. El control en lazo cerrado, concretamente el control vectorial, permite la aplicación de perfiles de posicionamiento suaves, más respetuosos con la mecánica del sistema, pero requiere realimentación de la posición. Como ya ha sido mencionado, el uso de sensores en entornos radiactivos debe limitarse debido a razones de fiabilidad. El control sin sensores es una opción conocida pero cuando la velocidad es nula o cercana a cero, como es el caso la mayoría del tiempo en los colimadores del LHC, la pérdida de observabilidad impide su uso. Para permitir el uso de sensores con los que cerrar el lazo de posición, pero sin reducir la fiabilidad del sistema, la posibilidad de comutar de lazo cerrado a abierto con el drive en funcionamiento es propuesta y validada. Dicha comutación hace posible el uso de control en lazo cerrado cuando los sensores de posicionamiento funcionan correctamente, y pasar a lazo abierto en caso de que los mismos fallasen.

Se presenta además una aproximación distinta al problema de las fuentes conmutadas trabajando con cables de gran longitud, tratando de eliminar el problema desde el punto de vista de la electrónica de potencia mediante un filtro de salida para motores paso a paso. Un filtro de dos etapas, una dedicada a filtrar el modo diferencial y otra el modo común es diseñado y validado experimentalmente. Con este filtro el comportamiento del drive mejora notablemente, logrando una repetibilidad en el posicionamiento incluso mejor que la del drive trabajando sin cables de gran longitud, y tanto las emisiones electromagnéticas radiadas, como el sobrevoltaje que llega al motor y las oscilaciones de corriente en el lado del drive son considerablemente reducidas.

Contents

List of acronyms	xxi
I Introduction	1
1 Introduction	2
1.1 The Large Hadron Collider	2
1.2 The Collimation system	4
1.3 Thesis organization	7
2 Hybrid Stepper Motors	9
2.1 Introduction	9
2.2 Motor model	11
2.2.1 Electrical model	11
2.2.2 Mechanical model	13
2.3 Collimator motor and cable used in the collimators	15
3 Problem Formulation	17
3.1 Introduction	17
3.2 Use of switched drives with long cables	18
3.2.1 Drive-side current	19
3.2.2 Common-mode current	20
3.2.3 Motor-side voltage	22
3.3 Use of stepper motors and open loop position control	22
3.4 Purpose of the thesis	24
4 The Stepper Motor Drive	26
4.1 Introduction	26

4.2	Previous work	26
4.2.1	Motor-Side Current estimation scheme	28
4.2.2	Controller design	30
4.3	The developed DSP Drive	33
4.3.1	Hardware design	34
4.3.2	Software design	35
4.3.3	3^{rd} harmonic current correction	37
4.3.4	H-tuning	38
4.3.5	Experimental results	39
4.4	Conclusions	44
II	Sensorless Estimation for Hybrid Stepper Motors	46
5	Introduction to Position and Torque Sensorless Estimation	47
5.1	Motivation	47
5.2	State of the art	49
5.2.1	On the use of the Extended Kalman Filter with Hybrid Stepper Motors connected Through Long Cables	49
5.2.2	On the Hybrid Stepper Motor Electrical Model	50
5.3	The Extended Kalman Filter	51
6	Application of the Extended Kalman Filter for a Sensorless Step- per Motor Drive Working With Long Cables	53
6.1	Introduction	53
6.2	The proposed approach	53
6.2.1	Model selection	54
6.2.2	Discrete-time, state-space version of chosen model	56
6.2.3	Estimation of the EKF's inputs and measurements	58
6.3	Simulation	65
6.3.1	Simulator description	65
6.3.2	EKF tuning method	67
6.3.3	Simulation results	68
6.4	Experimental application to an LHC collimator	74
6.4.1	Drive description	74
6.4.2	Test Setup Description	75

6.4.3	Experimental Results	77
6.5	Conclusions	81
7	Hybrid Stepper Motors Electrical Model Extensions and Their Application to Sensorless Estimation	84
7.1	Introduction	84
7.1.1	Standard electrical model revisited	85
7.1.2	Poor model fit	86
7.2	Proposed new model extensions	88
7.2.1	Position dependency	88
7.2.2	Current dependency	88
7.2.3	Position and Current dependency	89
7.3	Determination of the model structure	90
7.3.1	Position Dependency	90
7.3.2	Current Dependency	94
7.4	Model comparison	100
7.4.1	Position dependency	101
7.4.2	Current dependency	103
7.4.3	Position and Current Dependency	104
7.5	Model limitations	107
7.5.1	Performance	107
7.5.2	Range of usefulness	107
7.5.3	Application of the proposed model on sensorless estimation	108
7.6	Extended Kalman Filter: Theory and Experimental Results . . .	109
7.6.1	State-space model derivation theory	109
7.6.2	Experimental Results	110
7.7	Conclusions	112
III	Field Oriented Control for Stepper Motors	114
8	Background on Field Oriented Control	115
8.1	Introduction	115
8.2	Electric Motors position control strategies	117
8.2.1	Open-loop position control	117
8.2.2	Closed-loop position control	117

8.3 Field Oriented Control	119
8.3.1 Field oriented control applied to stepper motors	120
9 Control of stepper motors with Field Oriented Control	124
9.1 Introduction	124
9.2 Control scheme description and tuning procedure	124
9.2.1 Decoupling of the current control	124
9.2.2 Close the loop on i_q and i_d	126
9.2.3 Speed loop controller	126
9.2.4 Position loop controller	127
9.2.5 Control scheme description	128
9.2.6 Performance achieved	131
9.3 Practical issues	133
9.3.1 θ_0 calibration method	133
9.3.2 Velocity estimation	133
9.4 Closed to open position loop switch	135
9.5 Use of FOC and the switch in the LHC Collimators	142
9.6 Conclusions	146
IV Output filters	147
10 Introduction to Output filters	148
10.1 Introduction	148
10.2 State of the art for output filters	149
10.3 Output filters	150
11 Sine Wave Filters For Stepper Motors	153
11.1 Proposal	153
11.2 Sine wave filter design	153
11.2.1 The application	153
11.2.2 Differential Mode Filter	154
11.2.3 Common Mode Filter	158
11.3 Experimental validation	159
11.3.1 Effect of the filter on the motor currents	159
11.3.2 Effect of the filter on the motor voltages	159
11.3.3 Effect of the filter on the positioning	161

11.3.4 EMI	161
11.4 Conclusion	164
V Conclusions	165
12 Conclusions	166
12.1 Future work	168
12.2 Publications	169
VI Appendices	171
A Analytical formulas for the extended electrical model	172
B CERN Field Oriented Control Motor Applications	176
B.1 CINEL Stepper motor based Goniometer	176
B.2 CINEL Piezo Actuator Based Goniometer	180
Bibliography	185

List of Figures

1.1	CERN logo	3
1.2	CERN underground accelerator complex	3
1.3	Aerial view of the Large Hadron Collider area with the cycle of the CERNs accelerators highlighted	4
1.4	Picture in the LHC tunnel	5
1.5	Chain of accelerators and experiments at CERN	5
1.6	Collimator layout	6
1.7	Half 3D cut of a collimator	7
1.8	Thesis organization	8
2.1	Hybrid Stepper Motor separated rotor and stator	10
2.2	Schematic drawing of a simple hybrid stepper motor with 3 teeth and 2 phases	10
2.3	Motor phase equivalent electrical circuit	12
2.4	Motor phase high frequency equivalent electrical circuit including iron losses	13
2.5	Forces applied to the motor axis	14
2.6	Electromagnetic torque generated for a specific set of reference currents	15
3.1	Rack, collimator and the cable connecting them	18
3.2	Measured phase currents	21
3.3	Measured motor-side currents	21
3.4	Measured common-mode phase current.	23
3.5	Measured motor-side voltage.	23
3.6	Measured rotor angle and speed stepping in half-step mode.	25
4.1	2-port T-net cable model connected to motor phase	28

4.2 Comparison of $G_{err}(s)$ transfer function for two different cable lengths: 100 m and 1 km.	31
4.3 Motor phase current discrete controller	33
4.4 Standard stepper motor drive scheme	34
4.5 Connection of the DSP to the MOSFET h-bridges (not all the components represented)	35
4.6 Drive board	36
4.7 State machine diagram	36
4.8 Programmed interrupts	38
4.9 Third harmonic compensation current reference for the extreme values of α	39
4.10 Typical motor phase current waveforms on the drive and motor side for a 720 m cable length	40
4.11 Repeatability results for the SHS Star 2000, the modified SHS and the proposed drive	41
4.12 Repeatability histograms for 1/4 stepping mode	43
4.13 Repeatability histograms for 1/8 stepping mode	43
4.14 Low frequency spectrum of EMI emissions on drive side with a 720 m long cable.	44
4.15 The EMI test bench	44
6.1 Bode magnitude diagram of $G_{cm}(s)$ for two cable length extremes	55
6.2 Schematic view of drive, motor and cable	56
6.3 The approximation $\hat{H}_{est}(s)$ and the exact expression $H_{est}(s)$ for two cable lengths	61
6.4 Real part of $\hat{H}_{est}(s)$'s poles over a range of cable lengths	61
6.5 Low frequency cable model connected to motor phase	63
6.6 Comparison of the frequency responses of $H_v(s)$ using the complete impedance expressions and the approximation, for two cable length extremes	63
6.7 Simulation model structure	65
6.8 True (dashed) and estimated (solid) states for a 1 km cable	70
6.9 True (dashed) and estimated (solid) states for a 1 km cable with mismatch;	71
6.10 RMS of the mechanical angle estimation error	72

6.11 True (dashed) and estimated (solid) states for a 1 km cable at 150 step/s	73
6.12 LHC Vertical Collimator	76
6.13 Experimental test fixture	76
6.14 Experimental test setup	78
6.15 Position estimation (upper) and estimation error (lower) for a movement from out to in/beam	80
6.16 Torque estimation (upper) and estimation error (lower) for a movement from out to in/beam	80
6.17 Position estimation (upper) and estimation error (lower) for a trapezoidal movement	82
6.18 Torque estimation (upper) and estimation error (lower) for a trapezoidal movement	82
7.1 Discrepancy between measured voltage and standard model prediction.	87
7.2 Measured (dashed) and fitted (solid) open phase voltages.	92
7.3 Measured inductance at different positions.	93
7.4 Estimated and fitted Ψ_1^{PM}	96
7.5 Holding torque measured for different RMS current values.	99
7.6 Estimated and fitted L	101
7.7 Model fit with the position dependent model.	102
7.8 Model fit with the current dependent model.	104
7.9 Model fit with the position and current dependent model.	106
7.10 Fit percentage of the models for different RMS current datasets .	108
7.11 EKF based closed loop control of the HSM.	111
7.12 Drive signals during closed loop operation.	112
7.13 Long term position estimation by EKF.	113
7.14 Comparison of EKF using different HSM models.	113
8.1 Full-step mode rotor position and speed acquisition.	116
8.2 Currents represented in the different frames	121
8.3 Stepper Motor model diagram using the standard ab reference frame	121
8.4 dq frame Stepper Motor model diagram	123
9.1 Decoupling scheme for i_{dq}	125
9.2 Current loops in case of ideal decoupling	126

9.3	Simplified rotor speed loop	127
9.4	Fit of the system step response to a first order system	128
9.5	θ_m loop simplified	128
9.6	FOC blocks scheme	130
9.7	Full-step mode rotor position and speed acquisition, using closed-loop position control	131
9.8	Full-step mode step test in standard stepping mode. 10 repetitions are done	132
9.9	Full-step mode step test in FOC mode. 10 repetitions are done .	132
9.10	Stages of θ_0 calibration	134
9.11	Switch closed to open loop position stages	135
9.12	Switch closed to open loop position search stage	137
9.13	Switch closed to open loop position scheme	138
9.14	Switch from closed to open loop position control in operation . .	139
9.15	Zoom of the switch from closed to open loop position control in operation	139
9.16	Switch from open to closed loop position control in operation . .	140
9.17	Zoom of the switch from open to closed loop position control in operation	140
9.18	Phase currents during a switch transition form closed to open loop, $i_d^{ref} = 0A$. The vertical scale is 1A/division	141
9.19	Phase currents during a switch transition form closed to open loop, $i_d^{ref} = 0.5A$. The vertical scale is 1A/division	141
9.20	Phase currents during a switch transition form open to closed loop, $i_d^{ref} = 0.5A$. The vertical scale is 1A/division	142
9.21	LHC collimator linear stage	143
9.22	Motor position in the collimator linear stage working in open-loop, spring relaxed	144
9.23	Motor position in the collimator linear stage using FOC, spring relaxed	144
9.24	Motor position in the collimator linear stage working in open-loop, spring at the maximum compression	145
9.25	Motor position in the collimator linear stage using FOC, spring at the maximum compression	145
10.1	Typical motor-cable-drive system using an output filter.	150

10.2 Output filter stages.	151
10.3 Typical two stage induction motor output filter.	151
11.1 Output filter adapted to a single stepper motor phase	154
11.2 Simulation results for $R_{DM} = Z_0$	157
11.3 Zoom for the simulation results for $R_{DM} = Z_0$, motor side	157
11.4 Simulation results, motor side - Comparison of the proposed filter and those for $R_{0f} = Z_0$ values	158
11.5 Current in a motor phase with the output filter and a 720 meter cable	160
11.6 Closer view of the currents a motor phase with the output filter and a 720 meter cable	160
11.7 Motor side voltage with the output filter and a 720 meter cable. .	162
11.8 Motor side voltage with 720 meter cable	162
11.9 Repeatability results showing steady state position error histogram for the SHS Star 2000 drive with a short cable and without the output filter.	163
11.10 Repeatability results showing steady state position error histogram for the SHS Star 2000 drive with a 720 meter cable and with the proposed output filter.	163
11.11 Low frequency spectrum of the EMI emissions for the SHS drive .	164
B.1 CINEL stepper motor based goniometer working principle	177
B.2 CINEL stepper motor based goniometer prototype	177
B.3 CINEL stepper motor based goniometer 3D model	177
B.4 Crystal platform position with standard stepping mode - one step applied	179
B.5 Crystal platform position with standard stepping mode - 1 μrad steps	179
B.6 Crystal platform position with FOC - 1 μrad steps	179
B.7 Crystal platform positioning comparison - continuous motion . .	180
B.8 CINEL Piezo based goniometer scheme	181
B.9 CINEL Piezo based goniometer. Horizontal version (left) and ver- tical version (right)	181
B.10 CINEL Piezo based goniometer internal picture	182
B.11 CINEL Piezo based goniometer, rotational stage in open loop .	183

- B.12 CINEL Piezo based goniometer, rotational stage in closed loop . . 183

List of Tables

2.1	Maccon stepping motor parameter values	16
2.2	Cable parameter values	16
4.1	Repeatability test comparison without a long cable connecting the motor	40
4.2	Repeatability test comparison with modified commercial drive and a long cable connecting drive and motor	41
4.3	Repeatability performance in different stepping modes	42
6.1	Parameter values	78
6.2	Results for continuous movement from out-to-in	79
7.1	Parameters estimated for the standard hybrid stepping motor electric model	86
7.2	Magnitude for the first four harmonics of the motor induced voltages when no current is flowing in the phases.	91
7.3	Ψ_1^{PM} terms resulting from different current levels.	94
7.4	Inductance terms resulting from different current levels.	100
7.5	Parameters estimated for the position dependent model	102
7.6	Parameters estimated for the current dependent model	103
7.7	Parameters estimated for the position and current dependent model	106
7.8	Performance of the different models comparing fit and average computing time	107
7.9	EKFs Comparison	111
11.1	Filter component values.	156
11.2	Repeatability test results.	161

B.1	Overshoot and standard deviation comparison between stepping mode and FOC	178
B.2	Standard deviation of the parasitic yaw in the rotational stage in closed loop test	182

List of acronyms

- ADC** Analog to Digital Converter
AC Alternating Current
CERN European Organization for Nuclear Research
CM Common-Mode
CPU Central Processing Unit
DAQ Data AcQuisition
DC Direct Current
DM Differential-Mode
DSC Digital Signal Controller
DSP Digital Signal Processor
DTC Direct Torque Control
EKF Extended Kalman Filter
EMC Electro-Magnetic Compatibility
EMF Electro-Motive Force
EMI Electro-Magnetic Interference
FOC Field Oriented Control
HSM Hybrid Stepper Motor
IEC International Electrotechnical Commission
IGBT Insulated-Gate Bipolar Transistor
IIR Infinite Impulse Response
LHC Large Hadron Collider
LINAC Linear particle accelerator
LTI Linear Time-Invariant
LVDT Linear Variable Differential Transformer
MDC Motion Drive Control
MOSFET Metal Oxide Semiconductor Field-Effect Transistor
NRMSE Normalized Root Mean Square Error

PCB Printed Circuit Board

PMSM Permanent-Magnet Stepper Motor

PRS Position Readout and Survey

PWM Pulse Width Modulation

RAM Random Access Memory

RMS Root Mean Square

RMSE Root Mean Square Error

XINT eXternal INTerrupt

Part I

Introduction

Chapter 1

Introduction

This chapter introduces the framework and organization of this thesis. The work has been carried out at CERN, the European Organization for Nuclear Research, an organization devoted to the study of particle physics and operating the largest laboratory in the world with this mission.

CERN is situated on the French-Swiss border (Figs. 1.2 and 1.3), close to the city of Geneva. It was inaugurated 60 years ago as an effort for international collaboration after the Second World War and it is composed of over 20 member countries of which Spain is part and more than 40 countries in cooperation agreement, observers or in the process of joining.

1.1 The Large Hadron Collider

The Large Hadron Collider (LHC) (Fig. 1.4) is the latest addition to the CERN's accelerator complex (Fig. 1.5). It is a circular particle accelerator and collider, the largest and most powerful in the world, with a length of 27 km and built 100 meters underground.

The LHC was designed to collide hadron beams, protons and lead ions specifically, with an energy up to 7 TeV each beam, with the purpose of verifying the Standard Model, the current framework for particle physics.

Inside the collider two proton beams are accelerated in opposite directions at up to 99.99 % of the speed of light, and they collide in four interaction points, known as experiments, where the collision data is acquired for later study by the particle physicists. To make this possible, the superconducting magnets in the LHC must be cooled down to its working temperature, 1.9 Kelvin (-271 degrees



Figure 1.1: CERN logo

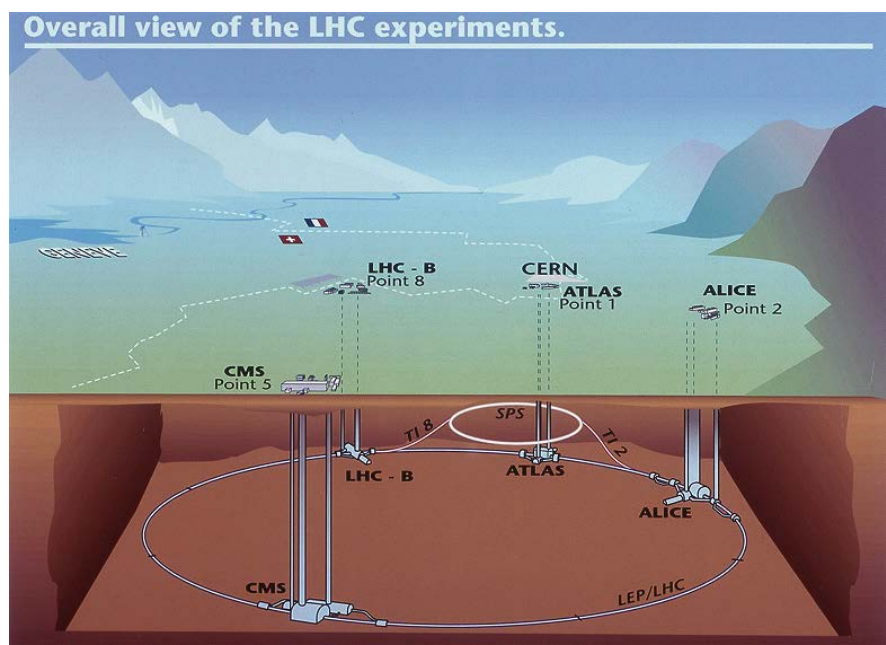


Figure 1.2: CERN underground accelerator complex



Figure 1.3: Aerial view of the Large Hadron Collider area with the cycle of the CERNs accelerators highlighted

Celsius approximately) in order to use the superconducting properties of the conductors. The LHC has already collided protons with an energy of 8 TeV, 4 per beam, and is currently in the so-called Long Shutdown 1, with works for upgrading it to work at its maximum energy.

In order for the LHC to work several historical accelerators at CERN are used in chain. The protons are produced and accelerated in the LINAC-II, a linear accelerator, and then they are accelerated in steps, first in the Booster, then the Proton-Synchrotron, the Super Proton-Synchrotron, and finally the LHC.

1.2 The Collimation system

The transverse energy density of the nominal beam in the LHC is 1000 times higher than that previously achieved in proton storage rings, reaching values up to 350 MJ for the 2 beams at the time. The energy in the two LHC beams is sufficient to melt almost 1 ton of copper. Tiny fractions of the stored beam suffice to quench a super-conducting LHC magnet or even to destroy parts of the accelerator.

To stop and absorb the energy from the particles that, expectedly or not, deviate their trajectory over a certain limit from the ideal beam path, there is a

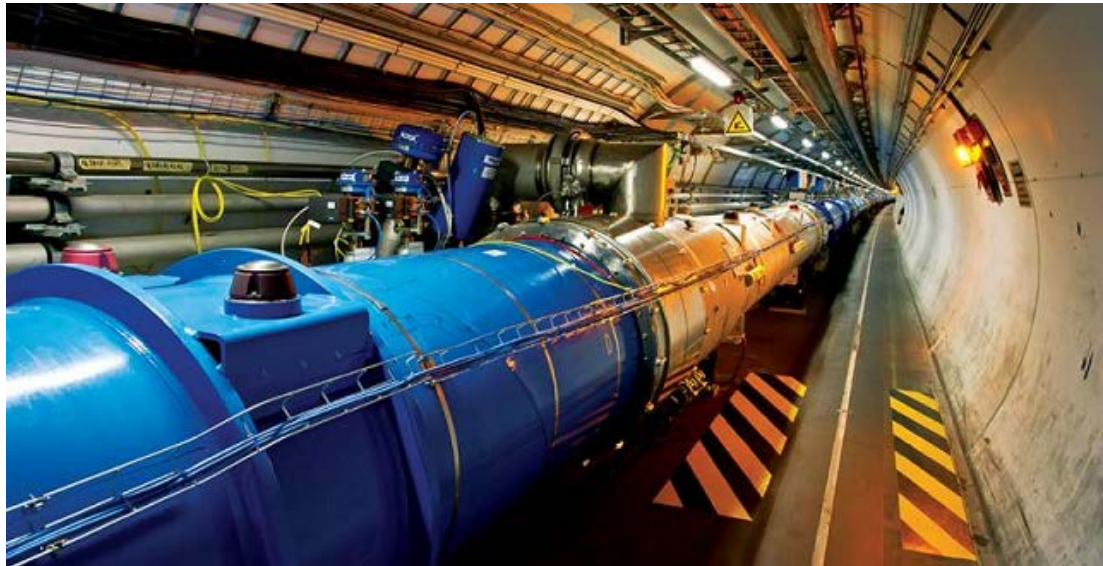


Figure 1.4: Picture in the LHC tunnel

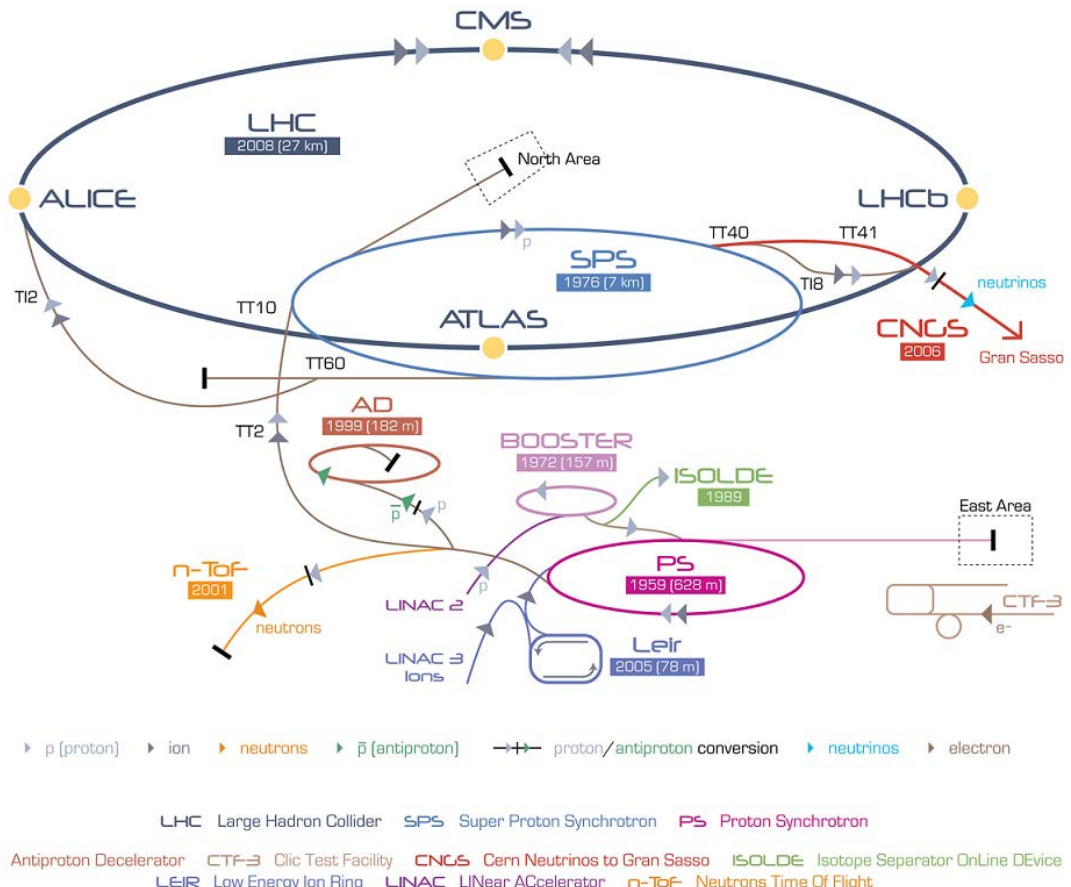


Figure 1.5: Chain of accelerators and experiments at CERN

beam cleaning system composed of over 100 collimators located around the LHC ring and the transfer lines, which protects the machine against beam losses and clean the beam of its halo.

Each collimator (Figs. 1.6 and 1.7) is based on two jaws of different materials that can move into the particle beam with a specified tilt angle, thanks to four stepping motors. The jaws are bars made of specially selected materials capable of receiving such impacts, such as carbon-carbon and graphite. These bars are able to move horizontally and vertically, depending on the type of collimator, to adjust the space between them and the beam.

This thesis work has been devoted to the modelling and control of the hybrid stepping motors used to move the jaws of the collimator. In chapter 3 the problems arising from the use of this electrical motor type in the accelerator environment is described in detail.

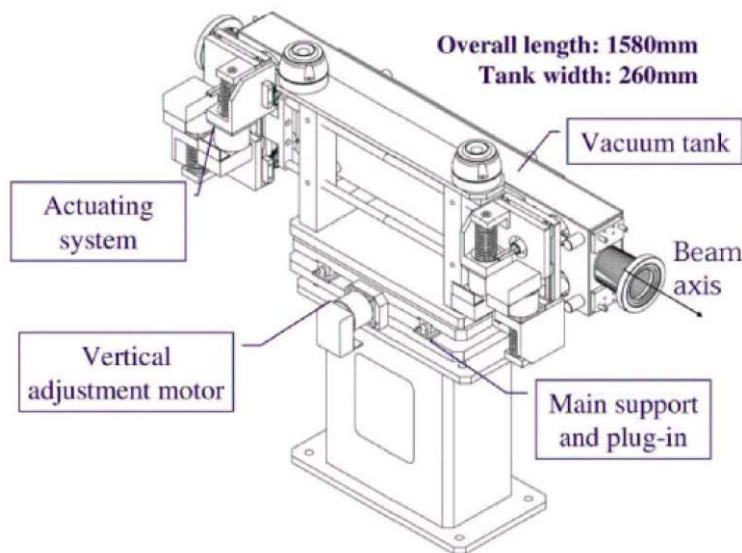


Figure 1.6: Collimator layout

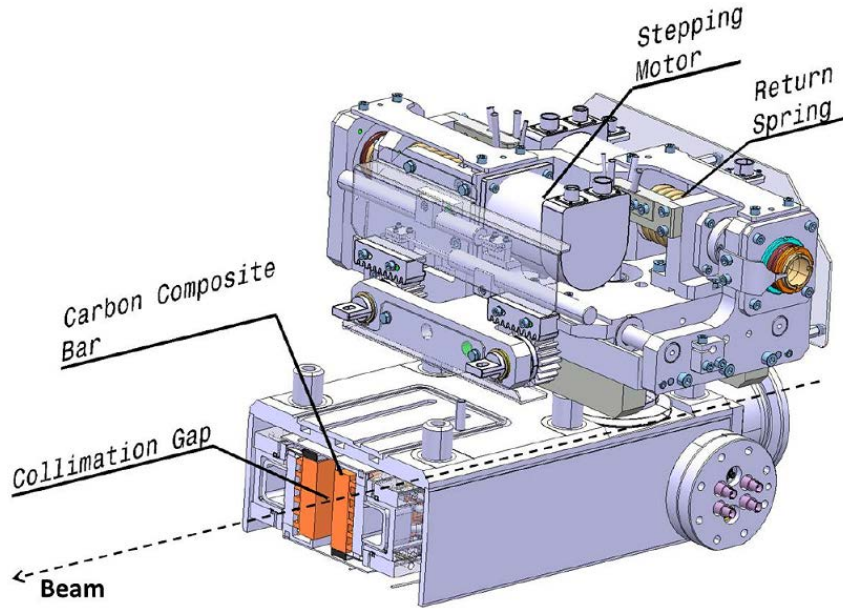


Figure 1.7: Half 3D cut of a collimator

1.3 Thesis organization

The organization of the thesis is presented in Fig. 1.8. Each part is described now:

- Part I is common to the whole thesis. It is dedicated to introducing its framework, presenting the motivation and formulating the problem that is dealt with, and presenting the previous and initial work upon which the thesis is developed.
- Part II first introduces sensorless state estimation for electrical motors and the state of the art of sensorless state estimation of Hybrid Stepper Motors (HSM). Then the application of the Extended Kalman Filter (EKF) to HSM driven through long cables is proposed and tested in simulation and experimentally. After this an extension of the HSM electrical model apt for real-time control and estimation is proposed and validated.
- Part III describes the state of the art of closed-loop position control for stepper motors. The option selected, Field Oriented Control (FOC), is then detailed, as well as its structure, implementation and tuning. A switch from closed to open loop position control is proposed and validated, dealing with

the problem of reliability in the collimation system and improving the drive performance.

- Part IV presents a different approach to the problem of HSM driven through long cables, by using power output filters to solve the problem created by the application of high frequency signals to transmission lines.
- Part V, common for the whole thesis, summarises all the work done on the modelling and control of stepper motors in radioactive environments, and presents the overall conclusions.

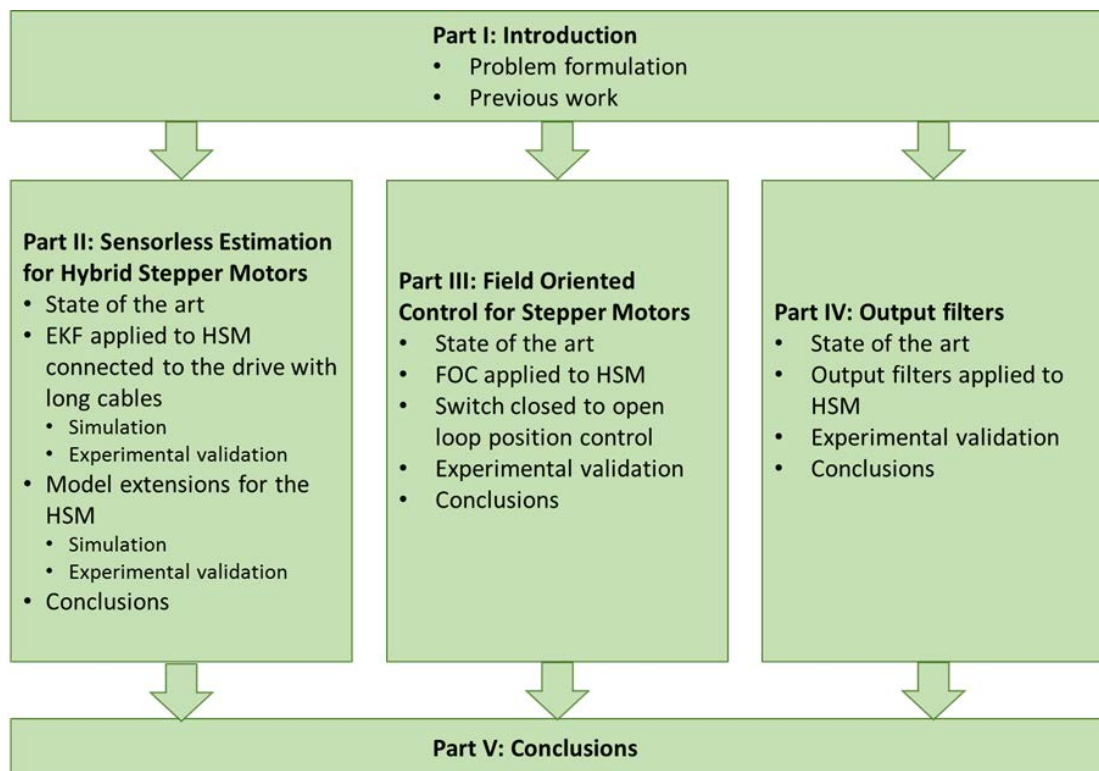


Figure 1.8: Thesis organization

Chapter 2

Hybrid Stepper Motors

2.1 Introduction

In section 1.2 it was mentioned that stepper motors are the actuator chosen to move the collimator jaws. This choice is based mainly on the fact that this kind of motor does not need position feedback to work with a relatively high accuracy, in addition to their great toughness, an essential feature in the given operating conditions.

Stepping motors are a well known solution for many industrial and consumer applications, with excellent literature describing them in detail (see [1] and [36]), and therefore only a brief introduction and model description of the type chosen, the hybrid stepping motor (Fig. 2.1) with 2 phases, is done now.

These motors offer a high holding torque and therefore are common in applications where the movement is held at static positions or varies in discrete steps. Moreover, despite usually being driven in open-loop position control, they have non accumulative positional error and are capable of accurate positioning since both stator and rotor have a series of teeth that tend to align in a specific known position when the proper current configuration is applied to the motor phases.

Their toothed structure allows a mechanical turn to be divided into many electrical turns, and therefore as the stepping sequence goes in predetermined phase currents, the motor moves through these electrical turns and at the same time through the mechanical turn. In Fig. 2.2 an example of a simple HSM, with only 3 teeth, is presented. As the currents are applied in the proper sequence in the motor phases, namely Phase A and Phase B, the north and south poles of the rotor align with one or other phase, producing the rotation.



Figure 2.1: Hybrid Stepper Motor separated rotor and stator

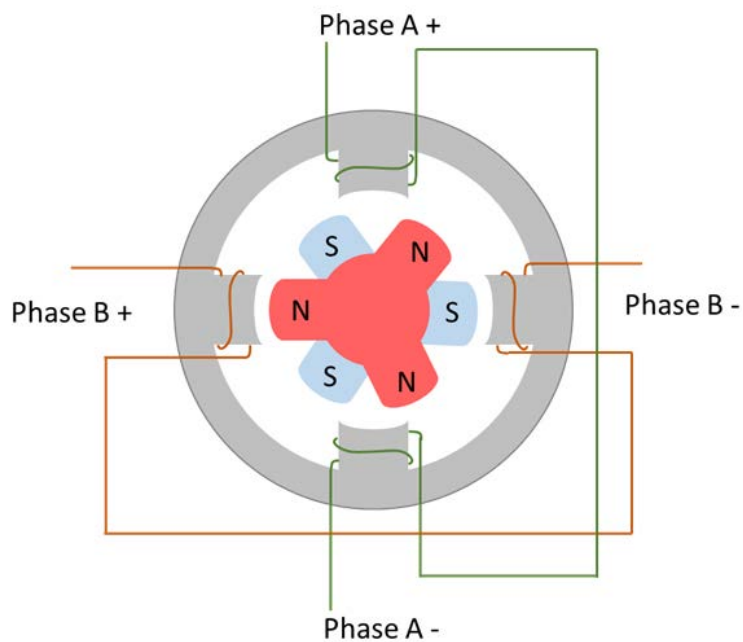


Figure 2.2: Schematic drawing of a simple hybrid stepper motor with 3 teeth and 2 phases

Many of the applications involving long cables to connect the motor either do not have precise positioning requirements or have the possibility of closing the loop on the shaft position with sensors such as encoders. Nevertheless when the motor is situated in harsh environments, it is not possible to use electronic sensors and achieve a high robustness.

Particle accelerators use positioning systems in multiple different applications, including collimators, movable targets, beam dumps and scrapers. Hybrid stepper motors are often used as the actuators in these applications. These motors, and their electronic drivers, are subject to a number of requirements that are relatively unique to accelerators. This is the case of the collimators in the LHC.

2.2 Motor model

The motor model can be separated into two sub-models, an electrical and a mechanical model. These have different time constants; the electrical model having faster dynamics.

2.2.1 Electrical model

Each of the two electrical phases of the stepper motor can be modelled at relatively low frequencies and currents as an RL circuit plus a back electromotive force (emf), as in Fig. 2.3. This circuit is described by the following equation:

$$L_w \frac{di_j(t)}{dt} = -R_w i_j(t) - e_j(t) + u_j(t) \quad \text{for } j = A, B \quad (2.1)$$

where R_w is the phase resistance, L_w the phase inductance, i_j the phase current, u_j the terminal voltage and the back emf voltages are described by:

$$\begin{aligned} e_A(t) &= -K_m \omega_m \sin p\theta_m \\ e_B(t) &= K_m \omega_m \cos p\theta_m, \end{aligned} \quad (2.2)$$

with K_m being the motor constant, p the number of motor pole pairs, ω_m the rotor angular speed and θ_m the motor mechanical angle. Taking the Laplace

transform of Eq. (2.1), we find:

$$I_j(s) = \frac{1}{Z_{mot}}(U_j(s) - E_j(s)) \quad \text{for } j = A, B$$

and

$$Z_{mot}(s) = L_w s + R_w \quad (2.3)$$

is the motor's electrical impedance.

High frequency motor phase model

In order to get the transfer functions involving Z_{mot} in the following chapters, an accurate model of the motor phase impedance is needed. A simple RL model of the motor phase impedance is not adequate for high PWM frequencies since the ferromagnetic components of the motor phase circuit have losses that are strong functions of the frequency.

The high frequency equivalent circuit, like the commonly adopted equivalent circuit of transformers (see [33]), has an iron-losses resistance, that models the dissipated active power, in parallel with an equivalent inductance, which has a value that is considerably lower than the nominal DC value. The presence of an iron-losses equivalent resistance has the effect of introducing a pole in the high frequency model of the motor phase impedance:

$$Z_{mot}^{HF} = \frac{R_w + sL_{eq}}{1 + s\tau_p} \quad (2.4)$$

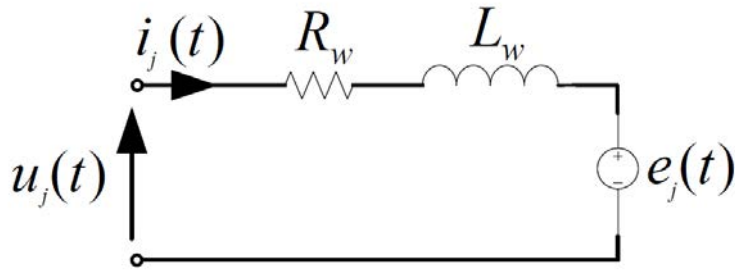


Figure 2.3: Motor phase equivalent electrical circuit

where L_{eq} is the equivalent of L_w and L_{fe} in parallel:

$$L_{eq} = \frac{L_{fe}L_w}{L_{fe} + L_w}$$

and

$$\tau_p = \frac{R_{fe}}{L_{eq}} \quad (2.5)$$

as in [52], where R_{fe} and L_{fe} are the resistance and inductance of the core losses modelling shown in Fig. 2.4.

2.2.2 Mechanical model

The mechanical part of the motor is modelled as a rigid body subject to various torques, as shown in Fig. 2.5:

$$J \frac{d\omega_m}{dt} = \tau_{em} - B\omega_m - \tau_{dm} - \tau_l \quad (2.6)$$

where

$$\tau_{em} = K_m (-i_{mot_A} \sin p\theta_m + i_{mot_B} \cos p\theta_m)$$

is the motor's electromagnetic torque, J its moment of inertia, B the viscous friction coefficient,

$$\tau_{dm} = T_{dm} \sin(2p\theta_m + \phi)$$

is the detent torque, T_{dm} the detent torque amplitude, ϕ a phase shift associated with τ_{dm} and τ_l the external load torque.

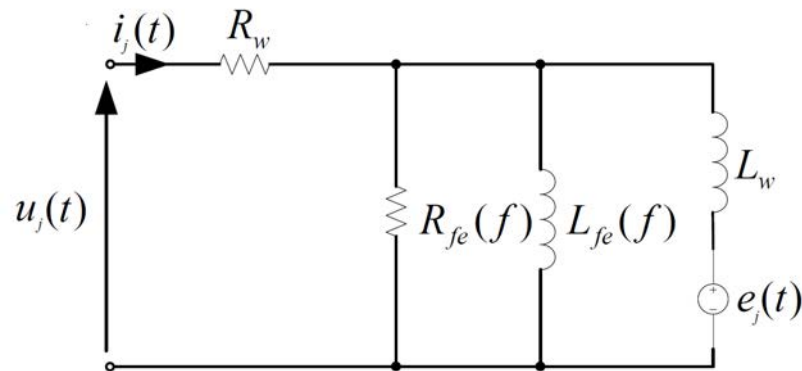


Figure 2.4: Motor phase high frequency equivalent electrical circuit including iron losses

It should be mentioned that the frequency of the motor's detent torque is taken as the electrical frequency's second harmonic since this was observed experimentally to be dominant for the motors used in the tests in [50]. This dominance of the second harmonic, over the theoretically predicted fourth, has been found elsewhere for hybrid stepper motors [88]. No loss of generality occurs, however, by modelling the detent torque as such and the proposed approach is equally valid for motors with different dominant detent torque harmonics.

When a specific set of reference currents is applied, the rotor magnet tends to align with the field generated by the motor phases. The electromagnetic torque as a function of the displacement angle between the rotor and the angle of the field generated, θ_{disp} , is shown in Fig. 2.6, for two different I_{RMS} current values. From this figure, we can see that if the rotor angle is behind the field generated, a positive electromagnetic torque results, pushing the rotor to align with the field. It can be also inferred that there is a static error when a external load is applied, since the rotor position resulting is the angle where τ_{em} compensates for the applied load.

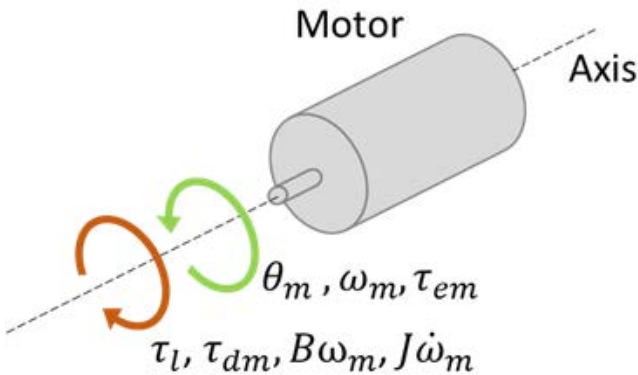


Figure 2.5: Forces applied to the motor axis

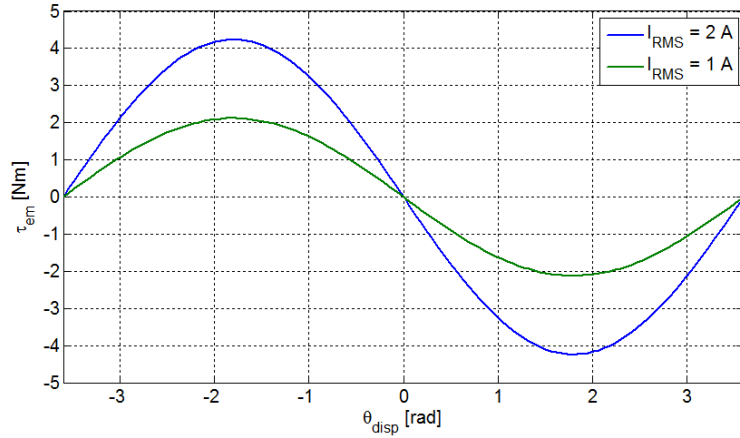


Figure 2.6: Electromagnetic torque generated for a specific set of reference currents

2.3 Collimator motor and cable used in the collimators

The parameters defining the motor and cables used in the LHC collimators are described here for reference.

The motor is a Maccon Hybrid Stepper Motor, with two phases, bipolar, $p = 50$ teeth, a rated current of 2 A RMS and holding torque of 3.5 Nm. The parameter values are summarized in Table 2.1.

The cable is a 24 twisted pair, multiwire cable. Its parameters were measured with an RLC meter and are shown in Table 2.2.

Table 2.1: Maccon stepping motor parameter values

Parameter	Value
R_w	3.2[Ω]
L_w	30[mH]
Nominal current (I_{RMS})	2 Amps RMS
Number of teeth (p)	50
Physical step size	1.8 degrees
K_m	1.75[Nm/A]
J	$1.3 \times 10^{-4}[kgm^2]$
B	0.05[Nms/rad]
T_{dm}	0.1505[Nm]
ϕ	0[rad]

Table 2.2: Cable parameter values

Parameter	Value
r	23.0 [Ω/km]
c	48.9 [nF/km]
l	0.6 [mH/km]
g	≈ 0 [S/km]

Chapter 3

Problem Formulation

3.1 Introduction

The collimators, presented in section 1.2, are located in highly radioactive areas due to the task that they perform.

This condition prevents the use of any electronics close to them, such as most sensors, the microcontrollers and computers running the control algorithms or the power electronics feeding the actuators that move the collimator jaws. Two important consequences of this fact are:

- The electronics involved in the control and supplying of these systems are installed in radiation free areas up to 800 meters away. This means that the actuators are connected to their drives by cables of this length as illustrated in Fig. 3.1. Modern drives are usually based on switched inverters. Long cables behave as transmission lines when switched voltages, containing high frequency components, are used.
- Position feedback for the motion control loop is limited to radiation hard sensors. In addition, the harsh conditions withstood by the collimators make any intervention to repair or replace any sensor or part difficult and expensive. Therefore, relying only on sensing feedback is preferably avoided.

The need to work without position feedback led to the choice of stepper motors as actuators in the collimation system. The two characteristics that make them a great match for the application are their relatively high accuracy in open loop control, eliminating the need for position feedback and their robustness, avoiding frequent maintenance.

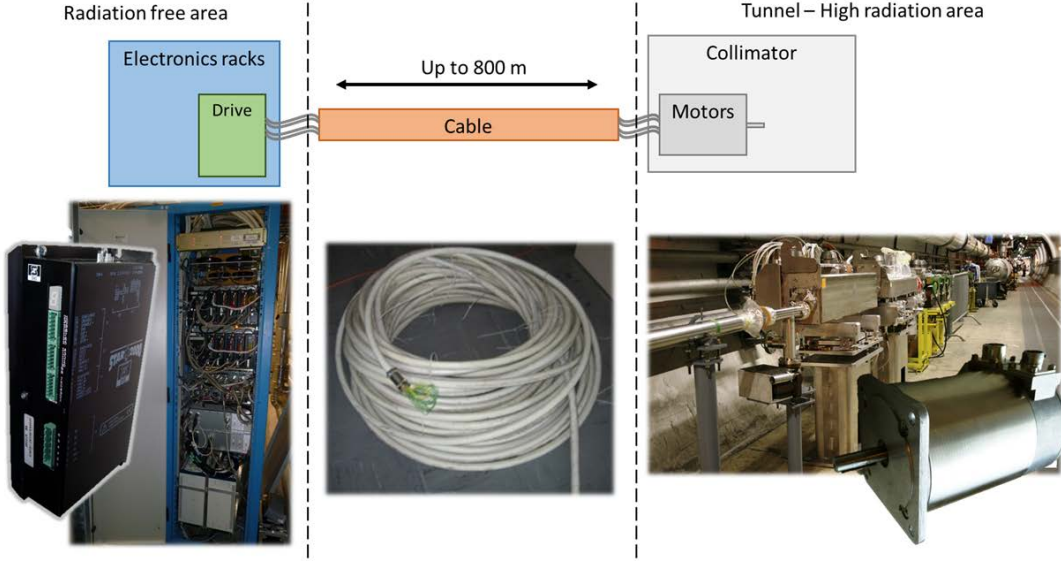


Figure 3.1: On the left side an electronic rack and a drive, in a radiation safe area, on the right the collimator with the motors in the accelerator tunnel, in highly radioactive areas, and on the middle the cable connecting them

In the following sections the consequences of the use of long cables with switched signals and stepper motors without position feedback is explained in detail.

3.2 Use of switched drives with long cables

Most stepper motor applications do not require long cables to transfer power to the motor. However, certain applications, such as in radioactive environments in particle accelerator complexes (e.g. the LHC at CERN) and nuclear power plants, or underwater applications, exist where the motor has to be located far from its power drive. These cases cannot be dealt with directly by most of these switched motor drives. The long cables, when high frequency PWM signals are applied, behave like transmission lines, leading to different problems preventing the motor drives from working appropriately.

Modern electric motor drives work mostly with discrete switches to improve efficiency compared to linear power supplies, feeding the phases of the motor with PWM voltage waveforms of high frequencies compared to the mechanical and electrical bandwidths of the motor, and high voltage amplitudes compared to the average values applied per chopping period to the motor.

This behaviour is normally acceptable since the phase of the motor is basically an inductor, and so it acts as a low pass filter for the current when the pulsed voltage is applied.

However, in the described cases where long cables are used, different effects arise. This situation has been studied in the general literature of transmission lines ([59]) and specifically when power motor drives are connected to AC motors. The effect and sizing of this phenomenon is shown in [37], where the most relevant cable and motor parameters are studied with specific focus on the over voltages produced on the motor-side. The critical parameters leading to motor-side voltages over twice the bridge voltage are also found. In [60] high frequency models of a cable and motor combination are presented.

In [25] the problem generated in the motor insulation is studied. The short rise time of technologies like MOSFET and IGBT combined with the high voltage used, produces such a high du/dt , the derivative of the voltage applied to the phase with respect to time, that the winding of the motor phase is equivalent to a network of capacitors, and therefore at switch on time the voltage is held by the first few turns, leading to turn-to-turn insulation damage.

Nevertheless, very little literature describing the use of stepper motors with long cables exists, to the author's knowledge, though the control problem is considered in [52, 53], where the motor-side current is estimated from the drive-side current, and the current control loop is closed on this estimation. Details of this work are given in chapter 4, as it is the starting point of the present thesis.

Now the most important effects on each part of these systems is detailed. When a pulsed voltage is applied to a long cable, the cable acts as a transmission line and, depending on the PWM chopping frequency, three important problems can arise: drive-side current, common-mode current and motor-side voltage.

3.2.1 Drive-side current

The first problem occurs at the drive-side of the cable, where a ringing phenomena in the current appears. This ringing effect is shown in Fig. 3.2, where a 20 kHz PWM voltage with 120 V amplitude and fixed duty cycle is applied to a motor phase through a 720 meter cable. The motor and cable used are the same models as the ones used in the LHC, described in section 2.3. In this case, the main ringing effect occurs at the 3rd harmonic of the PWM frequency, 60 kHz. This effect is due to the relative difference between the characteristic impedance of the

cable and the output impedance of the drive, the latter being much smaller than the former, and causing big current oscillations for negligible oscillations on the voltage.

The drive-side current can have large amplitude oscillations, over twice its mean value, and high frequency content, mainly at the harmonics of the PWM signal, depending on the cable length and characteristics. Some motor drives do not close the loop on the phase current, and therefore they do not have a problem with this phenomena though over-current warnings may be triggered. Many modern drives do, however, use current feedback control in order to achieve faster dynamics. Normally it then is a problem to deal with this current, specially with threshold based regulators such as hysteretic regulators, where the ringing on the current would trigger the controller comparators when the actual current in the motor is still far from the reference one. Dynamical controllers may work due to their frequency shaping action that can strongly attenuate the ringing components, which are high frequency components with respect to the normal closed loop bandwidths of the motor phase current.

One of the drives used during this work with a hybrid stepper motor is a commercial switched drive with a nominal RMS current of 2 A. In Fig. 3.3 it can be seen how using this drive the currents in the motor phases are far from the reference value when a 720 meter cable is used. This occurs because the comparators in the drive, which compare the current with the reference threshold, use the oscillating drive-side current, resulting in false detections of the current overcoming the reference and thus applying an erroneous control action to the cable.

3.2.2 Common-mode current

For ease of installation reasons, it is common to use multiwire cables when working with long cables, so that several motors can be driven via a single long cable. This situation leads to the second problem, the cross-talk between phases and between phases and shielding. This phenomena provokes an AC CM current in the phase. This CM current is superimposed on the DM current to form the one shown in Fig. 3.2.

These currents have two main negative effects. Firstly, as mentioned before, the current controller comparators may be triggered by current spikes, just like those due to cross talk. In Fig. 3.4 the CM current of a motor phase fed with a

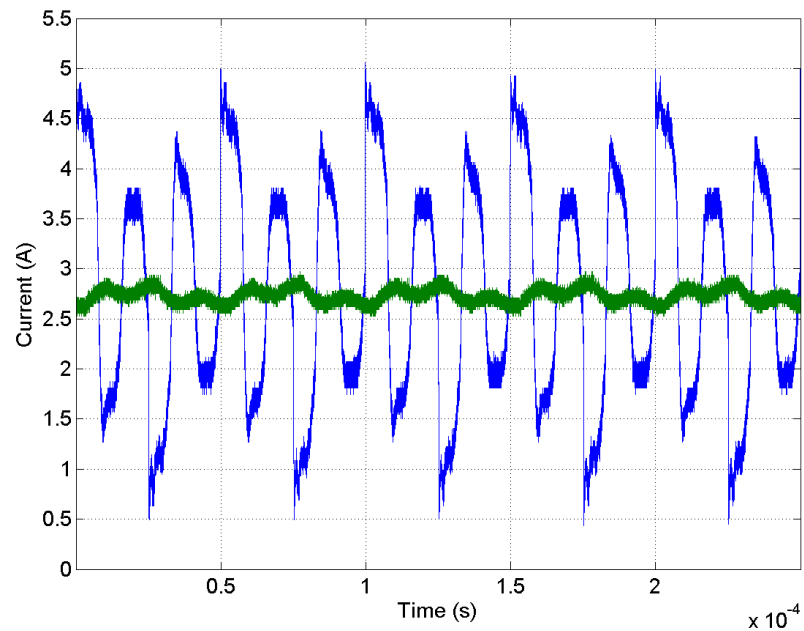


Figure 3.2: Measured phase currents. Blue: drive-side current, green: motor-side current

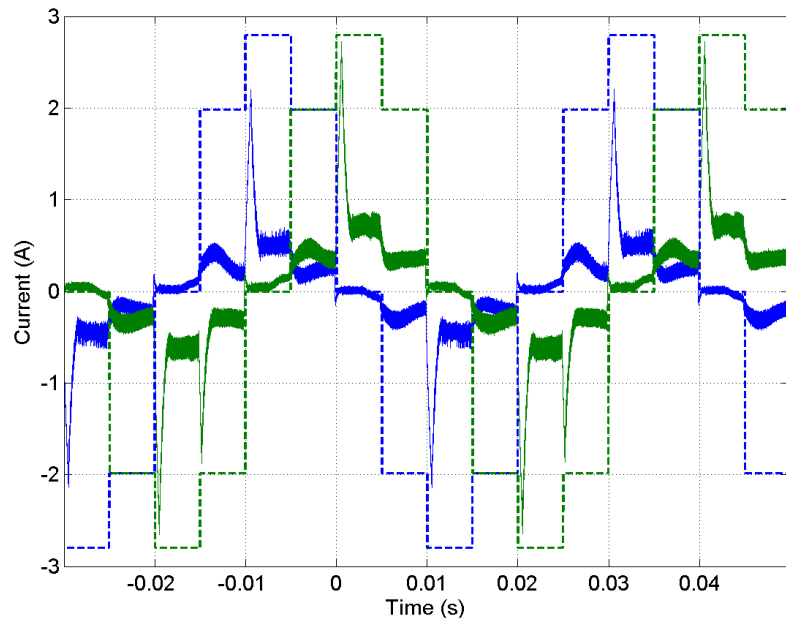


Figure 3.3: Measured motor-side currents. Blue: phase A real, green: phase B real, dashed blue: phase A reference, dashed green: phase B reference

fixed duty cycle, 120 V, 20 kHz PWM voltage through a 720 meter, 24 twisted pair, shielded, multiwire cable is shown. The current peaks in this case exceed 1.5 A, which may suffice to trigger the controller comparators when they should not.

Secondly, a CM current fed to a long cable produces significant EMI emissions, creating EMC problems. The consequences of CM currents and EMI emissions generated in motor applications have been addressed in [81] and [32].

3.2.3 Motor-side voltage

The third problem, at the other extreme of the cable, is the voltage across the motor terminals. In this case, the impedance of the motor at high frequencies is much higher than the characteristic impedance of the cable, causing big oscillations in the voltage for small oscillations on the current.

Depending on the combination of cable length, voltage rise time and PWM frequency, the oscillations may reach or even exceed twice the applied voltage in the drive-side of the cable. These oscillation also have relatively high frequency, that of the PWM frequency and its harmonics.

This effect may lead to insulation breakdown in the motor windings, due to the high voltage amplitude and derivative. Fig.3.5 shows these motor-side oscillations when a 120 V, fixed duty cycle, 20 kHz PWM voltage is applied through a 720 meter cable as the one used in the LHC collimators, described in section 2.3.

3.3 Use of stepper motors and open loop position control

Hybrid stepper motors are often used as the actuators in positioning systems. These are robust motors with a relatively high accuracy working in open loop positioning. For this to be possible, they rely on a precise mechanical construction and a high nominal electromagnetic torque. The nominal torque of the motor is chosen at least twice the maximum expected torque in the application. In this way, if this torque is not overcome, it can be assumed with a good confidence that the motor is within a known bound of the desired position.

However, in the event of higher than nominal load torques, stepper motors can lose steps. In order to prevent this, it is of interest to have real-time knowledge

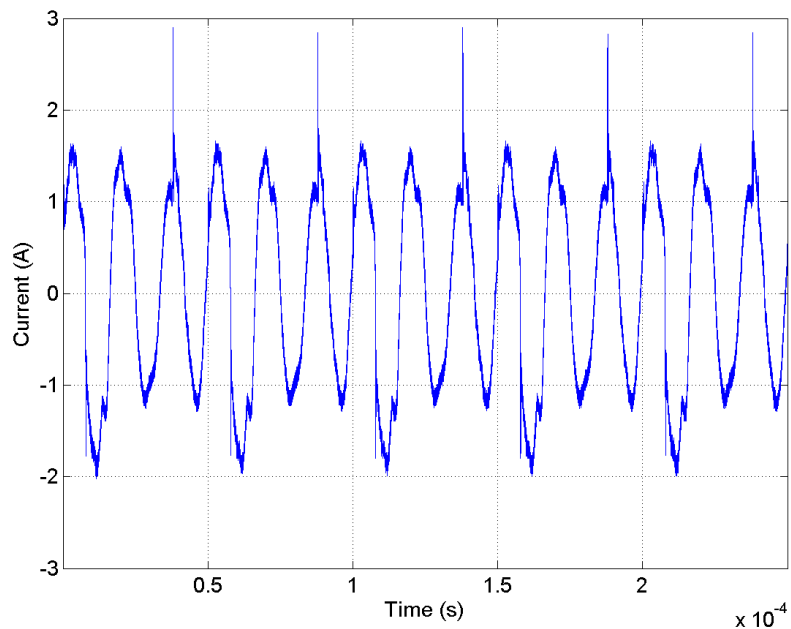


Figure 3.4: Measured common-mode phase current.

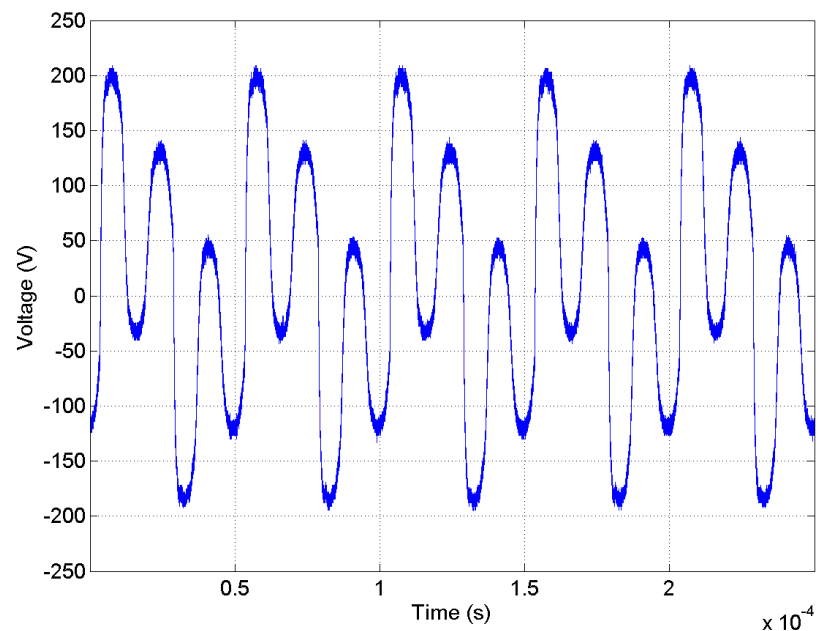


Figure 3.5: Measured motor-side voltage.

of the motor's position so that compensatory action can be taken to correct misalignments or lost steps. Rotary encoders and resolvers can both be used to provide motor position feedback, but they both increase the positioning system's cost and reduce its reliability. In the case at hand, the situation is even worse since on one side the sensors must be designed to be radiation hard and, on the other, it is not affordable to reduce the overall reliability of the system. Sensorless technology is, therefore, an attractive alternative.

In addition, stepper motors motion profiles are abrupt by nature. As their name indicates, these profiles are stepped, and therefore high accelerations are constantly applied. In Fig. 3.6 an example of the rotor's angle and speed in a sequence of steps in half-step mode is shown. It can be appreciated how the angle has big oscillations, leading to high instantaneous speeds. In this example, for an average speed of roughly 0.65 rads/sec, maximums of 16.4 rads/sec are reached.

This kind of motion profile is hard for the mechanics that are connected to the motor, and mechanical degradation is unavoidable. For this reason, the use of sensorless technology is again desirable in order to estimate the mechanical degradation of the collimators. This is possible thanks to the estimation and monitoring of the torque applied by the motor during the motion.

During the validation tests of the collimator mechanics, tight margins are set for the torque applied along the jaw motion range. If this torque changes during the lifetime of the collimator, sensorless torque estimation would allow it to be detected before a mechanical failure occurs, allowing for preventive maintenance during the planned technical stops of the machine, instead of reactive maintenance forcing a stop of the machine unexpectedly with the costs involved.

3.4 Purpose of the thesis

The purpose of this thesis work is to deal with the problems presented in this chapter.

The starting point is the work described in chapter 4. An algorithm to estimate the rotor position and the applied load torque with long cables is proposed, in order to detect steps lost and perform mechanical diagnostics of the collimator. It is developed and implemented in a real-time application. Improvements in the state-of-the-art for real-time state estimation applied to electrical motors are necessary for this application.

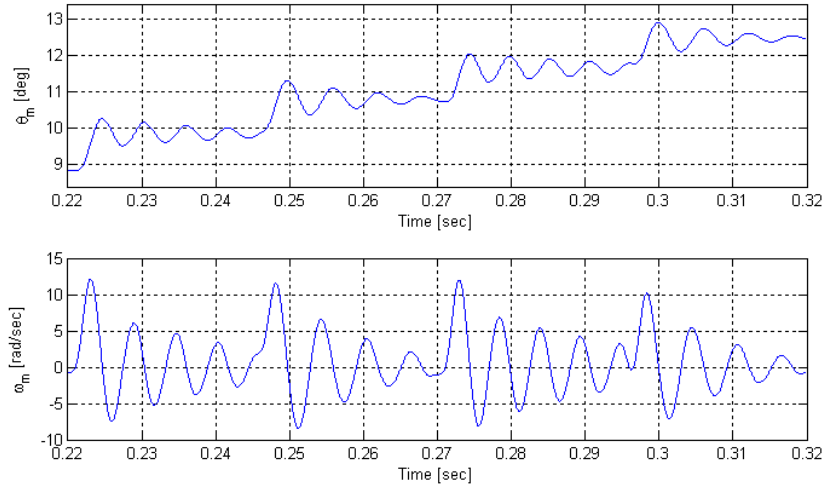


Figure 3.6: Measured rotor angle and speed stepping in half-step mode.

Then, the Field Oriented Control or Vector Control method is investigated for its use in position control of hybrid stepper motors and implemented in our application. The purpose of this is to smooth the aforementioned abrupt motion profile present in stepper motors in order to reduce vibration and improve mechanical lifetime. The result of several applications are presented. However, position feedback is needed for this type of control, and it is not desirable to rely on position sensors for the collimator control. A means to use these sensors whilst maintaining the reliability of the system in case of sensor failure is necessary.

To tackle the long cable problem a power approach can be taken, manipulating the actual cable-motor system before attempting to close the current loops. This is done with the proposal of output filters for stepper motors. Output filters are a standard solution for AC motors working with long cables in industry. However, their use with stepper motors has not been reported at the time of the present work.

Chapter 4

The Stepper Motor Drive

4.1 Introduction

This work started over the base of some previously developed work in the same project line. In the first part of this chapter, the aforementioned work is described, in order to give a better understanding of the context. In the second part the DSP Drive developed and used for the experimental validation during the thesis is presented.

4.2 Previous work

Analog solution

The first step in the bigger goal of controlling the collimator jaws position with high precision was to have a stepper drive able to work with long cables, up to 1 km. As presented in section 3.2, commercial PWM drives cannot work properly with cables of this length due to the high current ringing, and therefore a solution to overcome this problem was necessary.

This was achieved by a collaboration between CERN engineers and a private company to produce a modified version of one of their commercial drives, the SHS Star 2000.

This drive works at 20 kHz PWM chopping frequency and 135 V DC link voltage. It uses a non-linear control algorithm implemented with a state machine that applies a fixed frequency PWM with a minimum T_{on} time, i.e. the time where the voltage applied to the motor phase is the voltage of the power supply

used in the H-bridge, and uses a comparator which controls the PWM width, switching off the voltage applied if the current overcomes the reference and the minimum T_{on} has been applied.

It has been designed to work with up to 1 kHz equivalent closed loop bandwidth. This value has to be taken carefully since the concept of closed bandwidth is applicable only to linear systems. However, it gives a good idea of the response speed in closed loop of the system.

The solution developed is explained in detail in [19]. It consists on the use of a filtered version of the drive-side current by means of an analog filter implementing an estimation transfer function which from the drive-side measurement would provide the motor-side current estimation, and with this estimation the current loop could be closed.

This solution was implemented and it is the present solution working in the LHC [53]. However, it has several limitations. The values for the analog filter estimator were fixed by resistors in a board externally attached to the drive. This means that only motor side currents for some discrete cable lengths, of a specific cable type, could be estimated properly.

In addition, one of the main issues of drives when used in large installations such as the LHC is the emitted electromagnetic field. It can potentially generate interferences with very sensitive equipment installed either directly in the tunnel, since the cables run for hundreds meters all around the tunnel, or in racks mounted in suitable zones in order to be protected from ionizing radiations.

The most critical emitted frequencies from the power cables lie at the low end of the spectrum. Increasing the PWM frequency upwards has the double advantage of reducing the current ripple in the motor phase and potentially producing less powerful emissions in the low frequency range. To accomplish this, there has to be no subharmonics generated. Nonlinear and hysteresis current controllers cannot guarantee this constraint whereas fixed PWM period linear controllers do not have this drawback.

This fact lead to the proposal of a fully digital version of the drive in which the filter and controller could be calculated from the cable parameters and length, measurable from the drive with a simple test. The new controller to be implemented in this drive shall be a linear one, since it will avoid the generation of sub-harmonics of the chopping frequency and it can be made cable length dependent in a relatively simple way.

Digital solution

In [19] the first version of a 5th order digital estimation filter is proposed, based on the Taylor expansion of the hyperbolic functions that define the transmission line behaviour (details of this model are given in the following sections). In [52] an improved version, a 5th order filter based on a balanced Padé approximation to the hyperbolic functions is used. In [27], a similar approximation is used, but applied to the final transfer function relating drive-side and motor-side currents, instead of to the hyperbolic functions independently. In the latter approximation the order is reduced to 2nd instead of 5th as in the previous ones, after careful testing of the best estimation performance.

The motor-side current estimation scheme developed in the aforementioned work is explained next.

4.2.1 Motor-Side Current estimation scheme

Motor and cable model

When the motor phases are connected to a long cable, the behaviour of the system changes and therefore the model must be updated to include it. The electrical model includes now a transmission line between drive and motor while the mechanical model is unaffected by the presence of the cable.

The connecting cable can be represented by an equivalent 2-port T-net model. Using this model, each phase of the motor with its cable can be represented as in Fig. 4.1.

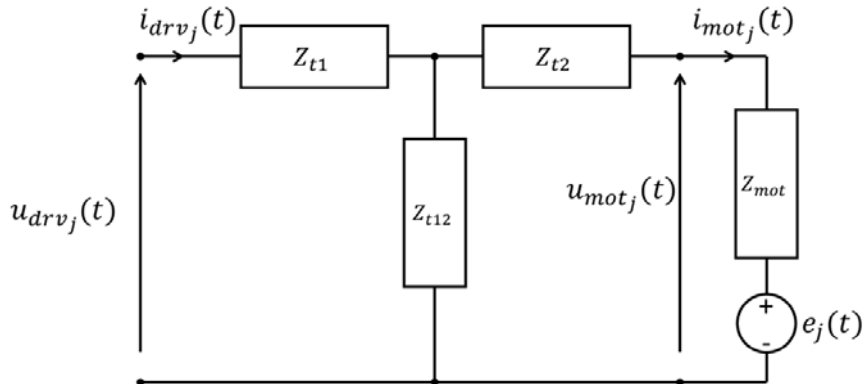


Figure 4.1: 2-port T-net cable model connected to motor phase

The three new impedances introduced are given as:

$$Z_{t1}(s) = Z_{t2}(s) = Z_0(s) [\coth(\gamma_0(s)h) - \operatorname{csch}(\gamma_0(s)h)] \quad (4.1)$$

and

$$Z_{t12}(s) = Z_0(s) \operatorname{csch}(\gamma_0(s)h) \quad (4.2)$$

where

$$\gamma_0(s) = \sqrt{(r + sl)(g + sc)}$$

is the propagation coefficient and

$$Z_0(s) = \sqrt{\frac{r + sl}{g + sc}}$$

is the characteristic impedance with h being the cable length, r , l , g and c being the resistance, inductance, conductance and capacitance of the cable per unit length respectively.

The electrical model for the cable and motor combination now links the drive-side current in phase j , i_{drv_j} , to the drive-side voltage in phase j , u_{drv_j} , and, in the Laplace domain, is given by:

$$I_{drv_j}(s) = G_{cm}(s)U_{drv_j}(s) + H_{cm}(s)E_j(s) \quad (4.3)$$

where

$$\begin{aligned} G_{cm}(s) &= \frac{1}{Z_{t1} + Z_{t12} || (Z_{t2} + Z_{mot})} \\ &= \frac{Z_0 \cosh(\gamma_0 h) + Z_{mot} \sinh(\gamma_0 h)}{Z_0 [Z_{mot} \cosh(\gamma_0 h) + Z_0 \sinh(\gamma_0 h)]} \end{aligned} \quad (4.4)$$

and

$$\begin{aligned} H_{cm}(s) &= \frac{Z_{t12}}{Z_{t1} + Z_{t12}} \frac{-1}{Z_{mot} + Z_{t2} + Z_{t1} || Z_{t12}} \\ &= \frac{-1}{Z_{mot} \cosh(\gamma_0 h) + Z_0 \sinh(\gamma_0 h)}. \end{aligned} \quad (4.5)$$

Note that the s dependence has been and will be omitted in some equations for clarity.

The De-Ringing Filter

In order to virtually eliminate the effects of the transmission line on the control signal the motor-side current has to be estimated from the only measurable signal available, the drive side current. To accomplish that it is possible to apply the current divider rule to the circuit shown in Fig. 4.1. The motor current can be evaluated by superposition as follows:

$$I_{mot_j} = \frac{Z_{t12}}{Z_{t12} + Z_{t2} + Z_{mot}} I_{drv_j} - \frac{1}{Z_{t12} + Z_{t2} + Z_{mot}} E_j \quad (4.6)$$

By means of the transmission lines equations (4.1) and (4.2), it is possible to write the following expression:

$$\begin{aligned} I_{mot_j} &= \frac{Z_0}{Z_0 \cosh(\gamma_0 h) + Z_{mot} \sinh(\gamma_0 h)} I_{drv_j} - \frac{\sinh(\gamma_0 h)}{Z_0 \cosh(\gamma_0 h) + Z_{mot} \sinh(\gamma_0 h)} E_j \\ &= G_{est} I_{drv_j} - G_{err} E_j \end{aligned} \quad (4.7)$$

Note that G_{err} and G_{est} are symbols for transfer functions, not conductances specifically, even though G_{err} has the dimensions of one.

Now the estimation error, $I_\epsilon(s) = G_{err}(s)E(s)$, should be evaluated. For hybrid stepping motors, the back electromotive forces of the motor phases are given in (2.2). Even for this type of motors, which have a high value of K_m , the maximum value of the back electromotive force is generally limited to few tens of volts since they are best suited to low speed applications. $G_{err}(s)$ can now be evaluated and the results shown in Fig. 4.2 for the motor and cable parameter values reported in tables 2.1 and 2.2, confirming that the estimation error $I_\epsilon(s)$ can be safely neglected for cable lengths of 1 km or even more. Indeed, even considering the worst case in which $G_{err}(s)$ has a maximum, the amplitude of the back emf at that frequency range is very limited so the attenuation due to $G_{err}(s)$ can be reasonably considered greater than 60 dB. This means that the motor-side current can be directly estimated from the drive-side current with good precision by applying $G_{est}(s)$ to I_{drv} .

4.2.2 Controller design

A linear controller that, at each PWM fixed period, sets the duty cycle of the Mosfet bridge has been implemented in order not to jeopardize the shift towards

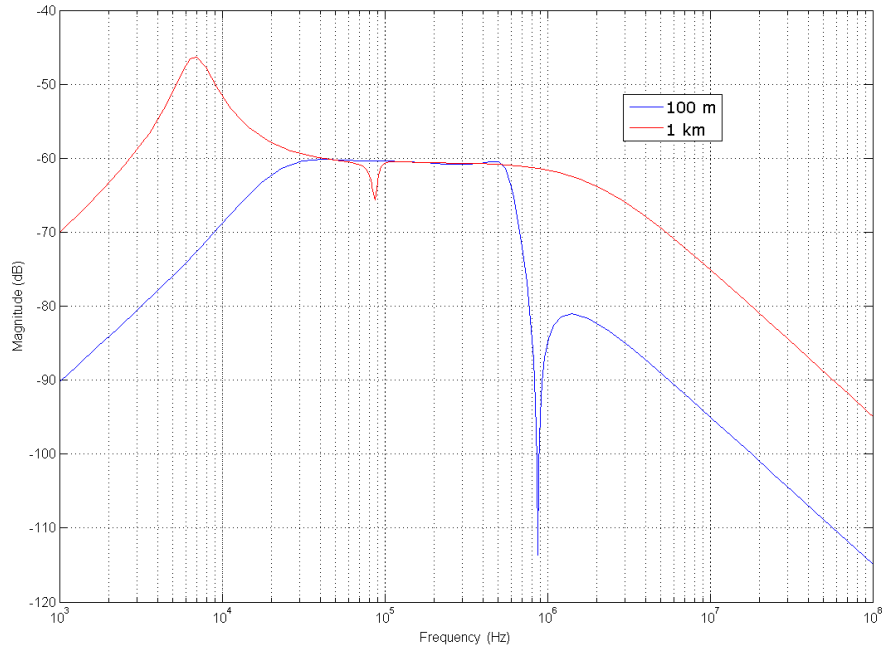


Figure 4.2: Comparison of $G_{err}(s)$ transfer function for two different cable lengths: 100 m and 1 km.

higher frequencies of the electromagnetic emitted power.

An inverse dynamics controller with an integral action has been designed for each motor phase current loop. It mainly has a single design parameter: the closed loop bandwidth B_{cl} .

Since the phase current is estimated by means of G_{est} , the system cable - motor phase can be approximated, for the controller design, by a simple RL circuit with the following time constant:

$$\tau_z = \frac{L_w + lh}{R_w + rh} \quad (4.8)$$

where R_w is the phase winding resistance, rh is the overall cable resistance, L_w is the DC (or slowly varying) phase inductance and lh is the overall cable inductance.

It is worth noting that the current references for the usual stepping mode drive are slow varying compared to the PWM frequency, so it has been decided to use the nominal DC value for the inductance, whereas this value would not have been adequate for the drive side current filtering by means of $G_{est}(s)$.

Taking into account that eventually a pole will be present in the motor phase impedance $Z_{mot}(s)$ (even if its position is not critical for the controller design)

the closed loop system can be reduced to a single time constant system with:

$$\tau_{cl} = \frac{1}{2\pi B_{cl}} \quad (4.9)$$

by means of the following controller:

$$C(s) = \mu \frac{1 + s\tau_z}{s(1 + s\tau_p)} \quad (4.10)$$

$$\mu = 2\pi B_{cl}(R_w + rh)$$

The value of τ_p , introduced in (2.5), has been fixed at $10\mu s$ after different tests. Even though it is a function of the frequency (see [52]), as already stated, its precise value is not critical for the controller design as long as it is sufficiently small compared to τ_z .

The continuous time controller has then been discretized by means of the Tustin transformation with a discretization period T_{cont} equal to the PWM period allowing the PWM duty cycle to be decided by the controller at each period. The controller has been parallelized to isolate the integral action in order to simplify the anti-windup implementation. The controller coefficients have been analytically expressed in terms of the motor and cable parameters and obviously in terms of the cable length. Those parameters are set once by the programming interface (together with many others) whereas the cable length is estimated by a self-tuning procedure (see [52]).

The scheme of the discrete time controller with causal Anti-Windup is depicted in Fig. 4.3. The integral and non-integral actions are clearly distinguished, the actuator saturation represents the DC voltage supply of the full H Mosfet bridge whose value is continuously monitored to keep the actuator model updated. The controller coefficients are expressed by the following equations ([50]):

$$A_1 = \frac{T_{cont} - 2\tau_p}{T_{cont} + 2\tau_p} \quad (4.11)$$

$$B_0 = B_1 = \mu T_{cont} \frac{\tau_z - \tau_p}{T_{cont} + 2\tau_p}$$

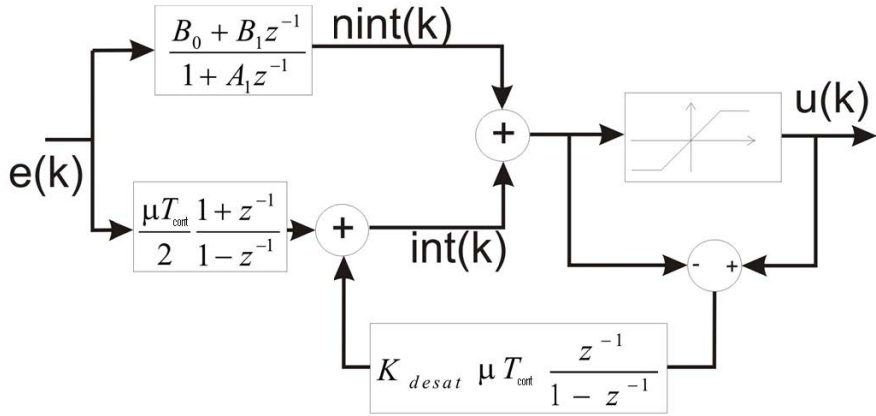


Figure 4.3: Motor phase current discrete controller

4.3 The developed DSP Drive

In the previous section the current solution applied in the LHC has been explained as well as the proposal for a new digital controller, which is implemented on an in-house developed DSP based drive. The goals to fulfil with this drive are:

- Ability to measure the cable and adapt the current estimation filter and controller coefficients.
- Improve positioning repeatability respect to the current solution.
- Reduce emissions, specially in frequencies below 18 kHz, and eliminate the presence of subharmonics of the chopping frequency.
- Establish an open platform for implementation of advanced techniques: sensorless state estimation, Field Oriented Control, etc.

Fig. 4.4 shows a blocks scheme of the stepper motor driver showing the current loops and the currents reference generator. The PWM block represents the H-bridge, through which the control actions calculated by the current controllers are applied to the motor phases. The motor can be seen as its electrical subsystem, composed by the winding resistance and inductance, and the electromechanical subsystem, which interacts with the electrical part with the back emfs. The most significant design choices implementing the drive are presented now.

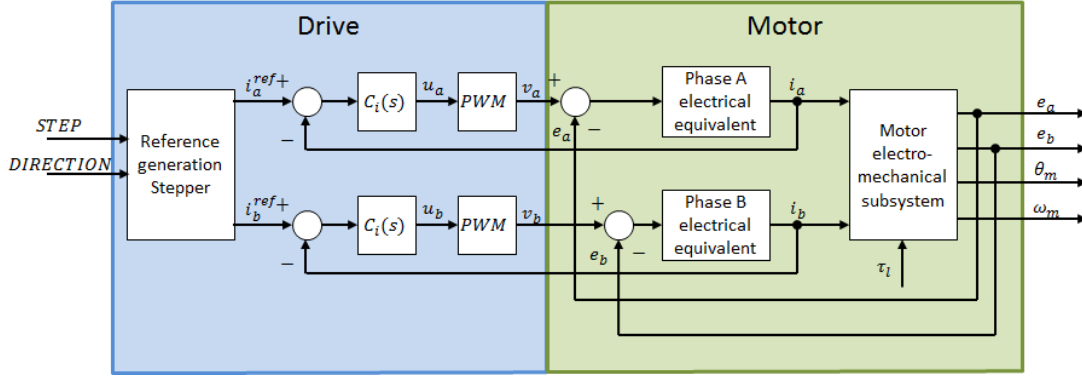


Figure 4.4: Standard stepper motor drive scheme

4.3.1 Hardware design

The power stage of the drive consists of two full Mosfet H-bridges connected to a DSP as shown in Fig. 4.5. The Mosfets used are *IRFB31N20D* ($I_D = 31A$, $R_{DS(on)}(max) = 0.082\Omega$, $V_{DSS} = 200V$). The nominal voltage V_{DD} of the drive is 135 V, but some margin is left for applications with longer cables.

The 8 Mosfets are driven by four *IR2183* Mosfet drivers, each one driving a full leg of the bridge. They are optically coupled to the PWM signals (through a *74HC540D* buffer) by means of 8 *6N137* optocouplers. Particular attention has been paid in the electronic design of the board and PCB routing to keep the power and the signal circuits separated.

At the core of the drive there is the *TI TMS320F28335*, a full floating point DSP of the DSC series which fulfils completely the requirements for the application having PWMs directly available to drive the bridge and a multiplexed 16 channel 12.5 MS/s, 12 bits ADC to acquire all the relevant signals.

The 150 MHz full floating point CPU simplifies noticeably the code development since no conversion to and from fixed point format is needed and considerably enhances the execution speed so the current estimation filters can run at 500 kS/s or even faster. The current measurements are made by means of two *LEM LTSR 6-NP* (measuring ranges ± 19.2 A, ± 12.8 A, ± 6.4 A, DC-200 kHz bandwidth -1 dB). A high measurement range is required in order to correctly reproduce the ringing at the filter inputs.

An anti-aliasing stage has been foreseen with a -3 dB bandwidth of 30 kHz which is the -3 dB maximum bandwidth of G_{est} (this corresponds to the estimated bandwidth of a 100 m cable, the cable and motor parameters are reported

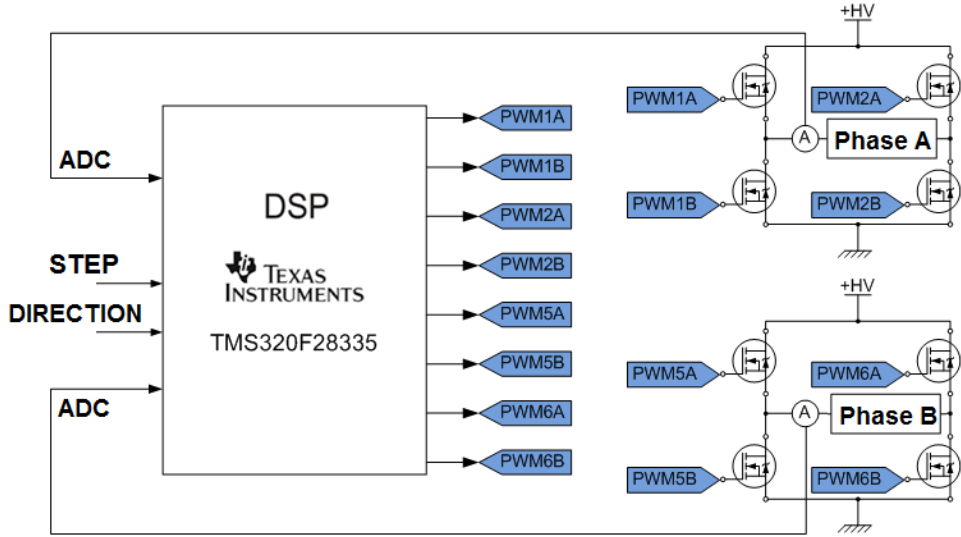


Figure 4.5: Connection of the DSP to the MOSFET h-bridges (not all the components represented)

in section 2.3. The anti-aliasing filter design is not critical since the nominal sampling rate is greater than 500 kS/s so at least one decade on the right of the maximum -3 dB bandwidth.

The board details are illustrated in Fig. 4.6, where the most important components have been highlighted. On the leftmost of the picture there are the two current sensors. Next to them, there are the Mosfet bridges covered by the heat sink. Next, on the right, the Mosfet drivers are visible and further on the right the optocouplers that electrically insulate the signal part of the board from the power part. On the right of the optocouplers there is eventually the DSP and the circuitry devoted to the communication.

4.3.2 Software design

The drive, whose state diagram is shown in Fig. 4.7, has been designed to be interfaced to any stepper module. The program is stored in the flash memory of the DSP and it is transferred to the RAM memory at power up. Once the initialization procedure is performed, the cable length measurement and the consequent tuning is performed during this phase, the DSP goes into an infinite empty loop waiting for the different interrupts (see Fig. 4.8).

These interrupts have a specific priority selected to satisfy the real time constraints. The fastest one, executing the current estimation filter, is executed with

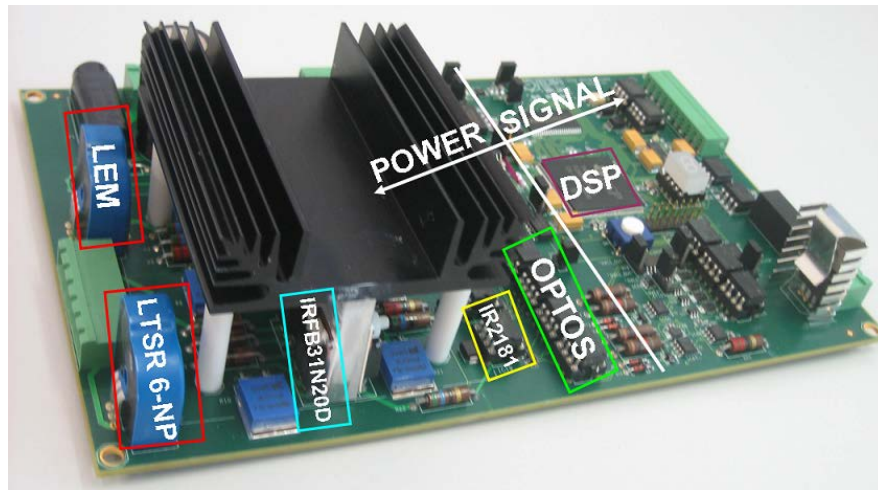


Figure 4.6: Drive board

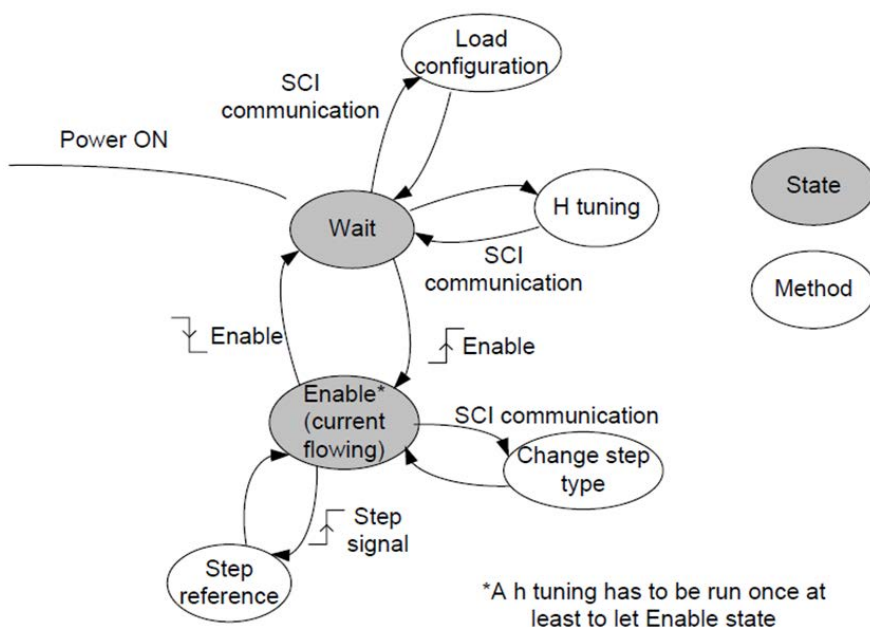


Figure 4.7: State machine diagram

the maximum priority, in order to do the motor current estimation with the highest possible accuracy. The next is the digital current controller interrupt, which calculates and sets the appropriate controller action through the PWM actions.

After the digital controller has been executed, which is the critical code in this interrupt, some diagnostics of the drive are performed, such as temperature readings of the bridge heat sink and over and under voltage of the power supply. Finally the step signal interrupt, which is asynchronous, is executed with the lowest priority. In Fig. 4.8 a scheme of the interrupts is shown.

4.3.3 3rd harmonic current correction

A feature implemented in the DSP drive is the 3rd harmonic current correction. The instantaneous electromagnetic torque produced by a two phase hybrid stepping motor is approximated by the following equation:

$$\tau_{em} = K_m(-i_{motA}\sin(p\theta_m) + i_{motB}\cos(p\theta_m)) \quad (4.12)$$

Higher harmonics are however not negligible ([22, 57]), the 3rd being the most significant. Its compensation has therefore been foreseen in the reference generation as shown in the following expression of the phase currents references:

$$\begin{aligned} i_{motA}(t) &= \sqrt{2}I_{RMS} [(1 - \alpha)\sin(2\pi ft) - \alpha\sin(3 \times 2\pi ft)] \\ i_{motB}(t) &= \sqrt{2}I_{RMS} [(1 - \alpha)\cos(2\pi ft) + \alpha\cos(3 \times 2\pi ft)] \end{aligned} \quad (4.13)$$

where

$$f = m \frac{f_{step}}{4}, \quad (4.14)$$

$m = 1, 1/2, 1/4, 1/8 \dots$ is the stepping mode (i.e. full step, half step and so on), f_{step} is the step rate, and $\alpha \in [-1/8, 1/4]$ is the 3rd harmonic current correction coefficient which is generally expressed in [%].

α is bounded in order not to alter the peak value of the current waveforms (clearly when $\alpha \neq 0$ the ratio of the peak value and the rms value is not $\sqrt{2}$ anymore, but the notation in (4.13) has been kept since the usual parametrization for the drives is in terms of rms values).

The identification of the optimal α in terms of positioning repeatability has to be carried out experimentally for different stepping modes. The references of the phase currents are generated according to (4.13). Those values are stored in

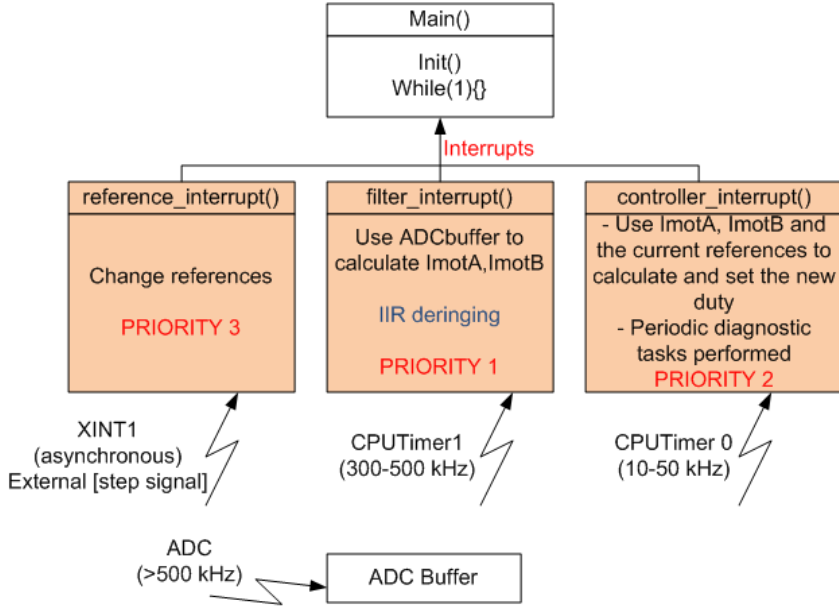


Figure 4.8: Programmed interrupts

arrays and, at each step edge received from a stepper module, the next values are set: an interrupt is triggered and served updating two pointers only. In Fig. 4.9 the effect of the 3rd harmonic reduction on the current reference waveform shape is shown graphically. With positive α the sinusoid is thin, whereas for negative α it is thick.

4.3.4 H-tuning

H-tuning is the name given to the procedure used to measure the cable length with the drive. The motor phase resistance and the cable characteristic values, needed for the procedure, have to be known in advance.

For the measurement, a current with a fixed known duty PWM is applied to the motor phases through the cable. To avoid dynamic effects on the current some time is allowed to extinguish the transients. The current is measured over a period of some milliseconds at a fast sampling rate for several PWM periods. The same is done in both phases and in both current directions, and the mean value of the four measurements is used to calculate the resistance of the phase with the cable included. Subtracting the phase resistance the total resistance of the cable is found, and with the resistance per kilometre the cable length is obtained.

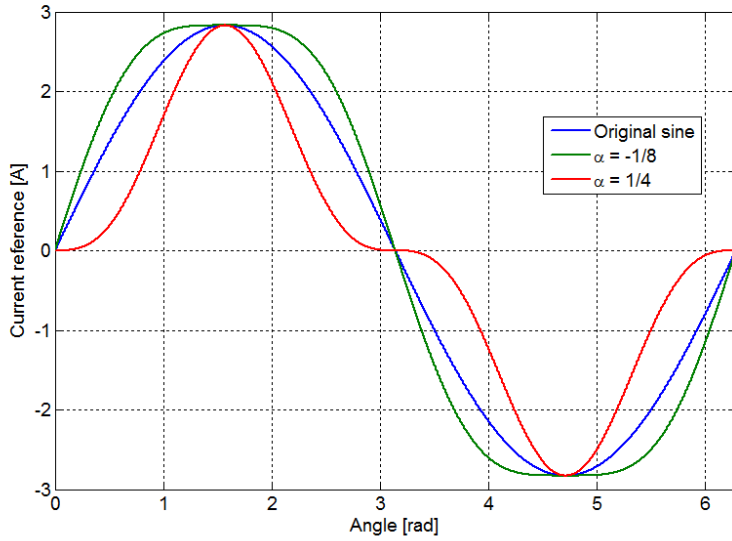


Figure 4.9: Third harmonic compensation current reference for the extreme values of α

4.3.5 Experimental results

Particular attention has been paid to the positioning repeatability and EMI emissions since these are the most critical performances that can be optimized only once a reliable phase current control has been achieved as shown in Fig. 4.10. In this figure the typical motor phase current waveforms on the drive and motor side for a 720 m cable length are shown, working in half-step mode with $f_{step} = 400$ step/s. The difference between the current measured by the drive and the current circulating in the motor phase is clear.

The Positioning Repeatability

Positioning repeatability tests have been performed with a test bench programmed in LabView®. The real angle step performed by the reference motor is measured with a 32768 lines/turn encoder. The angle measurement is performed 50 ms after the step has been completed in order to wait for the extinction of the mechanical transients.

In Table 4.1, the repeatability results without a long cable connecting the motor of the proposed drive are compared with a SHS Star 2000, the commercial drive mentioned in section 4.2. The repeatability is measured as the standard deviation of the angle after each step, σ , over the target angle, θ_{step} . This compar-

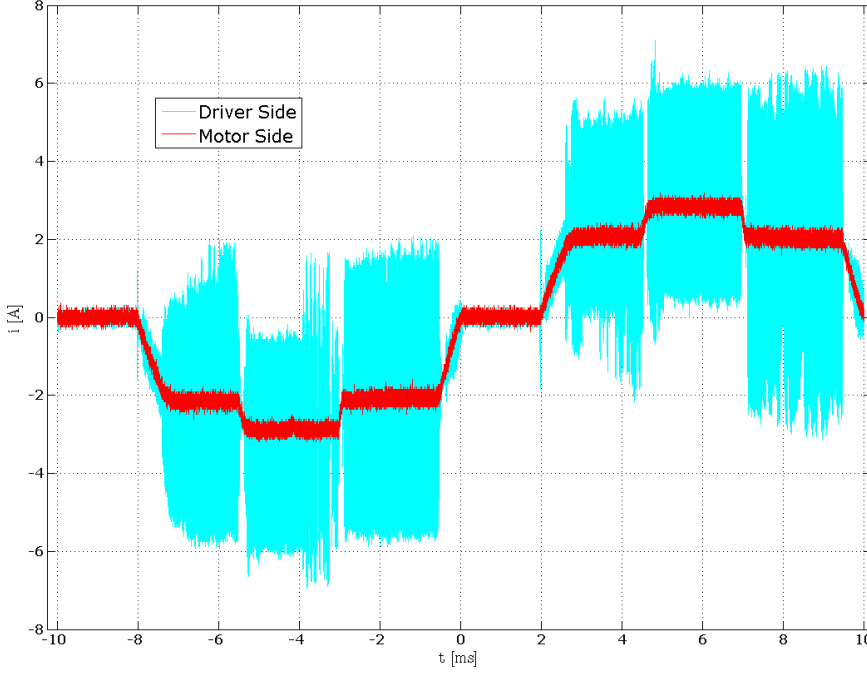


Figure 4.10: Typical motor phase current waveforms on the drive and motor side for a 720 m cable length

ison has been realized for the drive working in half step, and therefore $\theta_{step} = 0.9$ deg. The results show an improvement in the proposed drive, especially remarkable when the 3rd harmonic is set to its optimum value.

In Table 4.2, the proposed drive is compared with the SHS Star 2000 drive again, performing the same test with a long cable to connect the motor to the drive.

In Table 4.3 the results for the DSP drive with a 720 m cable long, working in 1/4 and 1/8 stepping modes, for a positive range of 3rd harmonic compensation are shown. At 12% correction the optimum for these stepping modes is achieved, yielding a noticeable improvement in the repeatability.

In Figs. 4.12 and 4.13 the sample positioning error distributions in 1/4 and

Table 4.1: Repeatability test comparison without a long cable connecting the motor

Drive	Cable length (m)	3 rd harmonic compensation [%]	$\sigma/\theta_{step} [\%]$	Figure
SHS Star 2000	0	-	4.8	Fig. 4.11 a)
Proposed drive	0	0	4.5	Fig. 4.11 b)
Proposed drive	0	18	4.1	Fig. 4.11 c)

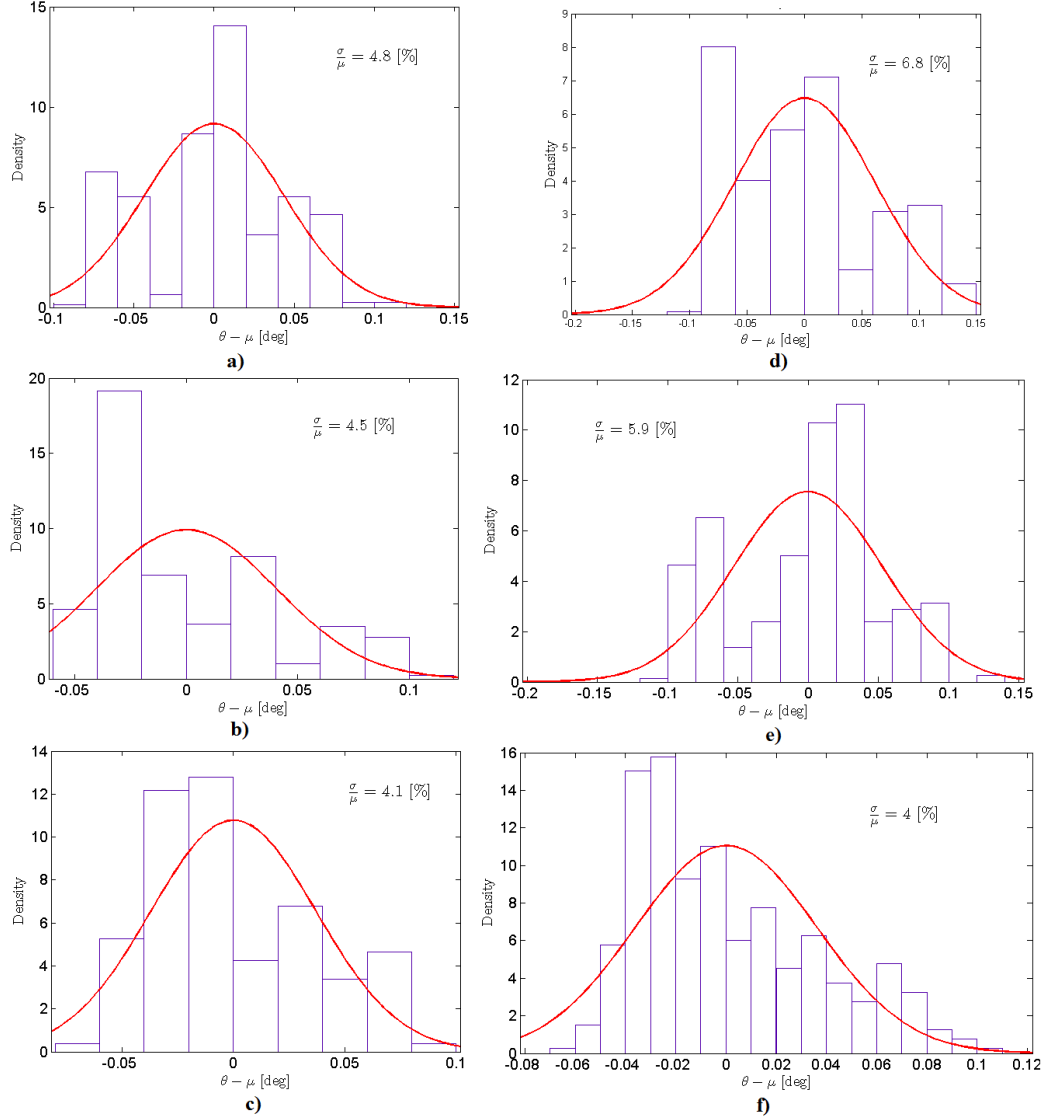


Figure 4.11: Repeatability results for the SHS Star 2000, the modified SHS and the proposed drive

Table 4.2: Repeatability test comparison with modified commercial drive and a long cable connecting drive and motor

Drive	Cable length (m)	3 rd harmonic compensation [%]	σ/θ_{step} [%]	Figure
Modified SHS	720	-	6.8	Fig. 4.11 d)
Proposed drive	720	0	5.9	Fig. 4.11 e)
Proposed drive	720	18	4.0	Fig. 4.11 f)

Table 4.3: Repeatability performance in different stepping modes

α [%]	Step Mode	
	$1/4$ $\theta_{step} = 0.450$ deg	$1/8$ $\theta_{step} = 0.225$ deg
0	47	51
4	35	38
8	20	17
12	6	8.2
16	20	27
20	48	51
24	69	73

$1/8$ stepping mode are shown. It is easy to appreciate how using different values of α results in moving the peaks of the histograms that eventually become a single peak when the optimum value is achieved (the bi-modal distributions becomes mono-modal). The positioning accuracy can therefore be noticeably increased with a suitable choice of the 3rd harmonic correction.

The EMI

Concerning the amplitude spectrum of the emitted field shown in Fig. 4.14, there are principally two different aspects to be discussed.

The envelope of the spectrum is due to the transmission line behavior of the cable. Its shape closely traces out the amplitude of the motor-cable impedance seen on the drive side whereas its placement, in the frequency spectrum, depends on the cable length. For different cable lengths the envelope shifts whilst keeping the same shape.

A comparison between the modified SHS, which works at 20 kHz, and the proposed DSP based prototype working at 50 kHz PWM frequency and running the estimation filter at 500 kS/s is shown. The modified SHS saturates the low frequency spectrum since subharmonics are also clearly present whereas the fixed PWM period linear regulator prototype drive have only the spectral lines of the first and the higher harmonics that can be easily shifted in case of interference with other sensitive equipment.

The spiral antenna sensing the magnetic field and complying with the standard *IEC 60478-5* Type A is connected to an *Agilent E7405A* EMC analyzer. A section of the twisted pair cable has been replaced by a section with straight

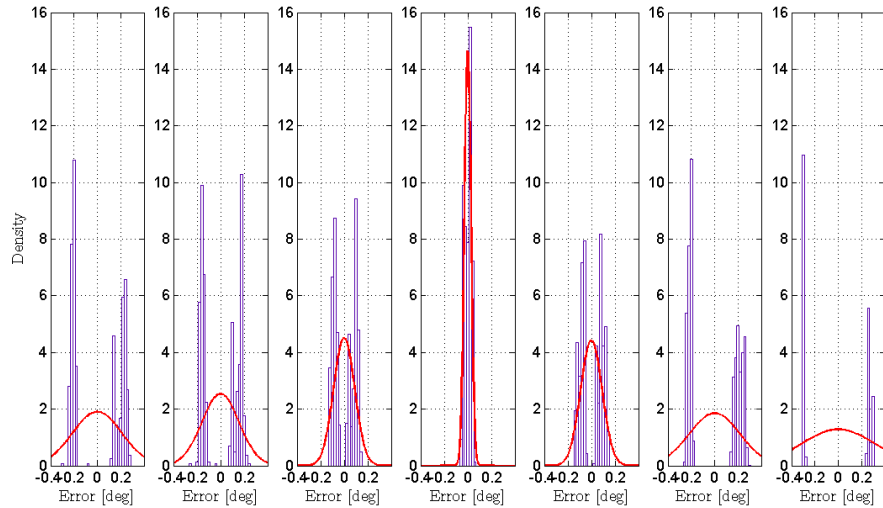


Figure 4.12: Repeatability histograms for 1/4 stepping mode ($\theta_{step}=0.45$ deg). From left to right the values of α are 0%, 4%, 8%, 12%, 16%, 20%, 24%

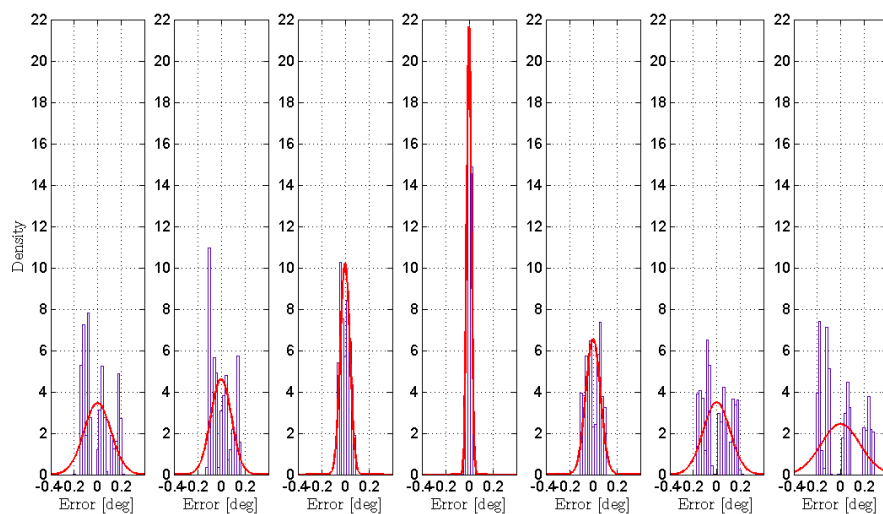


Figure 4.13: Repeatability histograms for 1/8 stepping mode ($\theta_{step}=0.225$ deg). From left to right the values of α are 0%, 4%, 8%, 12%, 16%, 20%, 24%

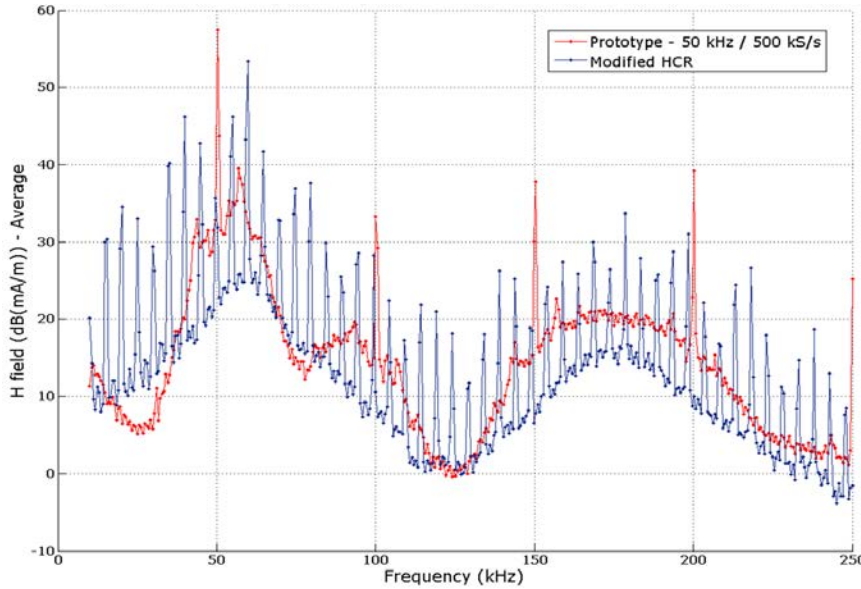


Figure 4.14: Low frequency spectrum of EMI emissions on drive side with a 720 m long cable.

conductors, as shown in Fig. 4.15, to allow more uniform measurements. The straight conductors cable section, the spiral antenna and the EMC analyzer have been placed on a conducting plane complying with the above mentioned standard.

4.4 Conclusions

In this chapter the developed DSP based PWM stepping motor drive has been presented. This drive is used during the rest of the thesis for most of the experimental set-ups.

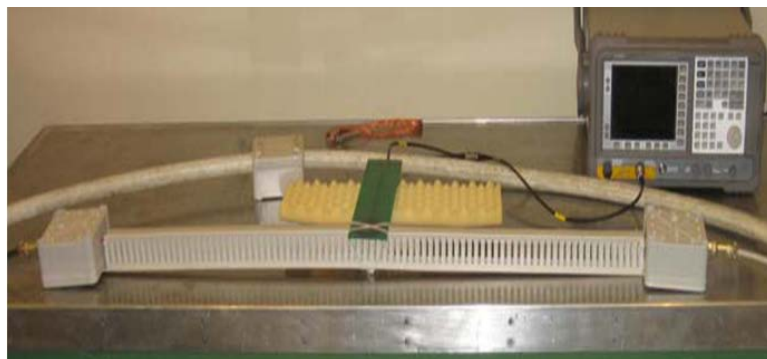


Figure 4.15: The EMI test bench

The prototype is operated at 50 kHz chopping frequency though this frequency is configurable, and it is designed to work with cables up to 1 km length. Measurement results show that the positioning repeatability is improved with respect to the modified commercial drive and can reach similar values with and without long cables when applying the appropriate 3rd harmonic correction on the phase current reference generation. The EMI emitted from the power cable has been drastically reduced with a linear controller and the achieved chopping frequency, which shifted the emitted energy spectrum to high frequencies.

Part II

Sensorless Estimation for Hybrid Stepper Motors

Chapter 5

Introduction to Position and Torque Sensorless Estimation

5.1 Motivation

Good motor positioning repeatability and the capability to detect lost steps is of great importance for a proper operation of the collimators. It is thus necessary to have real-time knowledge of the motor position in order that compensatory action can be taken to correct any misalignments.

However, working in a high radiation environment makes things more difficult than usual, as seen in chapter 3. Most position and torque sensors do not function correctly in these working conditions, and even though there are sensors like the Linear Variable Differential Transformer (LVDT) or the Resolver that can be constructed to be radiation-hard, the system cannot rely solely on them since failure is not affordable: intervention in the collimation areas is extremely difficult and expensive due to the radiation, even during the machine technical stops.

In addition, even if the stepping motors work at nominal torque, chosen by design to be at least twice the nominal load torque, having an estimate of the real load torque can be useful to warn of mechanical degradation. All the LHC collimators have passed acceptance tests where the load torques over the entire axes strokes have been measured and verified. Load torque warning thresholds can be easily determined for each collimator axis according to the collimator type and orientation.

For the aforementioned reason, high robustness is mandatory. Failure of the sensors must not be critical, and therefore redundancy through sensorless methods

is desirable.

With the increase in power and decrease in cost of embedded processors in recent years, the drives used to power and control stepper motors have become increasingly sophisticated. For example, in [88] compensation of the detent torque and several harmonics of the HSM in the quadrature axis component of the current is proposed, both for use in open loop, where the angle used for the Park Transform is the command position, and closed loop, where an encoder is used for position information, in order to prevent the motor characteristic resonances. Improved diagnostics can thus be achieved through the use of sensorless algorithms instead of via additional sensors, with their associated higher costs and lower reliability.

In this part, firstly the application of a well known sensorless technique, the Kalman Filter, and specifically its variation adapted to deal with non-linear systems, the Extended Kalman Filter, is proposed to get the desired estimate of motor position and torque despite the presence of long cables. Then novel HSM model extensions are proposed and used in the EKF to further improve the estimation performance.

The Kalman Filter is well documented, with classic books like [14] and more modern ones like [30, 79], to cite only a few. [58] is also a classic from literature where the Kalman Filter is explained in a very intuitive way thanks to a simple example where the author proposes to take the place of someone trying to estimate his own position. [31] gives as well a very friendly approach to the filter first with a single state example and then extending it to any number of states, by using the associated information matrix of a Gaussian distribution to explain the process for getting the filter equations.

The Kalman Filter is widely used in different industrial applications. In [3] a review of the main fields where it is used is given, sensorless control and diagnostics of motor drives being the main topics.

5.2 State of the art

5.2.1 On the use of the Extended Kalman Filter with Hybrid Stepper Motors connected Through Long Cables

Sensorless position and torque estimation techniques have been applied to Hybrid and Permanent Magnet Stepping Motors previously, largely due to the vast increase in computational power in modern embedded devices, such as Digital Signal Processors (DSP), at ever decreasing costs. [2] does a review of position estimation techniques for brushless permanent-magnet machines, by measurement of the back electro-motive force, the inductance variation and the flux-linkage variation, using direct estimation methods or observers. A similar review is performed in [38], focusing on brushless DC motors, but in addition the current injection method is considered and the estimation is presented for generators as well. [13] presents a review of high frequency injection methods for rotor position estimation.

A number of torque and position estimation techniques for stepping motors have been proposed using different methods. In [39] a disturbance observer is proposed for use with permanent-magnet stepper motors. Focused on hybrid stepper motors are some examples like [92], where a torque estimation technique without the feedback of speed or position sensors is proposed, and [94], where a damping control system using a speed and position observed based on a phase-locked loop that tracks the phase angle of the back electro-motive force voltage is presented. However, unlike the Extended Kalman Filter, they do not provide a unified method for full state estimation, rather only concentrating on a single signal.

Despite its relatively high computational complexity, the Kalman Filter, and more specifically the Extended Kalman Filter (EKF), has become one of the favoured approaches for sensorless position estimation in electric motors. For example in [12] the EKF is used to estimate position and angular speed in a permanent magnet synchronous motor drive and these estimations are used to close the angular control loop. In [87] the EKF is applied to estimate the same states for a brushless DC motor, with the addition that the filter is implemented both with fixed motor parameters and with online estimation of the stator resis-

tance, allowing for an improvement of the estimation specially at low speeds. An example of an application to induction motors can be found in [5].

The Kalman Filter estimates the motor states in an statistically optimal way despite the presence of both measurement and process disturbances. Furthermore, unknown inputs to the motor, such as an external load torque, can also be estimated in a structured way. This method has been used in different aspects of industry, e.g. in [77] the EKF estimates the unknown disturbance forces used for real-time active magnetic bearing control; in [45] the EKF is used to estimate unknown parameters and driving torque in an industrial manipulator with flexible joints.

State estimation for hybrid stepper motors, including the torque load, has been considered before in the literature, examples of this can be found in [62, 66, 67], where the filter is used for sensorless control of the motor, and in [6, 7] where in addition an effort to reduce the computational cost of the filter is done by proposing an steady-state Kalman filter. However, up to the date when this work was developed, the case of connecting the motor with long cables had not yet been dealt with for sensorless estimation.

As is discussed in chapter 6, direct application of the EKF to a model of cable plus motor is not feasible for real-time applications due to restricted processing power, and a way to overcome this is proposed and demonstrated.

In addition, the proposed philosophy to applying an EKF to a drive connected to a stepper motor by long cables is completely general and could be applied to other types of motors connected in this way, as are commonly found in particle accelerators, nuclear power plants, oil extraction [20] or underwater applications. In the food industry motors are placed in clean areas far from the drives. Even in some cases aerial vehicles use a long cable connecting the motor [8].

5.2.2 On the Hybrid Stepper Motor Electrical Model

The utilization of the EKF with HSM connected through long cables can be achieved successfully. Sensorless estimation allows the angular position of the motor to be estimated in real-time by optimally combining measurements of the motor electrical signals, current and voltage, with the prediction of a model of the motor. However, a consistent mismatch between the predicted voltage in the motor phase using the standard model for the HSM found in literature (see chapter 2) and the experimental results was noticed. In Fig. 7.1 this effect is

shown: there is a discrepancy when the phase has a non-zero current.

HSM modelling has received attention in the literature and typically the models fall into two categories, either for motor design or for control. Despite attempts to develop simpler models and analysis techniques e.g. [40, 41], models for motor design are normally of such high complexity that their use in real-time algorithms running on embedded processors is not possible. Models for control are at the other end of the complexity spectrum, being generic models that apply not only to HSMs , but also to Permanent Magnet Stepping Motors (PMSMs) and even more generally to permanent magnet AC synchronous motors. Practically all the references given for the use of EKF on HSM fall into this category.

This observation leads to the goal of improving the motor model whilst keeping it usable for real-time applications in embedded systems. Two extensions to the standard model of the electrical subsystem of an HSM, dependant on the rotor position and phase current respectively, are proposed in chapter 7. A combined model, which is simultaneously dependent on position and current is developed as well and magnetic theory is used to give an expression of the predicted electromagnetic torque. To demonstrate its success at reaching the goal, it is used in a real-time application.

5.3 The Extended Kalman Filter

In the previous section several references to the theory of the Kalman Filter and its extended version were given. A summary of its equations, which are used in this work, is given below.

For a discrete-time, nonlinear time-invariant system represented by the following state-space equations:

$$\begin{aligned}\mathbf{x}_{k+1} &= \mathbf{f}(\mathbf{x}_k, \mathbf{u}_k) + \mathbf{w}_k \\ \mathbf{y}_{k+1} &= \mathbf{h}(\mathbf{x}_{k+1}) + \mathbf{v}_{k+1},\end{aligned}\tag{5.1}$$

where $\mathbf{x}_k \in \mathbb{R}^n$ is the state vector at time step k , \mathbf{f} the real valued, differentiable state transition function, $\mathbf{u}_k \in \mathbb{R}^r$ the system input, $\mathbf{w}_k \in \mathbb{R}^n$ the process noise, $\mathbf{y}_k \in \mathbb{R}^m$ the measurement vector, \mathbf{h} the real valued, differentiable measurement function and $\mathbf{v}_k \in \mathbb{R}^m$ the measurement noise.

The following assumptions are made:

- **A1:** The process and measurement noises \mathbf{w}_k and \mathbf{v}_k are uncorrelated, zero-mean white-noise processes.
- **A2:** The initial state vector $\mathbf{x}_{0|0}$ is uncorrelated with both the process and measurement noises and has a known mean $\hat{\mathbf{x}}_{0|0}$ and covariance matrix $\mathbf{P}_{0|0}$.

Once the EKF has been initialised with values for $\hat{\mathbf{x}}_{0|0}$ and $\mathbf{P}_{0|0}$, two steps are executed consecutively at each time step:

1) Prediction:

$$\hat{\mathbf{x}}_{k+1|k} = \mathbf{f}(\hat{\mathbf{x}}_{k|k}, \mathbf{u}_k) \quad (5.2)$$

$$\mathbf{P}_{k+1|k} = \mathbf{A}_k \mathbf{P}_{k|k} \mathbf{A}_k^T + \mathbf{Q}_k$$

where $\mathbf{A}_k = \frac{\partial \mathbf{f}(\mathbf{x}_k, \mathbf{u}_k)}{\partial \mathbf{x}_k} \Big|_{\mathbf{x}_k=\hat{\mathbf{x}}_{k|k}}$ and $\mathbf{Q}_k \in \mathbb{R}^{n \times n}$ is the white process noise's covariance matrix.

2) Update:

$$\begin{aligned} \mathbf{K}_{k+1} &= \mathbf{P}_{k+1|k} \mathbf{H}_k^T \left[\mathbf{R}_{k+1} + \mathbf{H}_k \mathbf{P}_{k+1|k} \mathbf{H}_k^T \right]^{-1} \\ \hat{\mathbf{x}}_{k+1|k+1} &= \hat{\mathbf{x}}_{k+1|k} + \mathbf{K}_{k+1} [\mathbf{y}_{k+1} - \mathbf{h}(\hat{\mathbf{x}}_{k+1|k})] \end{aligned} \quad (5.3)$$

$$\mathbf{P}_{k+1|k+1} = \mathbf{P}_{k+1|k} - \mathbf{K}_{k+1} \left[\mathbf{R}_{k+1} + \mathbf{H}_k \mathbf{P}_{k+1|k} \mathbf{H}_k^T \right] \mathbf{K}_{k+1}^T \quad (5.4)$$

where $\mathbf{H}_k = \frac{\partial \mathbf{h}(\mathbf{x}_k)}{\partial \mathbf{x}_k} \Big|_{\mathbf{x}_k=\hat{\mathbf{x}}_{k+1|k}}$ and $\mathbf{R}_k \in \mathbb{R}^{m \times m}$ is the white measurement noise's covariance matrix.

Chapter 6

Application of the Extended Kalman Filter for a Sensorless Stepper Motor Drive Working With Long Cables

6.1 Introduction

In this chapter an approach for the EKF application to a motor drive in order to estimate a hybrid stepper motor's position when they are connected by long cables is proposed. This is one of the original contributions of this thesis. This approach is tested first in simulation and then in an experimental setup, applied on a real LHC collimator.

The DSP drive described in chapter 4 is the real-time platform on which the EKF algorithm is implemented. In standard operation it must service various interrupts including those of the motor current controllers and periodic drive monitoring tasks. Its computational resources are, therefore, limited, meaning that special attention to the EKF's computational load is required in its design.

6.2 The proposed approach

As seen in chapter 5.3, the EKF requires a model of the system whose states are going to be estimated, represented in state-space. In this case the system to be

driven includes the hybrid stepper motor and the long connecting cable.

6.2.1 Model selection

The EKF uses a discrete-time model, which can be obtained by discretising the model described in chapter 2 for the motor and chapter 4 for the cable. The system includes both the motor and the cable, and therefore the EKF should use the combined model of both.

The sampling period of the discrete-time model can be chosen such that the sampling frequency $f_s = 1/T$ satisfies:

$$6f_{bw} \leq f_s \leq 25f_{bw},$$

where f_{bw} is the bandwidth of the system producing the signals to be sampled [43].

In the case considered, the electrical sub-system containing the cable and the motor phase produces the highest frequency signals. As previously mentioned the drive applies the voltage to the system with a PWM signal. At a constant duty cycle, these PWM signals have fundamental harmonics at the chopping frequency, which for the collimators is typically chosen at 50 kHz due to EMI constraints [50]. Being similar to square waves, they also have non-negligible higher harmonics. Depending on the cable's length, the electrical sub-system can have a gain at the frequencies of these harmonics that is even greater than the gain at DC. This is demonstrated in Fig. 6.1, where the Bode magnitude diagram of $G_{cm}(s)$, the transfer function from the voltage applied to the cable and the resulting current, described in eq. (4.4), is plotted for two cable length extremes, using the typical cable and motor parameter values. These values are found in section 2.3.

Even only considering the first 3 harmonics a minimum sampling frequency of $6 \times 3 \times 50 \text{ kHz} = 900 \text{ kHz}$ would be required. The EKF algorithm is computationally demanding since it involves several matrix operations, including an inversion, and the complexity of those grows quickly with the matrices size, proportional in the state-space representation to the number of states of the system. Running the EKF at this magnitude of sampling frequency exceeds the computational power of standard DSPs and thus renders the model practically unusable for real-time industrial applications.

In [69] a similar argument is followed, starting by the modelling of the mo-

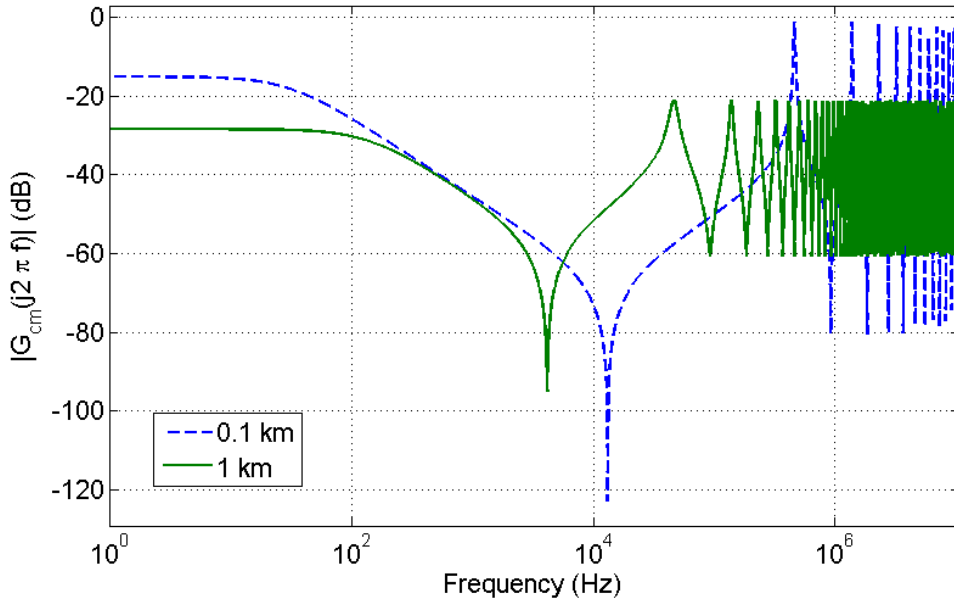


Figure 6.1: Bode magnitude diagram of $G_{cm}(s)$ for two cable length extremes

tor plus cable, with the approximation of the latter as a first order RLC stage, leading to the conclusion that even though the proposal is correct and works in simulation, it is not feasible to be implemented in a DSP platform due to the high computational load implied.

For this reason, the use of the motor model alone in the EKF is considered hereafter. Its electrical closed-loop bandwidth is typically at 1-2 kHz [50]. With this bandwidth, a sampling frequency for the EKF of 6-50 kHz can be used, which is much more reasonable for implementation on a DSP. In addition, the model is simpler than including the cable.

Using the motor model alone in the EKF means that its inputs and measurements are the motor-side voltages and currents respectively, which are not directly available. The available information is on the drive side, as shown in Fig. 6.2.

A different current estimation approach is proposed, using dedicated adaptive filters, which from the available drive side current measurements estimate the motor side current.

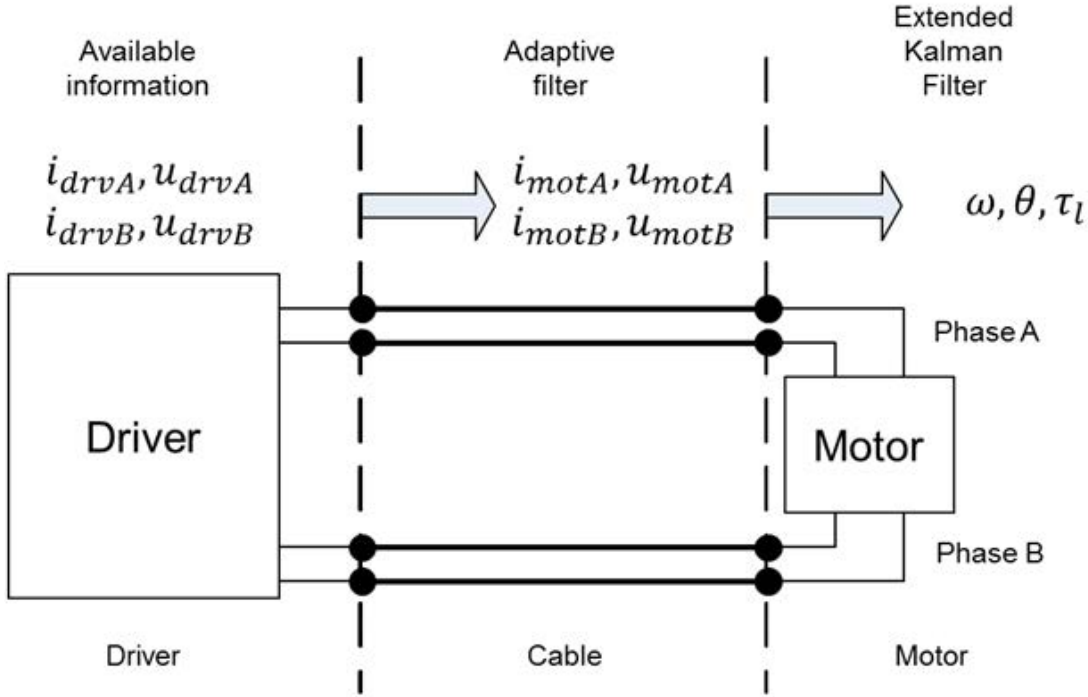


Figure 6.2: Schematic view of drive, motor and cable

6.2.2 Discrete-time, state-space version of chosen model

The EKF requires the state-space representation of the system. In chapter 2.2, the motor model is described in detail. The equations describing it are gathered in state-space form here:

$$\begin{aligned} L \dot{i}_{motA} &= -Ri_{motA} + K_m \omega \sin p\theta + u_{motA} \\ L \dot{i}_{motB} &= -Ri_{motB} - K_m \omega \cos p\theta + u_{motB} \\ J \dot{\omega} &= -i_{motA} K_m \sin p\theta + i_{motB} K_m \cos p\theta - B\omega - T_{dm} \sin(2p\theta + \phi) - \tau_l \\ \dot{\theta} &= \omega \end{aligned} \quad (6.1)$$

Since τ_l is unknown and unmeasurable in this application, it should be estimated by the EKF by augmenting the state vector. A model of τ_l is therefore required. In [95] the model state augmentation for non-stationary parameter estimation is intensively used, taking the variable to estimate as a 1st order random walk process and augmenting the state vector with it. In some publications (e.g. [6, 7, 62, 66, 67]), this same principle has been applied for unknown input

estimation, modelling the load torque in a hybrid stepper motor as:

$$\frac{d\tau_l}{dt} = d(t), \quad (6.2)$$

where $d(t)$ is a zero-mean, normally distributed, white noise. This same approach is followed.

The EKF requires discrete-time state transition and measurement equations of the system whose states are going to be estimated. Since only the model of the stepper motor is going to be used in the algorithm, these can be obtained from equations (6.1) and (6.2), resulting in the continuous-time state-space representation of the system represented in (6.3).

$$\begin{aligned}\dot{x}_1 &= a_{11}x_1 + a_{13}x_3 \sin px_4 + u_1 \\ \dot{x}_2 &= a_{22}x_2 + a_{23}x_3 \cos px_4 + u_2 \\ \dot{x}_3 &= a_{31}x_1 \sin px_4 + a_{23}x_2 \cos px_3 + a_{33}x_3 + a_{34} \sin(2px_4 + \phi) + a_{35}x_5 \\ \dot{x}_4 &= x_3 \\ \dot{x}_5 &= d(t)\end{aligned} \quad (6.3)$$

where x_i with $i = 1, \dots, 5$ are the state vector terms

$$\mathbf{x}(t) = \begin{bmatrix} i_{motA} \\ i_{motB} \\ \omega \\ \theta \\ \tau_l \end{bmatrix}, \quad (6.4)$$

u_1 and u_2 are the input vector terms

$$\mathbf{u}(t) = \begin{bmatrix} u_{motA} \\ u_{motB} \end{bmatrix} \quad (6.5)$$

and $a_{i,j}$ are the coefficients

$$\begin{aligned}a_{11} &= \frac{-R}{L} & a_{13} &= \frac{-K_m}{L} \\ a_{22} &= \frac{-R}{L} & a_{23} &= \frac{K_m}{L} \\ a_{31} &= \frac{-K_m}{J} & a_{32} &= \frac{K_m}{J} & a_{33} &= \frac{-B}{J} & a_{34} &= \frac{-T_{dm}}{J} & a_{35} &= \frac{-1}{J}.\end{aligned} \quad (6.6)$$

The measurement equation is given by the motor phase currents and therefore expressed in state-space form as

$$\mathbf{y} = \mathbf{h}(\mathbf{x}) = \begin{bmatrix} x_1 \\ x_2 \end{bmatrix} = \begin{bmatrix} i_{mot_A} \\ i_{mot_B} \end{bmatrix}. \quad (6.7)$$

In order to obtain the discrete state-space form that is required for the use with the EKF, the Forward Euler method is used with a sampling period of T_s . It consists on the approximation of the derivative of a variable with the equation (6.8).

$$\dot{x}_k \simeq \frac{x_{k+1} - x_k}{T_s} \quad (6.8)$$

where the state sub-index indicates the sampling instant, e.g. k for $k \times T_s$.

Applying (6.8) to the system described in (6.3), the state transition equation in (6.9) is obtained.

$$\mathbf{x}_{k+1} = \mathbf{f}(\mathbf{x}_k, \mathbf{u}_k) = \begin{bmatrix} (1 + a_{11}) x_{1,k} + a_{13} x_{3,k} \sin p x_{4,k} + b_{11} u_{1,k} \\ (1 + a_{22}) x_{2,k} + a_{23} x_{3,k} \cos p x_{4,k} + b_{22} u_{2,k} \\ f_{3,k} \\ x_{4,k} + T x_{3,k} \\ x_{5,k} \end{bmatrix} \quad (6.9)$$

where

$$f_{3,k} = a_{31} x_{1,k} \sin p x_{4,k} + a_{32} x_{2,k} \cos p x_{4,k} + (1 + a_{33}) x_{3,k} + a_{34} \sin(2 p x_{4,k} + \phi) + a_{35} x_{5,k},$$

$x_{i,k}$ and $u_{i,k}$ are the i^{th} component of the state and the input vectors at the discrete sampling instant k , respectively. The measurement equation remains unchanged, adopting only the index $k + 1$ to indicate the sampling instant.

$$\mathbf{h}(\mathbf{x}_{k+1}) = \begin{bmatrix} x_{1,k+1} \\ x_{2,k+1} \end{bmatrix}$$

6.2.3 Estimation of the EKF's inputs and measurements

As seen in the discretised model in the previous section, using exclusively the motor model in the EKF means that the algorithm's inputs and measurements are the motor-side voltages and currents, respectively. However, as previously stated,

these signals are not directly available in ordinary operation since measurements can only be made on the drive-side of the cable.

The cable's length, together with the relatively high chopping frequency of the PWM voltage signals, makes it act as a transmission line. This line's principal characteristics are those of a series resistor with a shunt capacitor across the motor's polarities. The capacitive behaviour induces large oscillations in the current at the cable's drive-end and, similarly, oscillations in the voltage at the cable's motor-end, both with frequency components close to those of the PWM's harmonics.

These oscillations on the drive-side current and motor-side voltage can be viewed as measurement and process noise, respectively, however the properties of these noises do not satisfy the assumption (A1) required for the EKF, as shown in chapter 5.3. This means that applying the Kalman filter on these signals is unlikely to produce reliable state estimates. Therefore, noise whitening filters are required.

The approach proposed is to use cable length adaptive estimators on the drive-side data. These estimators rely on the fact that the motor's dynamics are much slower than those of the cables. As previously discussed, the closed-loop bandwidth of the motor's phase currents is approximately 1-2 kHz. Since the motor electrical dynamics can be considered linear and time-invariant (LTI), with the back-emf acting as a slowly-varying disturbance, only frequency components of the motor phase voltages and currents within approximately a decade of this bandwidth significantly affect the current magnitude.

We are, therefore, only interested in estimating components of the motor-side signals within this lower range of frequencies. Since the cable can also be considered to be an LTI system in the frequency and signal amplitude ranges of use, it is possible to consider only the components of the drive-side signals at frequencies within this range. In the following subsections the estimators used to evaluate the motor-side currents and effective voltages are described.

Motor-side current estimator

Using the two port T-net cable model with the motor phase seen in chapter 4, Fig. 4.1, a transfer function between the drive-side current $I_{drv_j}(s)$ and the motor-side

current $I_{mot_j}(s)$ of phase j can be calculated, the estimator $H_{est}(s)$:

$$H_{est}(s) = \frac{I_{mot_j}(s)}{I_{drv_j}(s)} = \frac{Z_{t12}(s)}{Z_{t2}(s) + Z_{t12}(s) + Z_{mot}(s)}. \quad (6.10)$$

In this expression part of the the Back-EMF's contribution to $I_{mot_j}(s)$ is neglected. Nevertheless, as shown in [50], this contribution is negligible at standard motor operating speeds.

In the form expressed in (6.10), this transfer function is not directly implementable due to the transcendental hyperbolic functions leading to an infinite number of poles and zeros. Nonetheless, in the reduced frequency range of interest, it is possible to obtain an approximation, $\hat{H}_{est}(s)$, to this transfer function using a 2nd order Pade approximant. In Fig. 6.3 this approximation is plotted for two extremes of the cable length range. In the upper plot, superposition of the magnitudes can be appreciated, whilst for the bottom plot the magnitudes are nearly superimposed up to approximately 20 kHz.

The stability of this estimator is obviously of great importance. It is, however, difficult to prove analytically the filter's stability for all cable lengths due to the complexity of the coefficient expressions found via the Pade approximation procedure. Nonetheless, an empirical assessment has been made by evaluating the poles of $\hat{H}_{est}(s)$ over a grid of 100 cable lengths selected randomly from a uniform distribution in the range of interest i.e. [0.1 km, 1 km]. The poles of $\hat{H}_{est}(s)$ form a complex conjugate pair, their real parts are therefore the same. This value is plotted for each cable length in Fig. 6.4.

It can be seen that the real parts of the poles are all negative, ensuring, at least for the cable lengths considered, that $\hat{H}_{est}(s)$ is stable. Furthermore the values vary smoothly, despite the use of randomly distributed cable lengths, so it is unlikely that filters evaluated at inter-sample cable lengths would be unstable.

Since $\hat{H}_{est}(s)$ is cable length adaptive, it is logical to realise it as a digital filter $G_{est}(z)$ whose coefficients can be easily adapted to the cable used. The filter is, therefore, discretised using a Tustin transformation, chosen for its stability preserving property and good matching in the frequency domain. The sampling frequency used to discretise $\hat{H}_{est}(s)$ is normally higher than that used by the EKF, since its bandwidth can typically be higher, as seen in Fig. 6.3.

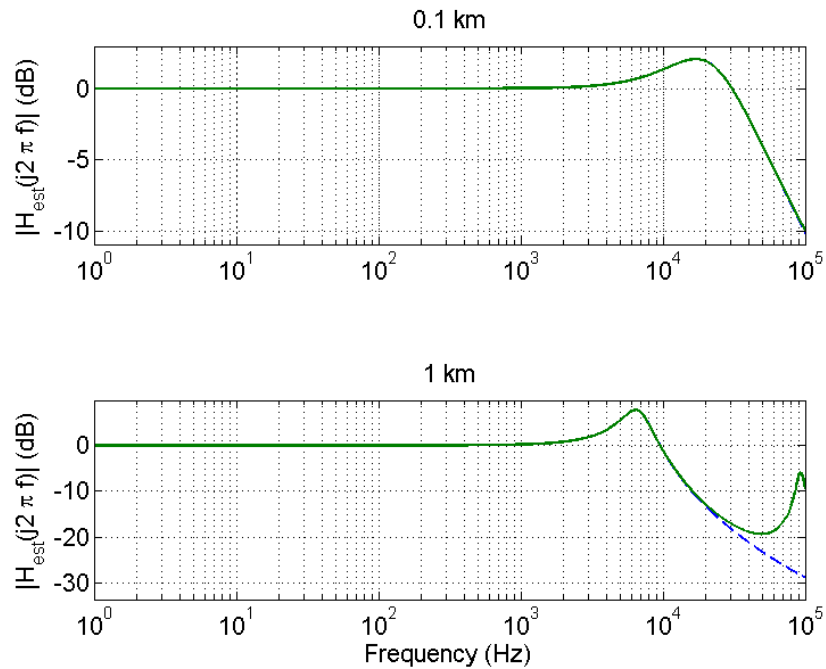


Figure 6.3: The approximation $\hat{H}_{est}(s)$ (dashed) and the exact expression $H_{est}(s)$ (solid) for two cable lengths.

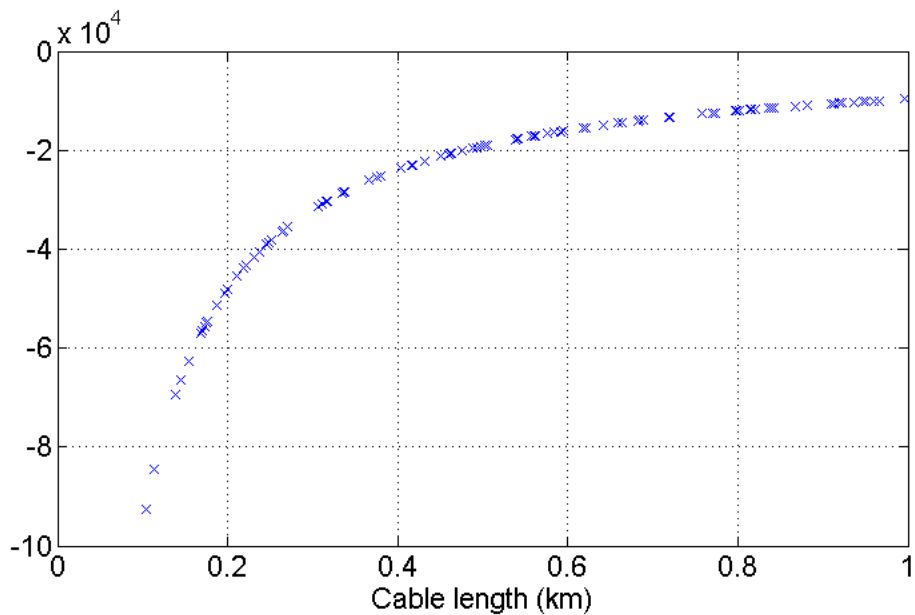


Figure 6.4: Real part of $\hat{H}_{est}(s)$'s poles over a range of cable lengths

Remarks:

- The motor impedance $Z_{mot}(s)$ used in $H_{est}(s)$ is different from that used in the EKF model, i.e. (2.3). It has been noted in [52] that the standard RL circuit does not accurately model the electrical dynamics above about 1 kHz. It is shown there that a high frequency pole at approximately 16 kHz should be added to the $Z_{mot}(s)$ model in (2.3). Since the EKF's main aim, however, is to estimate the lower frequency signal of the motor's position, only a negligible improvement in the estimation performance would be achieved by including this pole in the EKF's model, which would be far outweighed by the increased computational burden.
- If $G_{est}(z)$ is run at higher sampling rates than the EKF, its output should be downsampled for use in the EKF. Despite the low-pass characteristics of $G_{est}(z)$, it cannot necessarily be used as a digital anti-aliasing filter since its attenuation, especially for short cable lengths, may not be sufficient at the EKF's Nyquist frequency. In this case, a separate anti-aliasing filter should be used.

Motor-side voltage estimator

The motor-side voltage estimator is based on the idea that, within the relatively low frequency range of interest, the cable can be modelled such that the impedances Z_{t1} and Z_{t2} are replaced by resistors and Z_{t12} is replaced by a capacitor (see Fig. 6.5).

Neglecting the contribution from the Back-EMF, the transfer function between the motor-side and drive-side voltage of phase j is given by:

$$H_v = \frac{Z_{t12}Z_{mot}}{Z_{t1}(Z_{t2} + Z_{t12} + Z_{mot}) + Z_{t12}(Z_{t2} + Z_{mot})}.$$

Fig. 6.6 compares the frequency responses of this transfer function when the impedances are given by expressions (4.1) and (4.2) and when they are represented by 2 resistors and a capacitor, as in Fig. 6.5. The good correspondence between the two frequency responses at lower frequencies is evident.

Unfortunately it is not possible to directly implement $H_v(s)$ as the voltage estimator because it has a minimum bandwidth of over 3.3 MHz. This implies that a sampling rate in the order of 20 MHz would be necessary.

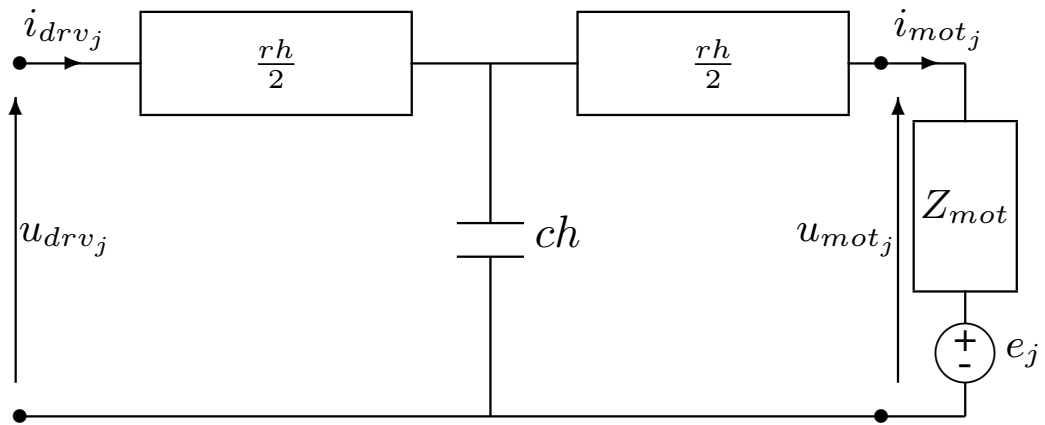
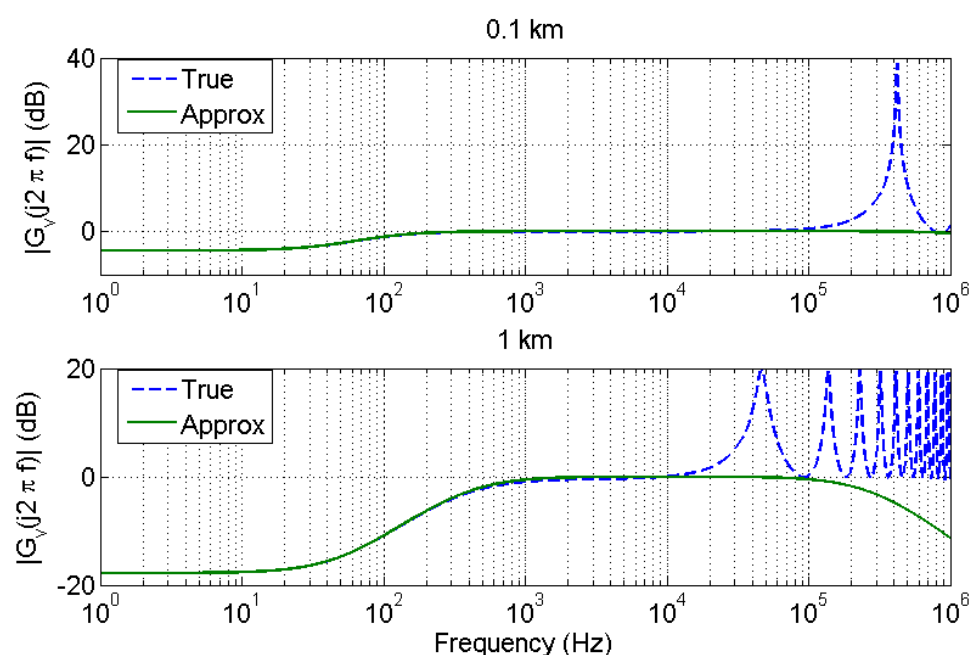


Figure 6.5: Low frequency cable model connected to motor phase

Figure 6.6: Comparison of the frequency responses of $H_v(s)$ using the complete impedance expressions and the approximation, for two cable length extremes

Nonetheless, using the circuit approximation, it is still possible to obtain an estimate of the motor-side voltage since the following relation holds:

$$u_{mot_j,k} = u_{drv_j,k} - \frac{rh}{2} (i_{mot_j,k} + i_{drv_j,k}). \quad (6.11)$$

It should be remembered that this expression holds for the low frequency model depicted in Fig. 6.5. The signals in it, therefore, refer to signals which are limited to the band of frequencies for which the model is valid. Low-pass filtered versions of $u_{drv_j,k}$, $i_{mot_j,k}$ and $i_{drv_j,k}$ are, therefore, required.

Since the computed control action is equal to the average voltage over a PWM chopping period, it can be directly used as a low-pass filtered version of $u_{drv_j,k}$. Using this value removes the need to increase the drive's electronic complexity with dedicated circuitry for the measurement of the instantaneous, AC voltage signals. The control algorithm for the drive's H-bridges should, nonetheless, be carefully designed to ensure that the desired average voltages are applied.

Moreover, a measurement of the slowly varying, DC bridge supply voltage should be available in order to calculate correctly the PWM signals' duty cycles. This measurement is typically available for drive diagnostics so the drive's complexity is not further increased.

$i_{mot_j,k}$ is available in its estimated form from the previously presented motor-side current estimator. It has a bandwidth equal to the current controller's closed-loop bandwidth, which is typically easily within the valid frequency band.

$i_{drv_j,k}$ can contain non-negligible frequency components at the PWM harmonic frequencies, as seen in Fig. 6.1, which violate the model's assumptions. Nonetheless these frequencies are greater than the frequency band of interest so they can be filtered out either analogically or digitally before the signal is used in the estimator expression (6.11).

Remark:

- The additional computing resources required for the above described estimators is less than would be needed for an EKF model incorporating even the low frequency cable dynamics. This is because the DSP is optimised to run Infinite Impulse Response (IIR) filters, such as $G_{est}(z)$, very efficiently, whereas the matrix manipulations required by the EKF are computationally very costly, especially for large matrices. The EKF incorporating these

dynamics would require 7 states and a more complex measurement state equation making it practically infeasible.

6.3 Simulation

In this section the effectiveness of the proposed method is demonstrated via simulation studies.

6.3.1 Simulator description

In order to validate the proposed approach, a realistic model of the drive-cable-motor system is required. For this purpose a high order, nonlinear model is developed using Mathworks's SimulinkTM. The model's main blocks, represented in Fig. 6.7, are

Reference generators: Generate the two phases' current references based on the desired stepping rate and mode. In the simulations full step, 1 phase on mode is used, with an RMS current reference value of 2 A. Full step mode corresponds to rotor steps of 1.8 degrees, as the modelled motor has $p = 50$.

Current controllers: Discrete-time linear PI current controllers, one per phase, operating at a sampling rate of 25 kHz and giving a closed-loop bandwidth of 1 kHz are implemented.

PWM: Control action modulators using a 120 V DC supply voltage, which compensates the voltage drops over the longest cable and allows the desired bandwidth to be achieved. It operates at a 50 kHz chopping frequency to prevent low frequency EMI emissions and reduce current ripple.

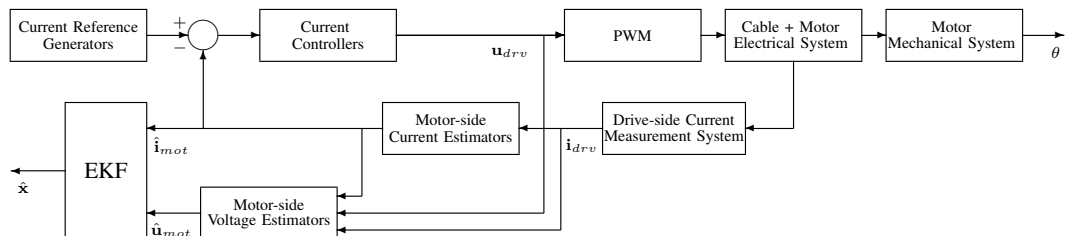


Figure 6.7: Simulation model structure

Cable and Motor electrical system model: Continuous-time, electrical system model using the parameter values in section 2.3. The cable model's hyperbolic terms are approximated by 4th order balanced Pade approximants [47, 80], allowing the cable dynamics to be approximated well up to 150 kHz over all cable lengths. The motor model uses the high frequency pole to model its high frequency dynamics accurately.

Motor mechanical system model: Continuous-time mechanical system model with parameter values given in section 2.3.

A load torque is applied to the rotor.

Drive-side current measurement system: Incorporates analog anti-aliasing filters, one per phase, taken as 2nd order Butterworth filters with bandwidths of 7 kHz. The cut-off frequency and order are chosen to achieve a trade-off between passing non-negligible frequency components of the currents which could affect the EKF estimation accuracy, yet acting as effective anti-aliasing filters and sufficiently attenuating components due to disturbances and noise above the Nyquist frequency of the EKF's sampling rate. This trade-off is valid since at 7 kHz the electrical system's closed-loop gain is approximately -17 dB, which can be considered negligible, and the anti-aliasing filters' gain at the Nyquist frequency is -10.5 dB, which can be considered sufficient suppression (see [42]). The low order filter has also been chosen to reduce the phase lag it introduces. It is also in this block that measurement noise is injected into the simulation. This noise has the following characteristics:

$$\mathbf{n}_k \in \mathcal{N}(\mathbf{0}, \mathbf{R}_n) \text{ where } \mathbf{R}_n = \text{diag}([0.05^2, 0.05^2])\mathbf{A}^2,$$

and is injected before the anti-aliasing filter.

Motor-side current estimators: $G_{est}(z)$ filtering the measured drive-side currents at a sampling frequency of 500 kHz.

Motor-side voltage estimators: Based on Eq. (6.11) and using the control actions as the drive-side voltages, the downsampled outputs of the anti-aliasing filters as the drive-side currents and the downsampled outputs of $G_{est}(z)$ as the motor-side currents.

Extended Kalman Filter: The EKF operates at the same sampling frequency as the current controllers, i.e. 25 kHz. It is coded according to the steps in Equations (5.2)-(5.4).

6.3.2 EKF tuning method

In order to have a well-performing EKF it is necessary to provide the algorithm with the process noise covariance matrix \mathbf{Q}_k and the measurement noise covariance matrix \mathbf{R}_k . The noise processes, whose covariances are represented by \mathbf{Q}_k and \mathbf{R}_k , contain contributions from various sources including:

- unmodelled dynamics, which are modelled in the full Simulink model but not in the reduced order EKF
- measurement noise arising from the measurement process
- estimation errors in the voltage and current estimates

In order to find appropriate values for \mathbf{Q}_k and \mathbf{R}_k , which are cable length dependent, an optimisation approach is used which solves the following optimisation problem:

$$\boldsymbol{\rho}^N = \arg \min_{\boldsymbol{\rho}} \sum_{k=0}^{N-1} \boldsymbol{\epsilon}^T(k, \boldsymbol{\rho}) \mathbf{W} \boldsymbol{\epsilon}(k, \boldsymbol{\rho})$$

such that

$$\boldsymbol{\rho} \geq \mathbf{0} \text{ and Equations (5.2) -- (5.4)}$$

where

$$\boldsymbol{\rho} = [\mathbf{Q}_k, \mathbf{R}_k]$$

and

$$\boldsymbol{\epsilon}(k, \boldsymbol{\rho}) = \mathbf{x}_{m,k} - \hat{\mathbf{x}}(k|k, \boldsymbol{\rho}),$$

$\mathbf{x}_{m,k}$ is a vector of measured states at instant k , \mathbf{W} is a weighting matrix and $\hat{\mathbf{x}}(k|k, \boldsymbol{\rho})$ is the a posteriori estimate (5.3) produced by the EKF using parameters $\boldsymbol{\rho}$.

This approach assumes that some or all of the state variables can be measured to provide the training set of data required for the proposed tuning approach. This, of course, is possible in simulation. It is, also, reasonable for the real application, where a one-off experiment could be performed with the necessary instrumentation.

The optimisation problem is a nonlinear one and therefore the risk of finding local minima exists. In order to reduce this risk a hybrid approach is employed, first using a Genetic Algorithm to find a solution in the region of the global minimum and then a gradient-based method to reduce the cost function further. Similar approaches using evolutionary algorithms have been successfully applied to Kalman Filter tuning in a range of applications e.g. [4, 11, 73, 78].

Certain reasonable assumptions are made which simplify the optimisation problem. The noise processes are assumed stationary and uncorrelated. Moreover the variances of the process noises affecting the currents are assumed equal, as well as those of the measurement noises. These assumptions lead to a reduced number of decision variables and ρ becomes $\rho = [Q_{11,22}, Q_{33}, Q_{44}, Q_{55}, R_{11,22}]^T$.

Initial values are required for $\hat{\mathbf{x}}_{0|0}$ and $\mathbf{P}_{0|0}$. The former is taken as the zero vector. The latter is set equal to $\alpha^2 \mathbf{Q}$ with $\alpha^2 = 10$ (see [23]), though it was found that the EKF's performance was relatively insensitive to the exact choice of α .

6.3.3 Simulation results

The model is used to generate two data sets per cable length, each with independent noise realisations, for 10 cable lengths. All data sets use a stepping rate of 20 step/s. Moreover the applied load torque has the form of a pulse stepping from 0.7 Nm to 1.4 Nm and back; these values were chosen as representative of a real load torque experienced in the collimators.

The first data set is used as the training set to estimate the covariance matrices and the second as a validation set.

The tuning procedure is used to tune EKFs for each cable length. The weighting matrix is taken as $\mathbf{W} = \text{diag}([1, 1, 0, 10, 5])$, which is motivated by the relevant importance placed on each state's estimation. Since the motor's angular position is of key importance it is given the highest weighting. Typically a good angular speed estimation is achieved when good position estimation occurs so it is not necessary to weight this specifically. The load torque estimation is of lower importance than that of the position so is weighted more lightly. Finally since the drive-side currents are already accurately estimated using their dedicated estimators, their estimation by the EKF can be weighted less heavily. In fact with little parameter mismatch in the EKF's model, the estimation performance is relatively insensitive to the weighting used. However, as will be seen later, when

parameter uncertainty is significant, the weighting of the most important state plays a key role in achieving its good estimation.

The true motor angular position and load torque are acquired during the simulation for use in the tuning procedure. In order for the procedure to be realistic, measurement noise is added to these acquisitions. In the angular position's case, a random process that is uniformly distributed in the interval $[-9.5874 \times 10^{-5}, 9.5874 \times 10^{-5}]$ rad is added. This choice is based on the quantization error occurring in a 32768 lines/turn rotary encoder. The load torque noise is a normally distributed, zero mean process with a variance of 9×10^{-6} (Nm)², based on experimental testbench data.

Fig. 6.8 shows the EKF's state estimates for a 1 km cable. The estimation achieves near superposition for the first 4 states (i_{mot_A} , i_{mot_B} , ω and θ).

It can be seen that the EKF functions properly and tracks the states well with the maximum Root Mean Square (RMS) angle estimation error over the cable lengths being 0.0878 mechanical degrees.

In order to make the simulation more realistic, uniformly distributed parameter mismatch is considered in all the parameters of the EKF and motor-side signal estimators. The i^{th} parameter is, therefore, randomly chosen in the interval $0.85\rho_i^0 \leq \rho_i \leq 1.15\rho_i^0$, where ρ_i^0 is the *true* value. The RMS percentage parameter mismatch over all the parameters used in the EKF and motor-side signal estimators is of 9.34 %. Fig. 6.9 shows the EKF's state estimates for a 1 km cable with parameter mismatch. Again, near superposition is achieved for the first 4 states (i_{mot_A} , i_{mot_B} , ω and θ).

It can be seen that the position estimation is still good, in spite of the parameter mismatch. The load torque tracking, however, is poor, compensating for the modelling error in order to achieve good position tracking, since this is the most heavily weighted state in the tuning procedure.

The RMS of the angle estimation errors achieved on the validation set of data at each length using the EKF tuned for that length on the estimation data set are evaluated. The same mismatch percentage for each parameter is used for all cable lengths. The results are presented in Fig. 6.10.

It can be seen that the worse case tracking, in terms of the RMS and mean values, occurs for the longest cable, due to its noise processes' increased variances. The maximum RMS angle estimation error is 0.1366 mechanical degrees. As expected this value is greater than found without parameter mismatch, nev-

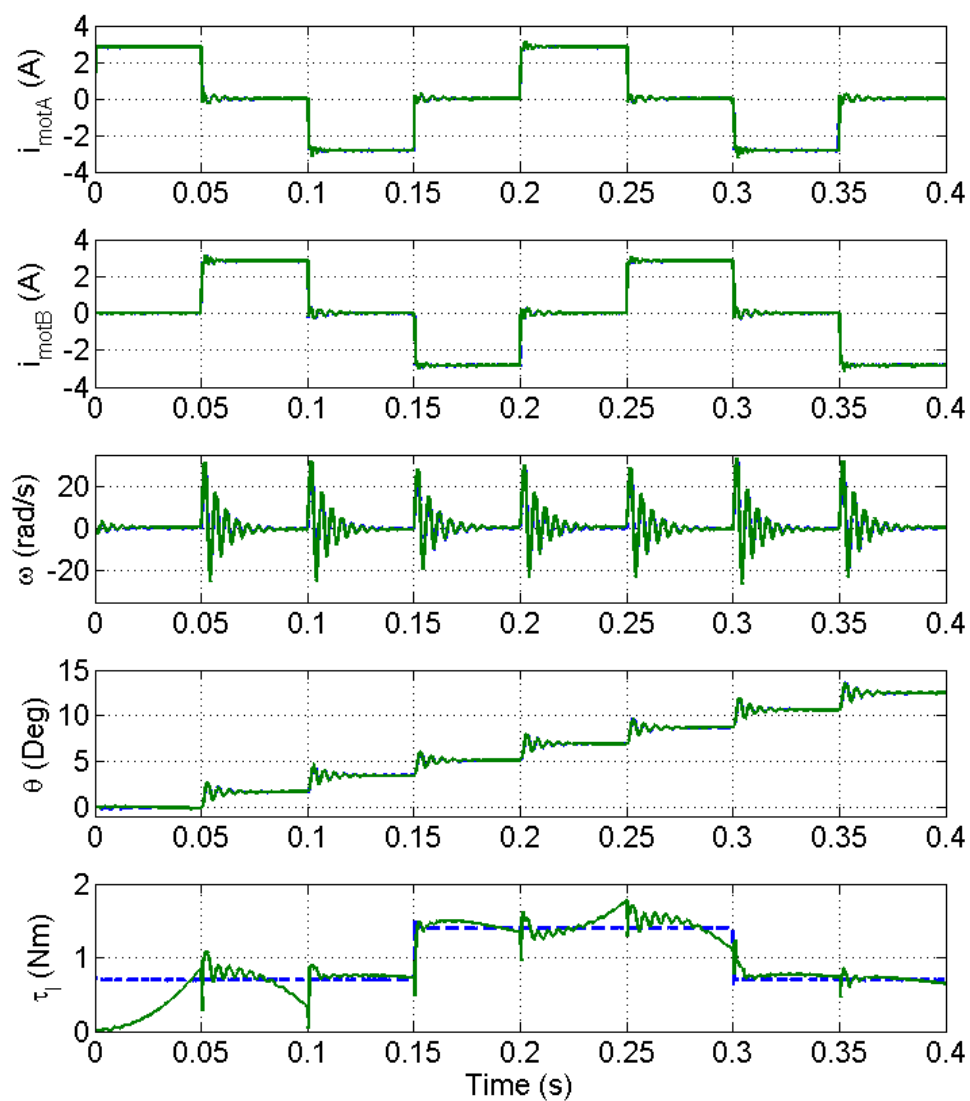


Figure 6.8: True (dashed) and estimated (solid) states for a 1 km cable

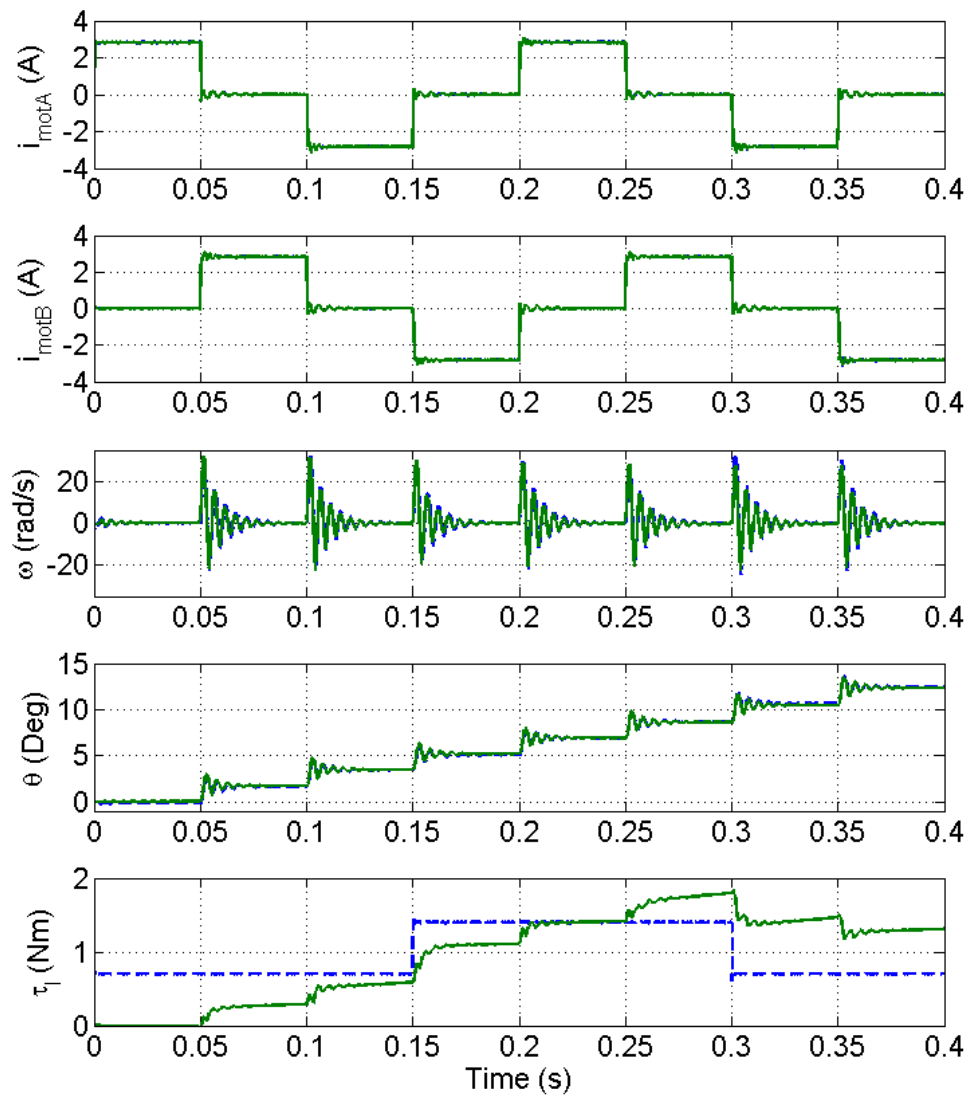


Figure 6.9: True (dashed) and estimated (solid) states for a 1 km cable with mismatch;

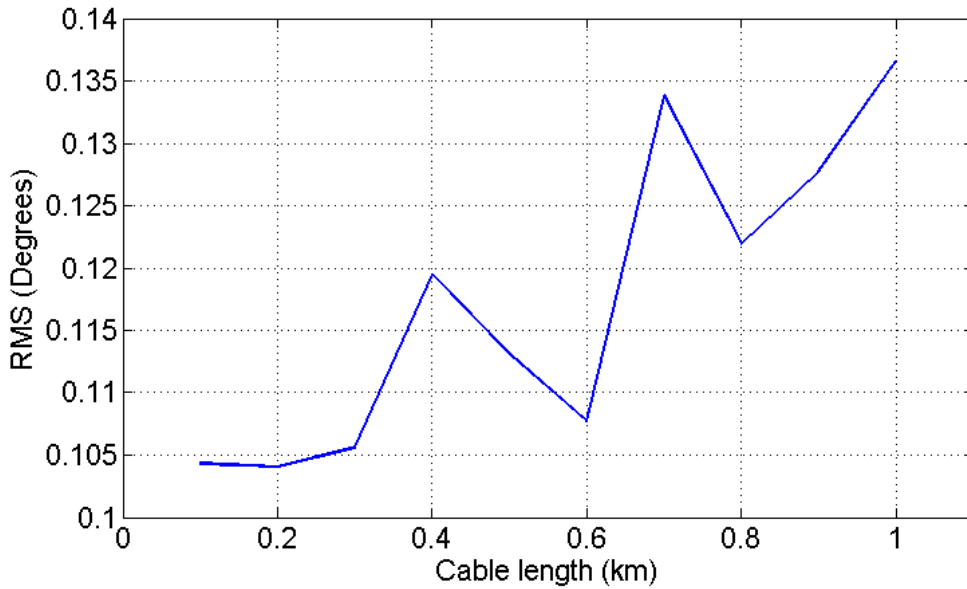


Figure 6.10: RMS of the mechanical angle estimation error

ertheless, as seen from Fig. 6.9, this tracking can still be considered acceptable, despite the relatively high parameter mismatch, and would allow lost steps to be detected.

A final simulation was performed to demonstrate the proposed filter design's ability to estimate accurately the motor's position in the actual case of step loss. This case was simulated by stepping the motor at 150 step/s; a rate at which the step commands coincide with the region of highest angular velocity in the step's settling region. Stepping in this condition is known to make step motors more prone to step loss [1]. The applied load torque is also changed to pulse from 0.7 Nm to 2.8 Nm and back, so as to further provoke step loss. The results, which were obtained with a 1 km cable, are shown in Fig. 6.11.

The estimation is close to superposition with the real values for the first four states, and it can be seen from the figure and the 0.1092 mechanical degrees RMS angle estimation error achieved that, despite the occurrence of step lost, the EKF based estimator is able to track the position with good accuracy.

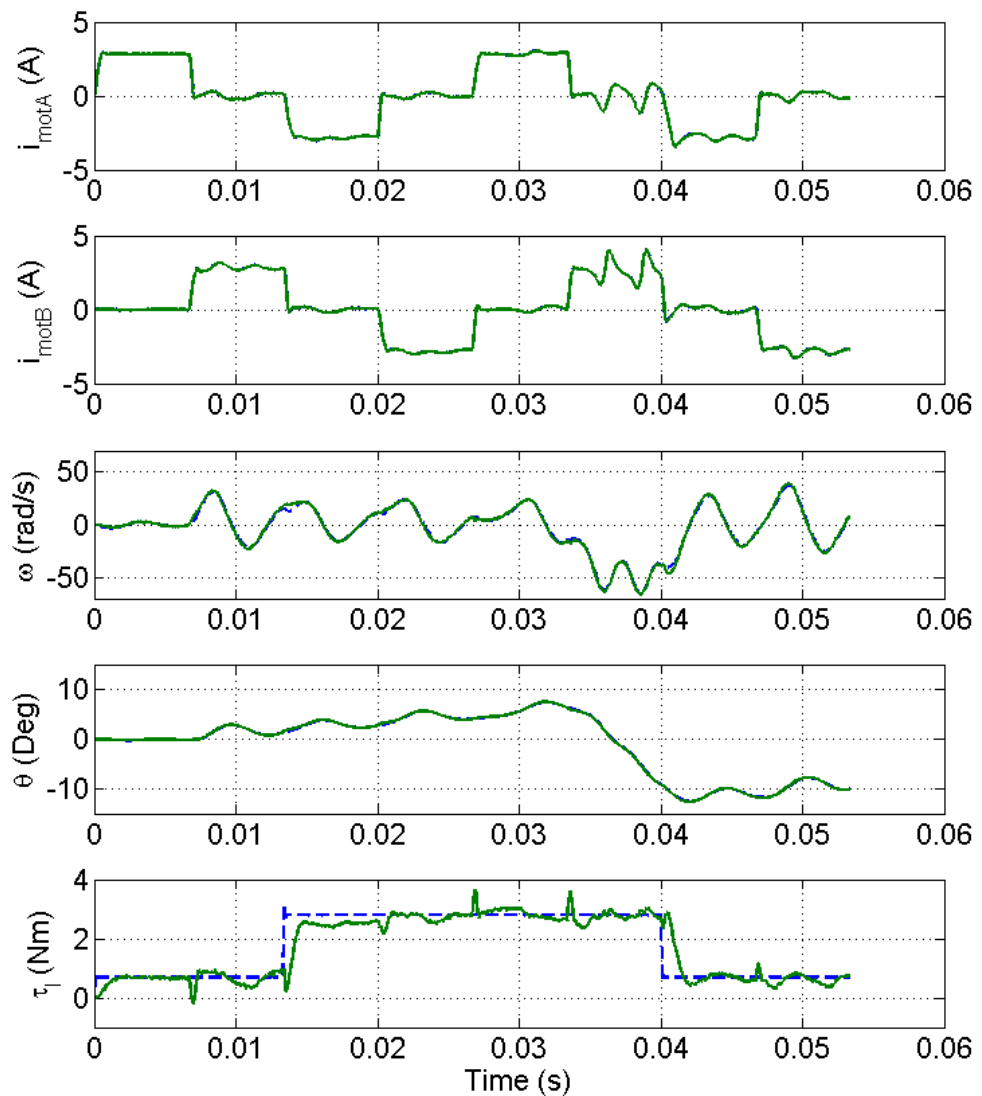


Figure 6.11: True (dashed) and estimated (solid) states for a 1 km cable at 150 step/s

6.4 Experimental application to an LHC collimator

The proposed estimation algorithm has been tested on a testbench based on a real collimator and a Data Acquisition (DAQ) system developed ad hoc to compare the estimation results with the real torque and position measured on a collimator axis. The different parts used for this test are described and experimental results are shown to validate the proposed approach.

6.4.1 Drive description

The drive used for this test has been described in chapter 4. The hardware remains unchanged but in this occasion the EKF has been implemented in c code for its use in real-time.

The motor-side voltage estimates can be estimated by Eq. (6.11). However, due to Digital Signal Processor (DSP) processing power constraints, it is not possible to obtain a low-pass filtered version of $\bar{i}_{drv_{j,k}}$ and its direct, unfiltered use in Eq. (6.11) results in aliasing occurring at the EKF sampling rate.

At the frequencies of interest, those which affect the EKF estimation performance, the following approximation is done:

$$\bar{i}_{drv_{j,k}} \approx \hat{i}_{mot_{j,k}} \quad (6.12)$$

And therefore (6.11) can be written as:

$$\hat{u}_{mot_{j,k}} = \bar{u}_{drv_{j,k}} - rh\hat{i}_{mot_{j,k}} \quad (6.13)$$

Finally, based on this result, the cable resistance can be lumped with that of the motor so the EKF can directly use the control action as its input, saving DSP operations, and the resistance used in the EKF model is the sum of that of the motor and that of the cable.

The interrupt running the controller is now in charge as well of executing the Kalman algorithm. The execution rate of this interrupt has been set to 25 kHz, which is necessary in order to achieve good control when a closed-loop bandwidth of 1-2 kHz is desired.

In this interrupt, the controller routine is executed first in order to fulfill the

real-time constraints. Then the Kalman filter algorithm is run and some system diagnostics are performed. The EKF uses the estimated motor-side mean voltage as its input, and the current estimated by the filter interrupt as its output. As seen previously it estimates the motor states, i.e. the motor-side currents, angular position, angular speed and the external torque applied to the shaft.

The code running the filter has been highly optimized in order to achieve the desired interrupt rate of 25 kHz, for this some of the steps described in [16] have been followed, as well as the tuning procedure proposed. This tuning procedure differs from the one described in section 6.3.2 and allows the system parameters to also be estimated, as well as the covariance matrices.

6.4.2 Test Setup Description

In order to test the estimation capabilities of the driver, it has been used on a real LHC collimator. A vertical collimator is used for the tests. It consists of two vertically movable jaws, each one driven by two stepper motors. Another stepper motor is used to displace the collimator horizontally. The collimator is shown in Fig. 6.12.

The five motors in the collimator are driven from a control rack, which controls up to 3 collimators. The rack contains 2 National Instruments PXIs, one of them running the Motor Drive Control (MDC) and the other one the Position Readout and Survey (PRS); and the stepper motor drivers used to drive the motors in the 3 collimators. Details on the LHC collimators low level control system can be found in [51].

For this experiment, one of the drivers in the rack was replaced by the developed driver to control one of the motors in the collimator, connecting it through a 720 meters cable. A special test fixture, shown in Fig. 6.13, was created in order to have real-time measurements of the motor position and the applied load torque.

For the position measurement, a Sick Stegmann Coretech DRS60 encoder was used, and its output signals are decoded by the DSCs Enhanced Quadrature Encoder Pulse Module and used to increment a counter, whose value is directly recorded. For the torque measurements, an NCTE Torque Sensor Series 2000 has been used. The output of this sensor is recorded with a LeCroy WaveRunner oscilloscope.

For the synchronization of oscilloscope and driver acquisitions, a digital output

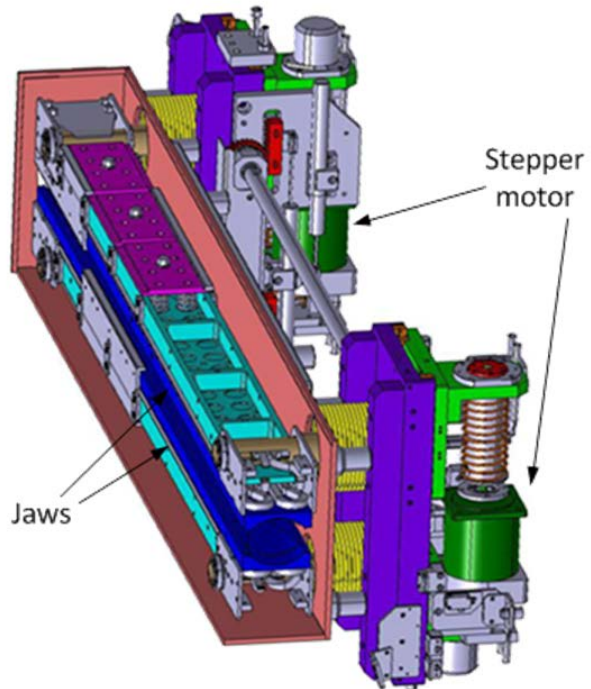


Figure 6.12: LHC Vertical Collimator

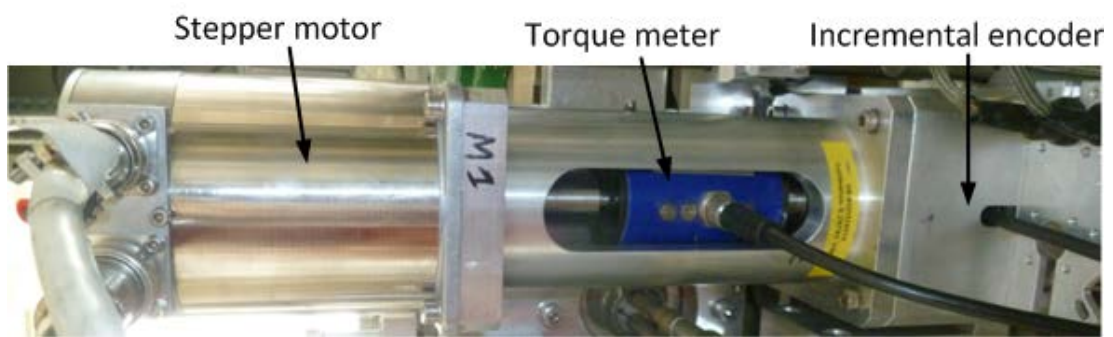


Figure 6.13: Experimental test fixture

signal from the driver, toggling at the internal driver acquisition instants at 25 kHz, is also acquired by the oscilloscope. A 2.5 MHz sampling rate is used in order to allow accurate offline detection of the synchronization signal edges to within one hundredth of a sampling period. A schematic diagram of the test set up is shown in Fig. 6.14.

These measurements are used for 2 different purposes: tuning the filter, since it is necessary to have position and torque measurements to follow the procedure described in [16], and validation of the EKF, where the Kalman filter is run in the driver.

In the tuning mode, the control actions calculated by the digital controller and the estimated motor-side currents were also acquired by the driver. In the validation mode, the EKF estimates the load torque and position for comparison purposes with the real values. The DSC can store over 2 seconds of data in the external memory at the controller rate of 25 kHz. Once an acquisition is requested from the driver through the serial communication, the trigger to start it is the first step signal received.

6.4.3 Experimental Results

Tuning experiment

In order to tune the EKF it was necessary to obtain a training data set. This acquisition was done using the DSP code in the tuning mode which acquires the motor-side current estimates, the control actions and the encoder count value and sends the synchronization signal to the scope for the load torque signal synchronisation.

A movement of the collimator jaw from the out position towards the in/beam position (positive mean speed) was requested at a rate of 20 steps/s, full step, 1 phase on mode. The stepping rate and mode, which is different from the standard collimator operating configuration, is chosen in order to obtain signals which are sufficiently rich in information in order to estimate the parameters. Using the acquired data, the tuning procedure was run to obtain the system parameters and noise covariance matrices, as required by the EKF. The estimated values can be found in Table 6.1.

It should be mentioned that the estimated B value is very small. Sensitivity tests have shown that its value can be increased by up to a factor of 10^6 with only

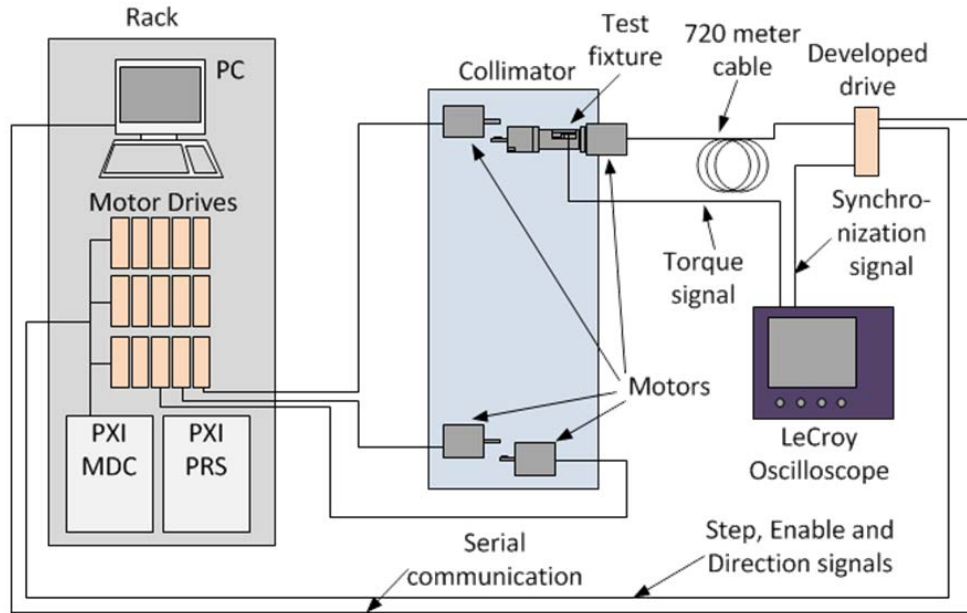


Figure 6.14: Experimental test setup

Table 6.1: Parameter values

Parameter	Value
$R + R_{cab}$	22.92Ω
L	46.43 mH
K_m	1.36 Nm/A
J	$6.05 \times 10^{-5} \text{ kgm}^2$
B	$5.68 \times 10^{-11} \text{ Nms/rad}$
T_{dm}	0.041 Nm
ϕ	-3.142 rad
$Q(1, 1)$	$4.55 \times 10^{-4} \text{ A}^2$
$Q(2, 2)$	$4.55 \times 10^{-4} \text{ A}^2$
$Q(3, 3)$	$21.62 \text{ rad}^2/\text{s}^2$
$Q(4, 4)$	$5.31 \times 10^{-7} \text{ rad}^2$
$Q(5, 5)$	$9.97 \times 10^{-4} \text{ Nm}^2$
$R(1, 1)$	$1.18 \times 10^{-1} \text{ A}^2$
$R(2, 2)$	$1.18 \times 10^{-1} \text{ A}^2$

relative changes in the position and torque tracking errors of the order of 10^{-5} . Above a certain threshold, however, its value becomes important for the load torque estimation performance since a too high viscous friction coefficient requires the load torque to compensate in order to achieve good position estimation. For the following validation tests the values in Table 6.1 were used.

Validation experiments

Two validation experiments were performed. The driver is set in validation mode in order that the EKF estimates of the motor position and load torque could be acquired. This time the standard operating configuration of the LHC collimator stepping motors was used i.e. 400 step/s, half step mode since this is the intended functioning mode for the driver.

As mentioned in chapter 5.3 the initial state must be provided to the EKF before it can run. The two current states are provided as the estimated motor-side phase currents. Since the EKF starts running with the acquisition when the first step signal is received, the initial speed is zero. The initial position is read from the encoder in these experiments, though in the future it can be read from the LHC Collimator resolvers, before the EKF runs independently as an alternative, redundant position sensor. The load torque is unknown before the EKF runs; its initial condition is therefore set to the arbitrary value of 0 Nm. Nevertheless, as will be seen the EKF can rapidly converge to the correct mean value, despite this initial offset.

The first experiment involved moving the collimator jaw continuously in the out-to-in direction. Again the start of the movement triggered the acquisition. The results can be seen in Fig. 6.15 and Fig. 6.16 for the position and load torque estimation respectively. The movement was repeated 3 times in order to assess the variation in the estimation performance. The mean and standard deviation (σ) of the error in the position and load torque estimation can be seen in Table 6.2.

Table 6.2: Results for continuous movement from out-to-in

Test	Mean($\Delta\theta$) (Deg)	$\sigma(\Delta\theta)$ (Deg)	Mean($\Delta\tau_L$) (Nm)	$\sigma(\Delta\tau_L)$ (Nm)
1	0.0661	0.1409	-0.0131	0.0172
2	0.0653	0.1415	-0.0148	0.0170
3	0.1086	0.1442	-0.0137	0.0174

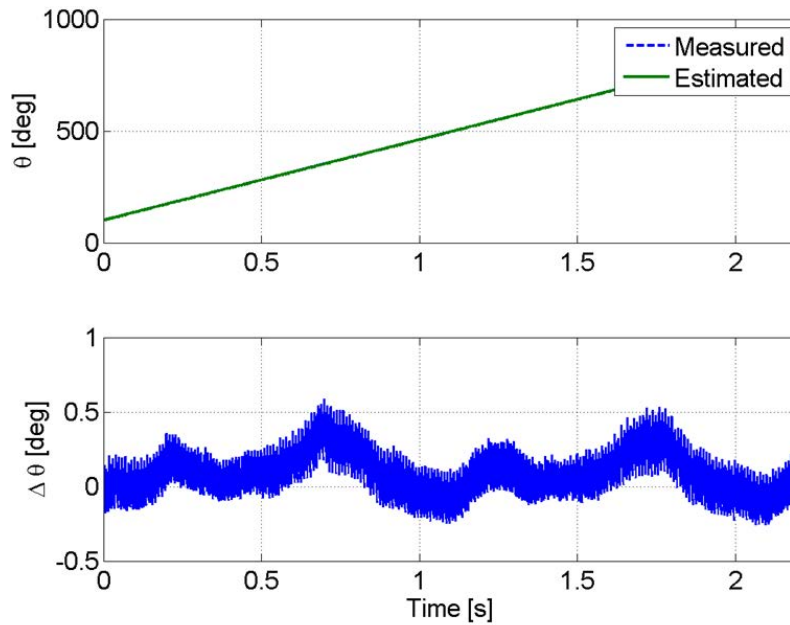


Figure 6.15: Position estimation (upper) and estimation error (lower) for a movement from out to in/beam

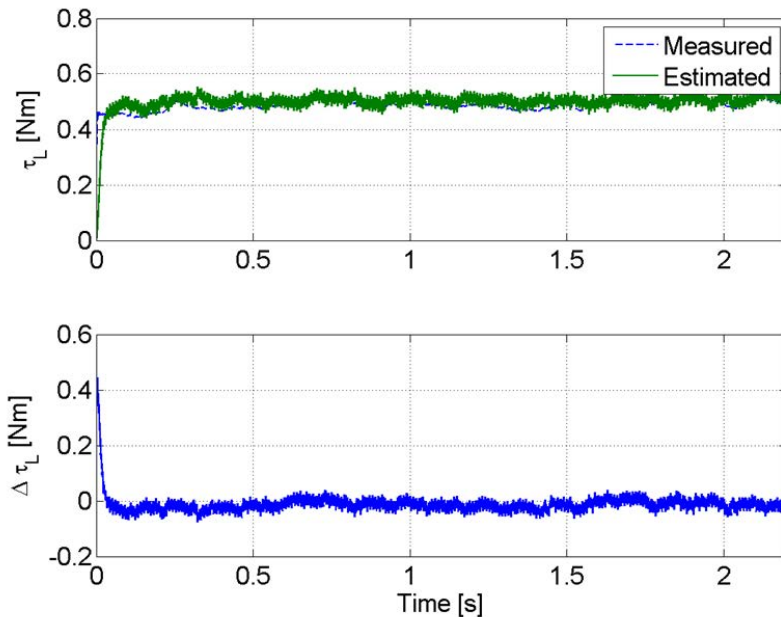


Figure 6.16: Torque estimation (upper) and estimation error (lower) for a movement from out to in/beam

It can be seen from the figures and Table 6.2 that good estimation is achieved for both signals. The estimation errors remain stable and, once converged from the initial state conditions, can be seen to be close to zero mean. Since, as can be seen from Fig. 6.15, the maximum position error for all 3 tests is less than the amplitude of a half step, equal to 0.9 degrees, the estimation can be used to detect lost steps.

Similarly, from Fig. 6.16 it can be observed that, once converged, the load torque estimation error is much less than 0.1 Nm. This uncertainty is sufficiently low for diagnostic purposes since allowable torque variations due to mechanical degradation are of the order of 0.5 Nm. This value is based on the fact that maximum nominal torques are approximately 0.8 Nm and a factor of safety of 2 has been used in the selection of the stepping motor rated torque.

The second experiment consisted of a movement in the out-to-in direction, followed by a stationary phase and then a movement in the in-to-out direction, producing a trapezoidal position trajectory. The position estimation and load torque estimation can be seen in Fig. 6.17 and Fig. 6.18, respectively.

It can be remarked that good zero-mean estimation is achieved during the out-to-in section. When the motor is stopped, a steady state estimation error occurs, however. This phenomenon is due to the poor observability that occurs when the motor speed is below a certain threshold since the Back-emf voltages, required for observability, become negligible.

This is an inherent limitation of observers, such as the EKF, and which should be taken into account in the design of any diagnostic system so that the estimation is not used during stationary periods. Once the motor starts moving again, observability is restored and the estimates converge to the true mean values again.

6.5 Conclusions

In this chapter an approach to applying the EKF for a sensorless stepper motor drive that can be used with long cables has been proposed, tested in simulation and then applied in an experimental setup.

It has been seen that, due to restricted computational power, compromises must be made with respect to the complexity of the model that can be used in the EKF. It has been shown that using only the motor model in the EKF and dedicated estimators to map the drive-side measurements onto motor-side signals,

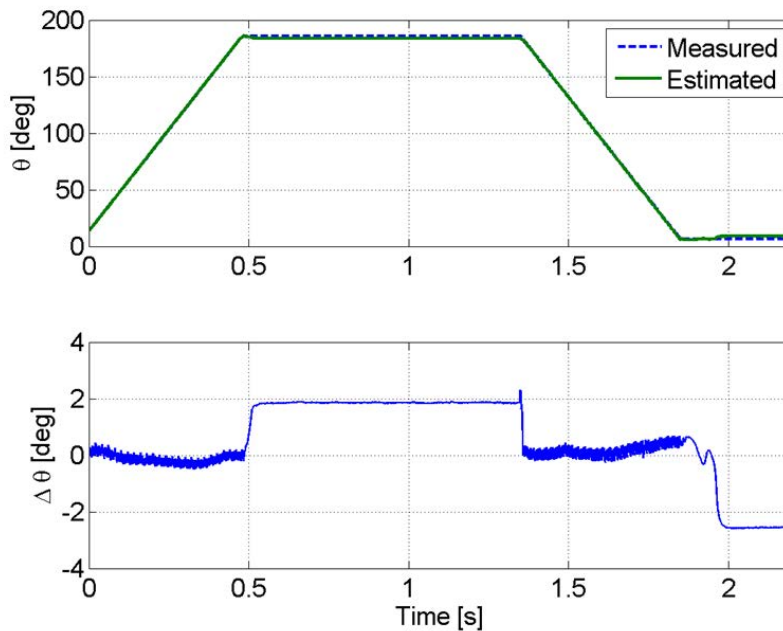


Figure 6.17: Position estimation (upper) and estimation error (lower) for a trapezoidal movement

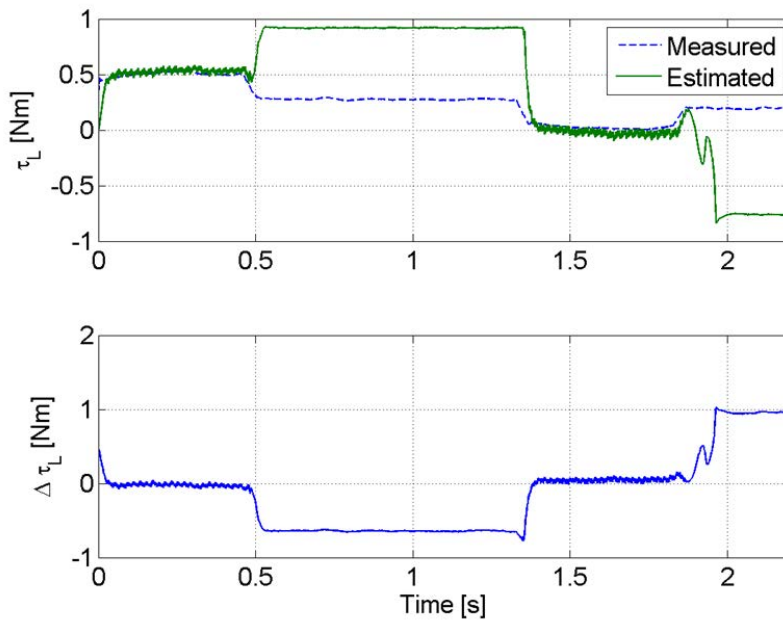


Figure 6.18: Torque estimation (upper) and estimation error (lower) for a trapezoidal movement

good position estimation can be achieved, in spite of model uncertainty.

For the experimental application, the EKF has been implemented in the drive presented in chapter 4, a real-time platform based on a DSP. Furthermore a testbench based around an LHC Collimator is presented in order to validate the proposed drives position and load torque estimation capabilities. It is seen that sufficiently good position and load torque estimation is possible to allow lost steps to be detected and the mechanical degradation of the collimator to be assessed.

Chapter 7

Hybrid Stepper Motors Electrical Model Extensions and Their Application to Sensorless Estimation

7.1 Introduction

In chapter 6, the Extended Kalman Filter was used for sensorless estimation of a motor separated from the driver through a long cable. Even though the results were satisfactory and the filter gives very useful estimations of rotor position and load torque, some consistent mismatch between the expected currents when the motor was being stepped and the real currents were observed.

In this chapter the limitations of the standard electrical model used for Hybrid Stepper Motor control and observation are described to motivate the development of an extended model, always with the goal in sight of its future application in a real-time platform. This new extended model is one of the original contributions of this thesis.

The evaluation of its performance and the computational cost for the different models, in order to assess their usability in embedded control systems, are presented. An experiment on an ad-hoc developed testbench to assess the holding torque current dependence and the coherency of the proposed model structure for this type of motor data is carried out. Finally, in order to show the usefulness for sensorless estimation of the proposed HSM model extensions, an Extended

Kalman Filter is defined and experimentally evaluated in a real time control application.

7.1.1 Standard electrical model revisited

The standard electrical motor model for a motor phase has already been presented in chapter 2.2, Eq. (2.1), it is rearranged and repeated as Eq. (7.1) for convenience. Henceforth we will focus only on the motor part of the model and therefore the currents and voltages will always be motor side, and the *mot* subscript omitted.

$$u_j(t) = Ri_j(t) + L\dot{i}_j(t) + e_j(t) \quad \text{for } j = A, B \quad (7.1)$$

This equation can be rewritten in the form of Eq. (7.2), before splitting the induced voltage into its separate components.

$$u_j(t) = Ri_j(t) + v_j^s(t) \quad \text{for } j = A, B \quad (7.2)$$

where $v_j^s(t)$ is the induced voltage for the standard electrical model.

The induced voltage is composed of two different sources. The first is the self-induced voltage, produced by the derivative of the current in the phase winding. The second is the back electromotive force, caused by the derivative of the flux produced by the rotor permanent magnet crossing the phase winding as it rotates. We can split it as in Eq. (7.3) leading back to the standard Eq. (7.1).

$$v_j^s(t) = \frac{d\psi_j^s(t)}{dt} = \frac{d}{dt} (L i_j(t) + \psi_j^{PM}(t)) = L \frac{di_j(t)}{dt} + e_j(t) \quad (7.3)$$

with ψ_j^s being flux linkage of phase j , and the superscript s stands for the standard model. The back electromotive forces, due to the relative movement of the rotor, are described by:

$$e_A(t) = \frac{d}{dt} \psi_A^{PM}(t) = \frac{d}{dt} \Psi^{PM} \cos p\theta(t) = -p\Psi^{PM} \omega(t) \sin p\theta(t) \quad (7.4)$$

and

$$e_B(t) = \frac{d}{dt} \psi_B^{PM}(t) = \frac{d}{dt} \Psi^{PM} \sin p\theta(t) = p\Psi^{PM} \omega(t) \cos p\theta(t). \quad (7.5)$$

In these equations, ψ_j^{PM} represents the flux linkage due to the permanent

magnet of phase j , with amplitude Ψ^{PM} .

In the following, the time dependency of the signals will be omitted for clarity of presentation.

7.1.2 Poor model fit

An experiment is performed on the Collimator Hybrid Stepper Motor (described in section 2.3). The motor is stepped in full step mode, corresponding to mechanical steps of 1.8° , with one phase energised at a time. This stepping mode requires the phase current to perform steps of $2\sqrt{2}$ A amplitude, which is achieved using closed-loop current control. The motor phase currents, voltages and angular position are acquired whilst the motor is stepping.

Using these measured signals, the parameters of the model presented on Section 7.1.1 are estimated using linear regression and the resulting values shown in Table 7.1. These values are obtained by calculating the mean and standard deviation of parameters estimated for 3 different datasets.

The simulated phase terminal voltage obtained from the model with these parameters for Phase A is compared with the measured voltage and shown in Fig. 7.1.

Despite the globally reasonable fit between the model output and the measurements, clear discrepancies can be seen in the regions corresponding to the non-zero current/voltage step regions. More precisely the model predicts oscillations at the nonzero, steady state current/voltage zones which are not seen in the measurements. These voltage oscillations, in fact, correspond to the induced voltages in the model from Eq. (7.4) - (7.5) and occur due to the nonzero angular velocity of the rotor at these times.

The results suggest that the induced voltage in the real motor is dependent on the current magnitude in a way that is not considered in the standard model.

Table 7.1: Parameters estimated for the standard hybrid stepping motor electric model

Parameter	Mean value	Standard deviation
$R(\Omega)$	4.095	0.033
$L(mH)$	31.367	0.019
$\Psi^{PM}(mWb)$	26.758	0.124

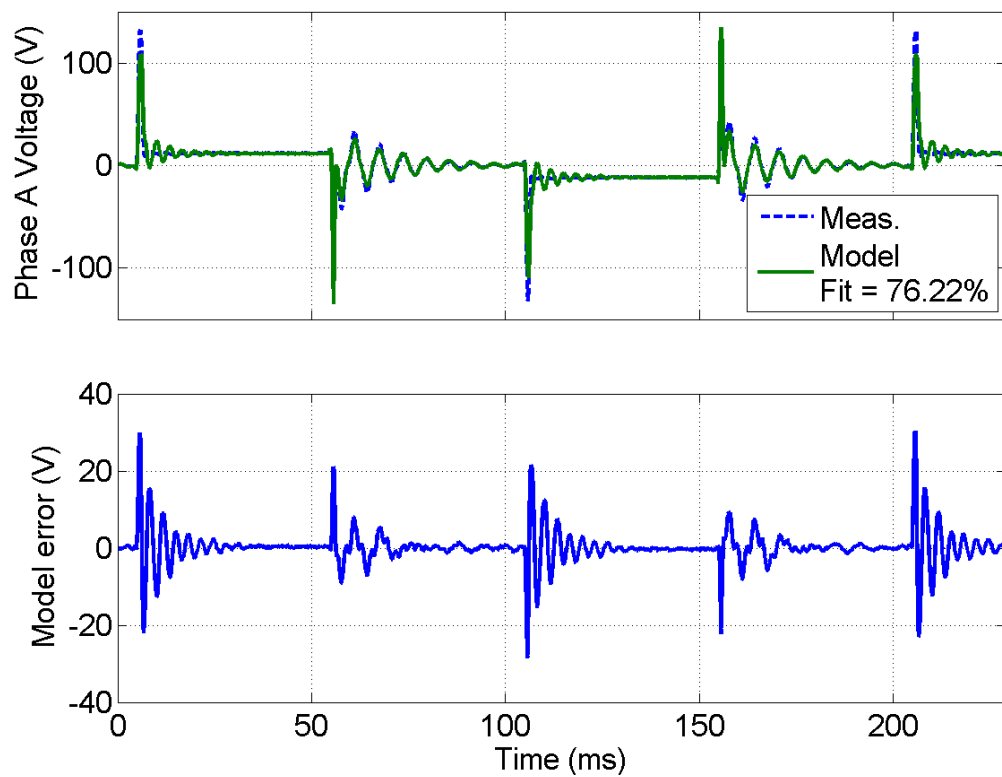


Figure 7.1: Discrepancy between measured voltage and standard model prediction.

7.2 Proposed new model extensions

In this section new model extensions are proposed which incorporate terms that can account for the mismatch of Section 7.1.2. Specifically terms that could explain the induced voltages current dependency are presented.

7.2.1 Position dependency

The literature on Hybrid Stepper Motors, in general, assumes that the phase inductance angular position dependence is negligible, e.g. [1, 36]. Whilst the effect may be less pronounced than in Variable Reluctance Stepper Motors, it, nonetheless, exists in HSMs due to the variation of the gap distance, and thus reluctance, between stator and rotor caused by their toothed profile. Furthermore its significance may not always be negligible. In [34, 46] it is shown that there is a dependence of the permeance on position, which produces a variation of the inductance and the flux linkage.

If this is the case then we have that the flux linking the stator phase j is given by:

$$\psi_j^{pd} = L_j(\theta)i_j + \psi_j^{PM}(\theta) \quad (7.6)$$

where phase j inductance $L_j(\theta)$ is now position-dependent.

By Faraday's law, the induced voltage in a phase is then:

$$v_j^{pd} = \frac{d\psi_j^{pd}}{dt} = \frac{dL_j}{d\theta}\omega i_j + L_j \frac{di_j}{dt} + \frac{d\psi_j^{PM}}{d\theta}\omega. \quad (7.7)$$

It can be seen from Eq. (7.7) that a position-dependent inductance indirectly leads to a current dependent induced voltage term.

7.2.2 Current dependency

A further effect can occur in the form of current level dependence. The flux linking the stator phase follows a magnetic circuit that contains the rotor permanent magnet, iron teeth, the air gaps between the rotor and stator and the stator iron cores.

As is well known in magnetic theory, a nonlinear relation exists between the flux magnitude in iron and the current level producing it, via the permeability, as seen in the B-H curve. Moreover, eventually saturation can occur at high flux

levels.

HSM can be more prone to saturation than other types of motor since they typically have a large number of small teeth, which can lead to high flux densities, see e.g. [40].

In [34, 46] the dependence of the permeance with current is also studied. It can, therefore, be important to consider this phenomenon in an HSM model. This means that in this case the flux linkage expression becomes current dependent:

$$\psi_j^{cd} = L_j(i_j)i_j + \psi_j^{PM}(\theta, i_j), \quad (7.8)$$

where both phase j inductance $L_j(i_j)$ and the flux linkage produced by the permanent magnet $\psi_j^{PM}(\theta, i_j)$ are now current-dependent. The latter is still position dependant since this dependence is considered in the standard model (7.2)-(7.5).

The current-dependency of the permanent magnet flux linkage can be explained by the fact that, for a certain operating point, the permanent magnet can be considered as a constant source of magnetomotive force [57]. The flux, and thus the linkage that it generates are, therefore, dependent on the overall reluctance of the magnetic circuit at that operating point, which in itself is a function of current, via the current dependent permeability term contained in the reluctance.

By Faraday's law, the induced voltage in a phase is:

$$v_j^{cd} = \frac{d\psi_j^{cd}}{dt} = \frac{dL_j}{di_j} \frac{di_j}{dt} i_j + L_j \frac{di_j}{dt} + \frac{\partial \psi_j^{PM}}{\partial i_j} \frac{di_j}{dt} + \frac{\partial \psi_j^{PM}}{\partial \theta} \omega. \quad (7.9)$$

7.2.3 Position and Current dependency

When neither of the dependencies, on position and on current, are negligible, a model combining them becomes necessary. The flux linkage combining both dependencies has the following expression:

$$\psi_j^{pcd} = L_j(\theta, i_j)i_j + \psi_j^{PM}(\theta, i_j). \quad (7.10)$$

By Faraday's law, the induced voltage is:

$$v_j^{pcd} = \frac{d\psi_j^{pcd}}{dt} = \frac{\partial L_j}{\partial i_j} \frac{di_j}{dt} i_j + \frac{\partial L_j}{\partial \theta} \omega i_j + L_j \frac{di_j}{dt} + \frac{\partial \psi_j^{PM}}{\partial i_j} \frac{di_j}{dt} + \frac{\partial \psi_j^{PM}}{\partial \theta} \omega. \quad (7.11)$$

7.3 Determination of the model structure

The equations for the electrical model of the motor with the different dependencies introduced has been presented. It is then necessary to find the models for each of the new terms introduced, keeping in mind that the final goal is to use them in a real-time embedded system. In this section the model structures are proposed and experimentally validated. All the tests are performed on the same two phase hybrid stepper motor as in section 7.1.2.

7.3.1 Position Dependency

Estimation of the Permanent Magnet Flux linkage as a function of the position

The permanent magnet flux linkage position dependency is assessed by using a speed controlled synchronous motor to drive the open-phase HSM at a constant reference speed of 190 rpm, approximately 3.1 turns per second.

The speed has been chosen to allow 3 mechanical turns to be acquired over a 2 seconds duration. The Nyquist-Shannon Sampling Theorem is easily satisfied when the data is acquired at a 25 kHz sampling rate, even assuming the first 10 harmonics to be significant. The motor open-phase voltages and angular position are acquired.

Since the phases are open, zero current can flow in them, thus removing all current dependent terms from the model (7.7), as shown in Eq. (7.12).

$$v_j^{pd} \Big|_{i_j=0} = \frac{d\psi_j^{PM}}{d\theta} \omega \quad (7.12)$$

The permanent magnet flux linkages with the phases are considered to be periodic as a function of position and to have a fundamental period equal to that of the motor electrical period. Using this assumption, a general model for the voltages induced by cutting of this flux linkage is thus:

$$\begin{aligned} v_A^{PM} &= \frac{d\psi_A^{PM}}{dt} = - \sum_{r=1}^M r p \Psi_r^{PM} \omega \sin(r p\theta + \phi_{PM,r}) \\ v_B^{PM} &= \frac{d\psi_B^{PM}}{dt} = \sum_{r=1}^M r p \Psi_r^{PM} \omega \cos(r p\theta + \phi_{PM,r}), \end{aligned} \quad (7.13)$$

where r is a summing index and M is the number of useful harmonics.

These models are fitted, in the least squares sense using linear regression, to the measured data for both phases simultaneously. The instantaneous speed is required for this fitting and is obtained via numerical differentiation of the measured position signal, having first noncausally, low-pass filtered it.

Table 7.2 shows the values obtained for the first four harmonics. Fig. 7.2 shows the measured and fitted voltages for the two phases.

It can be clearly seen from the table that only the first harmonic is significant, the others being at least 3 orders of magnitude smaller. Additionally, from the figure it can be seen that the model is sufficiently rich to allow a good fit of the measured data to be achieved.

Estimation of the inductance as a function of the position

Since the origin of the inductance position dependence is the periodic variation in air gap distance due to the motor toothed construction, the inductance variation is also expected to be periodic with a fundamental period equal to the motor electrical period.

The inductance position dependence was assessed by clamping the HSM rotor at 16 different positions within an electrical turn. The motor is positioned using the microstepping mode of an HSM drive, and then using a mechanical clamp to hold it in the desired positions. At each position an RCL meter, with a voltage excitation frequency of 50 Hz and RMS level of 2 V, is used to measure the inductance.

The frequency is chosen to be representative of the fundamental electrical frequency that occurs at standard stepping frequencies of 200 full steps/s. It is also low enough that parasitic capacitive effects between turns are negligible. The voltage level is chosen relatively low to avoid large currents, which could in turn

Table 7.2: Magnitude for the first four harmonics of the motor induced voltages when no current is flowing in the phases.

Parameter	Value
Ψ_1^{PM}	3.26×10^{-2} Wb
Ψ_2^{PM}	7.27×10^{-5} Wb
Ψ_3^{PM}	4.38×10^{-5} Wb
Ψ_4^{PM}	2.47×10^{-6} Wb

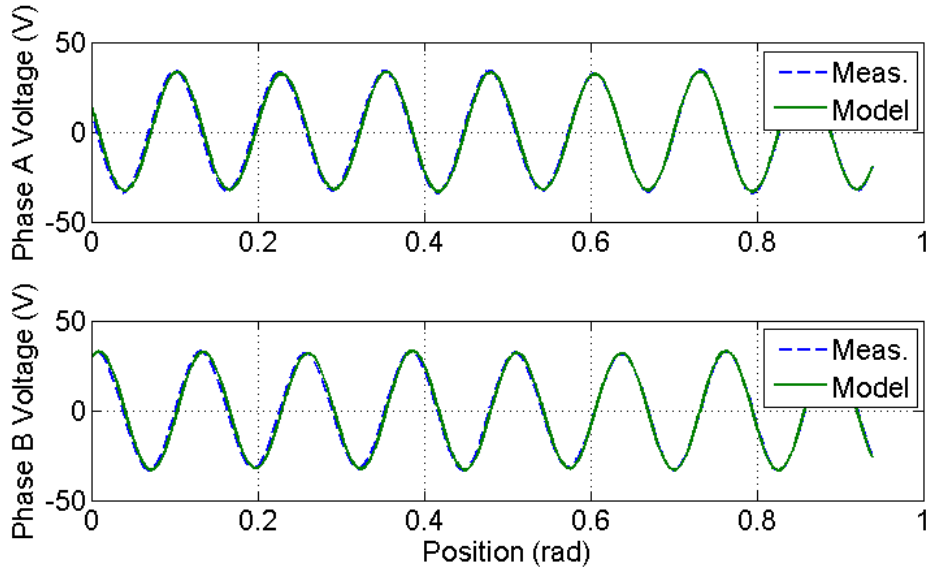


Figure 7.2: Measured (dashed) and fitted (solid) open phase voltages.

cause magnetic saturation.

The clamping of the rotor is necessary for two reasons. First, in order to avoid movement due to the, albeit small, excitation voltage and second, to have the capacity of stopping the motor at arbitrary positions, since once the current is removed from the phases, the rotor tends to align with the stator in specific angles due to the detent torque. Moreover, as can be seen from (7.7), with zero movement, all induced voltage terms due to relative movement of the rotor are zero, resulting in the model simplified to (7.14).

$$v_j^{pd} \Big|_{\omega=0} = L_j \frac{di_j}{dt} \quad (7.14)$$

Furthermore, since the meter excitation voltage is zero mean, and the system can be considered linear, so the current is also zero mean, removing effects of the current amplitude dependency. 16 different positions per electrical turn were used in order to satisfy the Nyquist-Shannon Sampling Theorem, assuming that the 8th harmonic would be negligible.

The results over 3 electrical turns are shown in Fig. 7.3.

As can be seen, the inductances are clearly position dependent. Moreover, their dependences are 180° out of phase between the two motor phases and can,

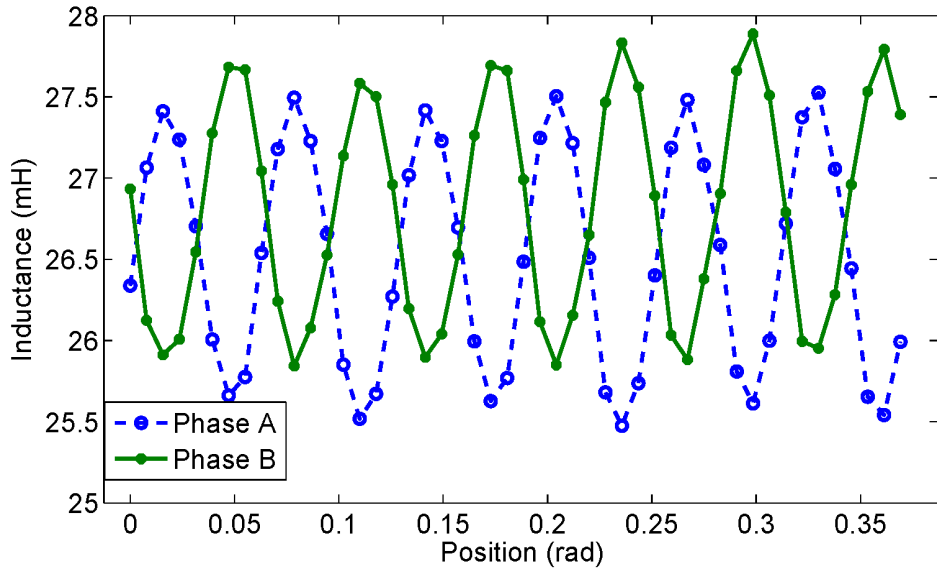


Figure 7.3: Measured inductance at different positions.

therefore, be described by:

$$\begin{aligned} L_A &= L_{0A} + \sum_{r=1}^N L_{rA} \cos(r p\theta + \phi_{L_A,r}) \\ L_B &= L_{0B} - \sum_{r=1}^N L_{rB} \cos(r p\theta + \phi_{L_B,r}), \end{aligned} \quad (7.15)$$

where r is a summing index and N is the number the useful harmonics.

This model differs from that typically found in the literature e.g. [71], where the variation is 90° out of phase. This 180° phase shift between phases can be explained by the fact that, for a two-phase HSM, when the rotor teeth are aligned with the stator teeth of one phase there exists the smallest air gap between the rotor and this phase, but the largest air gap between the rotor and the other phase. Since the phase inductance is greatest for the smallest air gap and vice versa, this explains the out of phase position dependency of the inductances of the two phases. In general, this phase difference is independent of the number of pole pairs but does change with the number of motor phases, the phase shift being equal to $360/n_p$ degrees where n_p is the number of phases.

The parameters of this inductance model are estimated from the measurements. The only significant harmonics are the DC component and the second

and have the following amplitudes:

$$\begin{aligned} L_{0_A} &= 26.51\text{mH} & L_{0_B} &= 26.81\text{mH} \\ L_{2_A} &= 1.03\text{mH} & L_{2_B} &= 1.02\text{mH}. \end{aligned}$$

The similarity between the phases is evident.

7.3.2 Current Dependency

Estimation of the permanent magnet flux linkage as a function of current

The permanent magnet flux linkage current dependency is assessed via two different experiments.

Constant speed experiment

The first experiment uses a similar test to that in Section 7.3.1, except this time a constant current is controlled in a single phase whilst the motor is driven at the constant reference speed of 190 rpm by the external synchronous motor.

Obviously this time the synchronous motor must overcome the holding torque of the motor. Since the current is maintained practically constant, the current derivative terms in (7.9) can be assumed zero, leaving only the last term in the expression:

$$v_j^{cd} \Big|_{i=\text{constant}} = \frac{\partial \psi_j^{PM}}{\partial \theta} \omega. \quad (7.16)$$

This last term includes the position derivative of the permanent magnet flux linkage, which is both position and current dependent. The current dependency of the permanent magnet flux linkage can, therefore, be assessed.

The currents, voltages and rotor position are acquired and Ψ_1^{PM} is estimated for the phase with the nonzero current. Table 7.3 shows the estimated Ψ_1^{PM} terms.

The reduction in Ψ_1^{PM} with increasing current magnitude is clearly obvious. This can be better visualised in Fig. 7.4 where the estimated values for Ψ_1^{PM} are

Table 7.3: Ψ_1^{PM} terms resulting from different current levels.

Mean Current (A)	0.13	0.67	1.19	1.72	1.97	2.53	3.01
Ψ_1^{PM} (mWb)	29.70	25.18	17.45	9.78	7.05	2.98	1.38

plotted against mean current.

Two models have been fitted to the data, an ‘exponential’ model with the form:

$$\Psi_1^{PM}(i) = a_\psi e^{-b_\psi i^2} + c_\psi \quad (7.17)$$

and a ‘linear’ model with the form:

$$\Psi_1^{PM}(i) = d_\psi |i| + f_\psi. \quad (7.18)$$

As can be seen from the figure, where the Root Mean Squared Error (RMSE) is displayed for each model, the exponential model achieves a better fit. Additionally it is Lipschitz continuous, which is an important property given the derivative terms found in (7.9) and (7.11).

The estimated parameters for the model are:

$$a_\psi = 29.36 \text{ mWb}$$

$$b_\psi = 0.39 \text{ A}^{-2}$$

$$c_\psi = 0.52 \text{ mWb}$$

Holding torque experiment

The second experiment involved measuring the motor holding torque at different current levels. Assuming that only the first position harmonic of the motor induced voltage is significant, we can obtain the expression for the torque by following the coenergy approach as presented in [26].

Using the equation (7.17) to express the current dependency of the flux, and leaving the inductance L with explicit dependency on the current, the flux linkage for phase A is:

$$\psi_A^{cd} = \psi_A^L + \psi_A^{PM} = L(i_A)i_A + \Psi_A^{PM}(i_A) \cos(p\theta). \quad (7.19)$$

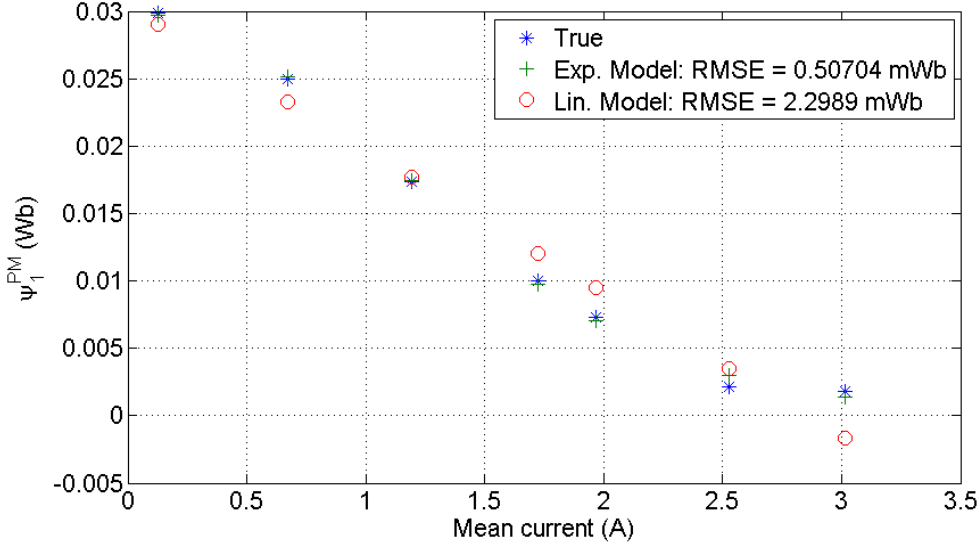


Figure 7.4: Estimated and fitted Ψ_1^{PM} .

The coenergy is:

$$\begin{aligned}
 W_A'^{cd} &= \int_0^{i_A} (\psi_A^{cd}) di = \int_0^{i_A} (L(i)i + \Psi_A^{PM}(i) \cos(p\theta)) di \\
 &= \int_0^{i_A} L(i)idi + \int_0^{i_A} (a_\psi e^{-b_\psi i^2} + c_\psi) \cos(p\theta) di \\
 &= f_L(i_A) + \left(\frac{a_\psi}{2} \sqrt{\frac{\pi}{b_\psi}} \operatorname{erf}(\sqrt{b_\psi} i_A) + c_\psi i_A \right) \cos(p\theta),
 \end{aligned} \tag{7.20}$$

where $\operatorname{erf}(\cdot)$ is the error function ¹ and $f_L(i)$ is an expression dependant only on the current.

For the purpose of this section, which is to obtain an expression for the torque, the explicit expression of the inductance L as a function of the current is not necessary since, to obtain the torque expression, the equation (7.20) is derived with respect to position θ , and so the derivative of the term $f_L(i)$ is 0. The current dependence of the inductance L is studied in the following section.

The torque produced by phase A is obtained deriving the coenergy with respect to the position θ :

$$\tau_A^{cd} = \frac{\partial W_A'^{cd}}{\partial \theta} = \left(\frac{a_\psi}{2} \sqrt{\frac{\pi}{b_\psi}} \operatorname{erf}(\sqrt{b_\psi} i_A) + c_\psi i_A \right) (-p) \sin(p\theta). \tag{7.21}$$

¹ Error function: $\operatorname{erf}(x) = \frac{2}{\pi} \int_0^x e^{-t^2} dt$

Following the equivalent procedure for phase B, the torque obtained is:

$$\tau_B^{cd} = \frac{\partial W_B'^{cd}}{\partial \theta} = \left(\frac{a_\psi}{2} \sqrt{\frac{\pi}{b_\psi}} \operatorname{erf}(\sqrt{b_\psi} i_B) + c_\psi i_B \right) p \cos(p\theta). \quad (7.22)$$

An experiment was performed whereby a range of constant current values were controlled in the phases in two different modes, One phase on and Two phases on.

For each I value, a slowly increasing external torque was applied to the HSM shaft using an external synchronous motor up to a pre-set limit. The current in each phase, position and applied torque were acquired using dedicated sensors. The pre-set limit of the applied torque was adjusted according to a bisection algorithm in order to converge to the maximum applied torque that did not cause step loss, as diagnosed by the position measurement. For each pre-set torque level 1000 torque measurements were acquired and averaged. The average torque that was measured during the penultimate run before steps were lost was taken as the holding torque. The mean current in the phases for this run was also noted.

The detent torque, $\tau_{dm}(\theta)$, has been estimated separately as having a magnitude of approximately 0.06 Nm. Similarly the static friction torque, T_{sf} , has been found to have an amplitude of approximately 0.09 Nm. These values are relatively negligible compared to standard electromagnetic torques so will be neglected henceforth.

Using the expressions for the produced torque (7.21)-(7.22), the holding torque can be written as:

$$\tau_h^{cd}(i_A, i_B) = \max_{\theta} |\tau_A^{cd} + \tau_B^{cd}|. \quad (7.23)$$

To obtain the maximum torque in equation (7.23), its extreme values have to be found by deriving it with respect to position θ and equating to 0.

In the One phase on case, phase A being the energised one, the angle giving the maximum torque is:

$$\theta_{max} = \frac{\pi/2 \pm k\pi}{p} \quad \text{with } k = 0, 1, 2, \dots$$

It can be seen in (7.21) that these are the values making the $|\sin(p\theta)|$ term equal to 1. In case that phase B were the energised one, the θ values making the

torque maximum would be:

$$\theta_{max} = \pm k\pi/p \quad \text{with } k = 0, 1, 2, \dots,$$

for which $|\cos(p\theta)|$ is equal to 1.

The resulting holding torque is, for the phase A case:

$$\tau_h^{cd}(I, 0) = p \left(\frac{a_\psi}{2} \sqrt{\frac{\pi}{b_\psi}} \operatorname{erf}(\sqrt{b_\psi} I) + c_\psi I \right). \quad (7.24)$$

Note that the result is the same energising phase B.

For the Two phases on case and the same current, the maximum torque is for the angles:

$$\theta_{max} = \frac{-\pi/4 \pm k\pi}{p} \quad \text{with } k = 0, 1, 2, \dots,$$

and the holding torque:

$$\tau_h^{cd}(I, I) = \sqrt{2}p \left(\frac{a_\psi}{2} \sqrt{\frac{\pi}{b_\psi}} \operatorname{erf}(\sqrt{b_\psi} I) + c_\psi I \right). \quad (7.25)$$

Fig. 7.5 shows the holding torques measured for different values of current I_{RMS} . It should be noted that for full and half step modes, the current applied to the motor phase is $I = \sqrt{2}I_{RMS}$ in the step that corresponds to One phase on and $I = I_{RMS}$ when the step corresponds to Two phases on.

It can clearly be seen how the holding torque is a nonlinear function of the current due to the nonlinear dependence of Ψ_1^{PM} on the current. Additionally a clear difference in the saturation between the ‘One phase on’ case and the ‘Two phases on’ case can be observed. This difference can be explained by the fact that with One phase on, for the same I_{RMS} value, more current is flowing in the phase and therefore it is closer to saturation than for the Two phases on case.

A fit is performed to the data for One phase on, using Equation (7.24) and the exponential model (7.17) for $\Psi_1^{PM}(I)$. The resulting model is then used with the data for both One phase on and Two phases on and its holding torque predictions for the two cases are also shown in Fig. 7.5. The estimated parameters for the

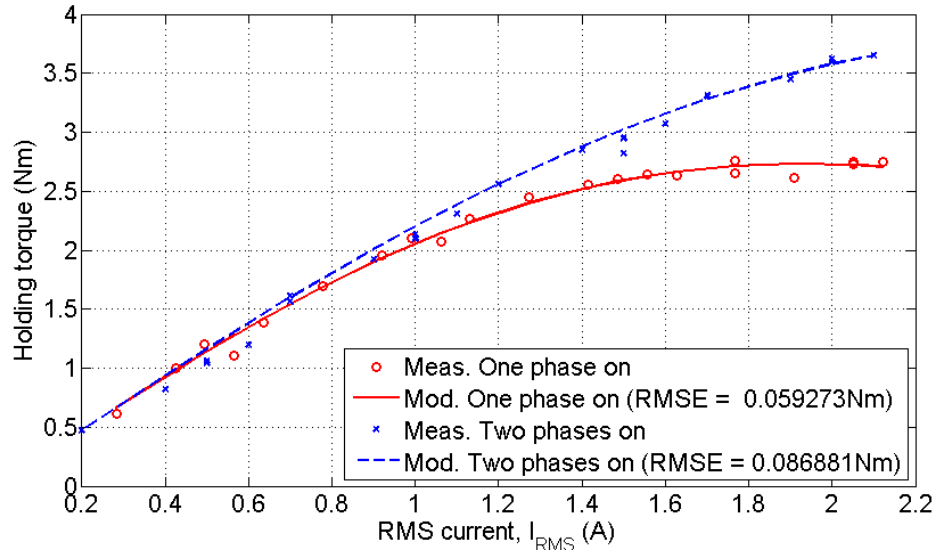


Figure 7.5: Holding torque measured for different RMS current values.

model are

$$a_\psi = 52.79 \text{ mWb}$$

$$b_\psi = 0.13 \text{ A}^{-2}$$

$$c_\psi = -19.36 \text{ mWb}$$

The good fit achieved with this model structure is evident from the corresponding RMSE values, which are small compared to the absolute torque values.

Estimation of the inductance as a function of the current

The current dependency of the inductance was evaluated by clamping the motor rotor in a fixed position, thereby eliminating any induced voltages due to relative movement and position dependence.

Square current waveforms with an amplitude of 100 mA, different mean values and a fundamental frequency of 50 Hz were then driven in a single motor phase. For each test at a different mean current value, the phase terminal voltage and current were acquired.

Since no induced voltage occurs, the phase can be modelled as an RL circuit. Linear regression was used to estimate values for the resistance and inductance for each data set. The inductance values can be seen in Table 7.4.

Table 7.4: Inductance terms resulting from different current levels.

I_{mean} (A)	0.00	0.39	0.78	1.18	1.57	1.96	2.35	2.74
L (mH)	31.2	27.4	24.7	22.9	21.7	20.8	19.9	19.3

The coherence between the values estimated at low current values and those found in Section 7.3.1, where a small current is also used, is obvious. As for Ψ_1^{PM} , a clear reduction in L with increasing current magnitude can be observed. This trend is shown in Fig. 7.6.

As previously, two models, an ‘exponential’ one and a ‘linear’ one, have been fitted to the data:

$$L(i) = a_L e^{-b_L i^2} + c_L \quad (7.26)$$

and

$$L(i) = d_L |i| + f_L. \quad (7.27)$$

Again the exponential model achieves a better fit, in terms of the RMSE, using the estimated parameters:

$$\begin{aligned} a_L &= 9.91 \times 10^{-3} \text{ H} \\ b_L &= 1.051 \text{ A}^{-2} \\ c_L &= 2.014 \times 10^{-2} \text{ H}. \end{aligned}$$

7.4 Model comparison

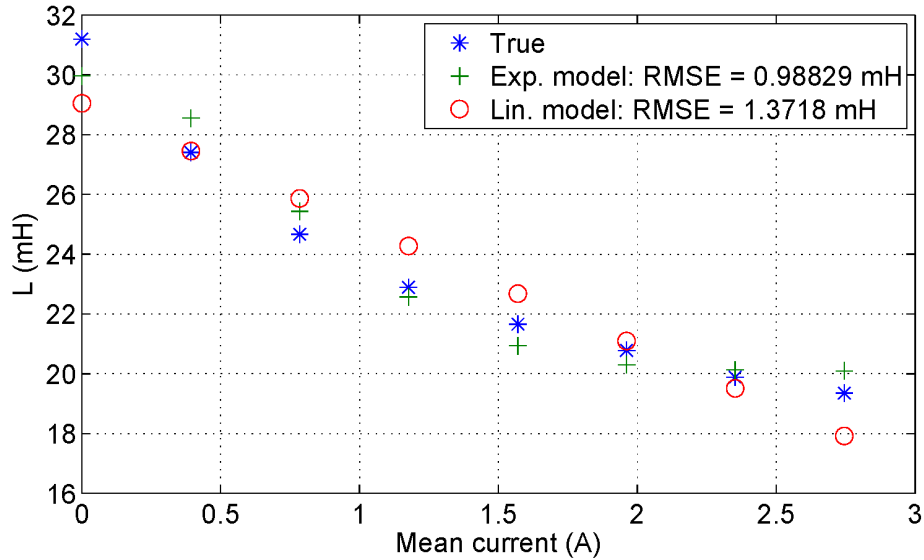
With the dependency of the terms demonstrated in the previous section and the model structures and orders determined, the complete models are fitted to standard stepping data and overall fitting performance compared in this section.

For the fitting some parameters are bounded to limit the search space to values with physical meaning, such as always having a decreasing exponential for the current dependant terms.

The models are compared using the Normalized Root Mean Square Error (NRMSE) fitness metric, defined as:

$$\text{fit}[\%] = 100 \left(1 - \frac{\|u - \hat{u}\|_2}{\|u - \bar{u}\|_2} \right), \quad (7.28)$$

with u the phase voltage, \hat{u} being the model prediction and \bar{u} the mean value of

Figure 7.6: Estimated and fitted L .

u .

The fit is evaluated on a different validation dataset to that used for the parameter estimation.

The standard model achieves a fit of 76.22 % (shown in Fig. 7.1).

7.4.1 Position dependency

It has previously been established that the most significant position dependent harmonic for the inductance is the second. Moreover it was seen that for the permanent magnet flux linkage, it is the first harmonic that is most important. Using this information, the model for Phase A becomes:

$$\begin{aligned}
 u_A &= Ri_A + v_A^{pd} = Ri_A + \frac{d\psi_A^{pd}}{dt} \\
 &= Ri_A + L_A \frac{di_A}{dt} + \frac{dL_A}{d\theta} \omega i_A + \frac{d\psi_A^{PM}}{d\theta} \omega \\
 &= Ri_A + (L_0 + L_2 \cos(2p\theta + \phi_{L,2})) \frac{di_A}{dt} \\
 &\quad - 2pL_2 \sin(2p\theta + \phi_{L,2}) \omega i_A - p\Psi_1^{PM} \omega \sin(p\theta + \phi_{PM,1}). \tag{7.29}
 \end{aligned}$$

This model was fitted by linear regression to the acquired phase A voltage signal, using the acquired current and position, and their derivatives, which were eval-

ated via noncausal filtering and numerical differencing. The estimated parameters are given in Table 7.5.

Fig. 7.7 shows the fit achieved with the position dependent inductance terms. It can be clearly seen that the fit is significantly improved over that achieved in Fig. 7.1. Nonetheless slight ripples in the regions of the discrepancy still exist. A fit of 89.62 % is obtained, compared to 76.22% for the standard model.

Table 7.5: Parameters estimated for the position dependent model

Parameter	Mean value	Standard deviation
$R(\Omega)$	4.168	0.033
$L_0(mH)$	32.487	0.005
$L_2(mH)$	4.367	0.008
$\phi_{L,2}(rad)$	-0.569	0.012
$\psi_1^{PM}(mWb)$	32.073	0.053
$\phi_{PM,1}(rad)$	1.289	0.006

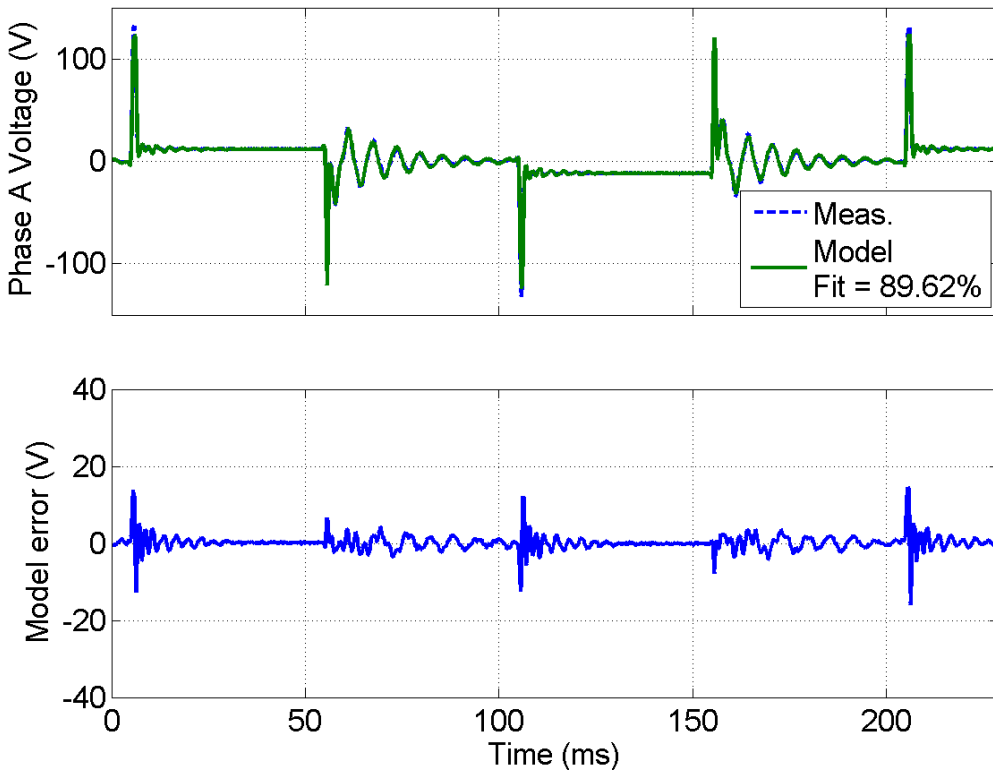


Figure 7.7: Model fit with the position dependent model.

7.4.2 Current dependency

The use of the current dependent terms in the model is next considered. As seen in the previous section, an exponential current dependency gives a good fit for both the inductance and permanent magnet flux linkage terms. The complete model using these terms is:

$$\begin{aligned}
u_A &= Ri_A + v_A^{cd} = Ri_A + \frac{d\psi_A^{cd}}{dt} \\
&= Ri_A + \frac{dL_A}{di_A} \frac{di_A}{dt} i_A + L_A \frac{di_A}{dt} + \frac{\partial\psi_A^{PM}}{\partial i_A} \frac{di_A}{dt} + \frac{\partial\psi_A^{PM}}{\partial\theta} \omega \\
&= Ri_A - 2a_L b_L i_A^2 e^{-b_L i_A^2} \frac{di_A}{dt} + (a_L e^{-b_L i_A^2} + c_L) \frac{di_A}{dt} \\
&\quad - 2a_\psi b_\psi i_A e^{-b_\psi i_A^2} \cos(p\theta + \phi_{PM,1}) \frac{di_A}{dt} - p(a_\psi e^{-b_\psi i_A^2} + c_\psi) \omega \sin(p\theta + \phi_{PM,1}).
\end{aligned} \tag{7.30}$$

As can be seen this model is nonlinearly dependent on its parameters. It is, therefore, not possible to estimate its parameters using linear regression. The parameters are thus estimated using a trust region reflective nonlinear optimisation routine to minimise a quadratic cost function between the model voltage prediction and the measured voltage. This routine was implemented using the *lsqnonlin* function in Matlab. It is initialised using the parameters found in Section 7.3.2 for the exponential function parameters and the values found via the linear regression for the standard model for R and $\phi_{PM,1}$. The parameters found after the nonlinear optimisation can be seen in Table 7.6.

Fig. 7.8 shows the fit achieved with the current dependent model. The fit is 91.28%, compared to 76.22% for the standard model and 89.62 % for the position

Table 7.6: Parameters estimated for the current dependent model

Parameter	Mean value	Standard deviation
$R(\Omega)$	4.155	0.033
$a_L(mH)$	1.628	0.053
$b_L(A^{-2})$	28.923	0.759
$c_L(mH)$	40.375	0.016
$a_\psi(mWb)$	42.211	0.238
$b_\psi(A^{-2})$	0.200	0.003
$c_\psi(mWb)$	-10.538	0.243
$\phi_{PM,1}(rad)$	1.380	0.006

dependent model. It is thus further improved upon from the model with position dependence. Furthermore, no residual ripples remain in the nonzero current regions.

7.4.3 Position and Current Dependency

Finally the combined dependency on position and current is considered. In the proposed model, the inductance combines the harmonic dependence on position and the exponential dependence on the current. This is done by assuming a decreasing exponential for the inductance terms L_0 and L_2 . The resulting inductance is:

$$L_A(\theta, i_A) = (a_{L_0} e^{-b_{L_0} i_A^2} + c_{L_0}) + (a_{L_2} e^{-b_{L_2} i_A^2} + c_{L_2}) \cos(2p\theta + \phi_{L,2})$$

With this position and current dependency on the model terms, the linear regression for their estimation is not possible, as for the current dependant model

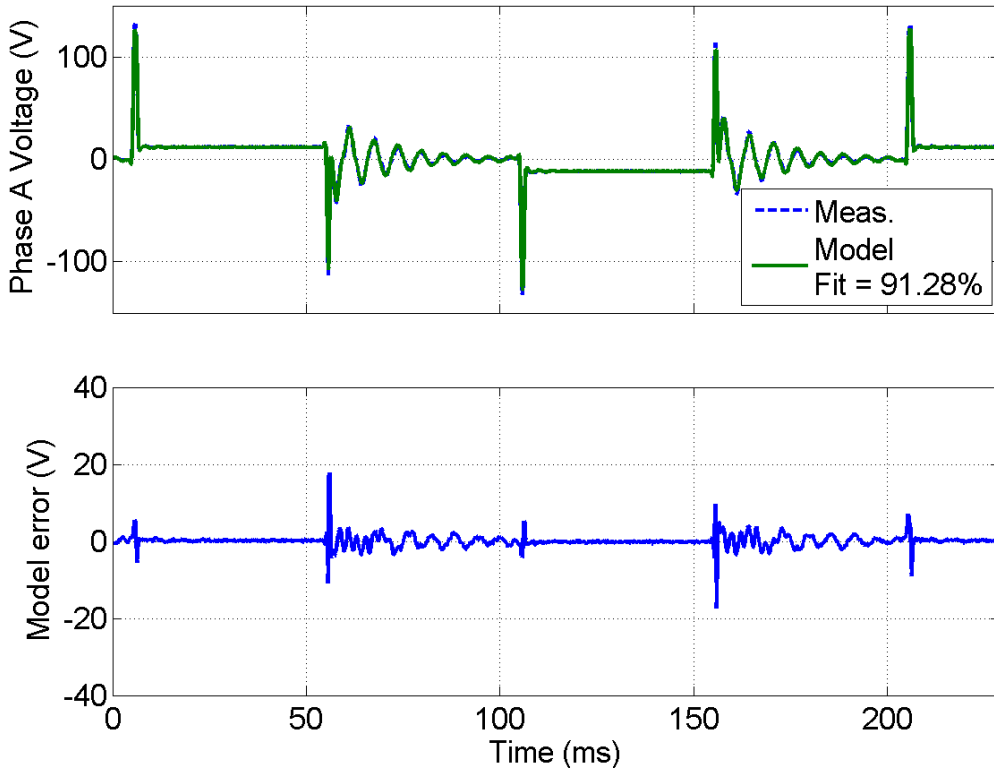


Figure 7.8: Model fit with the current dependent model.

presented in 7.4.2, and a nonlinear optimisation is necessary.

For the flux linkage due to the permanent magnet, the decaying exponential with the phase current is assumed, as well as a relation with the 1st harmonic of the angular position:

$$\psi_A^{PM}(\theta, i_A) = (a_\psi e^{-b_\psi i_A^2} + c_\psi) \cos(p\theta + \phi_{PM,1}) \quad (7.31)$$

The complete model combining these equations with the model in (7.11) and expanding, results in:

$$\begin{aligned} u_A &= Ri_A + v_A^{pcd} = Ri_A + \frac{d\psi_A^{pcd}}{dt} \\ &= Ri_A + \frac{\partial L_A}{\partial \theta} \omega i_A + \frac{\partial L_A}{\partial i_A} \frac{di_A}{dt} i_A + L_A \frac{di_A}{dt} + \frac{\partial \psi_A^{PM}}{\partial i_A} \frac{di_A}{dt} + \frac{\partial \psi_A^{PM}}{\partial \theta} \omega \\ &= Ri_A - 2p(a_{L_2} e^{-b_{L_2} i_A^2} + c_{L_2}) \sin(2p\theta + \phi_{L,2}) \omega i_A \\ &\quad - 2i_A^2 \frac{di_A}{dt} a_{L_0} b_{L_0} e^{-b_{L_0} i_A^2} - 2i_A^2 \frac{di_A}{dt} a_{L_2} b_{L_2} e^{-b_{L_2} i_A^2} \cos(2p\theta + \phi_{L,2}) \\ &\quad + (a_{L_0} e^{-b_{L_0} i_A^2} + c_{L_0}) \frac{di_A}{dt} + (a_{L_2} e^{-b_{L_2} i_A^2} + c_{L_2}) \cos(2p\theta + \phi_{L,2}) \frac{di_A}{dt} \\ &\quad - 2a_\psi b_\psi i_A e^{-b_\psi i_A^2} \cos(p\theta + \phi_{PM,1}) \frac{di_A}{dt} - p(a_\psi e^{-b_\psi i_A^2} + c_\psi) \sin(p\theta + \phi_{PM,1}) \omega \end{aligned}$$

For the nonlinear optimisation the same initial values used in 7.4.2 are used. For the exponential expression of L_2 , proportional values to those for the expression of L_0 with the relation L_2/L_0 are used for a_{L_2} and c_{L_2} , while b_{L_2} is left with the same value. The parameters obtained for this model are shown in Table 7.7, and the performance with the validation dataset is shown in Fig. 7.9. A fit value of 93.40 % is achieved, improving the one achieved by all the other models.

The error has been greatly reduced compared to the initial one shown in Fig. 7.1, but it is not zero. The remaining error in Fig. 7.9 is possibly due in part to the fact that the results presented are for a validation dataset and in part to further unmodelled phenomena such as magnetic hysteresis. Modelling magnetic hysteresis accurately, however, would significantly increase the model complexity, limiting its use in real-time applications. For this reason it has not been considered further in the present work, and even if it were, an exact model of a real system is unachievable, and there is always some prediction error (small enough though, to make the model useful for its desired purpose).

Table 7.7: Parameters estimated for the position and current dependent model

Parameter	Mean value	Standard deviation
$R(\Omega)$	4.180	0.033
$a_{L_0}(mH)$	1.945	0.097
$b_{L_0}(A^{-2})$	45.252	1.276
$c_{L_0}(mH)$	37.211	0.059
$a_{L_2}(mH)$	26.989	2.571
$b_{L_2}(A^{-2})$	0.018	0.002
$c_{L_2}(mH)$	-21.735	2.572
$\phi_{L,2}(rad)$	-0.375	0.015
$a_\psi(mWb)$	80.984	6.060
$b_\psi(A^{-2})$	0.039	0.003
$c_\psi(mWb)$	-48.802	6.060
$\phi_{PM,1}(rad)$	1.365	0.007

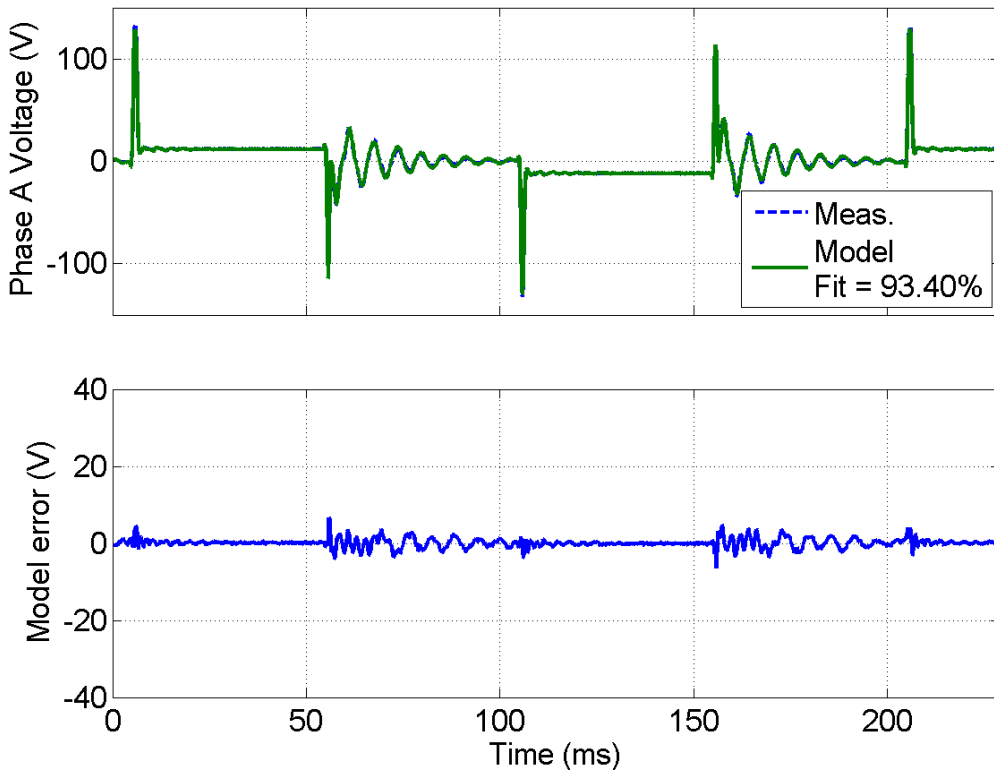


Figure 7.9: Model fit with the position and current dependent model.

7.5 Model limitations

7.5.1 Performance

The increased model prediction capability comes at the expense of a greater complexity. However the goal of the proposed model is to be used in embedded control systems, where the computing capabilities are limited and the increasing complexity makes the highly demanding real time constraints difficult to fulfil.

To assess and compare the proposed models a test simulating the models each 2000 times was performed, measuring the computing time. This is a comparative test and its absolute value cannot be extrapolated to that of an embedded processor, but it is useful to compare the increase in complexity of the proposed models. The results are shown in Table 7.8. The Fit improvement over the standard model is clear, reaching up to 22.27 % for the most complex model.

Nevertheless the computing cost also increases considerably. The position dependent model seems nonetheless to be well balanced with a high improvement in the fitting and a low computational expense.

It is, however, dependent on the hardware available and the code optimisation skills of the programmer to decide if the most complex model is worth its computational cost.

7.5.2 Range of usefulness

To assess the range in which the improvement given by the proposed models justifies the complexity, they are tested in a different experiment in which several RMS current levels were applied and the improvement achieved is compared.

For the position dependence, it is obvious that in any mode of use of the stepping motor it rotates through the whole range of positions, and therefore a

Table 7.8: Performance of the different models comparing fit and average computing time

	Standard model	Position dependency	Current dependency	Current and position dependency
Fit (%):	76.22	89.62	91.28	93.40
Improv.(%):	0.00	17.45	18.66	22.27
Time(ms):	0.07	0.09	3.65	4.77

fit for a specific position is not useful.

In Fig. 7.10, the fit for different current levels is shown.

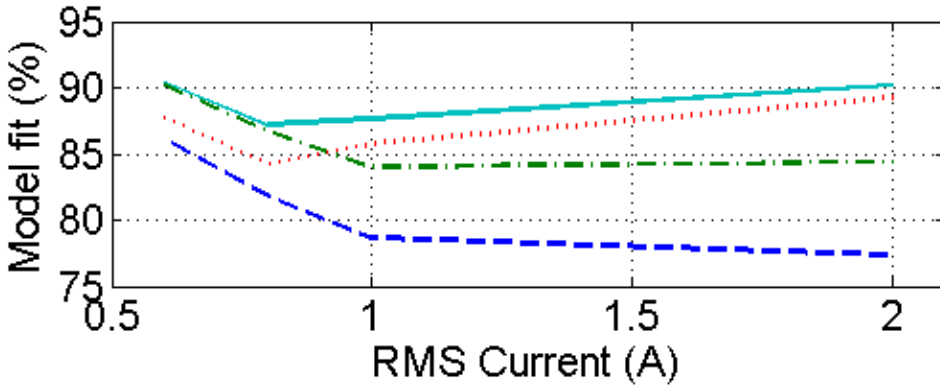


Figure 7.10: Fit percentage of the models for different RMS current datasets. Model assessed: (dashed) standard, (dotted) current dependent, (dash-dot) position dependant and (solid line) position and current dependent

The fit for all the different models is closer at low RMS current. The position dependent model improves the result of the standard model and the improvement is constant all over the different RMS current levels, as expected. The current dependent model is close to the standard model with low RMS currents, where the effect of the core saturation is low, and improves greatly compared to the standard model as the current goes higher. The position and current dependent model shows a better result in all the current levels, and the difference with the standard model is the biggest at high current level.

7.5.3 Application of the proposed model on sensorless estimation

The stepper motor model used in the Kalman filter ((6.3)-(6.7)) has a limitation given by the fact that observability is lost when the motor is not turning and therefore there are no back electromotive forces providing information. This fact is discussed in [67] and in section 6.4.3 the effect is shown when the motor holds a fixed position.

As has been demonstrated in this chapter, the back electromotive force is lower as the current in the phase increases due to the reduced flux linkage, and therefore it can be expected that if a sufficiently high current is applied in both phases, as might be the case in any stepping mode that energises both phases

at the same time, the observability would be reduced and even lost. It would therefore be important to dimension the motor such that significant saturation does not occur at nominal currents. An obvious solution useful for any any motor would be to use full-step mode with one phase on, since in this way there is always a motor phase with no current.

7.6 Extended Kalman Filter: Theory and Experimental Results

In this section, an Extended Kalman Filter, based on the position and current dependent model defined in the previous section, is derived. Its estimation and filtering performances in real time HSM control are also discussed and experimentally evaluated.

7.6.1 State-space model derivation theory

In order to apply the EKF, as seen in chapters 5 and 6, a stepping motor model expressed in state-space form should be used.

The formulation is taken as general as possible, so that its structure is valid for all the models presented in this chapter. In the Appendix A, the symbolic expressions are explicitly reported for reader's convenience, focusing on the most complete proposed HSM model with both position and current dependence.

Exploiting the voltage balance equations for each motor phase and the mechanical balance equation for a rigid body, the following system representing the HSM can be derived:

$$\begin{aligned}\dot{x}_1 &= \frac{\text{Num}_A}{\text{Den}_A} + \frac{u_A}{\text{Den}_A} \\ \dot{x}_2 &= \frac{\text{Num}_B}{\text{Den}_B} + \frac{u_B}{\text{Den}_B} \\ \dot{x}_3 &= \frac{\tau_A + \tau_B}{J} - \frac{B}{J}x_3 - \frac{T_{dm}}{J} \sin(2px_4) - \frac{x_5}{J} \\ \dot{x}_4 &= x_3 \\ \dot{x}_5 &= 0,\end{aligned}\tag{7.32}$$

where τ_A and τ_B are the two phase electromagnetic torques, and the state \mathbf{x} , the input \mathbf{u} and the output \mathbf{y} vectors are the same as described in equations (6.4),

(6.5) and (6.7), respectively, repeated below for convenience:

$$\mathbf{x}(t) = \begin{bmatrix} i_A \\ i_B \\ \omega \\ \theta \\ \tau_l \end{bmatrix} \quad \mathbf{u}(t) = \begin{bmatrix} u_A \\ u_B \end{bmatrix} \quad \mathbf{y} = \begin{bmatrix} i_A \\ i_B \end{bmatrix}$$

In order to obtain its discrete time version a forward Euler scheme is adopted:

$$\begin{aligned} x_1[k+1] &= x_1[k] + T_s \left(\frac{\text{Num}_A}{\text{Den}_A} + \frac{u_A}{\text{Den}_A} \right) [k] \\ x_2[k+1] &= x_2[k] + T_s \left(\frac{\text{Num}_B}{\text{Den}_B} + \frac{u_B}{\text{Den}_B} \right) [k] \\ x_3[k+1] &= x_3[k] + T_s \left(\frac{\tau_A + \tau_B - Bx_3 - T_{dm} \sin(2px_4) - x_5}{J} \right) [k] \\ x_4[k+1] &= x_4[k] + T_s x_3[k] \\ x_5[k+1] &= x_5[k], \end{aligned} \quad (7.33)$$

where T_s is the sampling period.

The derived discrete-time nonlinear time-invariant system in Eq. 7.33 is the representation (5.1) needed to apply the EKF.

Now the EKF can be used, following the iterative algorithm presented in Section 5.3.

7.6.2 Experimental Results

The experimental setup consists of the drive described in chapter 4 and used in chapter 6 for the EKF application with the standard electrical model.

The EKF, based on the new, full model extensions, was implemented on the DSC in order to provide enhanced filtering of the measured currents for use in the feedback loops as shown in Fig. 7.11 (note that the estimations \hat{x}_1 and \hat{x}_2 correspond to the currents i_A and i_B), as well as sensorless position and torque estimation.

As can be appreciated from this chapter and the Appendix A, the model used has increased significantly in complexity. A certain amount of code optimisation was necessary, nonetheless it was possible to get even the full model with both position and current dependency to run at the relatively high cycle rate of 25 kHz, demonstrating its applicability to real-time applications.

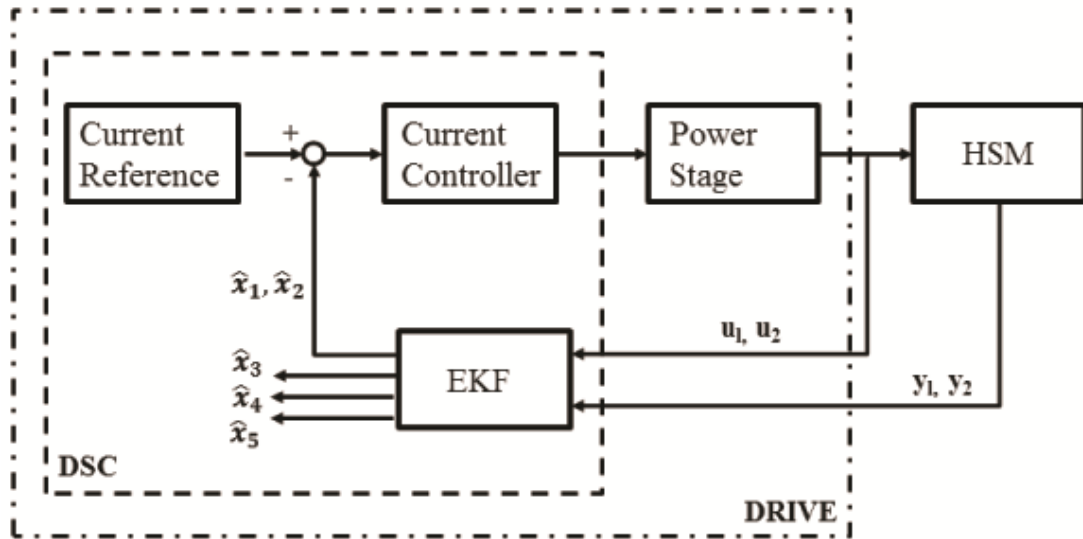


Figure 7.11: EKF based closed loop control of the HSM.

The same motor used in the modelling steps was used. A 32768 line/turn rotary quadrature encoder was used to measure the motor rotor position for both tuning and validation purposes.

The model parameters used in the EKF, as well as the covariance matrices, were tuned using a data-based technique similar to that described in [16] but modified to exploit the new model. The drive DAQ capabilities were used to acquire the phase currents, voltages and the encoder position simultaneously at 25 kHz, whilst the motor was stepping at full step, 20 step/s.

Fig. 7.12 shows the main waveforms of the proposed EKF operating in the feedback control loop. They highlight a correct operation of the HSM. In order to test the long term stability of the EKF, in Fig. 7.13 the estimated position is plotted, after many mechanical turns, corresponding to several hundred thousand time steps.

Finally, the EKF based on the position and current dependent model has been compared with the Standard model based one used in chapter 6. In Fig. 7.14,

Table 7.9: EKFs Comparison

Model	RMS error (rad)	Max error (rad)
Standard :	0.0016985	0.0065098
Position and Current:	0.0010955	0.004307

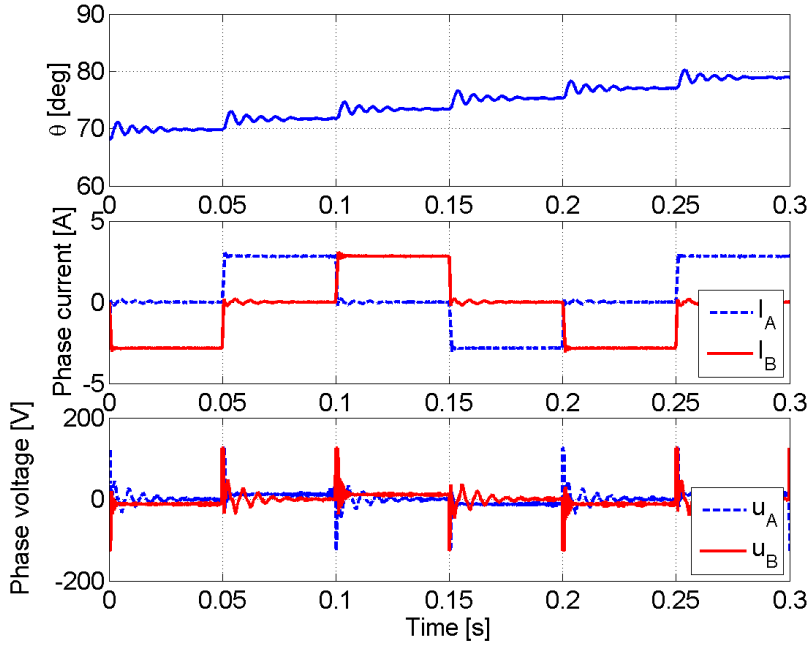


Figure 7.12: Drive signals during closed loop operation.

the comparison of the position estimations is shown. The benefit of adopting the proposed extended electrical model in the EKF is clear also for estimating quantities that are not directly employed in the feedback line. In Table 7.9 the RMS and max position estimation errors, for the two different approaches, are computed.

7.7 Conclusions

New extensions of the standard electrical model of a hybrid stepper motor used for control and observation purposes in modern, sophisticated drives are developed and compared in this chapter.

It has been seen that inclusion of position and current dependent inductance and permanent magnet flux linkage terms achieves a better fit to experimental data, particularly for large current amplitudes.

However there is a tradeoff between the model fit improvement and the increase in complexity, and it depends on the application which model is better to use, or which one can be afforded.

Moreover, an Extended Kalman Filter based on the position and current dependent HSM model has been formulated and implemented in a real time closed

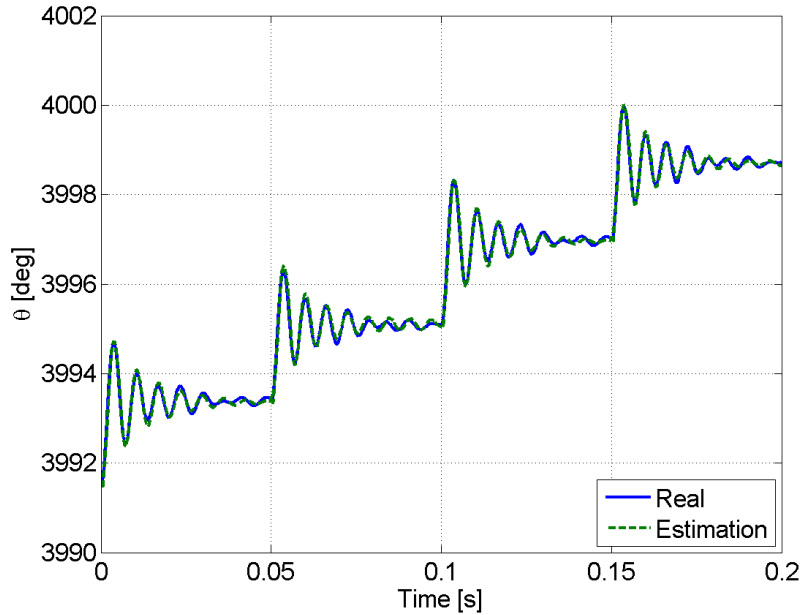


Figure 7.13: Long term position estimation by EKF.

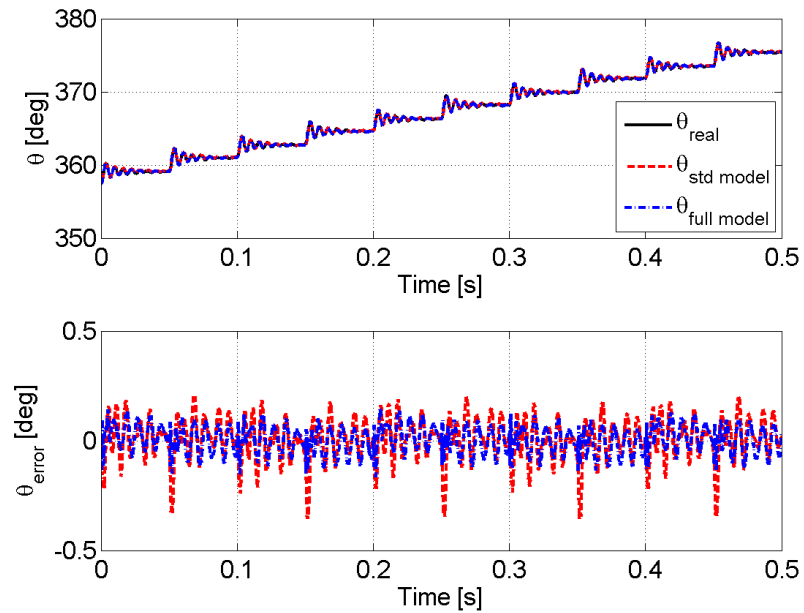


Figure 7.14: Comparison of EKF using different HSM models.

loop control architecture. From the experimental results, the proposed new EKF filter has very good accuracy and tracking capabilities with respect to an EKF based on the standard model.

Part III

Field Oriented Control for Stepper Motors

Chapter 8

Background on Field Oriented Control

8.1 Introduction

As we saw in section 3.3, stepper motors are typically used in open loop in positioning systems. We saw an example similar to the one presented in Fig. 8.1, where an acquisition of the rotor position and speed are shown. The large overshoot of over 50 % can be easily appreciated, followed by several oscillations. Looking at the speed, the rotor reaches again large values compared to the average speed, which in this case with 40 steps per second is 1.25 rad/sec, whereas the peak values reach 25 and -20 rad/sec.

In the LHC collimators, this jittery movement is tough for the mechanics. The worm screw connected to the motor to move the collimator jaw linearly wears and after a few years of use can need to be replaced, an expensive intervention. It is therefore desirable to attempt to extend its lifespan. This could be achieved with a smoother motion profile applied with the motor. To attain such a profile, closed-loop position control is proposed using Field Oriented Control (FOC).

However, in chapter 3 it was claimed that relying on position sensors, as needed for FOC, for critical operation, as is the case of the collimation system, is preferably avoided in the LHC collimators, since it would reduce the reliability of the whole system. A sensor failure could lead to the malfunctioning of the collimator, and thus to the beam dump and stop of the machine. The cost of such an event, plus the required maintenance of the collimator, is not affordable.

Sensorless control as presented in chapters 5 to 7 is an attractive option, but

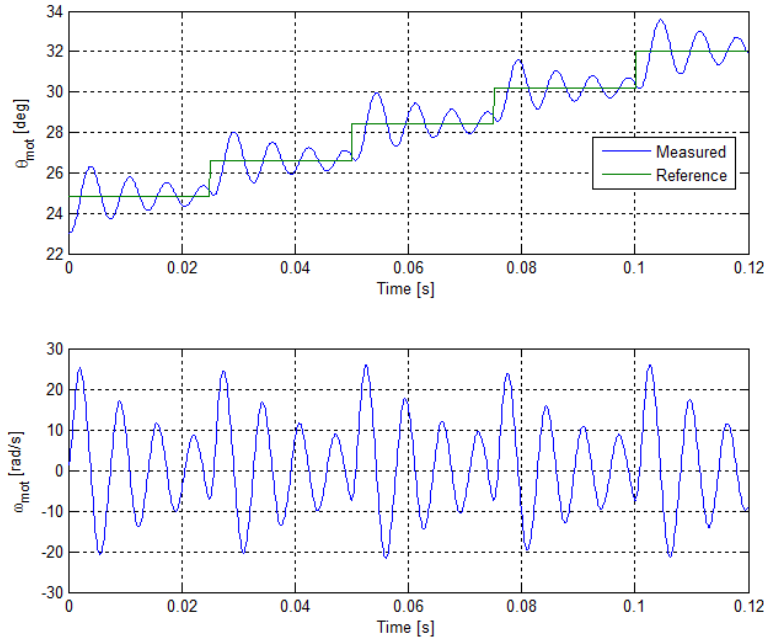


Figure 8.1: Full-step mode rotor position and speed acquisition.

it has the problem of the loss of observability when the rotor is stopped or at low speed. In the case of the collimators, these are the most common cases, and therefore sensorless estimation is not a reliable option to close the position loop. This fact does not interfere with its use for the purpose of mechanical health diagnostics, since the torque estimation is good during the parts of the motion profiles with non-zero speeds, as demonstrated in section 6.4.3.

To overcome these problems and take advantage of the smoother motion profile that can be achieved using a sensor and closing the position loop, but not reduce the reliability of the system, an automatic closed-to-open position loop switch is proposed. This switch is an original contribution of this thesis. With it, the motor can work in closed-loop position control, providing smooth motion profiles, but in the case of sensor failure, the loop is opened, continuing to work in standard open-loop position control. The sensors can be repaired during the next programmed machine technical stops, allowing for a continuous operation of the collimators and enlarging the collimator mechanics lifespan thanks to the smooth motion while the sensors are working.

A non-negligible trend in research is using stepper motors with the position loop closed in different ways, whether it be with a position sensor or with sen-

sorless techniques. In this chapter the different control strategies that are known to give good performance when applied to stepper motors and the state of the art of the chosen one for this work, FOC, are presented. In the next chapter, the position control scheme and the closed-to-open position loop switch is presented, as well as its application in the LHC collimators at CERN.

8.2 Electric Motors position control strategies

There are multiple control approaches for electric motor control, see e.g. [26, 84] for academic, and [93] for industrial references. Some of the most commonly used control strategies for AC motors have been explored for use in stepper motors. The most relevant ones are the following.

8.2.1 Open-loop position control

This strategy applies originally to Stepper Motors, being, as discussed in section 3.1, one of the main reasons for their choice as the actuator for the LHC collimators. Even though this strategy is the reason for being of stepper motors, and has satisfactory performance in multiple applications ([1, 36]), it has some limitations and drawbacks as exposed in section 8.1.

8.2.2 Closed-loop position control

Field Oriented Control

The operating principle of FOC is relatively simple: a change of coordinates for the electric and magnetic signals are applied from the static reference frame linked to the stator phases to the rotating frame linked to the rotor, where the torque produced is directly proportional to the current in one of the axis of this rotating frame, making its control relatively straightforward with closed-loop control.

FOC is the most popular control strategy for AC motors [93]. It is used to control the torque of the motor, and the speed and position control layers are built on top of the torque control. FOC became standard in induction machines [10] achieving high dynamics, close to DC motor drives. The main advantages of FOC are the smooth operation and the fast transient response. It has also been broadly researched for use with synchronous machines and stepper motors.

Thanks to its advantages and proven performance in all the motor types where it has been used, it has been chosen for closed-loop position control in this thesis, with the goal of achieving good positioning repeatability and fast and smooth dynamics. More details on its working principle and research applied to stepper motors are given in section 8.3.

Direct Torque Control

Direct Torque Control (DTC), considered originally in [21] and [85], is a method to control the torque in 3-phase AC motors. First the magnetic flux in the motor and the torque are estimated from the phases voltage and current measurements, and then a hysteresis band-limiting control is applied on both stator flux linkage and torque. Depending on the required action the switches in the 3-phase inverter are controlled in such a way that the flux and torque errors return within the tolerance band of the hysteresis comparators.

DTC is becoming one of the standards in AC motor high dynamic control together with FOC [90]. In [17] a performance comparison of both methods is done for induction motors. Even though DTC has been applied successfully to synchronous permanent magnet motor [96], the references for stepper motor applications are scarce, and to the author's knowledge is only used in [48] where the method is applied to a 3-phase stepper motor. In [29] DTC and FOC are compared for synchronous motors, concluding that both methods are close in performance and the advantages are application-specific. For steady state positioning FOC nonetheless turns out to have better performance. In [90] some difficulties for DTC working at low rotor speeds are reported. In spite of the possible solutions to this problem, and its advantages with respect to FOC, such as simplicity of implementation and fast torque control, it is not an attractive option for 2 phase stepper motors as proven by the lack of literature. This fact motivated the choice of FOC for closing the position loop.

Other approaches

FOC and DTC are the most common and successful control strategies for closed-loop motor control. However, there are other approaches used in specific applications or in different research branches. Some examples are discussed now.

In [9] Fuzzy Logic control is applied to the closed-loop speed control of stepper motors. A standard stepper motor drive is used and the fuzzy controller is im-

plemented in an upper layer, calculating the time between pulses sent to trigger the steps to obtain the desired speed trajectory. The method is proven to work and yield good results but still works in stepping mode so suffers from overshoot.

Neural networks has been applied for speed control of stepper motors [72]. In this paper two neural networks were used, one for identification and other for control, achieving a good performance at low and high speed. The neural network is implemented in a computer, external to the motor drive. [44] presents a neural network-based low-speed-damping controller, in order to remove nonlinear disturbances at low speed, implemented on a FPGA.

Iterative learning control has also been applied for precision control at low speed in [18], where it is used together with a proportional-derivative controller to minimize the motor's torque ripple. It can, however, only produce good results with repetitive trajectories.

Even though some of these approaches proved to give decent results, FOC strategy was chosen as control strategy for the above reasons.

8.3 Field Oriented Control

The Field Oriented Control technique, also known as vector control, is based upon the change of coordinates of the motor electrical and magnetic quantities from the fixed reference frame to a rotating reference frame moving with the rotor. In this rotating frame, the signals are represented in the so-called direct and quadrature axes.

The origin of the idea is from Andre Blondel in France, with the technique *Blondel two-reaction method*. It was then developed by R.E Dohery, C.A. Nickle and R.H. Park [63], the latter giving the name by which it is best known, the Park transform, though it is also known as the dq transform [26].

Brushed DC motors are popular due to their simplicity of control. In these motors, the phase angle between the phase current and the induced voltage is fixed mechanically by the commutator and the brushes. In AC motors, however, this angle has to be controlled in order to achieve the desired torque generation. Using FOC allows induction and synchronous motors to be driven in a similar way to brushed DC motors, since in the rotating coordinate system the torque produced is proportional to the quadrature current.

It should be noted that before applying the change of coordinates, systems

with 3 phases are reduced to a fixed 2 axis reference frame, which here will be referred to as the *ab* frame, with axis a and b. The transformation from 3-phase to the equivalent 2-phase system is known as the Clarke or $\alpha\beta$ transform [67].

8.3.1 Field oriented control applied to stepper motors

The change of reference frame used in FOC can be applied to HSM as well. It has already been used for HSM control for example in [35] where it is applied with position sensors and [62] where an Extended Kalman Filter is used, with the limitation of not being able to work in standstill due to the loss of observability when the back emfs are low.

In order to illustrate it in an easier way, its application to a permanent magnet stepper motor (PMSM) is shown now. Then the HSM application can be easily inferred. In Fig. 8.2 the voltage applied to the motor is represented in both the *ab* frame, fixed to the stator, and the rotational *dq* frame, fixed to the rotor.

The discrete equations for the HSM have been discussed in chapter 2 and are repeated here for convenience, but to ease the notation, from this point the currents are assumed to be always the motor currents since only the motor is considered, and not the cable as in the previous chapters where we needed to explicitly differentiate between motor and drive currents and voltages. Therefore only the sub-indexes *a* and *b* will be used.

From the standard equations representing a stepper motor:

$$\begin{aligned}\dot{L}i_a &= -Ri_a + K_m \omega_m \sin p\theta_m + u_a \\ \dot{L}i_b &= -Ri_b - K_m \omega_m \cos p\theta_m + u_b \\ J\dot{\omega}_m &= \tau_{em} - B\omega_m - T_{dm} \sin(2p\theta_m + \phi) - \tau_l \\ \dot{\theta}_m &= \omega_m\end{aligned}\tag{8.1}$$

where

$$\tau_{em} = K_m (-i_a \sin p\theta_m + i_b \cos p\theta_m).$$

we can represent the stepper motor model with blocks as in Fig. 8.3.

This standard model is based on the reference frame fixed to Phases A and B. It is possible however to represent voltages and currents in a rotating frame fixed to the rotor, as represented in Fig. 8.2.

There is a direct link between coordinates in both reference frames. The

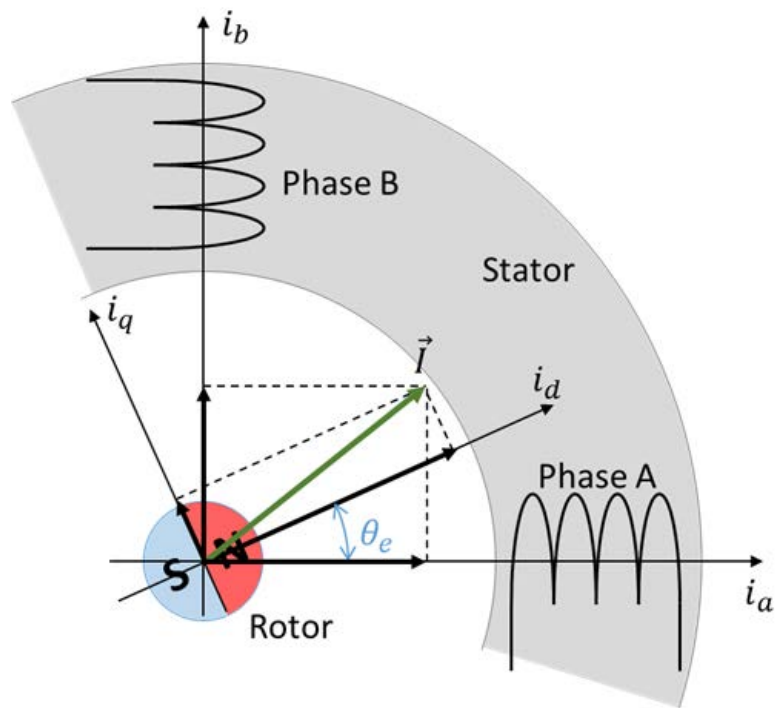
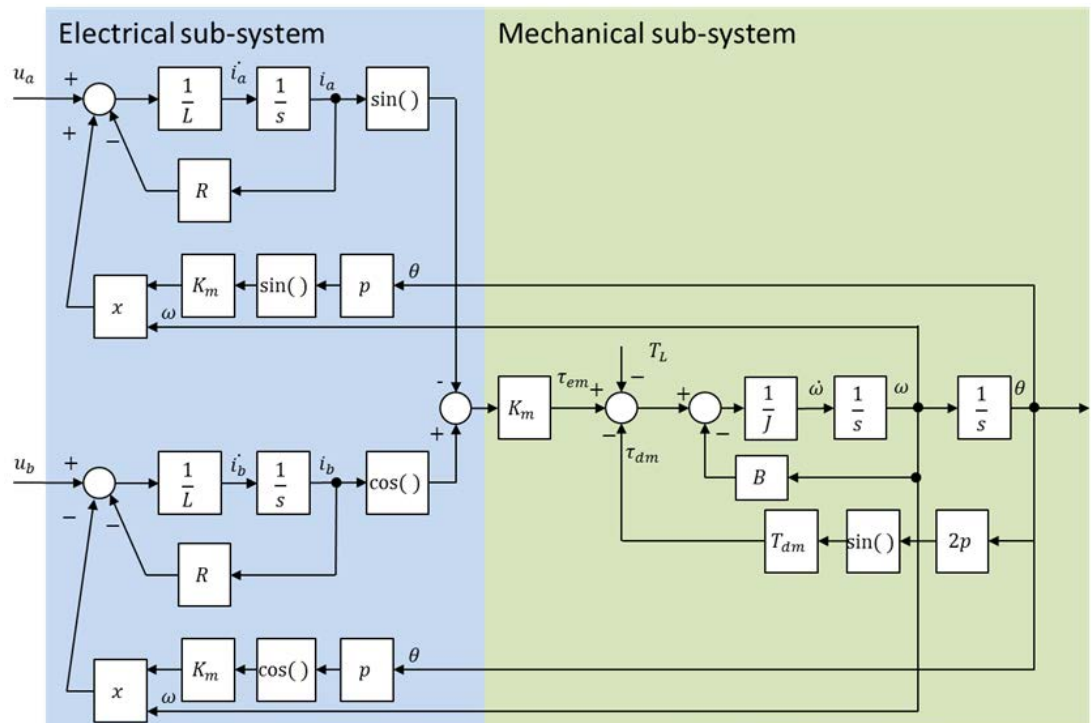


Figure 8.2: Currents represented in the different frames

Figure 8.3: Stepper Motor model diagram using the standard ab reference frame

conversion from the ab frame to the dq frame is called the direct Park Transform:

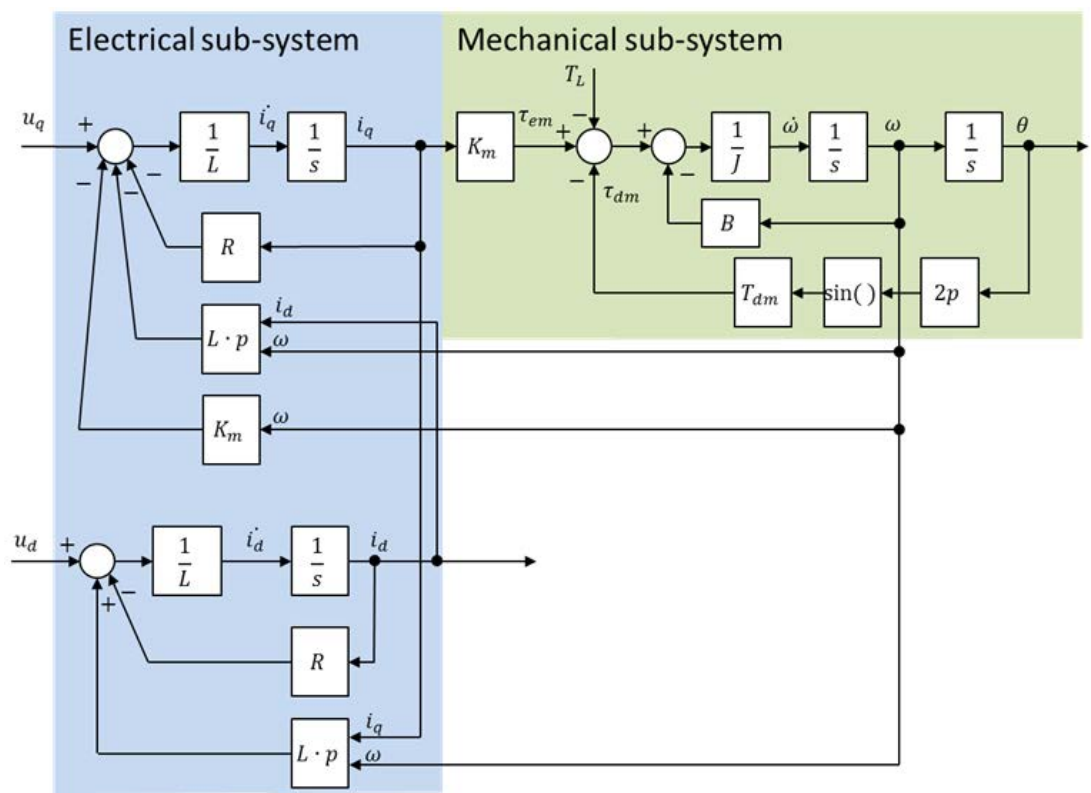
$$\begin{aligned} u_d &= u_a \cos(\theta_e) + u_b \sin(\theta_e) \\ u_q &= -u_a \sin(\theta_e) + u_b \cos(\theta_e) \end{aligned} \quad (8.2)$$

And the conversion from the dq to the ab frame is called the inverse Park Transform:

$$\begin{aligned} u_a &= u_d \cos(\theta_e) - u_q \sin(\theta_e) \\ u_b &= u_d \sin(\theta_e) + u_q \cos(\theta_e) \end{aligned} \quad (8.3)$$

If this conversion, and the equivalent for the currents, is applied to the equations (8.1), the model of the motor in the dq frame is obtained, given by the following equations and represented in Fig. 8.4.

$$\begin{aligned} \dot{Li_d} &= -Ri_d + pLi_q\omega_m + u_d \\ \dot{Li_q} &= -Ri_q - pLi_d\omega_m + u_q - K_m\omega_m \\ J\dot{\omega}_m &= K_mi_q - B\omega_m - T_{dm} \sin(2p\theta_m + \phi) - \tau_l \\ \dot{\theta}_m &= \omega_m \end{aligned} \quad (8.4)$$

Figure 8.4: *dq* frame Stepper Motor model diagram

Chapter 9

Control of stepper motors with Field Oriented Control

9.1 Introduction

In this chapter the FOC applied to stepper motors is presented. First the control scheme and tuning are described with the main practical issues for its implementation. Then the switch proposed to pass from closed to open position loop, and finally the application in one of the LHC collimators.

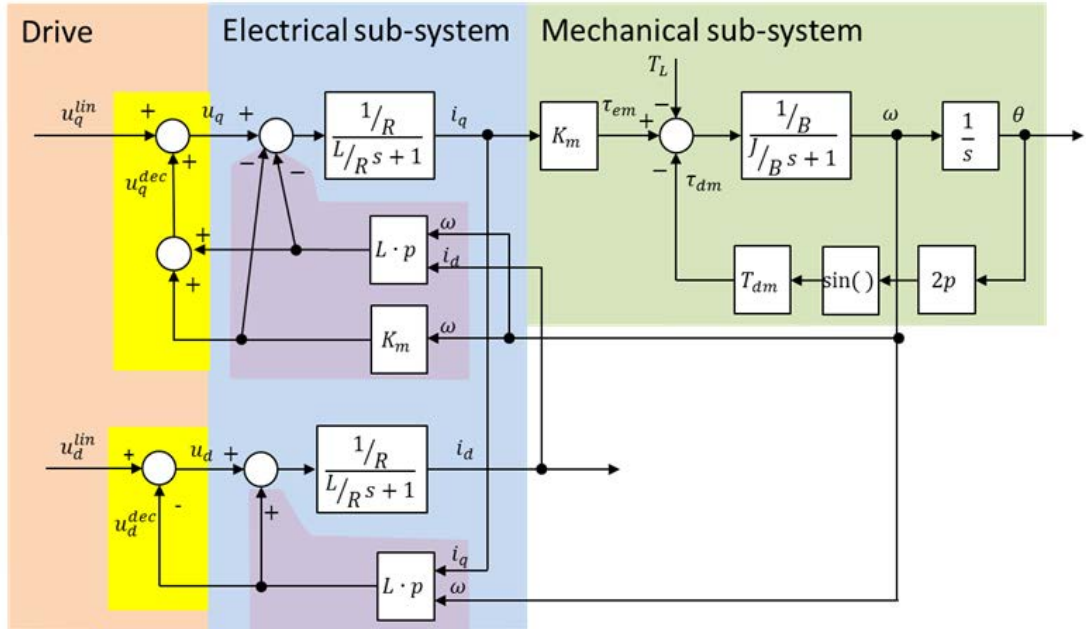
9.2 Control scheme description and tuning procedure

The control scheme is implemented in several steps, starting by the most internal layer and adding layers on top once the bottom one is working appropriately.

9.2.1 Decoupling of the current control

Looking back at Fig. 8.4, we can see that the currents i_d and i_q are coupled. Since the signals coupling them are available it seems logical to try to compensate for it. In Fig. 9.1 the system including this decoupling is represented. The part in yellow is implemented in the DSP Drive in such a way that it cancels the corresponding physical part marked in purple.

To achieve this, the drive adds to the desired u_d^{lin} and u_q^{lin} the quantities u_d^{dec} and u_q^{dec} respectively in order to compensate for the corresponding terms, with

Figure 9.1: Decoupling scheme for i_{dq} .

values:

$$\begin{aligned} u_d^{dec} &= -L_w p \omega_m i_q \\ u_q^{dec} &= L_w p \omega_m i_d + K_m \omega_m \end{aligned} \quad (9.1)$$

Once this is achieved the electrical subsystem is reduced to the linear system:

$$\begin{aligned} L_w \dot{i}_d &= -R_w i_d + u_d^{lin} \\ L_w \dot{i}_q &= -R_w i_q + u_q^{lin}, \end{aligned} \quad (9.2)$$

The following parameters are used in the decoupling and therefore need to be known:

- L_w , the motor phase inductance. The low frequency value of the inductance is used since the bandwidth of the current loop is 1-2 kHz, well below the frequencies in which the iron losses are significant.
- K_m , the torque constant of the motor.
- p , number of motor of teeth.

9.2.2 Close the loop on i_q and i_d .

Now the loop on both currents, i_q and i_d , is closed with a controller as shown in Fig. 9.2, where the blocks corresponding to the parts decoupled has been omitted in order to simplify the representation. This simplification is realistic if the decoupling between ω_m (back emf), i_q and i_d is ideal. In practice it is not ideal and the control loop sees the imperfections as disturbances.

This system has the same R_w and L_w as the original one in the ab frame, so the controller designed originally to deal with these currents is used here. This controller is described in chapter 4.2.2.

9.2.3 Speed loop controller

The next step is to close the loop on ω_m , as shown in Fig. 9.3, where once again the new part, marked in yellow, is added to the previously constructed system. For the speed controller calculation, the detent torque has been neglected, since for this loop it is seen as a non-linear disturbance to be compensated and is not taken into account in the linear controller design. Once again, the system is simplified from the one in Fig. 8.4, removing the parts that thanks to the decoupling cancel each other, and omitting the i_d loop, since it has no effect on the speed loop if the decoupling is properly achieved.

The block *Current loop* can be ideally approximated to unity in its bandwidth, which is expected to be 1-2 kHz. However, the controller $C_w(s)$ is in series with the current controller for i_q and therefore some conditions should be respected. A rule of thumb for the relation between the bandwidth of the internal loop, $M_{idq}(s)$

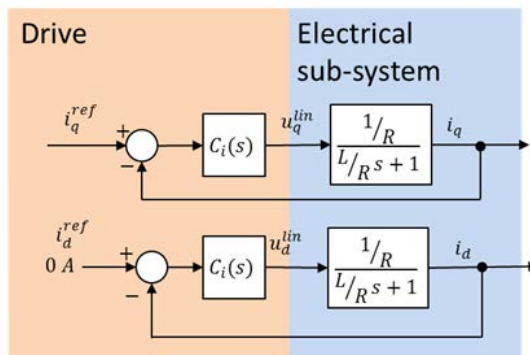


Figure 9.2: Current loops in case of ideal decoupling

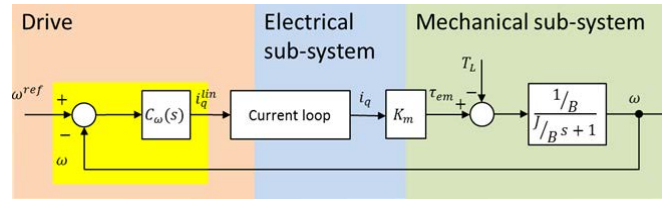


Figure 9.3: Simplified rotor speed loop

and the external loop $M_\omega(s)$ is given in [49, page 733], and it is:

$$f_{BW\omega_m} < \frac{1}{4} f_{BW i_d q} \quad (9.3)$$

where f_{BW} is the bandwidth frequency of each loop.

The current loop has been designed to achieve 1-2 kHz bandwidth. In practice it can work reliably at 1.5 kHz, the value that is used as reference. The resulting desired bandwidth for the speed loop is then:

$$f_{BW\omega} < 375 \text{ Hz} \quad (9.4)$$

To calculate the controller a frequency approach is followed. For this first the block in the mechanical subsystem in Fig. 9.3 must be identified.

A simple yet effective way to identify the mechanical block is by fitting a 1st order system to measured data. To do this a step in i_q is performed measuring the speed response, and then a first order system is fitted to the result from which we can get the values J and B and from this, plot the frequency response of the system. In Fig. 9.4 an example of the fit is shown. The controller is calculated afterwards to fulfil the desired closed loop bandwidth and achieve zero steady state error. A PI controller is therefore selected.

9.2.4 Position loop controller

One more loop is added on the position, on top of the speed loop. In Fig. 9.5 the new loop is shown, with the simplified version of the speed loop, the current loop omitted and the new part marked in yellow.

If the condition proposed in (9.3) is preserved we have:

$$f_{BW\theta_m} < \frac{1}{4} f_{BW\omega_m}, \quad (9.5)$$

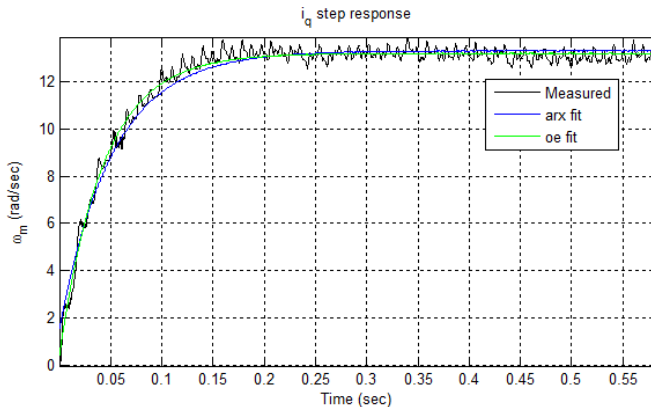


Figure 9.4: Fit of the system step response to a first order system

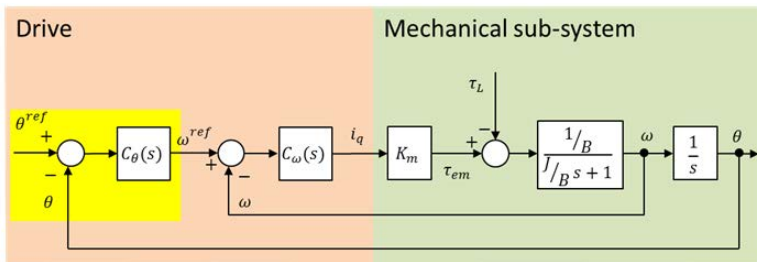


Figure 9.5: θ_m loop simplified

and the transfer function from ω_m^{ref} to ω_m is approximately equal to unity for the desired bandwidth of θ_m . If this condition is fulfilled, it suffices to use a proportional controller.

9.2.5 Control scheme description

The block representations of the system shown in the chapter so far are an abstraction of the real system, since even though the representation in the rotating frame is valid and coherent with it, the voltage can only be applied to the motor phases in the stator axes a and b. A block representation of the complete FOC system is depicted in Fig. 9.6, with the physical parts represented without the abstraction, and therefore including the coordinates transformation blocks.

This representation matches with the real system, where the h-bridge and the motor are represented by their own blocks and the sensors and DSP drive implement the rest of the blocks.

The blocks $C_\theta(s)$ and $C_\omega(s)$ are respectively the controllers obtained for the position and the speed loops. The blocks $C_i(s)$ are the current controllers. The

decoupling signals has been added to the control action calculated by the current controllers, resulting in u_q and u_d , the control action voltages to be applied to the system in the dq axis frame. The Park transform and Inverse Park transform blocks are in charge of the change of coordinates between the dq and the ab frames. The control action voltages u_a and u_b , obtained with the inverse Park transform from u_q and u_d , are applied to the h-bridge as a PWM to the appropriate MOSFETS.

To ease the understanding of the scheme, the position loop has been marked in blue, the speed loop in green, and the decoupling terms in orange.

A block particular to this realization of the FOC applied to HSM is the *Reference Generation FOC*. Since the goal is to have a drive that can be replaced by the current standard stepping drives, it is desired to keep the interface of the latter ones. Therefore, the reference generation block provides the θ_m^{ref} from the steps and direction received and depends on the stepping mode selected (full-step, half-step, ...).

Sampling frequency

The different new blocks meant to be implemented in the DSP are discretized first with the Bilinear transform. The current controllers are implemented as described in section 4.2.2. For the speed controller, the speed loop bandwidth was intended to be 375 Hz as we saw in the section 9.2.3. In [28, page 452] a rule of thumb is given to decide the sampling frequency of the digital controller, as:

$$f_{cont} > 20f_{closedloopBW} \quad (9.6)$$

This yields a sampling rate of at least 7.5 kHz. For simplicity in the implementation the position loop is executed in the same timed interrupt as the speed controller.

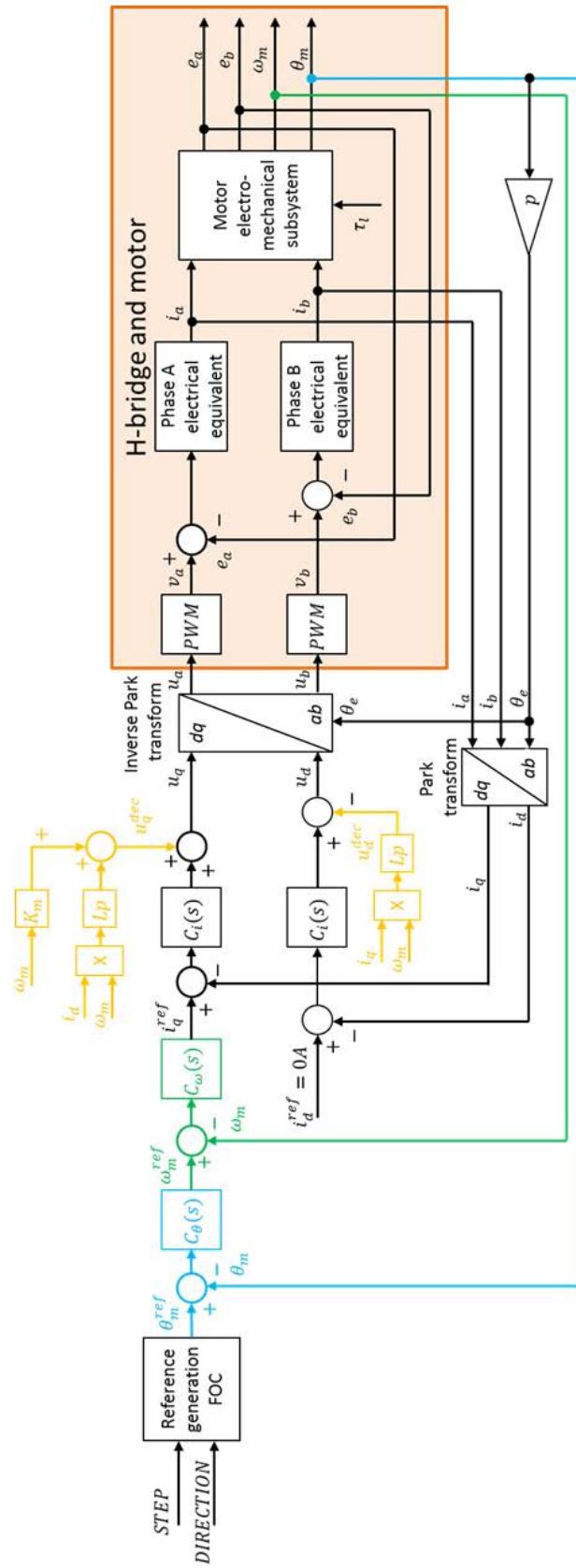


Figure 9.6: FOC blocks scheme

9.2.6 Performance achieved

The control scheme is implemented and tested with a real LHC collimator motor. The stepping profile from Fig. 8.1 is applied and the result is shown in Fig. 9.7. The reduction in overshoot and settling time compared to open loop is clear.

A comparison of the performance between both control methods is done with a test repeating a step in full-step mode 10 times and measuring the position of the motor, shown in Fig. 9.8 for the standard stepping mode and Fig. 9.9 for FOC.

FOC represents clearly better results with improvements in the settling time from 6.76 ms to 1.40 ms, in the overshoot from 81.96% to 2.72% and in the standard deviation of the steady state positioning error from 0.088 degrees to 0.015 degrees, on average.

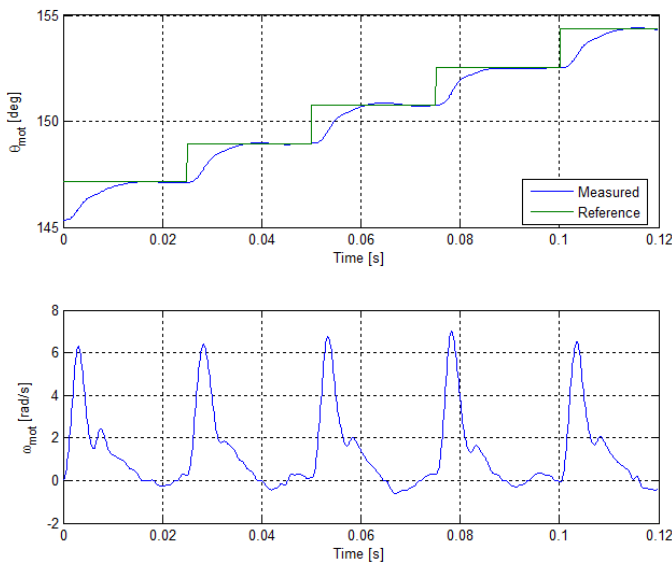


Figure 9.7: Full-step mode rotor position and speed acquisition, using closed-loop position control

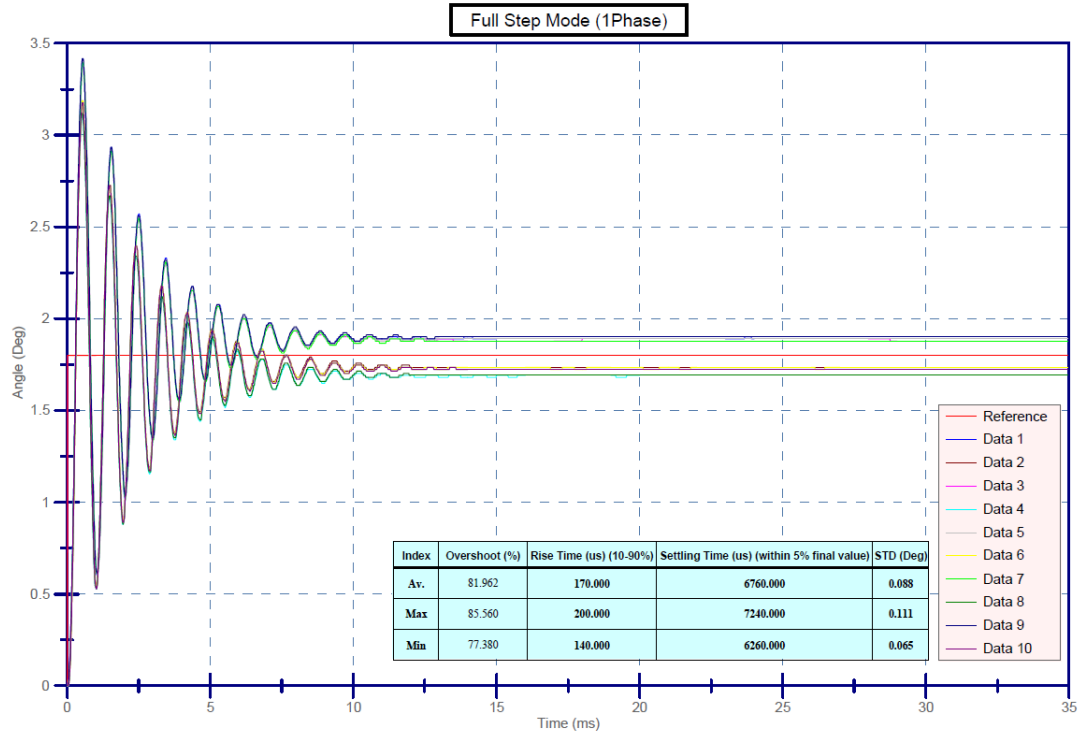


Figure 9.8: Full-step mode step test in standard stepping mode. 10 repetitions are done

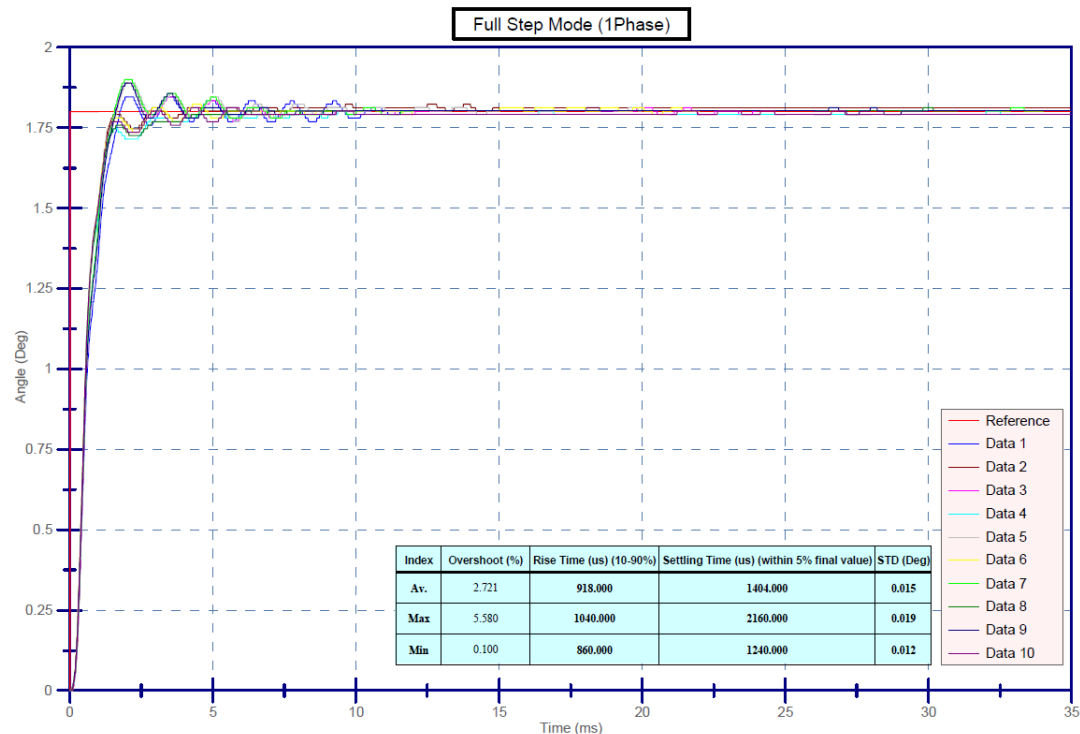


Figure 9.9: Full-step mode step test in FOC mode. 10 repetitions are done

9.3 Practical issues

Some issues particular to the application are worth mentioning since they have proved to be fundamental to be properly addressed.

9.3.1 θ_0 calibration method

The position sensors used in the collimators are mainly resolvers. The developed DSP Drive has an encoder input and therefore a resolver-to-encoder converter is necessary to use the sensor information in the loop.

The zero of the sensor, whether it is the resolver or the encoders used in the laboratory, and the electrical zeros of the rotor are not aligned, forming an angle that we will call θ_0 . It is necessary to know this angle in order to apply properly the Park transform, which is used in all the controllers in the scheme.

A procedure to perform the θ_0 measurement, which is possible even when we measure with the motor coupled to a system, has been developed, with the goal of avoiding abrupt mechanical shocks to the coupled systems.

A diagram of this procedure is shown in Fig. 9.10. On each cycle, we perform steps in standard open loop, at low current depending on the application to avoid brusque movements, until the step corresponding to $\theta_e = 0$ is reached. This position is the one with $i_a = I$ and $i_b = 0$, since with these currents applied, τ_{em} is zero only if $\theta_e = 0$, and it only deviates if a load torque is applied to the shaft. This load torque is in fact compensated by τ_{em} since θ_e is different from zero. To minimize this difference, the next step in the procedure is to increase the current to the maximum allowed. Since this increment of current and, in consequence, τ_{em} , is done once the final position is achieved, no mechanical step is applied, and only θ_e made as close to 0 as it can be achieved in open loop.

After a small time to let any transient extinguish, the angle is measured and the cycle repeated, until the 50 electrical turns have been measured, stepping in both directions. Once it is done, θ_0 is obtained by averaging the measured angles, converted to electrical turns.

9.3.2 Velocity estimation

Velocity estimation using an encoder is not a straightforward problem when the speed is low or zero [68]. The intuitive solution to get speed from position is to

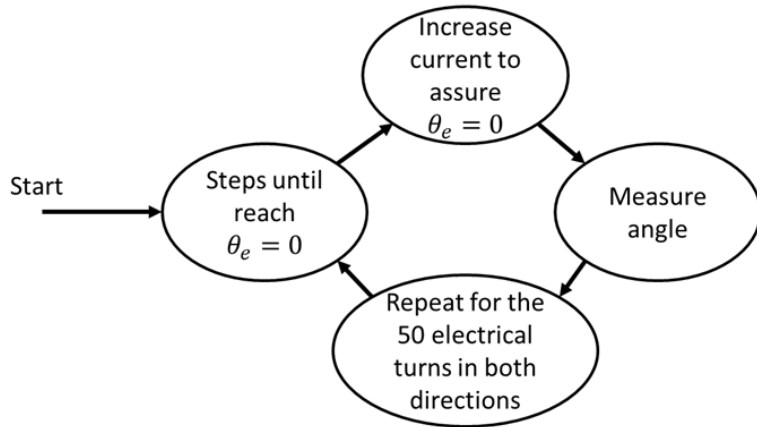


Figure 9.10: Stages of θ_0 calibration

use the amount increased in the encoder counter to get the speed dividing it by the sampling time used between readings of the encoder counter.

The sampling rate is set to 7.5 kHz as seen in section 9.2.5. At this frequency, the resolution of the velocity estimation is [84]:

$$\omega_{res} = \frac{2\pi}{P_{PR}T_{sampling}} [\text{rad/s}] \quad (9.7)$$

where P_{PR} is the number of pulses per revolution of the encoder. For a 8192 pulse encoder, 32768 after $\times 4$ decoding, the resolution with the sampling rate calculated would be 1.3696 rad/s, which is rather high when the nominal speed of the motor is 1 turn per second, 6.2832 rad/s.

A common method used for velocity estimation with quadrature encoders is to measure the time between encoder pulses. The resolution is then a function of the resolution of the clock used to measure this time. In the case of the DSP used, the clock is 150 MHz. With this method the speed estimated is:

$$\omega_{est} = \frac{\alpha}{mT_{clk}} [\text{rad/s}] \quad (9.8)$$

where α is the angle between encoder pulses, m the time counter counting every clock cycle and T_{clk} the clock period. In this case the resolution is non linear since we are inverting the number of cycles counted, but for some values lower than the resolution achieved with the previous method, we easily get resolutions below the mrad/s range.

A mix of both methods is used, using speed estimation measuring the increase

in the encoder counter at fixed time periods when the speed is higher than a set threshold and using the speed estimation measuring the time between encoder pulses when the speed is lower.

9.4 Closed to open position loop switch

In order to use the advantages of closed-loop position control whilst keeping the system operative in case of sensor failure, a procedure to automatically switch from closed to open loop position control in such a case is proposed. An application with stepper motors using a switch between closed and open loop is described in the patents [24, 86]. They propose to open the position loop when the motor is near its reference position and therefore it should be stopped, and to close it during motion. In none of them a methodology to keep the motor moving without perturbing the trajectory asked to the drive from the upper control layer is discussed, and in fact some details regarding the specifics of the switch implementation are omitted. More importantly, they rely on the position sensor for the operation. The main goal of the proposed switch is to give the drive not only the ability to continue operating when the sensor fails, but also allows it to continue its motion following the same position reference.

When the switch is triggered, the stages in Fig. 9.11 are followed. First, the system is working in closed-loop position control, relying on the position sensor to close the loop. If a sensor problem is detected, the switch is triggered and the drive looks for the position in standard stepping open-loop control that is nearest to the current position reference in FOC mode.

An example of the search stage is plot in Fig. 9.12. This is an example working in full-step mode, which allows the plot to be clearer. With higher resolution stepping modes, the figure would be much more populated by the different possible positions of the motor. A magnified section of the full circumference, which represents the whole mechanical turn, is displayed showing one of the 50

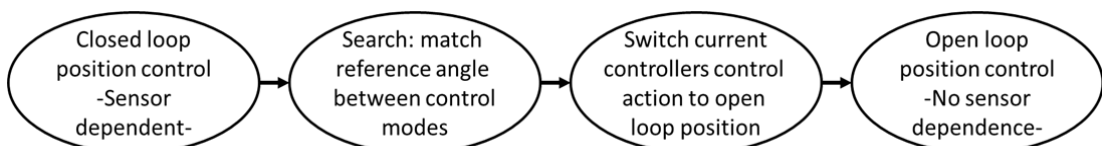


Figure 9.11: Switch closed to open loop position stages

electric turns in the HSM used. The electrical turn, corresponding to 7.2 degrees, is divided in full-step mode into 4 steps, represented in the figure by green arrows and numbered. The positions in the electrical turn are repeated continuously, 50 times along the whole mechanical turn. At the moment that the search stage is run, the FOC was following the reference θ_m^{ref} , represented by a orange arrow in the figure. The algorithm looks for the nearest angle corresponding to a step in the stepping mode selected, and the current references are set accordingly. Once this is done, the switch of control strategy to apply to the motors, shown in 9.13, can be made to begin operating in standard stepping mode (open-loop position control).

In this way, when the system actually switches to open loop control, the motor moves by a maximum angle equal to half the step size. Finally, the drive continues operating in open loop as a standard stepper motor drive.

The Fig. 9.13 shows the scheme of the switch implementation. The switch can be in either position 1, driving the motor in standard stepping mode, with the position control in open-loop, or in position 2, using FOC. The voltage applied to the motor phases depends on the working mode selected, and the transition between modes follows the procedure described above.

In Fig. 9.14 the result of using the switch during the motor operation is shown, and in Fig. 9.15 a zoom of the transition can be found. The motor position continues its way without perceptible difference, aside of the inherent behaviour difference between closed and open loop position control.

The reversed situation, switching from open to closed loop position, is also possible and in fact it has been implemented for completeness, although it has no direct practical application. In this case, the main issue to pay attention to is the transfer from open to closed loop of the controller, which has to implement a bumpless transfer. This is a known problem in PID control [65] and has to be addressed to avoid the integrator in the PI controller from accumulating error when the loop is not closed and therefore the control action calculated by the controller is not being applied. In Fig. 9.16 the motion of the motor is shown with the drive switching back and forth between closed and open loop modes. The mode in a specific instant can be inferred from the magnitude of the instantaneous speed, having clearly bigger oscillations in open loop. In Fig. 9.17 a zoom of the transition from open to closed loop is shown.

The phase currents during the switch from closed to open-loop can be seen in

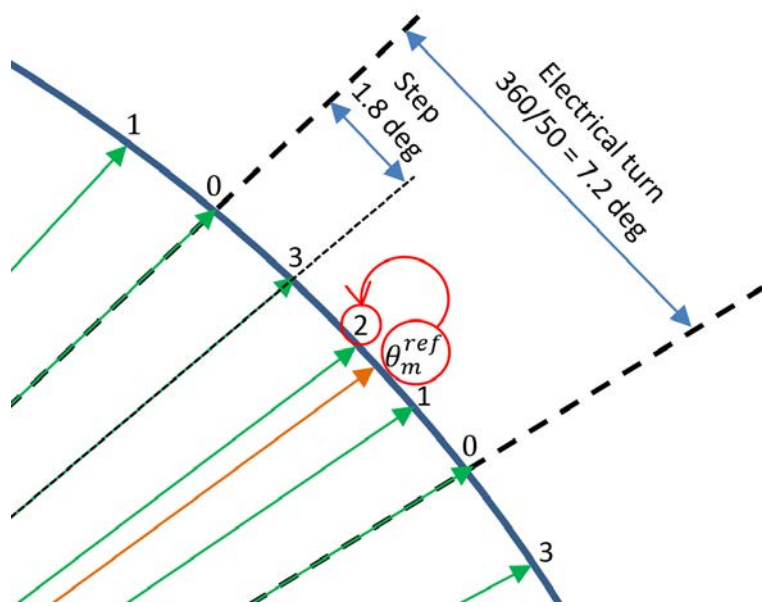


Figure 9.12: Switch closed to open loop position search stage

Fig. 9.18. In this figure the reference for the i_d current was zero and therefore the only current applied during closed-loop operation is the needed to rotate the motor with no load attached to the shaft, which is very low compared to the nominal values used in open loop. In order to have a clearer view of the current before the switch to open loop, the reference for i_d is set to 0.5 Amps and the result is shown in Fig. 9.19. The currents during a switch transition from open to closed-loop are shown in Fig. 9.20.

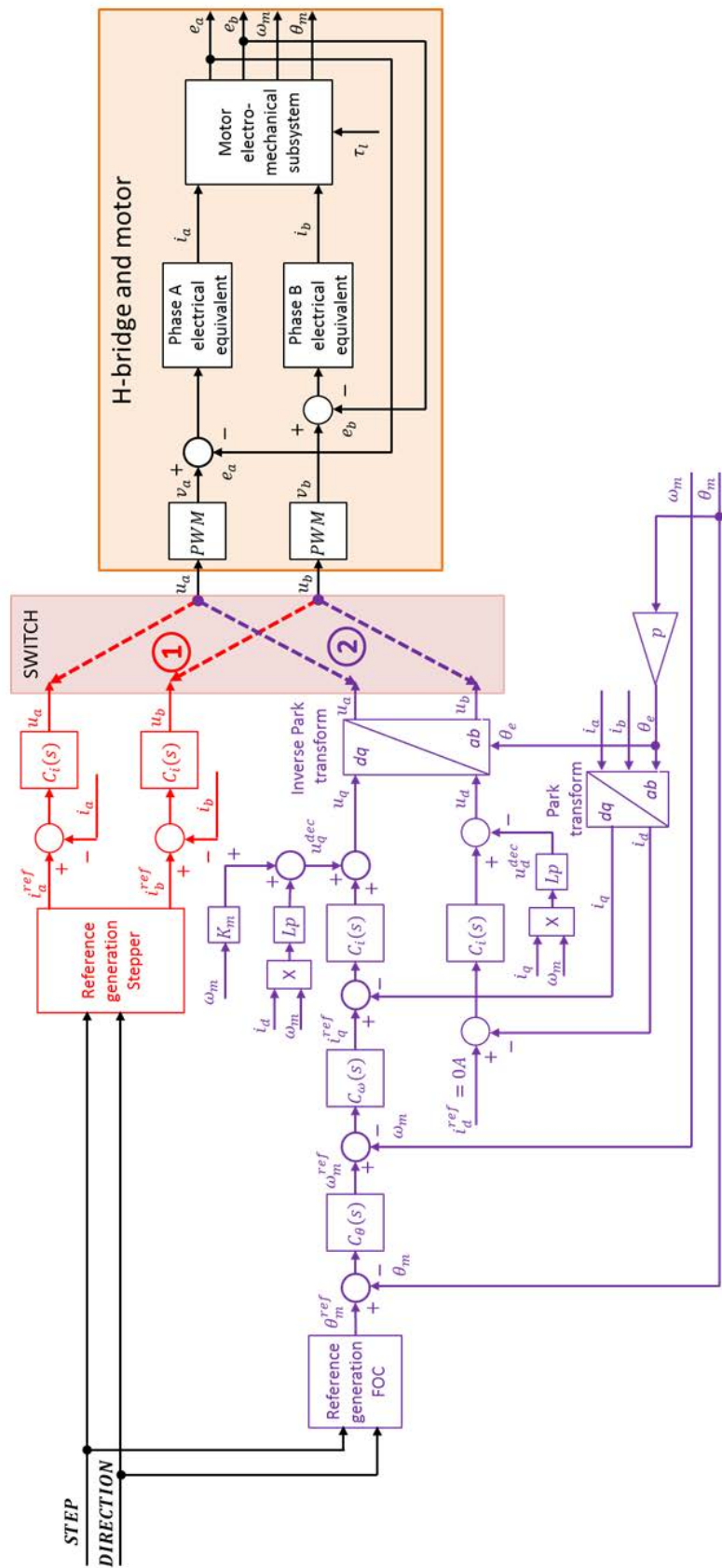


Figure 9.13: Switch closed to open loop position scheme

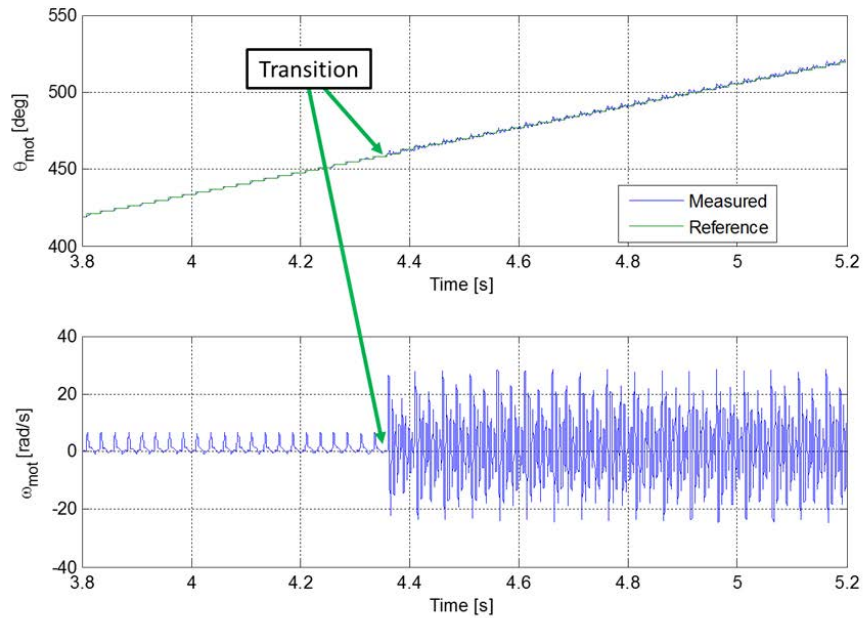


Figure 9.14: Switch from closed to open loop position control in operation

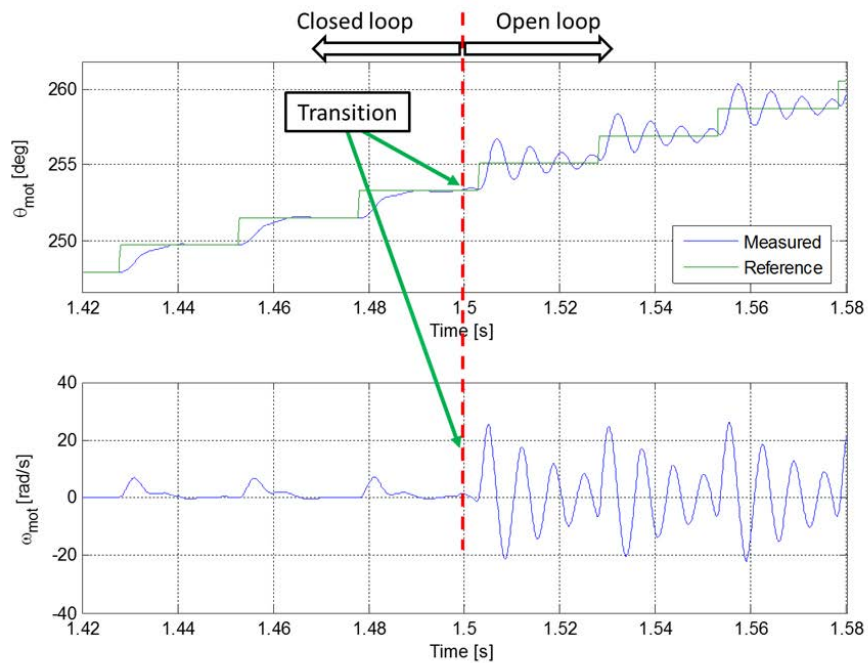


Figure 9.15: Zoom of the switch from closed to open loop position control in operation

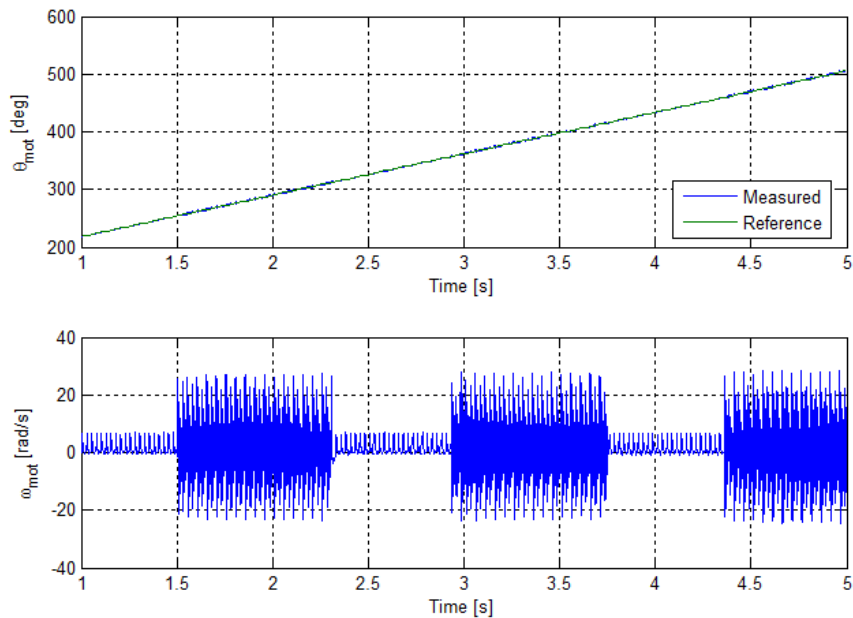


Figure 9.16: Switch from open to closed loop position control in operation

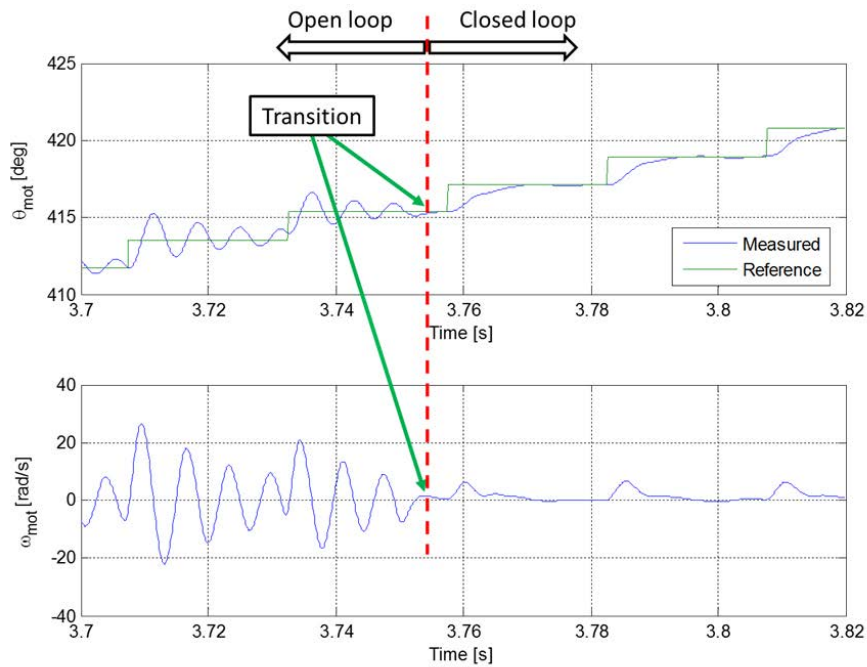


Figure 9.17: Zoom of the switch from open to closed loop position control in operation



Figure 9.18: Phase currents during a switch transition form closed to open loop, $i_d^{ref} = 0A$. The vertical scale is 1A/division

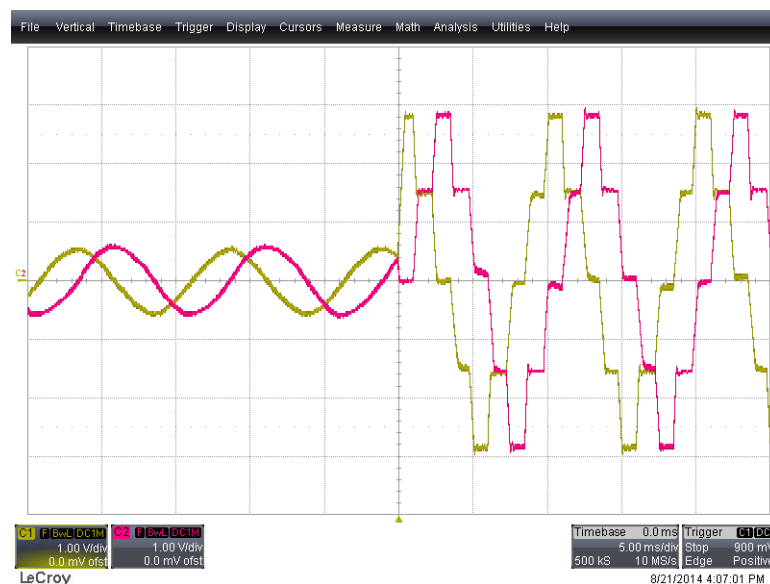


Figure 9.19: Phase currents during a switch transition form closed to open loop, $i_d^{ref} = 0.5A$. The vertical scale is 1A/division



Figure 9.20: Phase currents during a switch transition from open to closed loop, $i_d^{ref} = 0.5A$. The vertical scale is 1A/division

9.5 Use of FOC and the switch in the LHC Collimators

The first place where the new control approach was tested was in the LHC collimators. As explained in section 3.3 and again in this part, the mechanics in the LHC collimators can wear due to the strong vibrations induced by the motor running in standard stepping mode. It is probable that such wear may force the replacement of collimators before it was foreseen, with high costs. It is desirable to extend the lifetime of the collimator mechanics, and therefore the FOC working mode is under test in an LHC collimator linear stage like the one shown in Fig. 9.21.

In the collimator mechanism, the motor moves a worm screw that moves a block held by a spring linearly. As the block is moved away from the initial position, the force applied by the spring increases. For small movements, this spring can be seen as an external load disturbance. The FOC position controller should reject this disturbance and keep the steady-state position error near to zero. Instead, the standard stepping mode relies on the constant application of a torque higher than the maximum external torque, but even if the electromagnetic torque is high, the positioning error increases proportionally to the linear position, due to the spring nature.

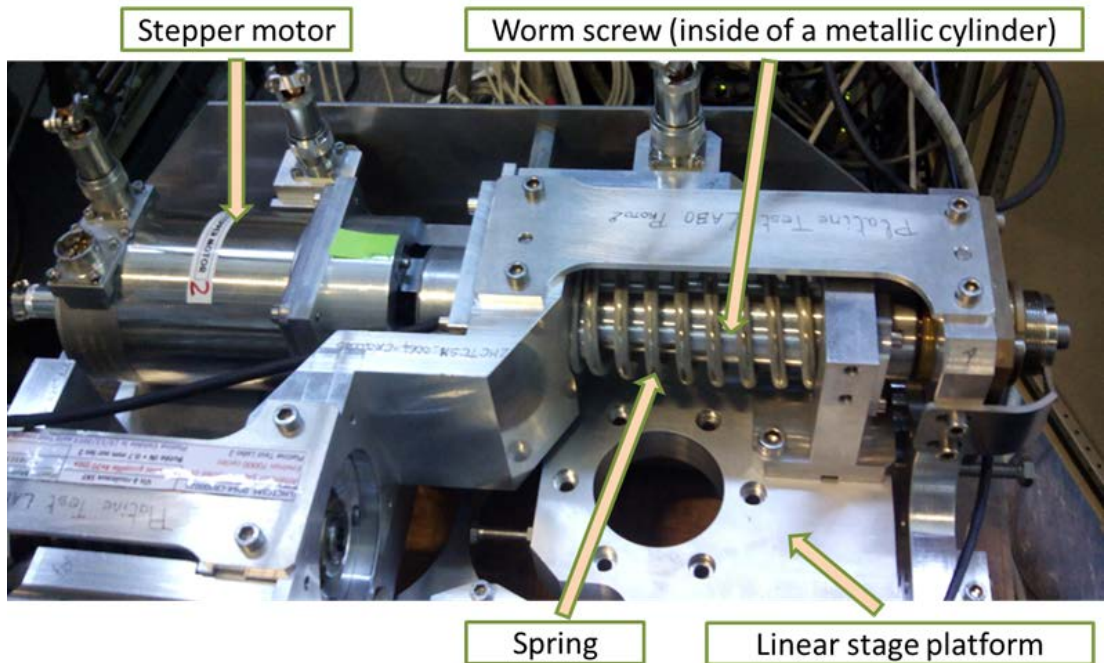


Figure 9.21: LHC collimator linear stage

The motor is stepped in the initial resting position of the collimator linear stage, with the spring relaxed and therefore exerting a minimum force. The position and speed of the motor are captured and shown in Figs. 9.22 and 9.23, for the drive working in standard stepping mode and in FOC mode respectively.

Then the motor is stepped in the extreme position of the collimator linear stage, with the spring supporting the maximum foreseen compression and therefore exerting the maximum force expected from it. The position and speed of the motor in this case are shown in Figs. 9.24 and 9.25, for the drive working in standard stepping mode and in FOC mode respectively.

The motion profile is clearly smoother using FOC. At the moment, a long-term test where the motor moves the block from one extreme to the other and back continuously is being run on the LHC collimator linear stage to assess if this smoother movement yields a lower wearing of the mechanics, as expected.

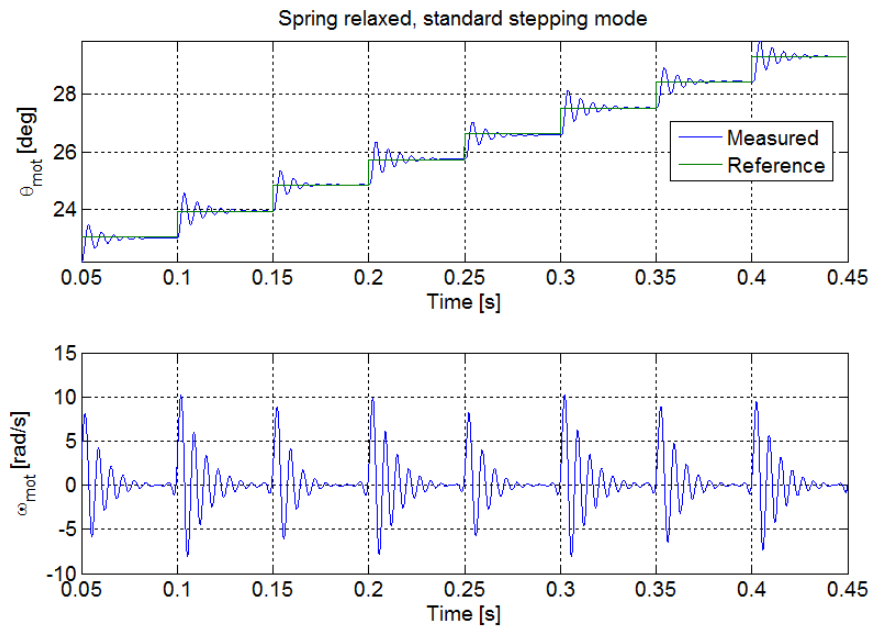


Figure 9.22: Motor position in the collimator linear stage working in open-loop, spring relaxed

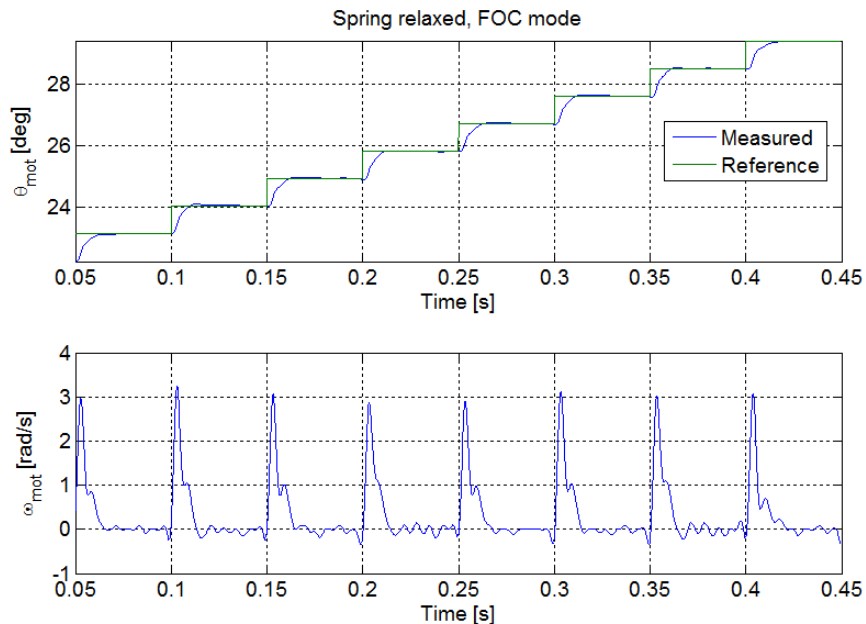


Figure 9.23: Motor position in the collimator linear stage using FOC, spring relaxed

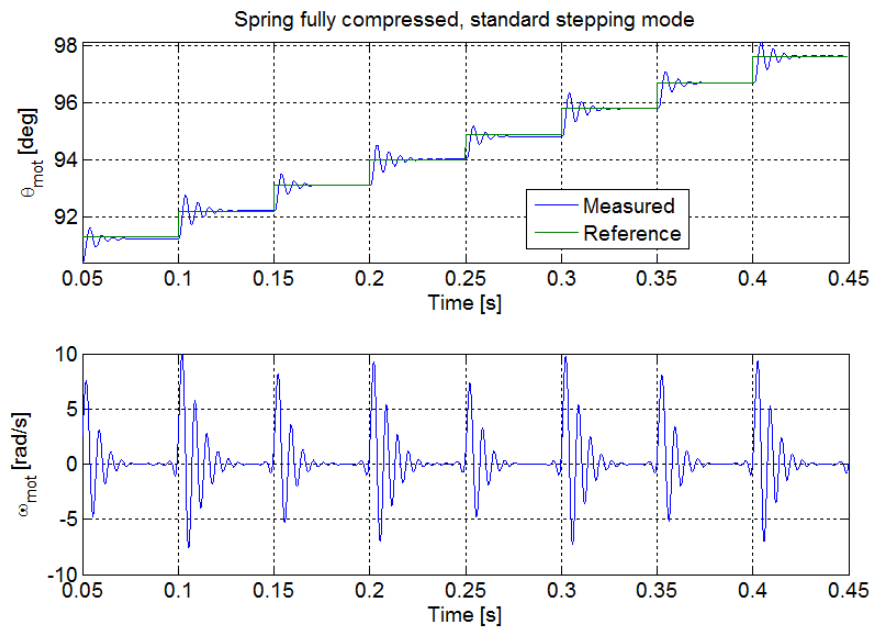


Figure 9.24: Motor position in the collimator linear stage working in open-loop, spring at the maximum compression

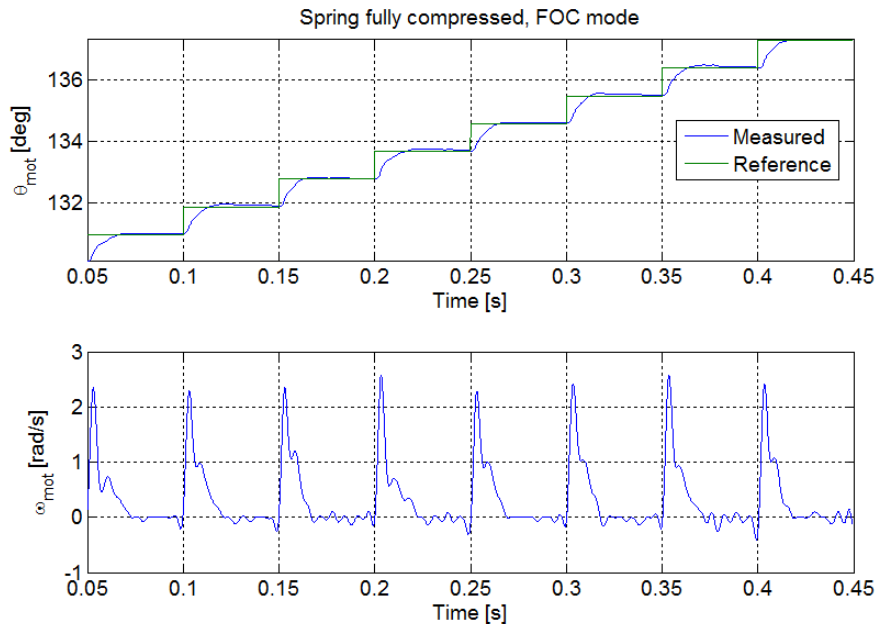


Figure 9.25: Motor position in the collimator linear stage using FOC, spring at the maximum compression

9.6 Conclusions

In this chapter the implementation and tuning of the Field Oriented Control applied to stepper motors has been described. A method to switch between closed-loop position control (FOC) and open-loop position control (standard stepping mode) has been proposed and validated constituting an original contribution of this work. With this switching system, the drive can be used by the upper control layers sending the commands to the drive without them noticing the position control type used by the drive. The motion profile is equally followed by the motor, with the only difference of a smoothed motion and reduced error thanks to the closed-loop control.

Using FOC has proved to be significantly smoother, representing a much less aggressive option of motor control for the mechanics. This is very attractive for the applications at CERN, were extending the lifespan of the mechanical systems represents an improvement in terms of material costs and maintenance work. In fact, it has proven to be an improvement for the positioning systems in some other applications in addition to the LHC collimators, as presented in appendix B. This fact combined with the proposed switched closed to open loop position control, which allows the high reliability of the system to be maintained, constitutes an attractive alternative to the standard stepping control.

Part IV

Output filters

Chapter 10

Introduction to Output filters

10.1 Introduction

In chapter 4 a solution to the problem of working with long cables and switched drives was explained. This is a solution based on a digital, cable length dependent estimation filter, thanks to which a standard switched inverter can work properly when long cables are used to connect drive and motor. This method allows good motor phase current control to be achieved.

However, the 3 effects described in chapter 3: drive-side large amplitude ringing phenomena in the current, (Fig. 3.2), Common-Mode currents in the phase (Fig. 3.4) and, at the motor-side of the cable, high voltage oscillations across the motor terminals (Fig. 3.5), are still present.

A different solution from that presented in chapter 4, based on passive filtering of the power signals, is presented in this chapter. This solution mitigates the 3 effects described above, reducing the EMI, enlarging the lifespan of the motor, and allowing off-the-shelf motor drives to work properly in the presence of long cables.

This solution, which is relatively well known in industry for induction and synchronous motors, is the use of output filters, also known as LC filters. The design presented and the use of output filters for stepper motors are an original contribution of this thesis.

10.2 State of the art for output filters

Output filters constitute a simple and robust solution for PWM drives feeding electric motors through long cables. They have been broadly studied for their application to induction and synchronous motors and are fairly standard in industry.

In [32] a broad view of the use of output filters in adjustable speed drives is given, from the origin and modelling of the high frequency phenomena, to the known mitigation techniques, proposing a new filter which has the common terminal of the common-mode capacitors clamped to the dc-link rails by means of diodes, limiting the voltage at this point to that of the dc-link and reducing the motor terminal voltage overshoot. In [25], the mechanism producing voltage oscillations, which can be up to twice the dc link voltage in the inverter is further explained. It also gives summary of the most common output filter options with their advantages -reducing high voltages and their high derivatives at the motor terminals- and disadvantages -cost, space and reduced inverter efficiency.

Some different design constraints and rules which are referred to for the design of the filter proposed in the next chapter are given in [83], where use of output filters for a medium voltage application is presented; [82], where a new stage in the filter, an LC trap intended to block the PWM frequency, is proposed; and [91], where the details of the low pass filtering needed from the output filter to avoid motor terminal overvoltage due to voltage reflections is studied.

The application of output filters to stepper motor has not been explored and only one application note, [89], which proposes an LC filter for a stepper motor, was found by the author. In this application note, the proposed LC filter is intended to work without a long cable, and therefore the design procedure is not sufficient to design a complete output filter for stepper motors as shall be presented here.

A solution to reduce the over voltages when over modulation occurs, and thus to reduce the ringing, is presented in [37], by acting on the way the PWM is applied in the transition into and out of the over modulation. Other solution based on passive filters is presented in [60] specially suitable when high voltages or their derivatives are an issue for the motor insulation.

10.3 Output filters

As introduced in chapter 3, when a long cable is used to connect a motor with a drive, the latter being a switched inverter applying a PWM voltage, it behaves as a transmission line. The mechanism producing these effects was explained there. Output filters, a common solution in industry for AC motors working with long cables, are summarized in the following section.

Output filters are placed at the output of the drive, between it and the cable, as shown in Fig. 10.1.

They typically consist of 2 stages, one meant to deal with the Differential Mode voltage and the other with the Common Mode voltage, as shown in Fig. 10.2 (the order of the stages is not necessarily as shown though it is the most common). The purpose of both stages of the output filter is to block or reduce the higher frequencies of the voltage applied to the cable and therefore reduce the adverse effects caused by this combination as described in chapter 3.

For each stage there are many possible topologies [32]. Fig. 10.3 shows a broadly used output filter, which is the starting point for the proposed filter in the next chapter. It consists of an RLC low-pass filter for the DM stage, whereas for the CM stage a toroidal choke is used.

These filters are characterized by their resonant frequency f_0 , given by:

$$f_0 = \sqrt{\frac{1}{2\pi L_{DM}C_{DM}}} \quad (10.1)$$

Output filters are classified in two main types depending on where the resonant frequency of the filter is set. When f_0 is above the PWM switching frequency, f_{PWM} , the filter limits the du/dt applied to the cable, but the motor-side voltage is still similar to the voltage drive-side. In this case they are called *du/dt filters*,

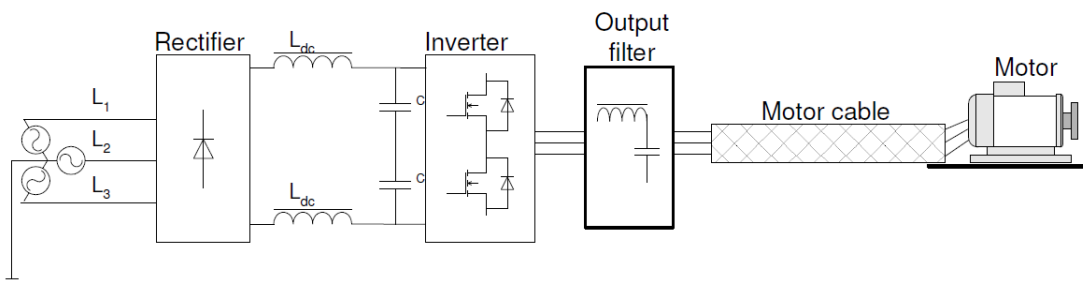


Figure 10.1: Typical motor-cable-drive system using an output filter.

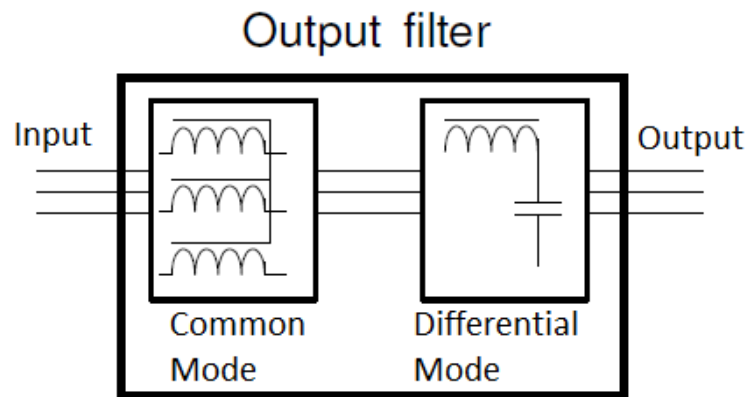


Figure 10.2: Output filter stages.

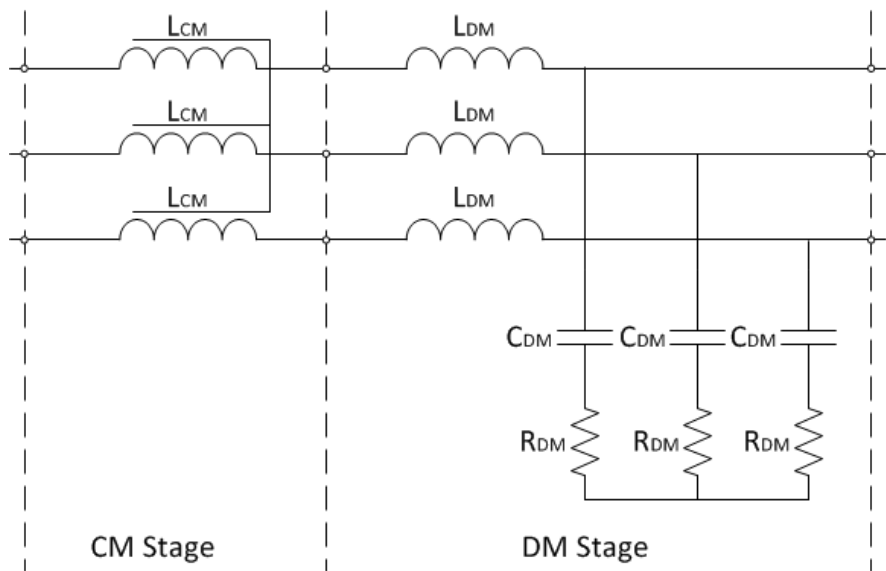


Figure 10.3: Typical two stage induction motor output filter.

since they limit the du/dt values of the voltage applied to the motor.

When f_0 is below f_{PWM} , they are called *sine-wave filters*. The name comes from the fact that the voltage across the motor terminal is closer to a sinusoid in this case. Usually f_0 is set at least 3 times lower than f_{PWM} to achieve a proper sinusoidal motor-side voltage.

For this application the resonant frequency of the filter is set well below the PWM frequency in order to achieve a strong attenuation of the voltage applied at this frequency. Therefore, the designed filter is of the sine-wave type.

Chapter 11

Sine Wave Filters For Stepper Motors

11.1 Proposal

In this chapter, a procedure for the design of output filters is illustrated via a real application. The main particularity of this application compared to that of induction and synchronous motors, in addition to the different electrical configuration, is that in stepper motors the current profile is made of steps as opposed to a sinusoidal waveform, requiring a relatively high bandwidth compared to the PWM frequency, making the design more challenging.

An adapted version of the filter from Fig.10.3 for a single stepper motor phase is proposed as shown in Fig.11.1. As in the original filter, it consists of two stages, a Common-Mode filter and a Differential-Mode filter. In the following both filter stages are designed by adapting guidelines given in the literature for induction motors.

11.2 Sine wave filter design

11.2.1 The application

For the design, the hybrid stepper motor and cable described in section 2.3 is used. The drive used is an SHS Star 2000 as described in section 4.2. The equivalent closed loop bandwidth of 1 kHz is used as reference value for the design with the addition of intensive simulation to validate the good behaviour of the filter.

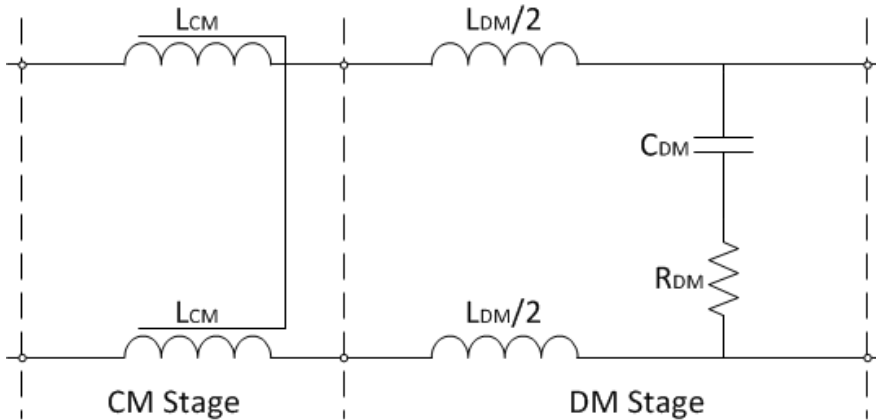


Figure 11.1: Output filter adapted to a single stepper motor phase

The nominal angular speed of the motor is 1 mechanical turn of the shaft per second, with a maximum peak of 10 turns per second. This corresponds to 50 and 500 electrical turns per second respectively.

11.2.2 Differential Mode Filter

The electrical circuit for a differential mode filter of a stepper motor phase is shown in Fig.11.1. It is a low pass voltage filter whose transfer function is the following:

$$G_v(s) = \frac{V_{out}(s)}{V_{in}(s)} = \frac{R_{DM}C_{DM}s + 1}{L_{DM}C_{DM}s^2 + R_{DM}C_{DM}s + 1} \quad (11.1)$$

where L_{DM} , C_{DM} and R_{DM} are respectively the differential mode filter inductance, capacitance and resistance.

The resonant frequency of the filter is given by the expression (10.1) and the characteristic impedance is

$$R_{0f} = \sqrt{\frac{L_{DM}}{C_{DM}}} \quad (11.2)$$

To choose the f_0 of the filter there are several guidelines. In [83] and [32] it is proposed to take f_0 10 times higher than the fundamental frequency of the voltage applied. In induction motors this frequency is usually 50/60 Hz for fixed speed drives. As mentioned in section 11.2.1, the maximum electrical frequency expected is 500 electrical turns per second, corresponding to a fundamental applied voltage of 500 Hz. Following the cited rule, the DM filter should have a resonant frequency of at least 5000 Hz in order to avoid excitation of the resonance of the filter and attenuation of significant frequency components at frequencies higher

than the fundamental due to the stepper current waveform.

A trade-off, nonetheless, exists since, in order to reduce the response to the PWM main frequency, the filter should provide sufficient attenuation at that frequency. The upper limit for f_0 is therefore set to 1/3 of f_{PWM} , to give an attenuation of 18 dB at this frequency (see [32]).

In summary, the bounds for the filter frequency are set to:

$$\begin{aligned} f_0 &> 10f_{out} = 5 \text{ kHz} \\ f_0 &< \frac{1}{3}f_{PWM} = 6.66 \text{ kHz} \end{aligned} \quad (11.3)$$

A second constraint is found in the resistance of the filter. In [91] it is proposed to set the resistance of the filter, R_{DM} , equal to the characteristic impedance of the cable, Z_0 :

$$R_{DM} = Z_0 = \sqrt{\frac{l}{c}} \quad (11.4)$$

Since at high frequencies the capacitor C_{DM} represents a short circuit and the inductor L_{DM} an open circuit, by setting the filter resistance to this value, the source reflection coefficient, given by:

$$\Gamma_s = \frac{R_s - Z_0}{R_s + Z_0},$$

is 0, as the resistor absorbs the reflected energy.

Given these 2 constraints, there is only one more required to fix the value of the 3 filter components. It is set in such a way that the transfer function of the filter is critically damped (see [82]) to a value of:

$$R_{DM} = \sqrt{\frac{4L_{DM}}{C_{DM}}} \quad (11.5)$$

With these 3 constraints, the combinations of R_{DM} , L_{DM} and C_{DM} corresponding to the extreme values allowed for f_0 are found from equations (11.1) for the 3dB attenuation at the cutoff frequency, (11.4) and (11.5).

These values are tested in simulation. With this filter the drive is capable of working with a 720 meter cable, as shown in Fig.11.2. In the upper plot the motor side current is shown, in the centre the motor side voltage and in the lower plot the power dissipated in the filter resistor. In Fig.11.3 a zoomed version of the simulation results is shown. An important step is achieved, since the drive is

working as desired while without the filter the currents were far from the reference values, as shown in Fig.3.3.

However, after extensive simulation, the power consumption in the filter resistor following these constraints was found to be rather high compared to similar performances achieved with lower power consumption. If the constraint (11.4) on the filter resistance, R_{DM} , is relaxed and values in its proximity are tested, it is found via simulation that better results in terms of power consumption can be achieved.

The criteria (11.4) is therefore replaced by minimising the power consumption in the filter resistance. Just with these constraints, the optimum is found by using an arbitrarily large inductance value and the corresponding capacitance value to fulfil the filter cutoff frequency constraint. Therefore, one more constraint, avoiding excessively big values of inductance, is used and the obtained values, shown in Table 11.1, are found to yield good results.

In Fig.11.4 the results obtained in simulation are shown and compared with the best of the previous 2 sets of filter values obtained with the original (11.3)-(11.5) constraints set.

With this filter, the power consumption is greatly reduced. This feature allows the filter to be implemented in a more compact space since the heat dissipation is less demanding.

The steady-state error observed in figures 11.2, 11.3 and 11.4 is due to the current control scheme used by the SHS Drive. This control, described in section 4.2, uses the drive-side current to close the current loop in its comparator, with the ringing superimposed (Fig. 3.2), and therefore there is a steady-state error in the motor-side current corresponding to the amplitude of the superimposed current ringing. In Fig. 11.5 it can be observed how the drive-side current peaks reach values very near the reference, the fixed values 0, 2 and $2\sqrt{2}$ Amps, whilst the motor-side current remains somewhat below this value.

Table 11.1: Filter component values.

Component	Value
R_{DM}	440 [Ω]
L_{DM}	5.0 [mH]
C_{DM}	0.12 [μF]
f_0	6.5 [kHz]
R_{0f}	204.12 [Ω]

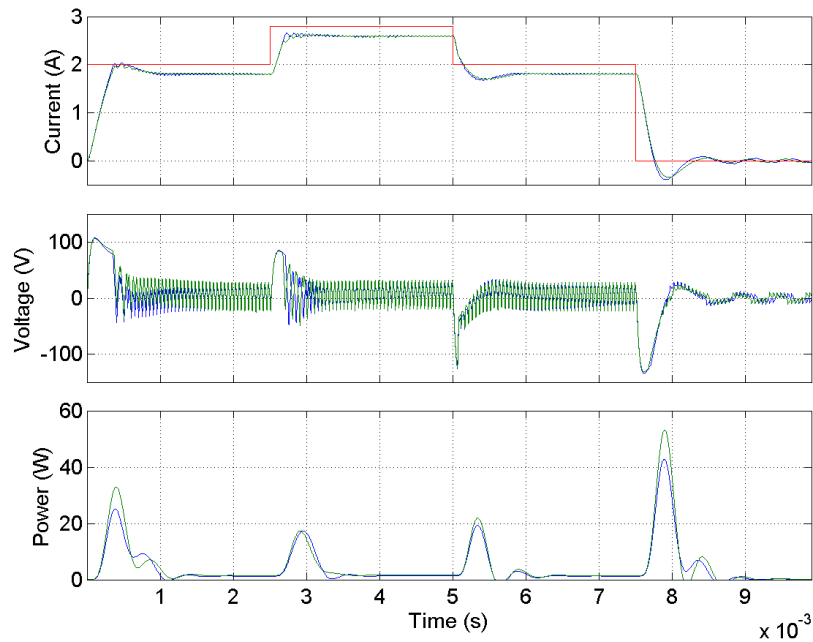


Figure 11.2: Simulation results for $R_{DM} = Z_0$, motor side. In blue the results for $f_0 = 5\text{kHz}$, in green for $f_0 = 6.67\text{kHz}$, and in red the current reference.

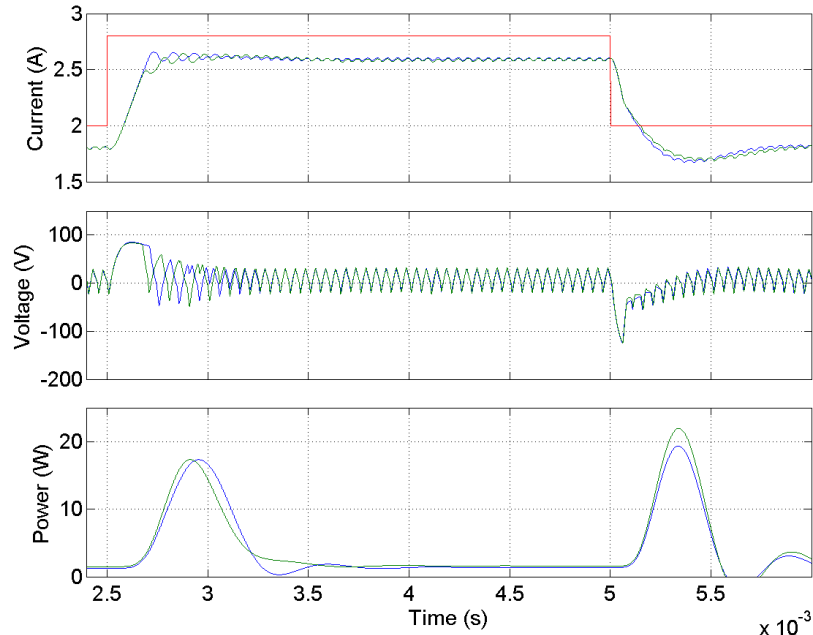


Figure 11.3: Zoom for the simulation results for $R_{DM} = Z_0$, motor side. In blue the results for $f_0 = 5\text{kHz}$, in green for $f_0 = 6.67\text{kHz}$, and in red the current reference.

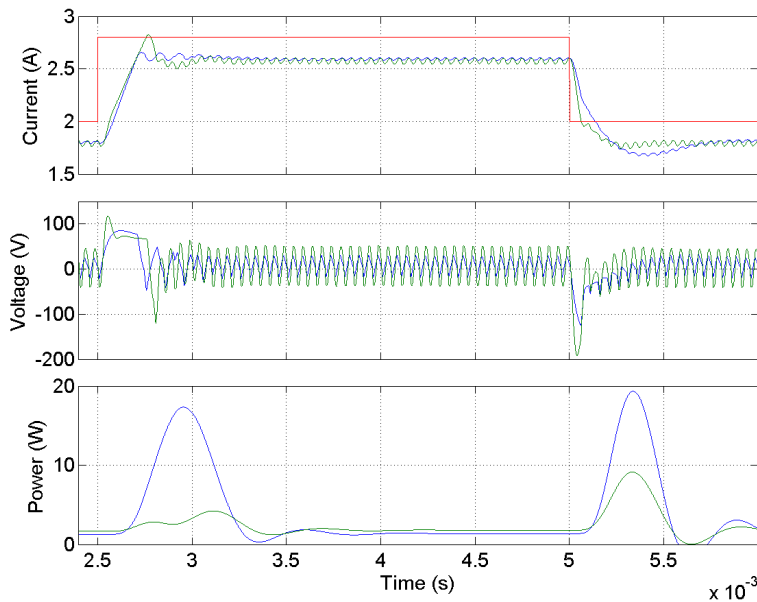


Figure 11.4: Simulation results, motor side - Comparison of the proposed filter values and those for $R_{0f} = Z_0$. Upper: motor side currents, centre: motor side voltages, lower: power dissipated in the resistor of the filters. Blue: results for $R_{0f} = Z_0$, green: for the proposed filter, red: current reference.

11.2.3 Common Mode Filter

Reducing the CM currents has a great importance for this kind of application, for 2 main reasons.

The first reason is to reduce the disturbance to the current controller, where the current spikes may trigger the comparators used to sense the current level.

As for the higher frequencies for the DM currents, long cables show low impedance for the CM currents for higher frequencies, due to the capacitive effect between wires and between wires and the shielding. At the frequency of the PWM and its harmonics, the CM impedance of the cable is low enough to present important spikes in the CM current as shown in Fig. 3.4.

The second reason is the reduction of the EMI emissions. As can be found in EMC literature, see e.g. [64], common mode currents have a great potential to produce radiated emissions, even a few microamperes of CM current can cause the same emissions as 1000 to 10000 times that current in DM.

Toroidal chokes are a well known solution for CM currents (see [32, 61, 64]). Their use is close to ideal given their low effect on the DM circuit. In Fig. 11.1 the CM filter is shown. For the DM circuit it has ideally no effect, since the flux

generated by the current in the DM current flowing to the motor is cancelled by that generated by the current flowing back from the motor. Instead, with respect to the CM circuit it represents twice the inductance since the CM current is equal in both wires and generates flux in the same direction. The flux generated adds up therefore and is double for a specific CM current.

The CM inductance is in series with the rest of the CM circuit. The goal is to reduce the CM current resulting from the PWM voltage and its harmonics. We focus therefore on the impedance of the CM inductance at this frequency. The magnitude of the impedance is given by:

$$|Z_{CM}| = |L_{CM}j\omega| \quad (11.6)$$

To get a high attenuation from the first harmonic of the PWM frequency, of at least between 1/1000 to 1/10000, the required inductance should be between 8 and 80 mH.

11.3 Experimental validation

An output filter prototype with the component values detailed in Table 11.1 and a 20 mH toroidal choke was built and tested with the drive and the motor described in sections 4.2 and 2.3 respectively. The results of its performance are detailed in the following.

11.3.1 Effect of the filter on the motor currents

In Fig.11.5, the currents for a phase are shown, and in Fig.11.6 a zoom is presented. It can be appreciated how the peak-to-peak amplitude of the oscillations of the drive side current, now approximately 0.5 A, has been greatly reduced with respect to Fig.3.2, where they reached an amplitude of over 3.5 A.

Furthermore, in the case with the filter, the frequency of the ripple is that of the PWM, and the oscillation at the 3rd harmonic of the PWM frequency is not appreciable anymore, as it was before.

11.3.2 Effect of the filter on the motor voltages

The voltages achieved at the terminals of the motor are shown in Fig.11.7. The overvoltages have been reduced and the peaks now only exceed the power supply

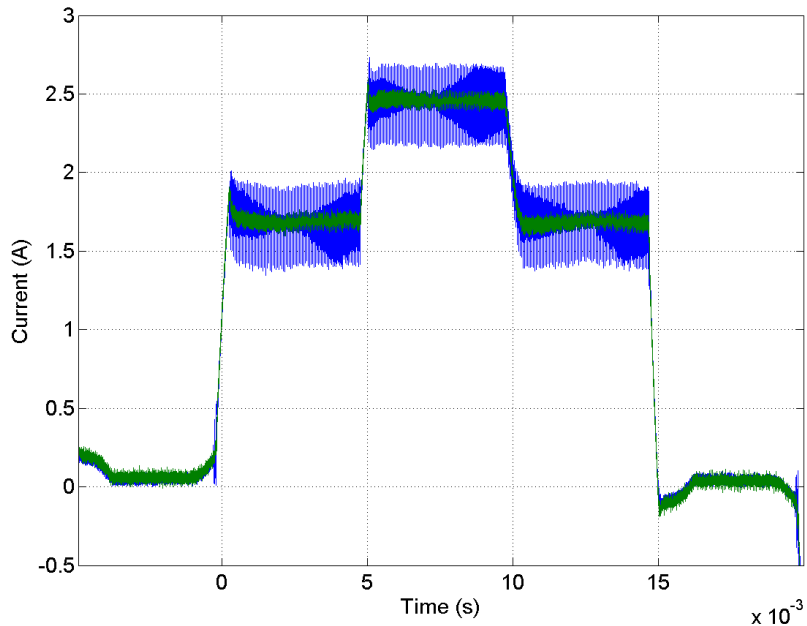


Figure 11.5: Current in a motor phase with the output filter and a 720 meter cable. Blue: drive side current, green: motor side current.

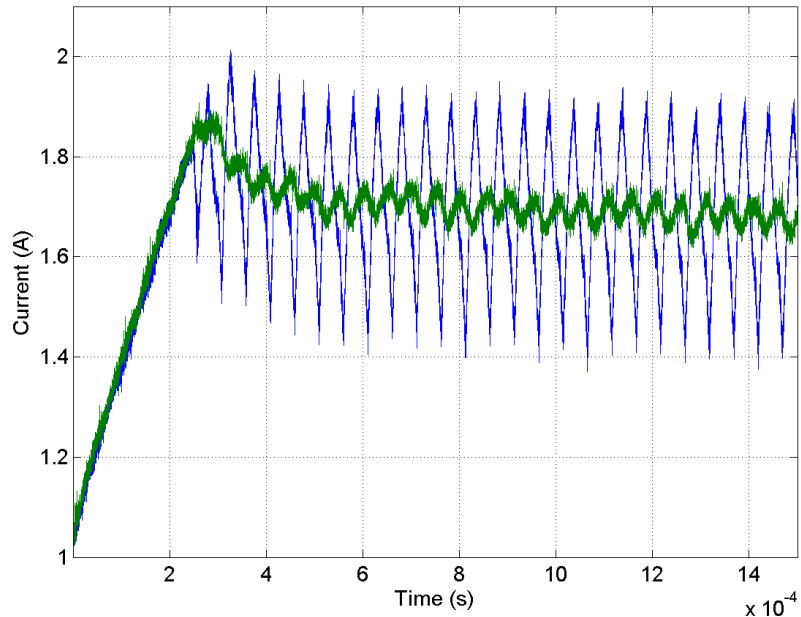


Figure 11.6: Closer view of the currents a motor phase with the output filter and a 720 meter cable. Blue: drive side current, green: motor side current.

voltage, $135V$, when there is a step in the current signals, and it is immediately reduced below this value. The amplitude in the steady state regions is significantly reduced compared to that found without a filter, as in Fig. 3.5. In Fig. 11.8 both voltages are compared and the difference is easily appreciable.

11.3.3 Effect of the filter on the positioning

The repeatability is measured as the standard deviation of the angular steady state positioning error after each step, σ , normalised by the target angle step, θ_{angle} . The target step angle when working with half-step stepping mode, as is done during the tests, is 0.9 degrees. 1600 steps are performed on each test.

The positioning repeatability results are shown in Fig.11.9 for the drive with neither a long cable nor the output filter, since as seen previously the drive does not work properly with a long cable and without a filter, and in Fig.11.10 for the drive working with both the output filter and a 720 meter cable. In Table 11.2 the numerical results are summarised.

The improvement introduced by the use of the output filter can be appreciated from the positioning repeatability, yielding better results than even without a long cable.

11.3.4 EMI

A comparative measurement is performed to assess the EMI emissions. A section of the cable shielding is stripped off and a spiral antenna is situated over it. This antenna complies with the standard *IEC 60478-5 Type A*, and the measurement is done over a conducting plane complying with the aforementioned standard.

The results of the emitted field are shown in Fig.11.11. The emissions are measured for the drive with a short cable and no output filter and for the drive with a 720 meter cable and the output filter.

There is a significant reduction of the emissions of approximately 40 dB over the entire frequency range studied.

Table 11.2: Repeatability test results.

	$\sigma [deg]$	$\sigma / \theta_{target} [\%]$
Short cable - No output filter	0.0583	6.5
720 m cable - Output filter	0.0538	6.0

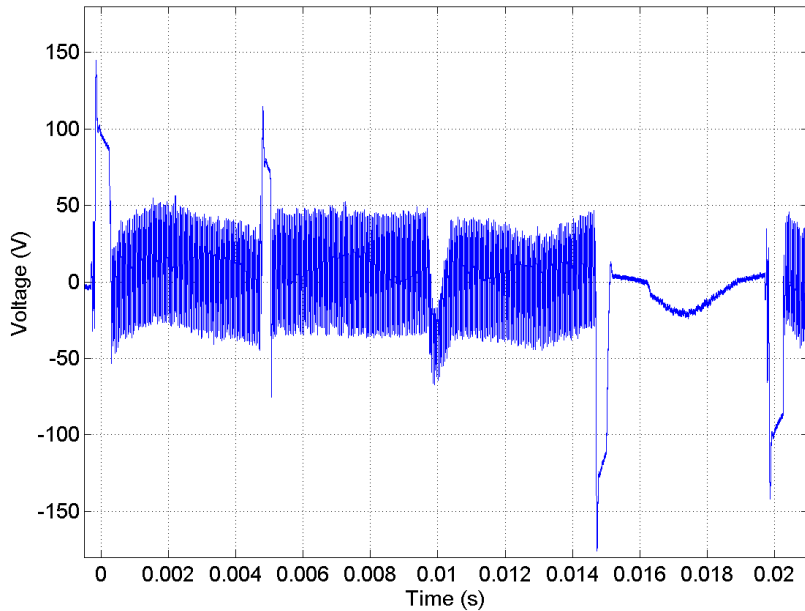


Figure 11.7: Motor side voltage with the output filter and a 720 meter cable.

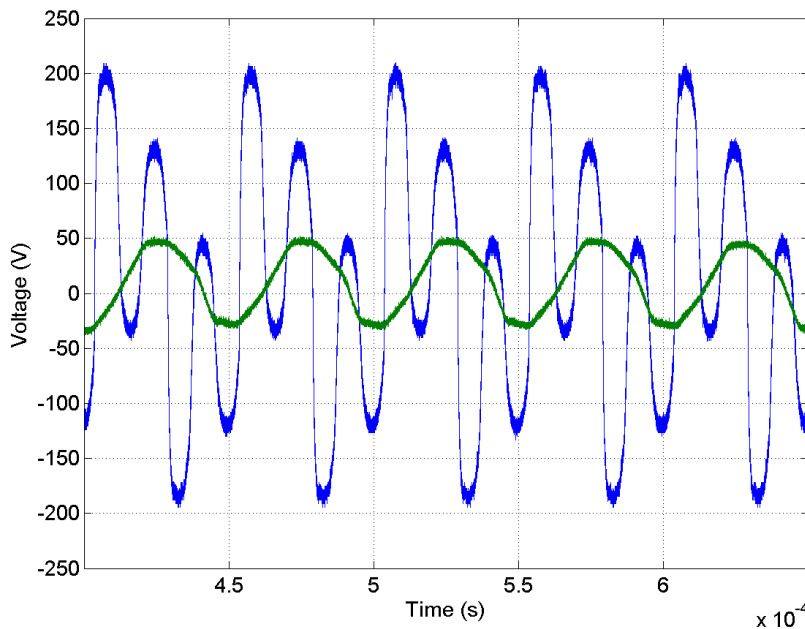


Figure 11.8: Motor side voltage with 720 meter cable. Blue: without filter, green: with filter.

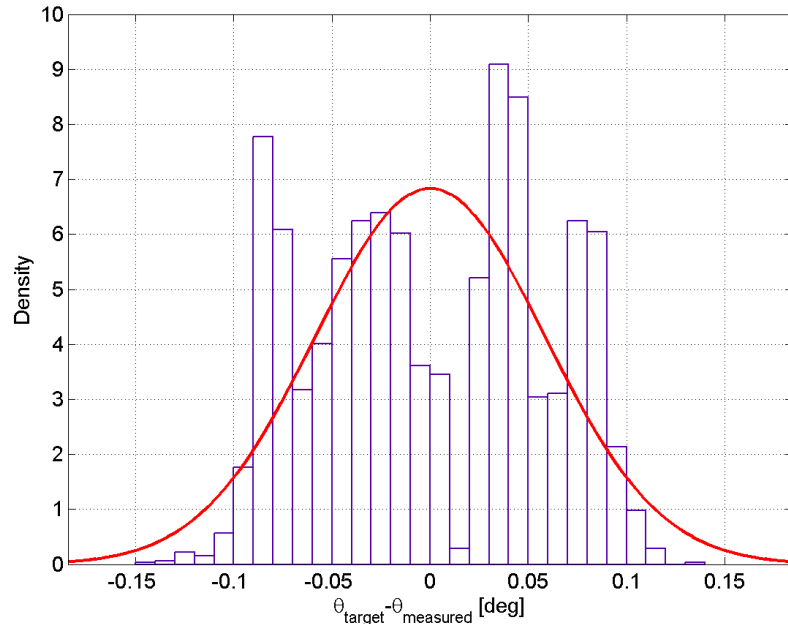


Figure 11.9: Repeatability results showing steady state position error histogram for the SHS Star 2000 drive with a short cable and without the output filter.

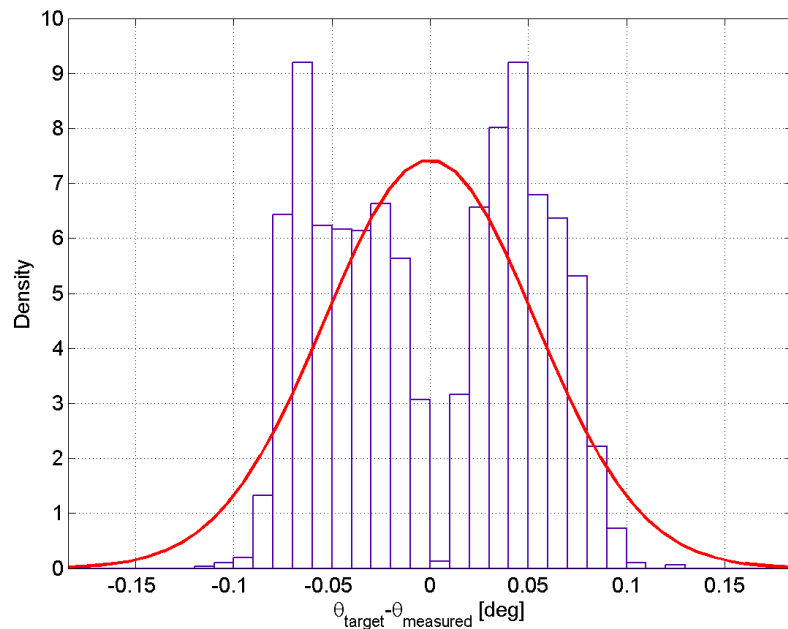


Figure 11.10: Repeatability results showing steady state position error histogram for the SHS Star 2000 drive with a 720 meter cable and with the proposed output filter.

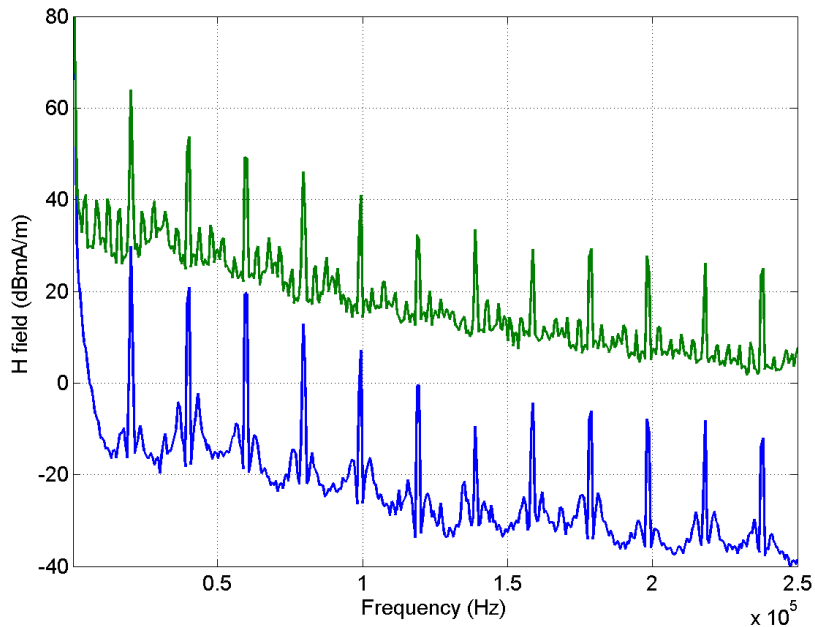


Figure 11.11: Low frequency spectrum of the EMI emissions for the SHS drive. In green: without output filter and with a short cable, in blue: 720 meter cable and output filter

11.4 Conclusion

An output filter for stepper motor drives has been designed and built. By using it, both the DM and the CM contributions to the ringing in the drive side current have been attenuated, allowing a standard commercial drive to work correctly with a long cable. This is not possible without the filter.

The motor side voltage has been greatly reduced, and thus the motor insulation stress by the high voltage and its derivative, which occurs without the filter, is in turn greatly reduced. The positioning repeatability has been improved even compared to the case of the drive working with neither a long cable nor the output filter. Finally, the EMI emissions have been significantly decreased.

In conclusion the output filter has been demonstrated to be a very effective and efficient solution for stepper motor drives. By using it, the issues associated with the use of long cables and chopping drives have been significantly reduced with a simple solution. The price for this improvement is the introduction of a few passive components and the power losses associated with them.

Part V

Conclusions

Chapter 12

Conclusions

In this thesis, the modelling and control of hybrid stepper motors in high radiation areas has been explored in detail. The problematic involved has been analysed, particular attention has been paid to the effects of using switched converters when long cables are present, and the difficulties of the limited possibility to use position sensors.

The first observable effect from the drive point of view, the ringing due to the transmission line characteristic of the long cable in the drive current, impeded the normal use of most off-the-shelf drives. The use of estimators has been previously proposed to obtain the motor currents and closing the current loop on these estimations.

From this point the problem arising from the difficulty to use position sensors in the harsh environment present in particle accelerators and the need to detect possible steps lost and mechanical degradation of the collimators led to the proposal to use sensorless methods for the motor mechanical states. **The first contribution of this thesis is to use the Extended Kalman Filter to estimate the Hybrid Stepper Motor position, speed and external torque, with a long cable connecting motor and drive.** It has been proposed, tested in simulation and validated experimentally on a real LHC collimator.

It has been demonstrated that a trade-off between model complexity and computational cost must be made to achieve a feasible real-time application. In this case it implied limiting the model of the system to be used in the Extended Kalman Filter to the motor without cable, and dealing with the high bandwidth cable dynamics by using a different faster estimation for the parts not included in the model used in the Kalman filter, i.e. the cable. Using this estimation scheme,

it has been demonstrated that the position, speed and load torque estimation are sufficiently good to allow the degradation of the collimator mechanics to be monitored and lost steps to be detected.

It was observed though that some mismatch between the expected signals and the observed ones existed when high phase currents were applied. This mismatch has been attributed to the saturation of the magnetic components constituting the magnetic circuit in the motor, specially, as was found in literature, in narrow parts of the magnetic flux path like the teeth both in stator and rotor. This fact limits the usability of the proposed method to either use it under a limited current level, or to include the current level effect in the model, if this were possible in a real-time estimation application. This lead to **the second contribution of the thesis, the proposal of new extensions of the standard electrical model of hybrid stepper motors, which could be used in control and estimation real-time applications.**

The electrical motor model has been extended by including position and current dependent inductance and permanent magnet flux linkage terms. It has been shown that the new model offers a better fit with real data acquired from a running hybrid stepper motor. Finally this model has been implemented in an EKF running in a DSP based drive, demonstrating the feasibility for real-time applications and the improvement in the mechanical states estimation, under a broader range of conditions, i.e. for large current amplitudes.

In addition to the consideration of the possibilities of sensorless estimation, closed-loop position control has been studied and applied to the LHC collimator motors. The controller structure to apply Field Oriented Control has been presented as well as the tuning and resolution of practical problems. The improvement with closed loop has been shown; obtaining a smoother motion profile compared to standard open loop. The overshoot and settling time of the position on each step are significantly reduced.

The third contribution of this thesis is the proposal of a switch between closed and open loop position control, which, combined with the developed Field Oriented Control scheme, allows the use of position sensors without reducing the reliability of the system. This switch is capable of performing a bumpless transfer between control modes. Moreover, the angular reference generation has allowed a stepper motor drive to be developed that with the advantages of the closed loop described, can be directly swapped

with the current stepper drives since the interfaces between the drive and the other systems are respected.

Using closed-loop position control represents a less aggressive option for the mechanics, thereby extending their lifespan. Furthermore, it has been shown that closed loop control can be a direct improvement in several applications at CERN not only for the LHC collimators, but also for 2 different types of goniometer used for the crystal collimation project.

In the context of the control of hybrid stepper motors in high radiation areas, a different approach to deal with the problematic created by the use of switched drives with long cables has been investigated. Output filters are a solution used mainly for AC motors in different applications of industry. However, the use of this type of filter with stepper motors has not been reported at the time of this work.

An output filter, specifically a Sine Wave Filter, for stepper motor drives has been designed and built, being the fourth and last contribution of the thesis. Using this filter reduces the differential and common modes of the voltage applied to the cable from the drive side, resulting in the attenuation of the aforementioned drive-side current ringing and the motor-side overvoltage. This allows commercial off-the-shelf drives to work properly without further modification with long cable, as it is the case in the LHC collimators, whilst enlarging the lifetime of the motor insulation.

In addition, experimental testing has proved that open-loop positioning repeatability of a commercial drive with a long cable and the sine wave filter has improved compared to the same drive with only a short cable. Testing has also shown that EMI emissions has been greatly reduced compared to the case without sine wave filter.

12.1 Future work

Several paths are promising to explore from the thesis results:

- Steady state Kalman filter for non-linear application. In this case, due to the big difference in bandwidths between the fast electrical dynamics and the slow mechanical ones, which are the ones containing the non-linearity, using the steady state Kalman filtering could be studied to release the processor from the heavier filter operations. This would allow for more

complex control techniques to be applied without the need to increase the computation power of the processor.

- Future extensions of the work done could be to use the position and speed estimations for closed-loop control.
- In line with the previous point, an application of the Kalman filter which could use the encoder or resolver information at a different and even at a variable rate would be interesting, in order to use the information already available in some collimator systems, where the resolvers are read at 400 Hz, and work using this extra information or continue to work with no position information in the case of a sensor failure.
- If the sensorless control is finally used to close the position loop, the switch presented in chapter 9 could be triggered when the quality of the estimation, i.e. the innovation covariance matrix, goes over a certain threshold.
- The sine wave filter has obvious applications and extending the study to look for different optimizations would be very interesting. A clear useful goal would be to achieve a physically small filter that could be easily integrated in the current installations with minimum installation complexity. For this, a good trade-off between common and differential modes attenuation, chopping frequency to use and power dissipation should be found.

12.2 Publications

The achieved results have been published in different journal and conference publications, listed below.

JCR journal publications:

- A. Masi, M. Butcher, M. Martino, and R. Picatoste. An application of the extended kalman filter for a sensorless stepper motor drive working with long cables. *IEEE Transactions on Industrial Electronics*, 59(11):4217–4225, nov. 2012. ISSN 0278-0046. doi: 10.1109/TIE.2011.2178213
- A. Masi, M. Butcher, R. Losito, and R. Picatoste. Dsp based smart sensorless stepping motor driver for lhc collimators. *Nuclear Science, IEEE Transactions on*, 60(5):3514–3520, Oct 2013. ISSN 0018-9499. doi: 10.1109/TNS.2013.2267055

- M. Butcher, A. Masi, R. Picatoste, and A. Giustiniani. Hybrid stepper motor electrical model extensions for use in intelligent drives. *Industrial Electronics, IEEE Transactions on*, 61(2):917–929, Feb 2014. ISSN 0278-0046. doi: 10.1109/TIE.2013.2254097

Conference publications:

- M. Martino, A. Masi, R. Losito, and R. Picatoste Ruilope. Low emission, self-tunable dsp based stepping motor drive for use with arbitrarily long cables. In *Conference record of the 12th LSS symposium*, 2010
- A. Masi, M. Butcher, R. Losito, and R. Picatoste. Dsp based smart sensorless stepping motor driver for lhc collimators. In *Real Time Conference (RT), 2012 18th IEEE-NPSS*, pages 1–7, June 2012. doi: 10.1109/RTC.2012.6418215
- R. Picatoste, M. Butcher, and A. Masi. Sine wave filter for stepper motor drives working with long cables. In *Electrical Machines (ICEM), 2012 XXth International Conference on*, pages 1075–1081, Sept 2012. doi: 10.1109/ICELMach.2012.6350009

Part VI

Appendices

Appendix A

Analytical formulas for the extended electrical model

The aim of this Appendix is to provide the reader with the analytical expressions of the symbolic ones introduced in Section 7.6, considering the position and current dependent model. It is worth noticing that for the other proposed models, the same reasoning could be followed.

In Eqs. 7.32-7.33, the analytical expression of Num_A , Den_A , Num_B , Den_B , are:

$$\begin{aligned}\text{Num}_A = & p(a_\Psi e^{-b_\Psi x_1^2} + c_\Psi) \sin(px_4 + \phi_\Psi)x_3 \\ & + 2p(a_{L_2} e^{-b_{L_2} x_1^2} + c_{L_2}) \sin(2px_4 + \phi_{L_2})x_3x_1 - Rx_1\end{aligned}$$

$$\begin{aligned}\text{Den}_A = & (a_{L_2} e^{-b_{L_2} x_1^2} + c_{L_2}) \cos(2px_4 + \phi_{L_2}) + (a_{L_0} e^{-b_{L_0} x_1^2} + c_{L_0}) \\ & - 2(a_{L_0} b_{L_0} e^{-b_{L_0} x_1^2})x_1^2 - 2(a_{L_2} b_{L_2} e^{-b_{L_2} x_1^2})x_1^2 \cos(2px_4 + \phi_{L_2}) \\ & - 2(a_\Psi b_\Psi e^{-b_\Psi x_1^2})x_1 \cos(px_4 + \phi_\Psi)\end{aligned}$$

$$\begin{aligned}\text{Num}_B = & -p(a_\Psi e^{-b_\Psi x_2^2} + c_\Psi) \cos(px_4 + \phi_\Psi)x_3 \\ & - 2p(a_{L_2} e^{-b_{L_2} x_2^2} + c_{L_2}) \sin(2px_4 + \phi_{L_2})x_3x_2 - Rx_2\end{aligned}$$

$$\begin{aligned} \text{Den}_B = & - (a_{L_2} e^{-b_{L_2} x_2^2} + c_{L_2}) \cos(2px_4 + \phi_{L_2}) + (a_{L_0} e^{-b_{L_0} x_2^2} + c_{L_0}) \\ & - 2(a_{L_0} b_{L_0} e^{-b_{L_0} x_2^2}) x_2^2 + 2(a_{L_2} b_{L_2} e^{-b_{L_2} x_2^2}) x_2^2 \cos(2px_4 + \phi_{L_2}) \\ & - 2(a_\Psi b_\Psi e^{-b_\Psi x_2^2}) x_2 \sin(px_4 + \phi_\Psi). \end{aligned}$$

The Jacobian matrix for the EKF in Eq. 5.2 is:

$$\mathbf{A} = \begin{bmatrix} a_{11} & 0 & T_s \frac{\dot{\text{Num}}_{Ax3}}{\text{Den}_A} & a_{14} & 0 \\ 0 & a_{22} & T_s \frac{\dot{\text{Num}}_{Bx3}}{\text{Den}_B} & a_{24} & 0 \\ \frac{T_s \dot{\tau}_{Ax1}}{J} & \frac{T_s \dot{\tau}_{Bx2}}{J} & 1 - \frac{T_s B}{J} & a_{34} & -\frac{T_s}{J} \\ 0 & 0 & T_s & 1 & 0 \\ 0 & 0 & 0 & 0 & 1 \end{bmatrix}, \quad (\text{A.1})$$

where:

$$\begin{aligned} a_{11} &= 1 + \frac{T_s \dot{\text{Num}}_{Ax1}}{\text{Den}_A} - \frac{T_s (\text{Num}_A + u_1) \dot{\text{Den}}_{Ax1}}{\text{Den}_A^2} \\ a_{14} &= \frac{T_s \dot{\text{Num}}_{Ax4}}{\text{Den}_A} - \frac{T_s (\text{Num}_A + u_1) \dot{\text{Den}}_{Ax4}}{\text{Den}_A^2} \\ a_{22} &= 1 + \frac{T_s \dot{\text{Num}}_{Bx2}}{\text{Den}_B} - \frac{T_s (\text{Num}_B + u_2) \dot{\text{Den}}_{Bx2}}{\text{Den}_B^2} \\ a_{24} &= \frac{T_s \dot{\text{Num}}_{Bx4}}{\text{Den}_B} - \frac{T_s (\text{Num}_B + u_2) \dot{\text{Den}}_{Bx4}}{\text{Den}_B^2} \\ a_{34} &= -\frac{T_s T_{d_m} 2p \cos(2px_4)}{J} + \frac{T_s (\dot{\tau}_{Ax4} + \dot{\tau}_{Bx4})}{J}. \end{aligned} \quad (\text{A.2})$$

In particular, $\dot{\text{Num}}_{Ax1}$, $\dot{\text{Num}}_{Ax3}$, $\dot{\text{Num}}_{Ax4}$ are the derivatives of Num_A , with respect to the state variables in the subscripts. Similar notation for the $\dot{\text{Den}}_A$ derivatives is adopted.

$$\begin{aligned} \dot{\text{Num}}_{Ax1} &= -2px_1 x_3 (a_\Psi b_\Psi e^{-b_\Psi x_1^2}) \sin(px_4 + \phi_\Psi) \\ &\quad + 2px_3 \sin(2px_4 + \phi_{L_2}) (a_{L_2} e^{-b_{L_2} x_1^2} + c_{L_2} - 2x_1^2 a_{L_2} b_{L_2} e^{-b_{L_2} x_1^2}) - R \end{aligned}$$

$$\begin{aligned} \dot{\text{Num}}_{Ax3} &= p(a_\Psi e^{-b_\Psi x_1^2} + c_\Psi) \sin(px_4 + \phi_\Psi) \\ &\quad + 2px_1 (a_{L_2} e^{-b_{L_2} x_1^2} + c_{L_2}) \sin(2px_4 + \phi_{L_2}) \end{aligned}$$

$$\begin{aligned}\dot{\text{Num}}_{\text{A}x4} = & p^2 x_3 (a_\Psi e^{-b_\Psi x_1^2} + c_\Psi) \cos(px_4 + \phi_\Psi) \\ & + (2p)^2 x_1 x_3 (a_{L_2} e^{-b_{L_2} x_1^2} + c_{L_2}) \cos(2px_4 + \phi_{L_2})\end{aligned}$$

$$\begin{aligned}\dot{\text{Den}}_{\text{A}x1} = & -2x_1 (a_{L_2} b_{L_2} e^{-b_{L_2} x_1^2}) \cos(2px_4 + \phi_{L_2}) - 6x_1 (a_{L_0} b_{L_0} e^{-b_{L_0} x_1^2}) \\ & + 4x_1^3 (a_{L_0} b_{L_0}^2 e^{-b_{L_0} x_1^2}) - 4x_1 (a_{L_2} b_{L_2} e^{-b_{L_2} x_1^2}) \cos(2px_4 + \phi_{L_2}) \\ & + 4x_1^3 (a_{L_2} b_{L_2}^2 e^{-b_{L_2} x_1^2}) \cos(2px_4 + \phi_{L_2}) - 2(a_\Psi b_\Psi e^{-b_\Psi x_1^2}) \cos(px_4 + \phi_\Psi) \\ & + 4x_1^2 (a_\Psi b_\Psi^2 e^{-b_\Psi x_1^2}) \cos(px_4 + \phi_\Psi)\end{aligned}$$

$$\begin{aligned}\dot{\text{Den}}_{\text{A}x4} = & -2p (a_{L_2} e^{-b_{L_2} x_1^2} + c_{L_2}) \sin(2px_4 + \phi_{L_2}) \\ & + 4px_1^2 (a_{L_2} b_{L_2} e^{-b_{L_2} x_1^2}) \sin(2px_4 + \phi_{L_2}) \\ & + 2px_1 (a_\Psi b_\Psi e^{-b_\Psi x_1^2}) \sin(px_4 + \phi_\Psi)\end{aligned}$$

Analogously, for the Num_B and Den_B derivatives:

$$\begin{aligned}\dot{\text{Num}}_{\text{B}x2} = & 2px_2 x_3 (a_\Psi b_\Psi e^{-b_\Psi x_2^2}) \cos(px_4 + \phi_\Psi) \\ & - 2px_3 \sin(2px_4 + \phi_{L_2}) \times (a_{L_2} e^{-b_{L_2} x_2^2} + c_{L_2} - 2x_2^2 a_{L_2} b_{L_2} e^{-b_{L_2} x_2^2}) - R\end{aligned}$$

$$\begin{aligned}\dot{\text{Num}}_{\text{B}x3} = & -p (a_\Psi e^{-b_\Psi x_2^2} + c_\Psi) \cos(px_4 + \phi_\Psi) \\ & - 2px_2 (a_{L_2} e^{-b_{L_2} x_2^2} + c_{L_2}) \sin(2px_4 + \phi_{L_2})\end{aligned}$$

$$\begin{aligned}\dot{\text{Num}}_{\text{B}x4} = & p^2 x_3 (a_\Psi e^{-b_\Psi x_2^2} + c_\Psi) \sin(px_4 + \phi_\Phi) \\ & - (2p)^2 x_2 x_3 (a_{L_2} e^{-b_{L_2} x_2^2} + c_{L_2}) \times \cos(2px_4 + \phi_{L_2})\end{aligned}$$

$$\begin{aligned}\dot{\text{Den}}_{\text{B}x2} = & 2x_2 (a_{L_2} b_{L_2} e^{-b_{L_2} x_2^2}) \cos(2px_4 + \phi_{L_2}) - 6x_2 (a_{L_0} b_{L_0} e^{-b_{L_0} x_2^2}) \\ & + 4x_2^3 (a_{L_0} b_{L_0}^2 e^{-b_{L_0} x_2^2}) + 4x_2 (a_{L_2} b_{L_2} e^{-b_{L_2} x_2^2}) \cos(2px_4 + \phi_{L_2}) \\ & - 4x_2^3 (a_{L_2} b_{L_2}^2 e^{-b_{L_2} x_2^2}) \cos(2px_4 + \phi_{L_2}) - 2(a_\Psi b_\Psi e^{-b_\Psi x_2^2}) \sin(px_4 + \phi_\Psi) \\ & + 4x_2^2 (a_\Psi b_\Psi^2 e^{-b_\Psi x_2^2}) \sin(px_4 + \phi_\Psi)\end{aligned}$$

$$\begin{aligned}\dot{\text{Den}_{Bx4}} = & 2p(a_{L_2}e^{-b_{L_2}x_2^2} + c_{L_2}) \sin(2px_4 + \phi_{L_2}) \\ & - 4px_2^2(a_{L_2}b_{L_2}e^{-b_{L_2}x_2^2}) \sin(2px_4 + \phi_{L_2}) \\ & - 2px_2(a_\Psi b_\Psi e^{-b_\Psi x_2^2}) \cos(px_4 + \phi_\Psi).\end{aligned}$$

Moreover, $\dot{\tau}_{A_{x1}}, \dot{\tau}_{A_{x4}}$, are the derivatives of τ_A , with respect to the state variables in the subscripts.

$$\begin{aligned}\dot{\tau}_{A_{x1}} = & - (2p)x_1 \left[c_{L_2} + \frac{a_{L_2}}{e^{b_{L_2}x_1^2}} \right] \sin(2px_4 + \phi_{L_2}) \\ & - (p) \left[c_\Psi + \frac{a_\Psi}{e^{b_\Psi x_1^2}} \right] \sin(px_4 + \phi_\Psi) \\ \dot{\tau}_{A_{x4}} = & - (2p)^2 \left[c_{L_2} \frac{x_1^2}{2} - \frac{a_{L_2}}{2b_{L_2}e^{b_{L_2}x_1^2}} + \frac{a_{L_2}}{2b_{L_2}} \right] \times \cos(2px_4 + \phi_{L_2}) \\ & - (p)^2 \left[c_\Psi x_1 + \frac{a_\Psi \sqrt{\pi} \operatorname{erf}(\sqrt{b_\Psi} x_1)}{2\sqrt{b_\Psi}} \right] \cos(px_4 + \phi_\Psi).\end{aligned}$$

Similar notation for the τ_B derivatives is held:

$$\begin{aligned}\dot{\tau}_{B_{x2}} = & (2p)x_2 \left[c_{L_2} - \frac{a_{L_2}}{e^{b_{L_2}x_2^2}} \right] \sin(2px_4 + \phi_{L_2}) \\ & + (p) \left[c_\Psi + \frac{a_\Psi}{e^{b_\Psi x_2^2}} \right] \cos(px_4 + \phi_\Psi) \\ \dot{\tau}_{B_{x4}} = & (2p)^2 \left[c_{L_2} \frac{x_2^2}{2} - \frac{a_{L_2}}{2b_{L_2}e^{b_{L_2}x_2^2}} + \frac{a_{L_2}}{2b_{L_2}} \right] \times \cos(2px_4 + \phi_{L_2}) \\ & - (p)^2 \left[c_\Psi x_2 + \frac{a_\Psi \sqrt{\pi} \operatorname{erf}(\sqrt{b_\Psi} x_2)}{2\sqrt{b_\Psi}} \right] \times \sin(px_4 + \phi_\Psi).\end{aligned}$$

Appendix B

CERN Field Oriented Control Motor Applications

B.1 CINEL Stepper motor based Goniometer

A different approach for the collimation systems is being researched and tested at CERN. This approach, known as crystal collimation, intends to use bent silicon crystals as primary collimators to direct the beam halo onto a secondary absorber, instead of directly stopping the desired particles. The theoretical details and working principle of this project are outside the scope of this work, but can be found in its original proposal [76] and later publications [75].

The aforementioned crystals have to be positioned next to the beam with an angular accuracy of 1 micro-radian [74]. A prototype of a goniometer was proposed and built in collaboration with the Italian company CINEL with the goal of achieving such a specification.

A schematic view of the working principle is shown in Fig. B.1. The stepper motors M1 and M2 move the platform where the crystal is mounted in order to align it with the beam line. The motor M1 alone displaces a platform connected through a lever arm to the crystal platform. The latter is fixed to the lever arm and rotates with it as indicated in the figure, allowing the crystal to be positioned at the desired angle.

In Figs. B.2 and B.3 a picture of the prototype and the 3D model are shown respectively.

This prototype has been tested intensively with standard stepping drives, and even though the positioning accuracy and resolution were fulfilled, the strong

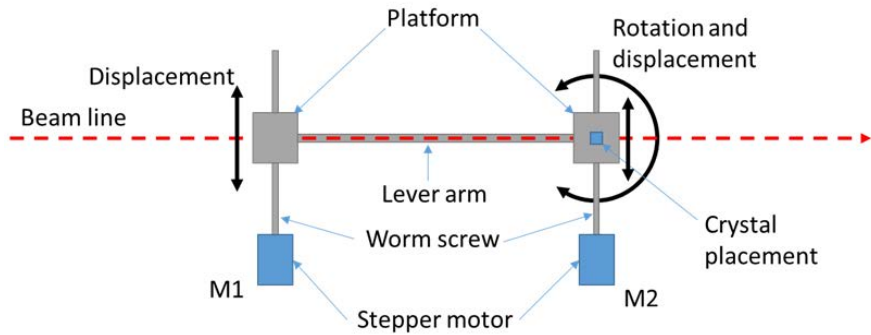


Figure B.1: CINEL stepper motor based goniometer working principle

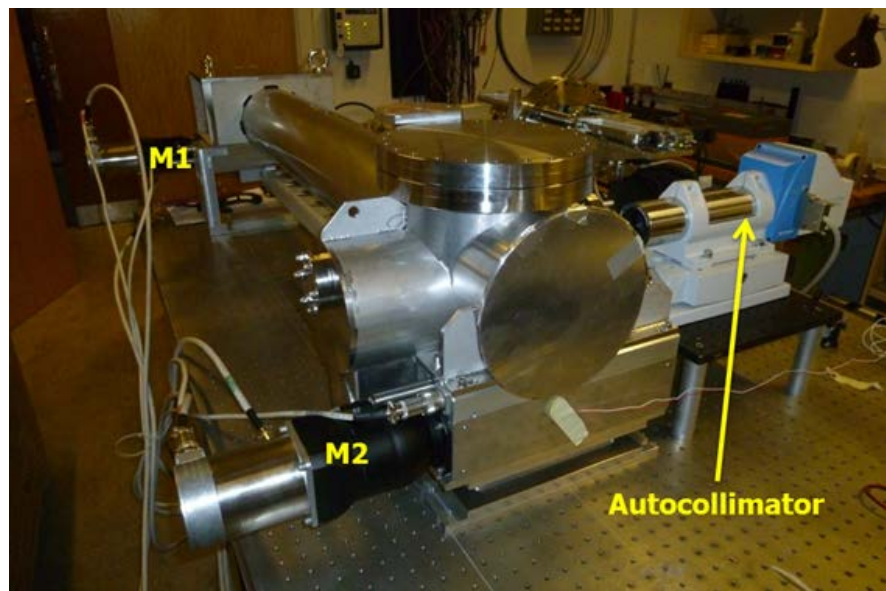


Figure B.2: CINEL stepper motor based goniometer prototype

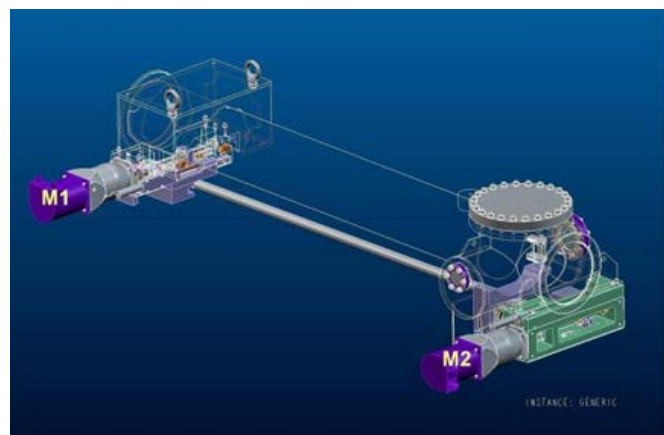


Figure B.3: CINEL stepper motor based goniometer 3D model

stepping motion applied with the motor excites the mechanical structural resonance and large overshoots appear. In Fig B.4 the angle in the crystal platform is measured when one step in half step mode is applied in axis M1. This angle is measured with an interferometer, measuring 2 distances to a mirror attached to the crystal platform and applying trigonometry to obtain the angle.

In order to smooth the overshoot in the crystal platform, it seems logical to avoid the introduction of high frequencies when moving it, as the standard stepping mode does. For this reason, both methods of motor control are tested and compared to achieve a better motion profile in the crystal platform.

For the comparison, the stepping mode choice is based on the best result for the standard stepping mode in previous results obtained, which corresponds to 1/4 step mode (1600 steps per rotor revolution). Two different tests are performed:

Applying 1 μrad steps: 1 μrad steps are applied each time, corresponding to 40 motor steps, applied at the rate corresponding to 2 rotor turns per second. Figs. B.5 and B.6 show the result for standard stepping mode and FOC, respectively.

Continuous motion: Continuous stepping at a rate corresponding to 2 rotor turns per second is applied. The standard deviation is calculated after de-trending the signal. Fig. B.7 shows the result for both working modes.

In the table B.1 the average of the results obtained is shown. From the figures and the table, it is clear that using FOC a great improvement in overshoot reduction and standard deviation reduction is achieved.

Table B.1: Overshoot and standard deviation comparison between stepping mode and FOC

Mode	1 μrad steps Overshoot (μrad)	Continuous STD (μrad)
Stepping:	5.1921	1.3763
FOC:	1.8403	0.9235

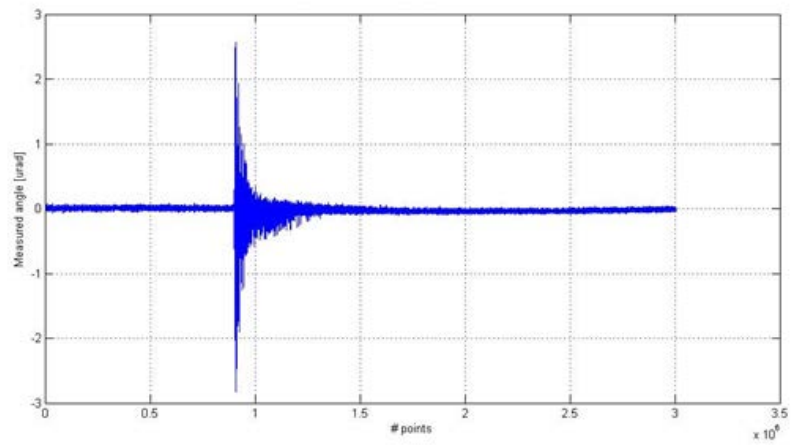


Figure B.4: Crystal platform position with standard stepping mode - one step applied

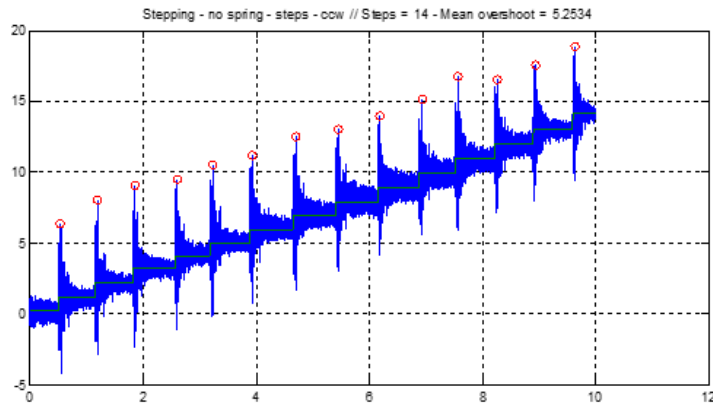


Figure B.5: Crystal platform position with standard stepping mode - 1 μ rad steps

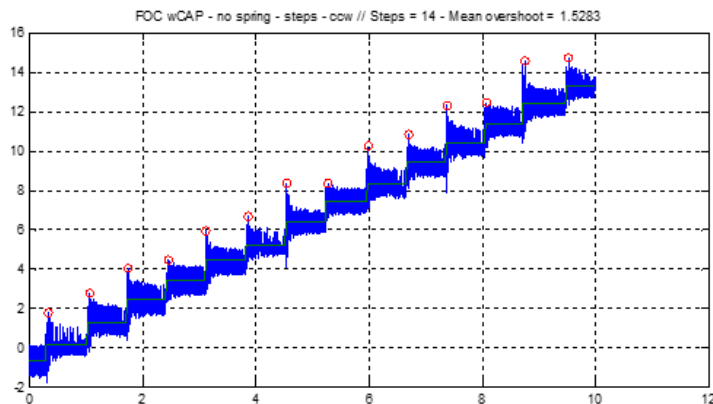


Figure B.6: Crystal platform position with FOC - 1 μ rad steps

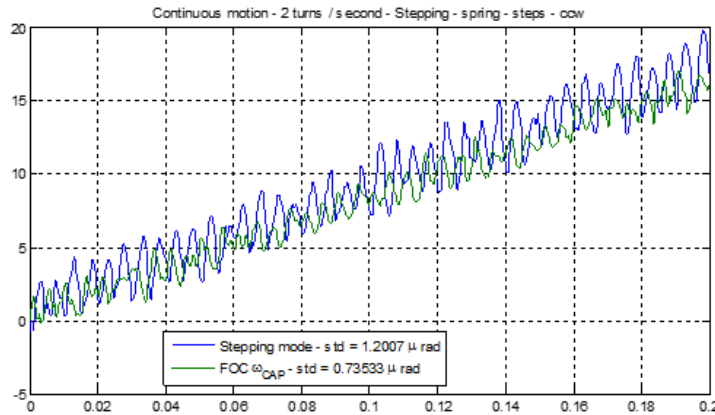


Figure B.7: Crystal platform positioning comparison - continuous motion

B.2 CINEL Piezo Actuator Based Goniometer

Also within the crystal collimation project, a different approach has been used for the design and prototyping of a second type of goniometer, based on piezo actuators for the angular positioning of the crystal. This design has been done in collaboration with the same company, CINEL.

In Fig. B.8 the basic working principle of the goniometer is presented. It consists of 2 stages. The first is a rotational stage, which supports the crystal and its holder and is moved with a piezo actuator. This stage is in charge of the angular positioning of the crystal, and the details of its operation are outside the scope of this work. The second one is the linear stage, in charge of moving the whole rotational stage in order to position the crystal in the beam line, and is actuated with stepper motors.

In Figs. B.9 and B.10 an external and an internal picture of the prototype are shown, respectively. There are 2 versions of the collimator, one of them rotates the crystal horizontally and the other one vertically.

The linear stage motion has been tested intensively with a standard stepping drive, and the vibration induced by the motor led to some problems of sensor alignment in the rotational stage. The sensor used to measure the crystal angular position is an interferometer, and is very sensitive to vibrations. For this reason, FOC was also tested for the movement of the linear stage.

A test is performed in which the linear stage is moved from one extreme of its motion range (outer switch) to the other one (inner switch). During this motion, the yaw angle (Fig. B.8) of the rotational stage is measured continuously with

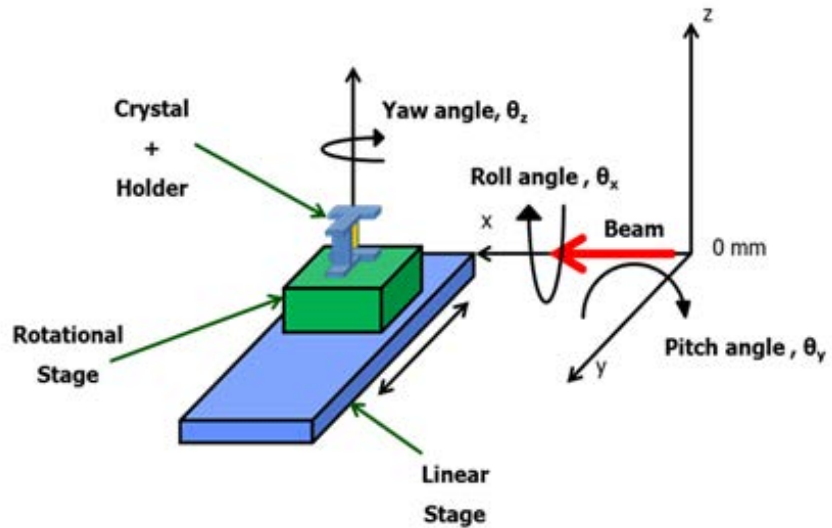


Figure B.8: CINEL Piezo based goniometer scheme

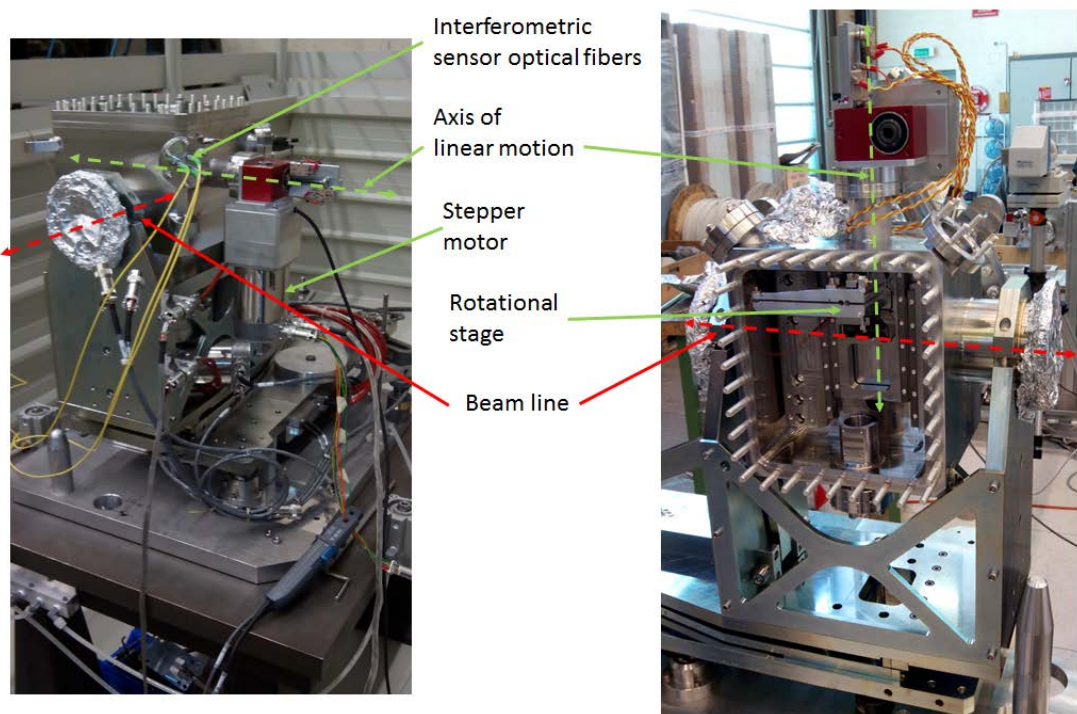


Figure B.9: CINEL Piezo based goniometer. Horizontal version (left) and vertical version (right)

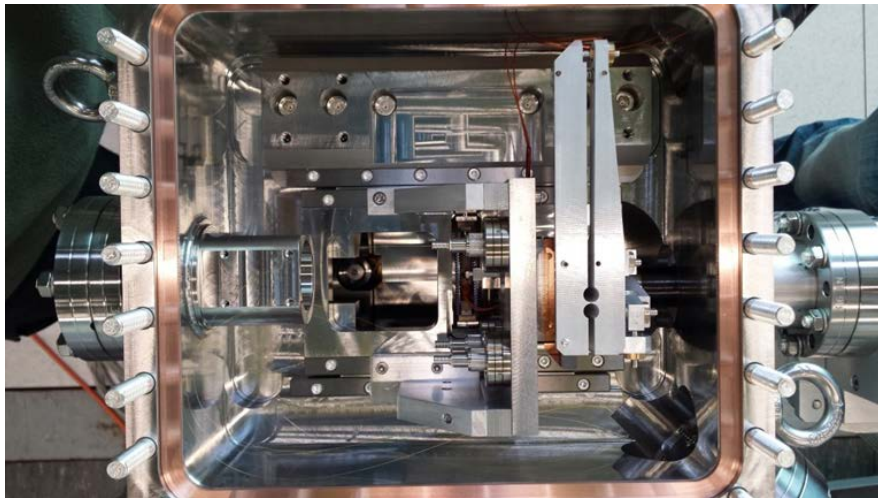


Figure B.10: CINEL Piezo based goniometer internal picture

the interferometer. This test has two parts, one where the rotational stage is not actuated by the piezo, and other one where the rotational stage is in closed loop holding its position.

In Fig. B.11 the results for the test performed with the rotational stage in open loop are shown. The measured yaw angle show that the oscillations along the linear range are significantly bigger in the stepper working mode than using FOC. The net increase in the angle is due to the mirror support deformation during the linear displacement.

In Fig. B.12 the results for the test performed with the rotational stage in closed loop are shown. Closing the loop in the rotational stage means that the piezo actuator follows the reference yaw angle given. For this test this reference is be zero, i.e. to hold the position during the movement. As result, the net increase of the yaw angle is zero in this occasion, but the oscillations during the movement are again significantly smaller in the FOC case. In table B.2 the result of this test is summarized quantitatively.

Even though improving the support of the interferometric sensor components

Table B.2: Standard deviation of the parasitic yaw in the rotational stage in closed loop test

Interferometer	
Mode	STD (μrad)
Stepping:	10.7805
FOC:	4.4462

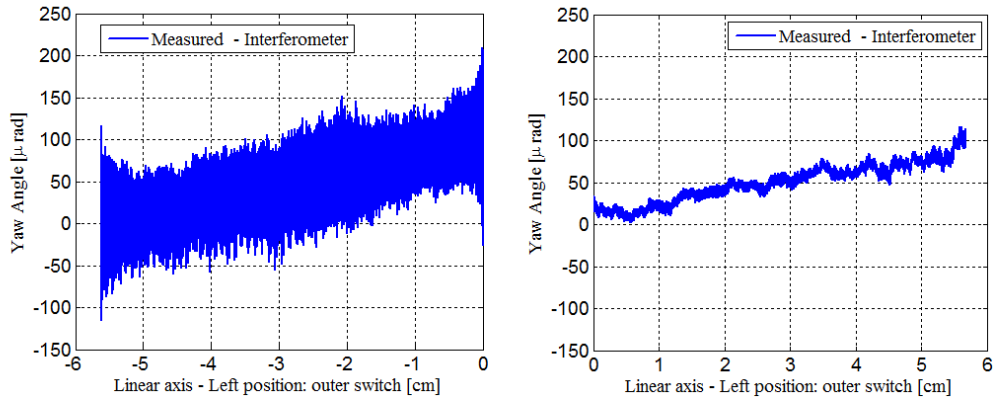


Figure B.11: CINEL Piezo based goniometer, rotational stage in open loop, full linear range motion parasitic yaw in standard stepping mode (left) and FOC (right)

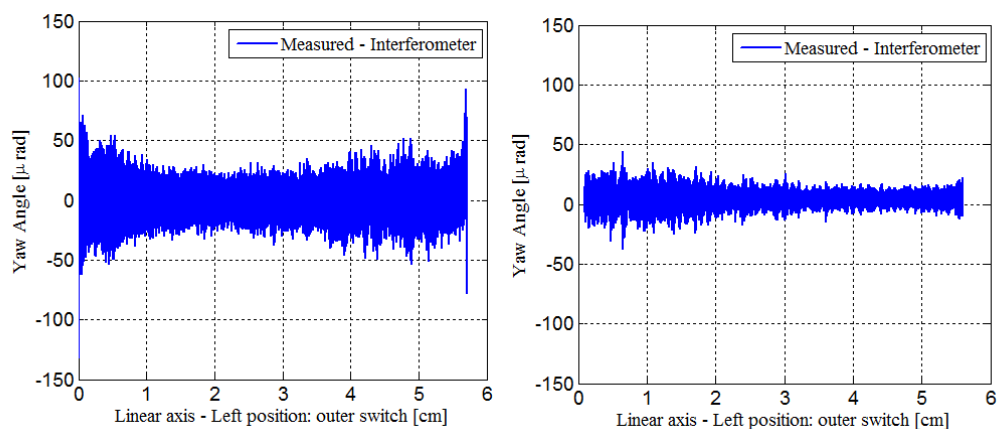


Figure B.12: CINEL Piezo based goniometer, rotational stage in closed loop, full linear range motion parasitic yaw comparison in standard stepping mode (left) and FOC (right)

in the rotational stage has improved the situation regarding the sensor misalignment provoked by the vibrations, using FOC seems a better option to avoid further problems with this type of highly sensitive sensor.

Bibliography

- [1] P.P. Acarnley. *Stepping motors: a guide to theory and practice*. Number 63. Iet, 2002.
- [2] P.P. Acarnley and J.F. Watson. Review of position-sensorless operation of brushless permanent-magnet machines. *IEEE Transactions on Industrial Electronics*, 53(2), 2006.
- [3] F. Auger and M. Hilairat. Industrial applications of the kalman filter: A review. *IEEE Transactions on Industrial Electronics*, PP(99):1, 2013. ISSN 0278-0046. doi: 10.1109/TIE.2012.2236994.
- [4] L.D. Avendano-Valencia, L.E. Avendano, J.M. Ferrero, and G. Castellanos-Dominguez. Improvement of an extended kalman filter power line interference suppressor for ecg signals. In *Computers in Cardiology, 2007*, pages 553–556, sep. 2007. doi: 10.1109/CIC.2007.4745545.
- [5] M. Barut, S. Bogosyan, and M. Gokasan. Speed-sensorless estimation for induction motors using extended kalman filters. *IEEE Transactions on Industrial Electronics*, 54(1):272–280, 2007.
- [6] M. Bendjedia, Y. Ait-Amirat, B. Walther, and A. Berthon. Sensorless control of hybrid stepper motor. In *2007 European Conference on Power Electronics and Applications*, pages 1–10. IEEE, 2007.
- [7] M. Bendjedia, Y. Ait-Amirat, B. Walther, and A. Berthon. Position control of a sensorless stepper motor. *IEEE Transactions on Power Electronics*, 27(2):578587, 2012.
- [8] M. Bendjedia, A. Khlaief, and M. Boussak. Sensorless speed control of outrunner pmsm drive connected to long cable for flying remote operative vehicle. pages 2252–2258, Sept 2012. doi: 10.1109/ICELMach.2012.6350195.

- [9] F. Betin, D. Pinchon, and G.-A Capolino. Fuzzy logic applied to speed control of a stepping motor drive. *Industrial Electronics, IEEE Transactions on*, 47(3):610–622, Jun 2000. ISSN 0278-0046. doi: 10.1109/41.847902.
- [10] J. Bocker and S. Mathapati. State of the art of induction motor control. In *Electric Machines Drives Conference, 2007. IEMDC '07. IEEE International*, volume 2, pages 1459–1464, May 2007. doi: 10.1109/IEMDC.2007.383643.
- [11] L. Bodizs, B. Srinivasan, and D. Bonvin. Preferential estimation via tuning of the kalman filter. In *DYCOPS 7*, page 108, 2004.
- [12] S. Bolognani, R. Oboe, and M. Zigliotto. Sensorless full-digital PMSM drive with EKF estimation of speed and rotor position. *IEEE Transactions on Industrial Electronics*, 46(1):184–191, 1999.
- [13] F. Briz and M.W. Degner. Rotor position estimation. *IEEE Industrial Electronics Magazine*, 5(2):24 –36, June 2011. ISSN 1932-4529. doi: 10.1109/MIE.2011.941118.
- [14] R. G. Brown and P. Y. C Hwang. *Introduction to Random Signals and Applied Kalman Filtering*. John Wiley & Sons, 1985.
- [15] M. Butcher, A. Masi, R. Picatoste, and A. Giustiniani. Hybrid stepper motor electrical model extensions for use in intelligent drives. *Industrial Electronics, IEEE Transactions on*, 61(2):917–929, Feb 2014. ISSN 0278-0046. doi: 10.1109/TIE.2013.2254097.
- [16] Mark Butcher, Alessandro Masi, Michele Martino, and Andrea Tacchetti. Implementation and tuning of the extended kalman filter for a sensorless drive working with arbitrary stepper motors and cable lengths. In *XXth International Conference on Electrical Machines (ICEM)*, pages 2216 –2222, sept. 2012. doi: 10.1109/ICELMach.2012.6350190.
- [17] D. Casadei, F. Profumo, G. Serra, and A Tani. Foc and dtc: two viable schemes for induction motors torque control. *Power Electronics, IEEE Transactions on*, 17(5):779–787, Sep 2002. ISSN 0885-8993. doi: 10.1109/TPEL.2002.802183.

- [18] W.D. Chen, K.L. Yung, and K.W. Cheng. A learning scheme for low-speed precision tracking control of hybrid stepping motors. *Mechatronics, IEEE/ASME Transactions on*, 11(3):362–365, June 2006. ISSN 1083-4435. doi: 10.1109/TMECH.2006.875574.
- [19] G. Conte. Control optimization of the LHC stepping motor drivers. Master’s thesis, Universita degli Studi di Napoli Federico II, 2006.
- [20] A.C.S. de Lima, R.M. Stephan, A. Pedroso, and J. Mourente. Analysis of a long distance drive for an induction motor. 2:867–872 vol.2, Jun 1996. doi: 10.1109/ISIE.1996.551057.
- [21] M. Depenbrock. Direct self-control (dsc) of inverter-fed induction machine. *Power Electronics, IEEE Transactions on*, 3(4):420–429, Oct 1988. ISSN 0885-8993. doi: 10.1109/63.17963.
- [22] R. Devasahayam, V.T.S. Achary, M. H. Ravichandran, S. Simon, P. Muralikrishna, C. C. Joseph, and P. M. Varghese. Performance enhancement of a 720-step stepper motor for solar array drive of indian remote sensing satellites to achieve low power micro-stepping. In *Power Electronics and Drive Systems, 2003. PEDS 2003. The Fifth International Conference on*, volume 1, pages 264–268 Vol.1, Nov 2003. doi: 10.1109/PEDS.2003.1282784.
- [23] H. Durrant-Whyte. *Introduction to Estimation and the Kalman Filter*. Australian Centre for Field Robotics, 2001.
- [24] Timothy A Ferris, Stephen M Fortescue, and Gaston Palombo. High performance incremental motion system using a closed loop stepping motor, May 27 1986. US Patent 4,591,774.
- [25] P.T. Finlayson. Output filters for PWM drives with induction motors. *Industry Applications Magazine, IEEE*, 4(1):46 –52, jan/feb 1998. ISSN 1077-2618. doi: 10.1109/2943.644886.
- [26] A. E. Fitzgerald, C. Jr. Kingsley, and S. D. Umans. *Electric Machinery*. McGraw-Hill, 2003.
- [27] Hamed Shisheh Foroush. Angle estimation in a pwm stepper motor driver by kalman filtering. Master’s thesis, cole polytechnique fdrale de Lausanne (EPFL), 2010.

- [28] Gene F Franklin, Michael L Workman, and Dave Powell. *Digital control of dynamic systems*. Addison-Wesley Longman Publishing Co., Inc., 1997.
- [29] Xavier del Toro Garcia, Branislav Zigmund, Angela A Terlizzi, Rastislav Pavlanin, and Ligui Salvatore. Comparison between foc and dtc strategies for permanent magnet synchronous motors. *Advances in Electrical and Electronic Engineering*, 5(1-2):76–81, 2011.
- [30] M.S. Grewal and A.P. Andrews. *Kalman filtering: theory and practice using MATLAB*. Wiley-IEEE Press, 2008.
- [31] S. Hang. Understanding extended kalman filter. Technical report, Faculty of Engineering and Information Technology, University of Technology Sydney, 2010.
- [32] N. Hanigovszki. *EMC output filters for adjustable speed drives*. PhD thesis, 2005.
- [33] S.Y.R. Hui, J.G. Zhu, and V.S. Ramsden. A generalized dynamic circuit model of magnetic cores for low- and high-frequency applications. ii. circuit model formulation and implementation. *Power Electronics, IEEE Transactions on*, 11(2):251–259, Mar 1996. ISSN 0885-8993. doi: 10.1109/63.486173.
- [34] Seong Gu Kang and D.K. Lieu. Torque analysis of combined 2d fem and lumped parameter method for a hybrid stepping motor. In *Electric Machines and Drives, 2005 IEEE International Conference on*, pages 1199 –1203, may 2005. doi: 10.1109/IEMDC.2005.195874.
- [35] H Kellermann, P Hildinger, G Brandenburg, and J Heinzl. Field oriented position control of a hybrid stepper motor. In *Proc. of the EPE Conference*, volume 3, pages 908–913, 1995.
- [36] T. Kenjo and A. Sugawara. *Stepping motors and their microprocessor controls*. Clarendon Press Oxford, 1994.
- [37] R.J. Kerkman, D. Leggate, and G.L. Skibinski. Interaction of drive modulation and cable parameters on ac motor transients. *Industry Applications, IEEE Transactions on*, 33(3):722–731, May 1997. ISSN 0093-9994. doi: 10.1109/28.585863.

- [38] T. Kim, H.W. Lee, and M. Ehsani. Position sensorless brushless dc motor/generator drives: review and future trends. *Electric Power Applications, IET*, 1(4):557–564, 2007.
- [39] W. Kim, D. Shin, and C.C. Chung. Microstepping using a disturbance observer and a variable structure controller for permanent-magnet stepper motors. *IEEE Transactions on Industrial Electronics*, 60(7):2689–2699, July 2013. ISSN 0278-0046. doi: 10.1109/TIE.2012.2198033.
- [40] T. Kosaka and N. Matsui. Simple nonlinear magnetic analysis for three-phase hybrid stepping motors. In *Conference Record of the 2000 IEEE Industry Applications Conference*, volume 1, pages 126–131. IEEE, 2000.
- [41] C. Kuert, M. Jufer, and Y. Perriard. New method for dynamic modeling of hybrid stepping motors. In *37th IAS Annual Meeting. Conference Record of the Industry Applications Conference*, volume 1, pages 6–12. IEEE, 2002.
- [42] M.D. Laan. *Signal Sampling Techniques for Data Acquisition in Process Control*. PhD thesis, University of Groningen, 1995.
- [43] I.D. Landau and G. Zito. *Digital control systems: design, identification and implementation*. Springer Verlag, 2006.
- [44] Quy Ngoc Le and Jae-Wook Jeon. Neural-network-based low-speed-damping controller for stepper motor with an fpga. *Industrial Electronics, IEEE Transactions on*, 57(9):3167–3180, Sept 2010. ISSN 0278-0046. doi: 10.1109/TIE.2009.2037650.
- [45] C.A. Lightcap and S.A. Banks. An extended kalman filter for real-time estimation and control of a rigid-link flexible-joint manipulator. *IEEE Transactions on Control Systems Technology*, 18(1):91 –103, jan. 2010. ISSN 1063-6536. doi: 10.1109/TCST.2009.2014959.
- [46] Ki-Chae Lim, Jung-Pyo Hong, and Gyu-Tak Kim. Characteristic analysis of 5-phase hybrid stepping motor considering the saturation effect. *IEEE Transactions on Magnetics*, 37(5):3518 –3521, sep 2001. ISSN 0018-9464. doi: 10.1109/20.952651.

- [47] S. Lin and E.S. Kuh. Transient simulation of lossy interconnects based on the recursive convolution formulation. *IEEE Transactions on Circuits and Systems. 1, Fundamental theory and applications*, 39(11):879–892, 1992.
- [48] Weijie Lin and Zhuo Zheng. Simulation and experiment of sensorless direct torque control of hybrid stepping motor based on dsp. In *Mechatronics and Automation, Proceedings of the 2006 IEEE International Conference on*, pages 2133–2138, June 2006. doi: 10.1109/ICMA.2006.257623.
- [49] Roland Longchamp. *Commande Numrique De Systmes Dynamiques - Cours D'automatique*. PPUR Presses polytechniques, 2006.
- [50] M. Martino, A. Masi, R. Losito, and R. Picatoste Ruilope. Low emission, self-tunable dsp based stepping motor drive for use with arbitrarily long cables. In *Conference record of the 12th LSS symposium*, 2010.
- [51] A. Masi and R. Losito. Lhc collimators low level control system. *IEEE Transactions on Nuclear Science*, 55(1):333–340, Feb. 2008. ISSN 0018-9499. doi: 10.1109/TNS.2007.914206.
- [52] A. Masi, G. Conte, R. Losito, and M. Martino. Dsp-based stepping motor drivers for the lhc collimators. *IEEE Transactions on Nuclear Science*, 55(1 Part 1):341–348, 2008.
- [53] A. Masi, G. Conte, R. Losito, and M. Martino. Driving the LHC collimators stepping motors over 1 km with high accuracy avoiding EMI effects. In *Proceedings of IPAC2011, San Sebastian, Spain*, 2011.
- [54] A. Masi, M. Butcher, R. Losito, and R. Picatoste. Dsp based smart sensorless stepping motor driver for lhc collimators. In *Real Time Conference (RT), 2012 18th IEEE-NPSS*, pages 1–7, June 2012. doi: 10.1109/RTC.2012.6418215.
- [55] A. Masi, M. Butcher, M. Martino, and R. Picatoste. An application of the extended kalman filter for a sensorless stepper motor drive working with long cables. *IEEE Transactions on Industrial Electronics*, 59(11):4217 –4225, nov. 2012. ISSN 0278-0046. doi: 10.1109/TIE.2011.2178213.
- [56] A. Masi, M. Butcher, R. Losito, and R. Picatoste. Dsp based smart sensorless stepping motor driver for lhc collimators. *Nuclear Science*,

- IEEE Transactions on*, 60(5):3514–3520, Oct 2013. ISSN 0018-9499. doi: 10.1109/TNS.2013.2267055.
- [57] N. Matsui, M. Nakamura, and T. Kosaka. Instantaneous torque analysis of hybrid stepping motor. *IEEE Transactions on Industry Applications*, 32(5): 1176 –1182, sep/oct 1996. ISSN 0093-9994. doi: 10.1109/28.536880.
- [58] P. Maybeck. *Stochastic Models, Estimation, and Control. Vol. 1*. Academic Press, 1979.
- [59] Giovanni Miano and Antonio Maffucci. *Transmission Lines and Lumped Circuits*. Academic Press, 2001.
- [60] A.F. Moreira, T.A. Lipo, G. Venkataraman, and S. Bernet. High-frequency modeling for cable and induction motor overvoltage studies in long cable drives. *Industry Applications, IEEE Transactions on*, 38(5):1297–1306, Sep 2002. ISSN 0093-9994. doi: 10.1109/TIA.2002.802920.
- [61] M.J. Nave. On modeling the common mode inductor. In *Electromagnetic Compatibility, 1991. Symposium Record., IEEE 1991 International Symposium on*, pages 452 –457, aug 1991. doi: 10.1109/ISEM.C.1991.148275.
- [62] C. Obermeier, H. Kellermann, G. Brandenburg, and J. Heinzl. Sensorless field oriented speed control of a hybrid stepper motor using an extended kalman filter. In *7th European Conference on Power Electronics and Applications (EPE'97)*, 1997.
- [63] R.H. Park. Two-reaction theory of synchronous machines generalized method of analysis-part i. *American Institute of Electrical Engineers, Transactions of the*, 48(3):716–727, July 1929. ISSN 0096-3860. doi: 10.1109/T-AIEE.1929.5055275.
- [64] Clayton R. Paul. *Introduction to Electromagnetic Compatibility*. John Wiley & Sons, 2006.
- [65] Youbin Peng, D. Vrancic, and R. Hanus. Anti-windup, bumpless, and conditioned transfer techniques for pid controllers. *Control Systems, IEEE*, 16 (4):48–57, Aug 1996. ISSN 1066-033X. doi: 10.1109/37.526915.

- [66] J. Persson and Y. Perriard. An optimized extended kalman filter algorithm for hybrid stepper motors. In *The 29th Annual Conference of the IEEE Industrial Electronics Society, IECON'03.*, volume 1, pages 297–300, 2003.
- [67] Jan Persson. *Innovative Standstill Position Detection Combined With Sensorless Control of Synchronous Motors*. PhD thesis, cole Polytechnique Fdrale de Lausanne, 2005.
- [68] R. Petrella, M. Tursini, L. Peretti, and M. Zigliotto. Speed measurement algorithms for low-resolution incremental encoder equipped drives: a comparative analysis. In *Electrical Machines and Power Electronics, 2007. ACEMP '07. International Aegean Conference on*, pages 780–787, Sept 2007. doi: 10.1109/ACEMP.2007.4510607.
- [69] R. Picatoste. Development of a stepper motor drive and kalman filter application for the lhc collimation system. Master's thesis, Universidad Politecnica de Madrid, 2010.
- [70] R. Picatoste, M. Butcher, and A. Masi. Sine wave filter for stepper motor drives working with long cables. In *Electrical Machines (ICEM), 2012 XXth International Conference on*, pages 1075–1081, Sept 2012. doi: 10.1109/ ICElMach.2012.6350009.
- [71] P. Rocco, G. Gruosso, and G. Magnani. Mechatronic model of oscillations in hybrid stepper motors. In *2010 IEEE/ASME International Conference on Advanced Intelligent Mechatronics*, pages 726 –731, july 2010. doi: 10.1109/ AIM.2010.5695852.
- [72] A Rubaai, M.J. Castro-Sitiriche, M. Garuba, and L. Burge. Implementation of artificial neural network-based tracking controller for high-performance stepper motor drives. *Industrial Electronics, IEEE Transactions on*, 54(1): 218–227, Feb 2007. ISSN 0278-0046. doi: 10.1109/TIE.2006.888785.
- [73] N. Salvatore, A. Caponio, F. Neri, S. Stasi, and G.L. Casella. Optimization of delayed-state kalman-filter-based algorithm via differential evolution for sensorless control of induction motors. *IEEE Transactions on Industrial Electronics*, 57(1):385–394, 2010. ISSN 0278-0046.
- [74] Walter Scandale. Ua9 report for 2013. Technical report, CERN, 2013.

- [75] Walter Scandale. The ua9 experiment on crystal-assisted collimation at the cern-super proton synchrotron: Tutorial 48. *IEEE Instrumentation & Measurement Magazine*, 1094(6969/14), 2014.
- [76] Walter Scandale and Michela Prest. Proposal of the crystal experiment. Technical report, CERN, 2008.
- [77] T. Schuhmann, W. Hofmann, and R. Werner. Improving operational performance of active magnetic bearings using kalman filter and state feedback control. *IEEE Transactions on Industrial Electronics*, 59(2):821 –829, Feb. 2012. ISSN 0278-0046. doi: 10.1109/TIE.2011.2161056.
- [78] K.L. Shi, T.F. Chan, Y.K. Wong, and S.L. Ho. Speed estimation of an induction motor drive using an optimized extended kalman filter. *IEEE Transactions on Industrial Electronics*, 49(1):124–133, 2002.
- [79] D. Simon. *Optimal state estimation: Kalman, H ∞ and nonlinear approaches*. John Wiley and Sons, 2006.
- [80] S.P. Singh, J.H. Burry, and B. Watson. *Approximation theory and spline functions*. D Reidel Pub Co, 1984.
- [81] G.L. Skibinski, R.J. Kerkman, and D. Schlegel. EMI emissions of modern PWM AC drives. *Industry Applications Magazine, IEEE*, 5(6):47 –80, nov/dec 1999. ISSN 1077-2618. doi: 10.1109/2943.798337.
- [82] Y. Sozer, D.A. Torrey, and S. Reva. New inverter output filter topology for PWM motor drives. *Power Electronics, IEEE Transactions on*, 15(6):1007 –1017, nov 2000. ISSN 0885-8993. doi: 10.1109/63.892815.
- [83] J.K. Steinke. Use of an LC filter to achieve a motor-friendly performance of the PWM voltage source inverter. *Energy Conversion, IEEE Transactions on*, 14(3):649 –654, sep 1999. ISSN 0885-8969. doi: 10.1109/60.790930.
- [84] Seung-Ki Sul. *Control of electric machine drive systems*, volume 88. John Wiley & Sons, 2011.
- [85] I Takahashi and T. Noguchi. A new quick-response and high-efficiency control strategy of an induction motor. *Industry Applications, IEEE Transactions on*, IA-22(5):820–827, Sept 1986. ISSN 0093-9994. doi: 10.1109/TIA.1986.4504799.

- [86] Takashi Takebayashi, David Cho, Dipen Gokhale, and Pavel Tomov. Stepping motor control system and method for controlling a stepping motor using closed and open loop controls, August 19 2007. US Patent App. 11/206,943.
- [87] B. Terzic and M. Jadric. Design and implementation of the extended kalman filter for the speed and rotor position estimation of brushless dc motor. *IEEE Transactions on Industrial Electronics*, 48(6):1065, 2001.
- [88] K.W.-H. Tsui, N.C. Cheung, and K.C.-W. Yuen. Novel modeling and damping technique for hybrid stepper motor. *IEEE Transactions on Industrial Electronics*, 56(1):202 –211, jan. 2009. ISSN 0278-0046. doi: 10.1109/TIE.2008.2008791.
- [89] Unitrode. Uc3717 and l-c filter reduce emi and chopping losses in step motor. Technical report, Texas Instruments, 1999.
- [90] Peter Vas. *Sensorless vector and direct torque control*. Oxford Univ. Press, 1998.
- [91] A. von Jouanne and P.N. Enjeti. Design considerations for an inverter output filter to mitigate the effects of long motor leads in ASD applications. *Industry Applications, IEEE Transactions on*, 33(5):1138 –1145, sep/oct 1997. ISSN 0093-9994. doi: 10.1109/28.633789.
- [92] J. D. Wale and C. Pollock. A low-cost sensorless technique for load torque estimation in a hybrid stepping motor. *IEEE Transactions on Industrial Electronics*, 46(4):833841, 1999.
- [93] Dave Wilson. Motor control compendium [online], 2010. URL http://focus.ti.com/download/trng/docs/c2000/TI_MotorControlCompendium_2010.pdf.
- [94] S. Yang and E. Kuo. Damping a hybrid stepping motor with estimated position and velocity. *IEEE Transactions on Power Electronics*, 18(3):880887, 2003.
- [95] Peter C. Young. *Recursive Estimation and Time-Series Analysis: An Introduction for the Student and Practitioner*. Springer Verlag, 2nd edition, 2011.

- [96] L. Zhong, M.F. Rahman, W. Y. Hu, and K. W. Lim. Analysis of direct torque control in permanent magnet synchronous motor drives. *Power Electronics, IEEE Transactions on*, 12(3):528–536, May 1997. ISSN 0885-8993. doi: 10.1109/63.575680.